

In vitro reconstitution of HIV-1 capsid transport

Author:

Peng, Wang

Publication Date:

2021

DOI:

<https://doi.org/10.26190/unsworks/2033>

License:

<https://creativecommons.org/licenses/by/4.0/>

Link to license to see what you are allowed to do with this resource.

Downloaded from <http://hdl.handle.net/1959.4/100123> in <https://unsworks.unsw.edu.au> on 2024-04-19



In vitro reconstitution of HIV-1 capsid transport

Wang Peng

A thesis in fulfilment of the requirements for the degree of

Doctor of Philosophy

School of Medical Science

Faculty of Medicine

Nov 2021

Thesis submission for the degree of Doctor of Philosophy

Thesis Title and Abstract

Declarations

Inclusion of Publications
Statement

Corrected Thesis and
Responses

Thesis Title

In vitro reconstitution of HIV-1 capsid transport

Thesis Abstract

The HIV-1 capsid interacts with multiple host factors during its early life cycle to achieve successful infection. In this thesis we aim to expand our understanding of how interactions between the capsid and host cell factors regulate viral activities, with chapter 4 and 5 specifically focusing on the cytoplasmic transport process. Based on cellular and biochemical evidence, recent studies suggest that HIV-1 capsid hijacks both dynein and kinesin-1, via the adaptor proteins BICD2 and FEZ1 respectively, for active transport along microtubule network. We will present our work to reconstitute these complexes and demonstrate their motilities along microtubules *in vitro*, providing more direct evidence to support these models.

To investigate the interactions between HIV-1 capsid and the motor adaptors, we applied a fluorescence fluctuation spectroscopy based binding assay and a total internal reflection microscopy (TIRFm) based binding assay. These approaches allowed us to generate quantitative descriptions of the interactions between HIV-1 capsid and the adaptor proteins.

Subsequently, we reconstituted the motor-adaptor-cargo complexes (DDBC and KFC) using recombinant proteins as well as components isolated from native tissues. We have successfully demonstrated both the dynein- and kinesin-dependent transport of HIV-1 capsid along microtubules *in vitro* using a TIRFm based single molecule motility assay. We also further characterized the motile behaviors and properties of the KFC complex.

Our work validated the proposed models for the cytoplasmic transport of HIV-1 capsid and demonstrated the minimum requirement for this process. In general, this work has made solid contributions towards the understanding both HIV virology and motor-driven cargo transport, as well as opened opportunities to a range of exciting research questions in both fields.

Thesis submission for the degree of Doctor of Philosophy

Thesis Title and Abstract

Declarations

Inclusion of Publications
Statement

Corrected Thesis and
Responses

ORIGINALITY STATEMENT

☒ I hereby declare that this submission is my own work and to the best of my knowledge it contains no materials previously published or written by another person, or substantial proportions of material which have been accepted for the award of any other degree or diploma at UNSW or any other educational institution, except where due acknowledgement is made in the thesis. Any contribution made to the research by others, with whom I have worked at UNSW or elsewhere, is explicitly acknowledged in the thesis. I also declare that the intellectual content of this thesis is the product of my own work, except to the extent that assistance from others in the project's design and conception or in style, presentation and linguistic expression is acknowledged.

COPYRIGHT STATEMENT

☒ I hereby grant the University of New South Wales or its agents a non-exclusive licence to archive and to make available (including to members of the public) my thesis or dissertation in whole or part in the University libraries in all forms of media, now or hereafter known. I acknowledge that I retain all intellectual property rights which subsist in my thesis or dissertation, such as copyright and patent rights, subject to applicable law. I also retain the right to use all or part of my thesis or dissertation in future works (such as articles or books).

For any substantial portions of copyright material used in this thesis, written permission for use has been obtained, or the copyright material is removed from the final public version of the thesis.

AUTHENTICITY STATEMENT

☒ I certify that the Library deposit digital copy is a direct equivalent of the final officially approved version of my thesis.

Thesis submission for the degree of Doctor of Philosophy

Thesis Title and Abstract

Declarations

Inclusion of Publications
Statement

Corrected Thesis and
Responses

UNSW is supportive of candidates publishing their research results during their candidature as detailed in the UNSW Thesis Examination Procedure.

Publications can be used in the candidate's thesis in lieu of a Chapter provided:

- The candidate contributed **greater than 50%** of the content in the publication and are the "primary author", i.e. they were responsible primarily for the planning, execution and preparation of the work for publication.
- The candidate has obtained approval to include the publication in their thesis in lieu of a Chapter from their Supervisor and Postgraduate Coordinator.
- The publication is not subject to any obligations or contractual agreements with a third party that would constrain its inclusion in the thesis.

☒ The candidate has declared that **some of the work described in their thesis has been published and has been documented in the relevant Chapters with acknowledgement**.

A short statement on where this work appears in the thesis and how this work is acknowledged within chapter/s:

The results from paper "Functional analysis of the secondary HIV-1 capsid binding site in the host protein cyclophilin A" published in "Retrovirology" is contained in part into thesis Chapter 3 (section 3.2; page 65-81). Acknowledge of the contributions from the co-authors have been made at the beginning of Chapter 3 and in the acknowledgements section. Consents from the co-authors have also been acquired to use this paper as part of my thesis.

Candidate's Declaration



I declare that I have complied with the Thesis Examination Procedure.

Acknowledgements

The work contained in this thesis was carried out at the Molecular Machines groups as part of Single Molecule Science at UNSW, Sydney. I was supported by the International postgraduate research scholarship (UIPA) during my PhD candidature.

I would like to thank my supervisor, Dr. Till Böcking for his amazing guidance and support throughout my PhD candidature. You have been an extremely insightful, patient, and caring mentor and you have made my PhD experience way more enjoyable than I would have expected. I would also like to thank my mentors Dr. Jeff Stear for baby-sitting me in the lab all the time, and Dr. David Jacques for continuous feedbacks on my research. Till, Jeff, and David guided me through my candidature and established me as a young scientist with confidence; highly appreciated.

Thanks to the lovely people in the Structural Virology & Molecular Machines groups (current and alumni): to Derrick for showing me lab stuff when I started and for being an honest friend, to my science buddy K.M for sharing the ups and downs, to Vaibhav for the good lunch times and good science advice, to Andrew for providing constructs and for calling Ubers for me when I was too drunk to do it myself, to James for the assistance with data analysis, and to Conall, Sophie, Nan, Claire, Martin, Maggie, Ruijie, Raphael, Shivani, Chantal, Ilina, Miro. I will be missing the time we spent together with smiles on my face.

Thanks to the community of students from Lowy level 3 for being such wonderful people to be around with and for the drinking nights.

Hey 2-beer-clubbers, you guys are just awesome; making the Friday afternoons brighter than they already were.

Thanks to Arthur, Feyza, Jac, and Krystyna for gifting heads of euthanized mice.

Thanks to the staff at EMU, especially Natasha who trained me, for the help with electron microscope imaging.

Thanks to our collaborators Richard J McKenney and Gary Brouhard for gifting constructs and for the expertise advice on the project.

Thanks to the co-authors to allow me incorporating the published paper into my thesis Chapter 3.

This sounds weird, but thanks to the short distance between Lowy and Coogee; the days to watch sunrise at Coogee beach before walking to morning work would be missed.

And to my family; in my culture we do not really say thanks to family members, I love you all.

Table of Contents

Acknowledgements	iv
List of Figures	xi
List of Tables	xiii
Publications and conferences	xiv
List of abbreviations and symbols	xv
1. Literature review	1
1.1. HIV	2
1.1.1. HIV and AIDS	2
1.1.2. HIV-1 viral structure and life cycle	2
1.1.2.1. HIV-1 genome structure	2
1.1.2.2. HIV-1 virion structure	4
1.1.2.3. HIV-1 life cycle	5
1.1.3. HIV-1 capsid	7
1.1.3.1. Roles of HIV-1 capsid	7
1.1.3.2. Structure of HIV-1 capsid	8
1.1.3.2.1. HIV-1 CA monomer	9
1.1.3.2.2. HIV-1 CA hexamers and pentamers	9
1.1.3.2.3. HIV-1 capsid lattice	10
1.1.3.3. HIV-1 capsid uncoating	12
1.1.3.4. Canonical binding interfaces of HIV-1 capsid and interacting host factors	14
1.1.3.4.1. The CypA-binding loop and interacting host factors	14
1.1.3.4.2. The central pore and interacting host factors	17
1.1.3.4.3. The NTD-CTD interface and interacting host factors	19
1.1.3.4.4. The tri-hexamer interface and interacting host factors	20
1.2. HIV-1 retrograde transport	21
1.2.1. Microtubules	21
1.2.2. Dynein dependent transport	24
1.2.3. Kinesin-1 dependent transport	25

1.2.4.	Model of HIV-1 retrograde transport	26
1.3.	Motor protein complexes	28
1.3.1.	Dynein motor complex	28
1.3.1.1.	Dynein	28
1.3.1.2.	Dynactin	31
1.3.1.3.	Dynein-dynactin-BICD2N (DDB) and Dynein-dynactin-BICD2-capsid (DDBC) complexes	32
1.3.2.	Kinesin-1 motor complexes	33
1.4.	Research proposal and research aims	35
2.	Materials and methods	37
2.1.	TIRFm (total internal fluorescence microscopy)	38
2.1.1.	Microscope set up	38
2.1.2.	Microfluidic device set up	38
2.1.3.	Surface chemistry in the microfluidic flow channels	39
2.1.4.	TIRFm binding assay	39
2.1.5.	TIRFm motility assay	40
2.1.6.	Single molecule photobleaching	41
2.1.7.	Image analysis	42
2.2.	HIV-1 capsid	44
2.2.1.	Plasmid constructs	44
2.2.2.	HIV-1 CA protein expression and purification	45
2.2.3.	Fluorescent labelling of HIV-1 CA protein	47
2.2.4.	In vitro assembly of HIV-1 capsid	47
2.2.4.1.	<i>In vitro</i> assembly of HIV-1 CA to produce cones that are stabilized, remain soluble, and are labelled with fluorophores	47
2.2.4.2.	<i>In vitro</i> assembly of CA tubes on coverslip	48
2.2.5.	Immobilization of the self-assembled HIV-1 capsids on modified coverslip	48
2.3.	Microtubule	48
2.3.1.	Tubulin purification	48
2.3.1.1.	The TOG-affinity protocol	49
2.3.1.2.	The high-molarity buffer protocol	49
2.3.2.	Fluorescent labelling of tubulin	50

2.3.3.	Polymerization of microtubules	50
2.3.4.	Immobilization of microtubules on modified coverslip	51
2.4.	Other recombinant proteins	51
2.4.1.	Cyclophilin A	51
2.4.2.	hFEZ1 (human fasciculation and elongation protein zeta-1) protein	51
2.4.2.1.	Plasmid constructs	51
2.4.2.2.	hFEZ1 proteins expression and purification	52
2.4.3.	mBICD2 (mouse protein bicaudal D homolog 2)	53
2.4.3.1.	Plasmid constructs	53
2.4.3.2.	mBICD2 protein expression and purification	53
2.4.3.3.	mBICD2N (aa 25-400) protein expression and purification	56
2.4.4.	hKif5B (human kinesin-1 heavy chain)	56
2.4.4.1.	Plasmid constructs	56
2.4.4.2.	hKif5B proteins expression and purification	57
2.4.4.3.	Fluorescent labelling of dark hKif5B and purification	57
2.4.5.	hMAP7 (human microtubule associated protein 7)	57
2.4.5.1.	Plasmid constructs	57
2.4.5.2.	hMAP7 proteins expression and purification	58
2.5.	Isolated protein complexes from brain	58
2.5.1.	DDb (dynein-dynactin-BICD2N)	59
2.5.2.	DD (dynein-dynactin)	59
2.6.	Reconstitution of motor-adaptor-(capsid) complexes	60
2.6.1.	DDb(rec)	60
2.6.2.	DDB (dynein-dynactin-BICD2)	60
2.6.3.	DDBC (dynein-dynactin-BICD2-capsid)	60
2.6.4.	KFC (Kif5B-FEZ1-capsid)	60
2.6.5.	KF (Kif5B-FEZ1)	61
2.7.	Negative staining electron microscopy	61
2.8.	SPR (surface plasmon response)	61
3.	HIV-1 capsid serves as a lattice that interacts with host factors	62
3.1.	Introduction	63

3.2. HIV-1 capsid interacts with CypA: Published paper ‘Functional analysis of the secondary HIV-1 capsid binding site in the host protein cyclophilin A’	65
3.3. <i>In vitro</i> assembly of HIV-1 CA to produce cones that are stabilized, remain soluble, and are labelled with fluorophores	82
3.4. The self-assembled HIV-1 capsids (from CA A92E/A204C) interact with known capsid binders	84
3.5. Summary	85
<u>4. <i>In vitro</i> reconstitution of dynein-dependent transport of HIV-1 capsid</u>	<u>86</u>
4.1. Introduction	87
4.2. BICD2 interacts with HIV-1 capsid	88
4.2.1. Quantitative analysis of the BICD2-capsid interaction	88
4.2.2. BICD2 binds to HIV-1 capsid primarily via the R18 ring	90
4.3. Reconstitution and visualization of the DDBC complex walking along microtubules	92
4.4. Discussion	94
<u>5. <i>In vitro</i> reconstitution of kinesin-dependent transport of HIV-1 capsid</u>	<u>96</u>
5.1. Introduction	97
5.2. FEZ1 interacts with HIV-1 capsid	98
5.2.1. Quantitative analysis of the FEZ1-capsid interaction	98
5.2.2. FEZ1 binds to HIV-1 capsid primarily via the R18 ring	100
5.3. Reconstitution and visualization of the KFC complex walking along microtubules	101
5.3.1. Reconstitution of KFC motility	102
5.3.2. The R18 ring of HIV-1 capsid is required to form a processive KFC complex	107
5.3.3. Effects of fluorescent labels and the CA R18G mutation on motility parameters	109
5.4. HIV-1 capsid is a passenger of the Kif5B-FEZ1 complex	114
5.4.1. Kif5B and FEZ1 can form a processive KF complex without a cargo	114
5.4.2. Comparison between KF and KFC complexes	116
5.5. Discussion	118
<u>6. Conclusions and future directions</u>	<u>121</u>
<u>7. References</u>	<u>126</u>
<u>8. Supplementary information</u>	<u>147</u>

8.1. Immobilization of pre-assembled microtubules and HIV-1 capsids on modified surfaces	148
8.2. SDS PAGE showing the purified proteins	149
8.3. Summary of the interaction measurements between BICD2 or FEZ1 and HIV-1 capsids assembled from CA A92E/A204C or CA A204C	150
8.4. Analysis to identify “pause” time and calculate average speed	151
8.5. Statistical analysis of the landing rates of KFC complexes with different composition	152
8.6. Preliminary analysis comparing the motility of KF and KFC complexes	153

List of Figures

Fig. 1.1. HIV-1 genome and virion.	3
Fig. 1.2. HIV-1 life cycle.	5
Fig. 1.3. HIV-1 CA, subunits, and capsid.	8
Fig. 1.4. Models of HIV-1 capsid uncoating.	13
Fig. 1.5. Canonical binding motifs of HIV-1 capsid and known interacting host factors.	15
Fig. 1.6. Microtubule structure and plus-end dynamics.	22
Fig. 1.7. Fictional model of the retrograde transport of HIV-1 viral core.	27
Fig. 1.8. Dynein, dynactin, and dynein motor complexes.	29
Fig. 1.9. Dynein heavy chain and the dynein powerstroke cycle.	31
Fig. 1.10. Kif5 structure, autoinhibition, activation, and mechanochemical cycle.	34
Fig. 1.11. Cartoon showing the experimental design for the <i>in vitro</i> reconstitution and visualization of dynein- and kinesin-dependent transport of HIV-1 capsid.	36
Fig. 2.1. Schematic display of hFEZ1 constructs.	52
Fig. 2.2. Schematic display of mBICD2 constructs.	54
Fig. 2.3. Schematic display of hKif5B constructs.	56
Fig. 2.4. Schematic display hMAP7 constructs.	58
Fig. 2.5. Schematic display of the purification processes for DDb(pu), DD, and reconstitution of DDb(rec), DDBC complexes.	59
Fig. 3.1. Representative negative stain EM images of HIV-1 capsid assemblies.	82
Fig. 3.2. Preparation of pre-assembled, conical, soluble, stabilized, and fluorescence labelled HIV-1 capsid.	83

<u>Fig. 3.3. The self-assembled HIV-1 CA capsids (from A92E/A204C) interact with known capsid binders.</u>	84
<u>Fig. 4.1. Quantitative analysis of BICD2-capsid interaction based on a TIRFm binding assay.</u>	89
<u>Fig. 4.2. BICD2 binds to HIV-1 capsid primarily, but not solely, via the R18 ring of capsid.</u>	91
<u>Fig. 4.3. Dynein-dependent transport of HIV-1 capsid: DDBC motility assay.</u>	93
<u>Fig. 5.1. Quantitative analysis of FEZ1-capsid interaction based on a TIRFm binding assay.</u>	99
<u>Fig. 5.2. FEZ1 binds to HIV-1 capsid primarily, but not exclusively, via the R18 ring.</u>	100
<u>Fig. 5.3. Kinesin-1 (Kif5B)-dependent transport of HIV-1 capsid: KFC combination with dark Kif5B, sfGFP-FEZ1 and AF647-labelled HIV-1 capsid.</u>	103
<u>Fig. 5.4. KFC motility assays of additional KFC combinations.</u>	105
<u>Fig. 5.5. KFC motility assays of KFC combinations containing HIV-1 capsid lacking the R18 ring.</u>	108
<u>Fig. 5.6. Average speed comparison of the KFC combinations.</u>	110
<u>Fig. 5.7. Run length comparison of the KFC combinations.</u>	112
<u>Fig. 5.8. Landing rate comparison of the KFC combinations.</u>	113
<u>Fig. 5.9. Kif5B and FEZ1 can form a processive KF complex.</u>	115
<u>Fig. 5.10. Comparison of KF and KFC motile behaviors.</u>	117
<u>Fig. 8.1. Immobilization of assembled microtubules or HIV-1 capsids on modified surfaces.</u>	148
<u>Fig. 8.2. Reducing SDS PAGE with Coomassie staining showing most of the purified proteins used in this thesis.</u>	149
<u>Fig. 8.3. Summary of BICD2 or FEZ1 binding to HIV-1 capsids assembled from CA A92E/A204C or A204C.</u>	150
<u>Fig. 8.4. Identification of pauses in an example trajectory.</u>	151
<u>Fig. 8.5. Comparison of parameters describing the trajectories of KF and KFC particles.</u>	153

List of Tables

<u>Table 2.1. Summary of HIV-1 capsid binders examined in the TIRFm binding assays.</u>	<u>40</u>
<u>Table 2.2. Summary of motor complexes examined in the TIRFm motility assays.</u>	<u>41</u>
<u>Table 2.3. HIV-1 CA protein constructs.</u>	<u>44</u>
<u>Table 2.4. Primers for FEZ1 point mutagenesis.</u>	<u>52</u>
<u>Table 4.1. Comparison of the concentrations of components used for reconstituting the DDBC and KFC complexes.</u>	<u>95</u>
<u>Table 5.1. Sample preparation for KFC complex reconstitution and KFC motility assay.</u>	<u>102</u>
<u>Table 5.2. Summary of the KFC complexes examined in sections 5.3.1-5.3.2.</u>	<u>109</u>
<u>Table 5.3. Sample preparation for KF complex reconstitution and KF motility assay.</u>	<u>114</u>
<u>Table 5.4. Quantifications of the FEZ1-capsid interaction compared to literature.</u>	<u>118</u>
<u>Table 8.1. One-way ANOVA-Tukey's with multiple comparisons test of the landing rates of KFC complexes with different compositions.</u>	<u>152</u>

Publications and conferences

Publications

Peng, W., J. Shi, C. L. Márquez, D. Lau, J. Walsh, K. M. R. Faysal, C. H. Byeon, I. L. Byeon, C. Aiken and T. Böcking (2019). "Functional analysis of the secondary HIV-1 capsid binding site in the host protein cyclophilin A." *Retrovirology* 16(1): 10.

Lau, D., J. C. Walsh, **W. Peng**, V. B. Shah, S. Turville, D. A. Jacques and T. Böcking (2019). "Fluorescence Biosensor for Real-Time Interaction Dynamics of Host Proteins with HIV-1 Capsid Tubes." *ACS Appl Mater Interfaces* 11(38): 34586-34594.

Renner, N., D. L. Mallery, K. M. R. Faysal, **W. Peng**, D. A. Jacques, T. Böcking and L. C. James (2021). "A lysine ring in HIV capsid pores coordinates IP6 to drive mature capsid assembly." *PLoS Pathog* 17(2): e1009164.

Oral presentation

Wang Peng, Jeffrey H. Stear, Richard J. McKenney, David A. Jacques, Till Böcking. "*In vitro* reconstitution of HIV-1 capsid transport". Retrovirues Meeting, Cold Spring Harbour (Online), May 2021.

Poster presentation

Wang Peng, Jeffrey H. Stear, Richard J. McKenney, David A. Jacques, Till Böcking. "*In vitro* reconstitution of HIV-1 capsid transport". Dynein Meeting 2021, Online, Sep 2021.

List of abbreviations and symbols

2-LTR	2-Long terminal repeat
AAA+	ATPase associated with diverse cellular activities
AIDS	Acquired immune deficiency syndrome
Arp1	Actin related protein 1 (dynactin subunit)
Arp11	Actin related protein 11 (dynactin subunit)
AF488	Alexa Fluor 488
AF568	Alexa Fluor 568
AF647	Alexa Fluor 647
ATP	Adenosine triphosphate
B_{max}	Maximum specific binding
bp	Base pair
BICD2	Bicaudal D homolog 2 protein
BICD2N	N-terminus truncation (aa 25-400) of BICD2
CA	Capsid protein
CAP-Gly	Cytoskeleton-associated protein glycine-rich
CapZ α	F-actin-capping protein subunit alpha (dynactin subunit)
CapZ β	F-actin-capping protein subunit beta (dynactin subunit)
CCR5	C-C chemokine receptor type 5
CD4	Cluster of differentiation 4
cDNA	Complementary DNA
CPSF6	Cleavage and polyadenylation specificity factor 6
CTD	Carboxyl terminal domain
CypA	Cyclophilin A

dATP	Deoxyadenosine triphosphate
DD	Dynein-dynactin
DDb	Dynein-dynactin-BICD2N
DDB	Dynein-dynactin-BICD2
DDBC	Dynein-dynactin-BICD2-capsid
dNTPs	Deoxynucleoside triphosphates
DHC	Dynein heavy chain
DIC	Dynein intermediate chain
DLC	Dynein light chain
DLIC	Dynein light intermediate chain
DTT	Dithiothreitol
EM	Electron microscopy
Env	Envelope protein
ESCRT	Endosomal sorting complexes required for transport
FEZ1	Fasciculation and elongation protein zeta 1
FG	Phenylalanine glycine
Gag	Gag polyprotein
GDP	Guanosine diphosphate
gp120/41	Surface envelope glycoprotein 120/41
GMPCPP	Guanosine-5'-[(α,β)-methyleno] triphosphate
GTP	Guanosine-5'-triphosphate
HCB	Hexacarboxybenzene
hFEZ1	Human FEZ1
HIV	Human Immunodeficiency Virus
hKIF5B	Human Kif5B (Kinesin-1 heavy chain family 5B)

hMAP7	Human microtubule associated protein 7
IN	Integrase
IP6	Inositol 6 phosphates
IPTG	Isopropyl β -d-1-thiogalactopyranoside
ITC	Isothermal titration calorimetry
JIM	James' Immobilised Microscope Suite
LC8	Dynein light chain 2
kb	Kilo base
K_d	Dissociation constant
kDa	Kilo Dalton
KF	Kif5B-FEZ1
KFC	Kif5B-FEZ1-capsid
KHC	Kinesin heavy chain
KIF5B	Kinesin-1 heavy chain family 5B
KLC	Kinesin light chain
MA	Matrix protein
MAP7	Microtubule associated protein 7
MAPs	Microtubule associated proteins
mBICD2	Mouse BICD2
MHC	Major Histocompatibility Complex
MTOC	Microtubule-organizing center
MxB	Myxovirus resistance protein B
NDD	N-terminal dimerization domain (dynein)
NC	Nucleocapsid protein
NPC	Nuclear pore complex

NTD	Amino terminal domain
Nup153	Nucleoporin 153
Nup358	Nucleoporin 358
ORF	Open-reading frame
p24/25/27/50/62/150	Dynactin subunit 3/5/6/2/4/1
PCA	Protocatechuic acid
PCD	Protocatechuate-3,4-dioxygenase
PDMS	Poly-dimethylsiloxane
PIC	Pre-integration complex
PR	Viral protease
R18 ring	A ring structure formed by six arginine 18
RB1	Dynein light chain 1
REV	Regulator of the expression of virion protein
RNP	Ribonucleoprotein
rNTPs	Ribonucleoside triphosphates
RT	Reverse transcriptase
RTC	Reverse transcription complex
γTuRC	γ-tubulin ring complex
Sec24C	Protein transport protein SEC24 homolog C
SPR	Surface Plasmon Resonance
+ssRNA	Positive-sense single-strand RNA
Tat	Transcriptional trans-activator
Tctex1	Dynein light chain 3
TIRFm	Total Internal Reflection Fluorescence microscopy
TNPO3	Transportin-3

TRIM5	Restriction factor tripartite motif 5
TRN-1	Transportin-1
Trolox	6-hydroxy-2,5,7,8-tetramethylchroman-2-carboxylic acid
Vif	Viral Infectivity Factor
Vpr	Viral Protein R
Vpu	Viral Protein U
WT	Wild type
τ	Decay constant

Chapter 1

Literature review

1. Literature review

1.1. HIV

1.1.1. HIV and AIDS

Human immunodeficiency virus (HIV) is the causative pathogen of acquired human immune deficiency syndrome (AIDS) [1]. While the earliest known cases of HIV infection date from the 1960s, this disease first became widespread from 1981. Since this time, AIDS has claimed approximately 36 million lives while roughly 37 million people are currently living with AIDS [2]. HIV is transmitted by direct contact with contaminated body fluids. Activities like percutaneous inoculation, mucosal surfaces contact, and particularly unprotected sex, are the common routes of HIV propagation [3].

HIV-1 and HIV-2 are the two main types of HIV virus, with HIV-1 being more pathogenic [4, 5]. HIV-1 can be further divided into M, N, O and P groups, with group M primarily responsible for the worldwide HIV epidemic [6]. HIV-1 mostly attacks CD4+ (CD4 positive) T lymphocyte [7] but can also infect dendritic cells, macrophages and other cell types [8, 9]. HIV viral infection causes a progressive death of CD4+ T cells, which leads to chronic deficiencies in the immune system.

Despite extensive efforts to develop HIV-1 vaccine, with 7 trials completed to date [10], AIDS remains incurable. The current treatment strategy against HIV-1 targets various phases of the retroviral life cycle ranging from viral fusion and entry to reverse transcription, integration, and protease processing [11]. This type of combined antiretroviral therapy has been successful in suppressing virus replication to undetectable levels, turning AIDS into a chronically manageable disease [12]. However, not all patients can receive the antiretroviral therapy due to the high cost and the fact that the treatment need to be maintained regularly over the course of the patient's life [13]. In addition, HIV has extremely high mutation rate [14] that contributes to the development of resistance to existing antiretroviral drugs. Therefore, continuing research on HIV virus is necessary to develop new AIDS treatments.

1.1.2. HIV-1 viral structure and life cycle

1.1.2.1. HIV-1 genome structure

HIV-1 belongs to the *Retroviridae* family and *Lentivirus* genus. The viral genome consists of two identical copies of positive-sense single-stranded RNA with a length of approximately 9.7 kb (**Fig.**

1.1.A). Each RNA strand contains 9 open reading frames which can be classified into 3 groups: structural genes (*gag*, *pol* and *env*), regulatory genes (*tat* and *ref*) and accessory genes (*nef*, *vif*, *vpr* and *vpu*) [15]. It is also suggested that the secondary RNA structure of HIV-1 genome modulates viral protein expression [16, 17]. The nine genes encode 15 proteins. The *Gag* gene encodes the Gag protein precursor, the main structural protein which gives rise to p17 matrix protein (MA), p24 capsid protein (CA), sp1 (between CA and NC), nucleocapsid proteins (NC), sp2 (between NC and P6), and p6. The N-terminus of the Gag protein is myristoylated co-translationally, allowing it to be anchored to the plasma membrane for virion assembly [18, 19]. A ribosomal shift at the *gag-pol*

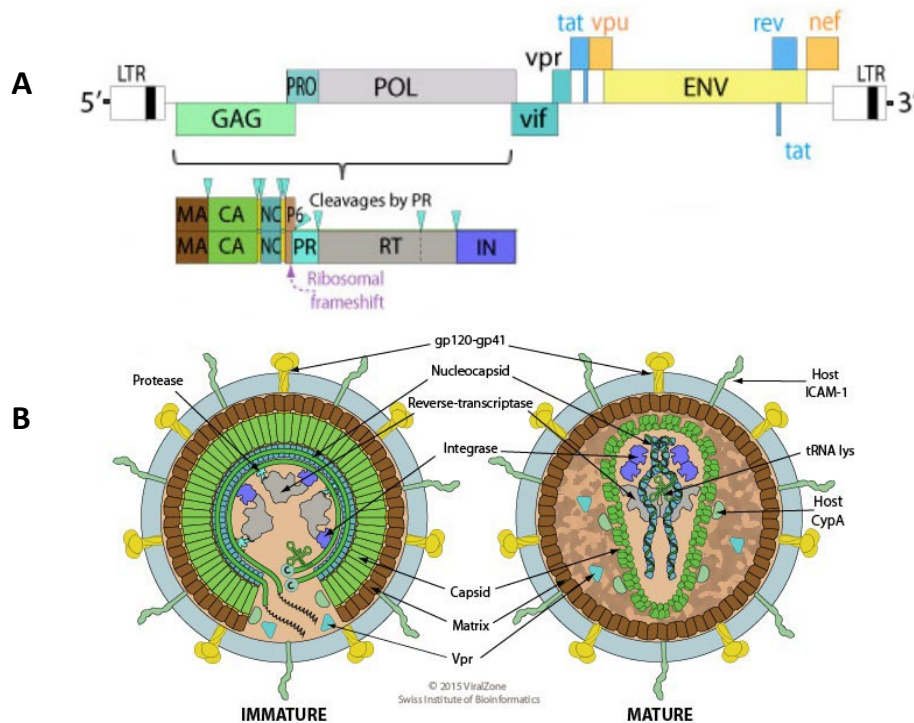


Fig. 1.1. HIV-1 genome and virion. **A.** The HIV-1 genome contains 2 identical copies of positive-sense single-stranded RNA (+ssRNA) molecules. Each strand (~9.7 kb) encodes 9 open reading frames flanked by two long terminal repeats at both ends. The genes can be divided into three groups: structural genes (*gag*, *pol* and *env*), regulatory genes (*tat* and *ref*) and accessory genes (*nef*, *vif*, *vpr* and *vpu*). **B.** Immature (left) and mature virions (right). The HIV-1 virion is a spherical particle with a diameter between 100-200nm. The main structural features are the viral membrane, structural protein matrix, capsid and viral genome (from outermost to the innermost). Images adapted from ViralZone (<https://viralzone.expasy.org/7>).

junction (with a frequency of 5-10%) lead to the expression of Gag-Pol precursor [20]. The Pol precursor is subsequently cleaved into viral protease (PR), reverse transcriptase (RT) and viral integrase (IN) [21]. PR plays a proteolytic role during virion maturation [18], while RT and IN are responsible for protein reverse transcription and integration of viral genome into host genome respectively [22, 23]. This frameshift mechanism is employed by HIV-1 virus to produce fewer catalytic proteins (PR, RT and IN) relative to the main structural proteins (MA, CA and NC) [24, 25]. The *Env* gene encodes glycoprotein precursor gp160, which is then processed into envelope proteins gp120 and gp41. Gp120 localizes to the outer face of the viral membrane while gp41 is a transmembrane protein; together they form the spike complex, which is responsible for target-cell-recognition, attachment, and fusion [26, 27]. The regulatory genes *tat* and *rev* encode the viral transcriptional trans-activator (Tat) and the regulator of expression of the virion (Rev). Tat enhances the efficiency of viral gene expression [28] and Rev mediates export of viral mRNA into cytoplasm [29]. The accessory genes *nef*, *vpu*, *vif* and *vpr* encode the negative regulatory factor (Nef), the viral protein U (Vpu), viral infectivity factor (Vif) and viral protein R (Vpr) respectively. These accessory proteins modulate viral infectivity by interacting with various host factors [30-34].

1.1.2.2. HIV-1 virion structure

HIV-1 virions are spherical particles approximately 100-200 nm in diameter [35, 36]. The main features of mature virions are the viral membrane, structural protein matrix, capsid and viral genome. (**Fig. 1.1.B**, Right). The viral membrane is composed of a lipid bilayer derived from the plasma membrane of infected host cells during viral assembly [37]. There are approximately 14 glycoprotein spikes, each composed of 3 gp120 and 3 gp41 subunits, integrated on the outer face of the viral membrane that facilitate viral entry [38]. ICAM-1 from the host cell is also incorporated into the viral membrane to assist viral entry [39]. The matrix shell is associated with the inner face of the viral membrane, and is comprised of 2000-5000 MA protein [40]. MA plays a key role in modulating the early and late steps of viral morphogenesis [41]. Inside the MA shell is the conical-shaped capsid, which consists of approximately 1500 CA protein [42]. The capsid is deposited into the host cell cytoplasm following viral fusion and plays a key role in viral infection by shielding the HIV-1 genome from the host immune response as well as interacting with a range of host factors through its canonical host-factor-binding-interfaces. The capsid encapsulates the viral genome, which is comprised of two copies of positive-sense single-stranded RNAs which are tightly bound by NC proteins that stabilize the viral genome [43]. Viral genome, NC, IN, RT, and packaged host tRNA-

lys altogether form the ribonucleoprotein complex [44]. It should also be noted that the above description applies to the structure of a mature HIV-1 virion in an immature virion, prior to the PR-mediated cleavage of Gag and Gagpol precursors [37], the Gag and Gagpol molecules are arranged in a radial manner (**Fig. 1.1.B**) inside the MA shell.

1.1.2.3. HIV-1 life cycle

Overall, the HIV-1 life cycle describes the process by which a HIV-1 virus productively infects a target cell, leading to the production of progeny HIV-1 viruses. This sequence of events is generally divided into the early phase (**Fig. 1.2.A-D**: cell recognition and entry, cytoplasmic transport, nuclear entry, completion of reverse transcription, capsid uncoating and integration of the proviral DNA, whereby the order of events is still under debate and some processes overlap) and the late phase (**Fig. 1.2.E-I**: transcription, nuclear export, viral protein expression, assembly, budding and maturation).

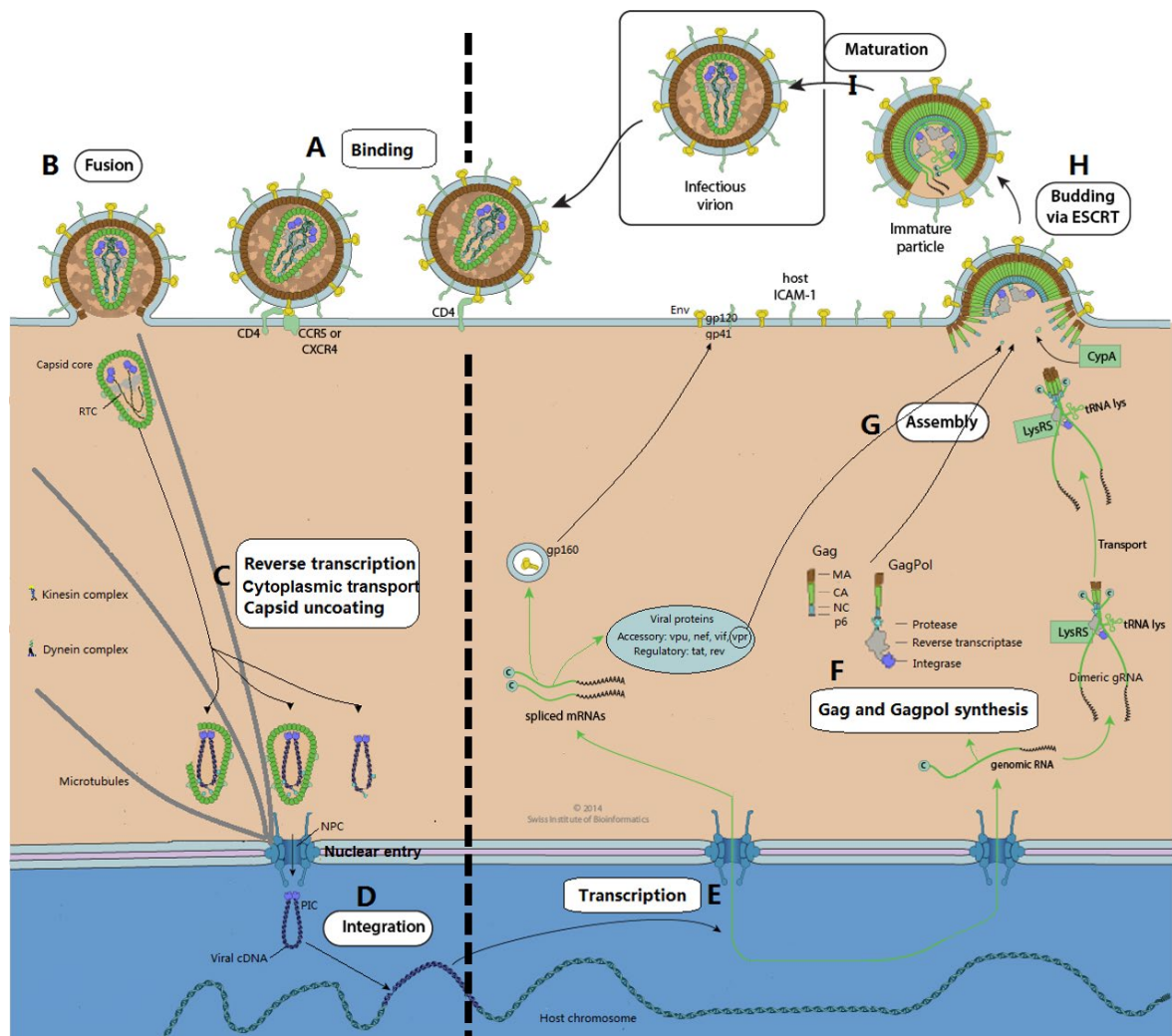


Fig. 1.2. HIV-1 life cycle. A-D. Early life cycle of HIV-1 infection. **A.** Target cell recognition. **B.** Membrane fusion and cell entry. **C-D.** Cytoplasmic transport and nuclear entry coupled with reverse transcription and capsid uncoating, followed by integration. **E-H.** Late life cycle of HIV-1 infection. **E-F.** Production of viral RNA and viral proteins **G.** Transport and assembly of the viral components at the inner cell membrane. **H-I.** Viral budding, release and maturation. Image adapted from ViralZone (<https://viralzone.expasy.org/5096>).

Early phase of HIV-1 life cycle

The HIV-1 life cycle begins with the recognition and binding of an infectious virion to a target cell (**Fig. 1.2.A**). The viral glycoprotein gp120 first recognizes and binds onto CD4 receptors of the host cell membrane, which triggers a conformational change of gp120 promoting its binding to the co-receptor CCR5 (C-C chemokine receptor-5) or CXCR4 (CXC chemokine receptor-4) [26, 45]. These events induce a conformational change of gp41, which leads to the fusion of the virion with the cell membrane and the release of the viral core into the cytoplasm (**Fig. 1.2.B**) [46].

Upon cell entry, reverse transcription is initiated while the viral core is transported towards the nucleus (**Fig. 1.2.C**). Reverse transcription describes the production of viral cDNA by using cellular deoxynucleoside phosphates (dNTPs) as substrates, cellular ATP as energy, and the viral RNA genome as template [47, 48]; the process is facilitated by the reverse transcription complex (RTC), which defines the complex containing the viral RNA genome and associated proteins [49]. Upon finalization of reverse transcription, the viral complex containing viral cDNA and associated components is then referred as a pre-integration complex (PIC)[50]. Alongside with reverse transcription, the viral core comprising capsid and RTC/PIC is transported towards the nucleus by exploiting the microtubule network and motor protein complexes including dynein and kinesin [51-54]. When the viral core reaches the nucleus, it docks at the nuclear pore complex (NPC) and is actively translocated into the nucleus [55-57]. The viral core containing the RTC/PIC is released into the nucleus and the viral DNA is integrated into the host genome at selected sites as facilitated by the viral integrase and assisting proteins [58, 59] (**Fig. 1.2.D**). Alternatively, the viral DNA could form a 2-long terminal repeat instead of integration because of non-homologous end joining, leading to failed infection [60]. Capsid uncoating, which is defined as the disassembly and release of capsid lattice from the viral core, is functionally coupled with all other processes in the

early life cycle; however, the precise timing, location, and mechanism of uncoating is still under debate (see **1.1.3.2**).

Late phase of HIV-1 life cycle

The provirus is transcribed by host RNA polymerase II and the resulting mRNAs, either spliced mRNA or viral RNA, are exported into the cytoplasm (**Fig. 1.2.E**). The viral RNA serves as mRNA for Gag and GagPol synthesis [25], with GagPol being expressed as a result of the programmed frameshift as discussed above (**Fig. 1.2.F**). The spliced mRNA is translated into viral regulatory proteins (Rev, Tat), accessory proteins (Vpu, Nef, Vif, Vpr) [61], and the structural protein gp160 [62]. Rev, Tat, Vpu, Nef, Vif, Vpr serve as regulators of viral replication, with Rev and Tat being active in the nucleus while Vpu, Vef and Vif are active in the cytoplasm [63]. Gp160 is glycosylated in the Golgi network and cleaved into gp120 and gp41 prior to being transported to the cell periphery to serve as envelope proteins (Env) [62].

Viral assembly proceeds in lipid rafts at the cell membrane when the Gag/GagPol precursors are recruited to the cell periphery (**Fig. 1.2.G**) [37]. Domains of MA direct Gag/GagPol to targeting sites at the plasma membrane [64, 65] and aid Env incorporation [62]. Gag interacts with dimeric assemblies of the viral genomic RNA, leading to the packaging of viral RNA. The viral accessory protein Vpr [63], together with host factors such as cyclophilin A (CypA) [66] and inositol hexaphosphate (IP6) [67], are packaged into the virion. Following viral assembly, the immature virion buds and releases from the host cell via the endosomal sorting complexes required for transport (ESCRT) pathway [37] (**Fig. 1.2.H**). Concomitant with virion release, viral PR cleaves Gag and GagPol precursors, leading to the maturation of the virion and the structural rearrangement described above [22, 37] (**Fig. 1.2.H**).

1.1.3. HIV-1 capsid

1.1.3.1. Roles of HIV-1 capsid

The HIV-1 capsid is functionally involved in multiple aspects of HIV-1 early infection including innate immune response evasion [56, 68, 69], reverse transcription [70-72], retrograde transport [51-53, 73, 74], timely uncoating, nuclear entry [56, 75, 76], and integration site targeting [77, 78]. All these steps are regulated by the interactions between various host factors and capsid lattice or CA protein, and by the spatiotemporal integrity of capsid. In other words, the capsid has evolved as a finely tuned complex which exploits host factors to manipulate its spatiotemporal stability for successful

infection. HIV-1 CA is genetically fragile, i.e., many point mutations would lead to deficient replication [79], potentially by altering capsid stability or by disrupting the interactions between capsid and host factors. As such, HIV-1 capsid has been considered an attractive therapeutic target. Increasing numbers of host factors and novel small molecules have been recently demonstrated to bind the capsid. However, in many cases, the mechanisms underlying these interactions remain unclear.

1.1.3.2. Structure of HIV-1 capsid

The HIV-1 capsid is a fullerene cone that houses the viral genome along with essential viral proteins and host factors (**Fig. 1.1.B**, right). This protein shell consists of approximately 1500 copies of CA protein (p24), which form approximately 250 hexamers and exactly 12 pentamers that facilitate the curvature for closure of the structure [80, 81] (**Fig. 1.3.D**). In this thesis 'CA' will be used to describe the monomeric protein (p24) and 'capsid' will be used to describe the assembled capsid shell.

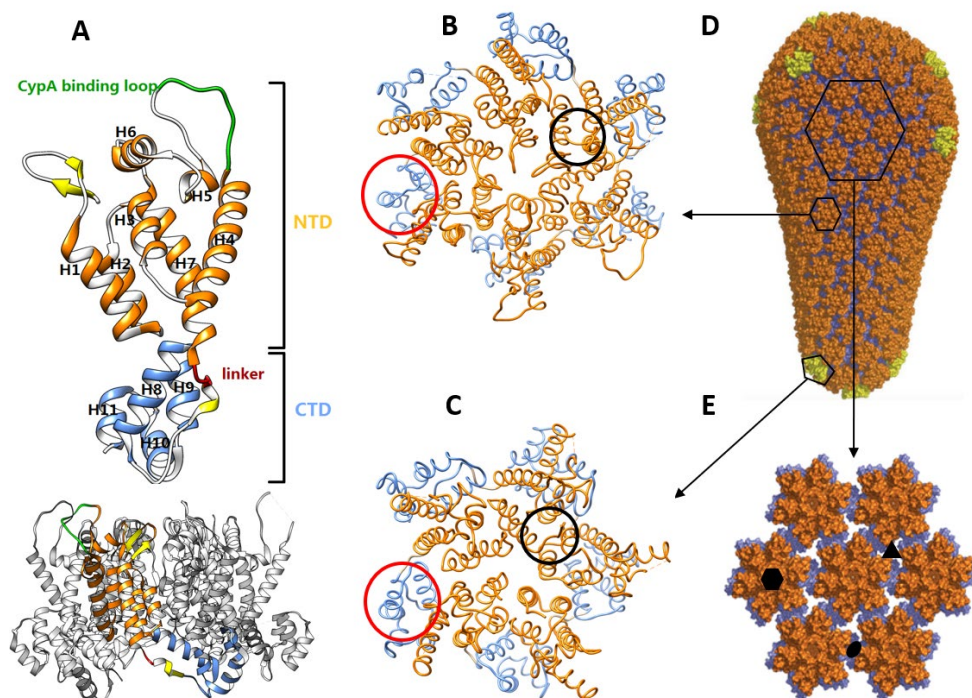


Fig. 1.3. HIV-1 CA, subunits, capsid. **A.** Top) Side view of a CA monomer with its main secondary structures indicated. The NTD and CTD are colored in orange and blue, respectively. Bot) 1 CA monomer highlighted in the context of a CA hexamer (sideview). **B-C.** Top views of CA hexamer (**B**) and CA pentamer (**C**), with the representative positions of the intra-subunit interaction (NTD-NTD) and the inter-subunit interaction (CTD-CTD) highlighted with black and red circle, respectively. **D.**

3D model of HIV-1 capsid with hexamers shown in orange and pentamers shown in yellow. **E.** Hexamer of hexamers. Representative 6-fold, 3-fold and 2-fold axis are indicated by black hexagon, triangle, and ellipse, respectively. Images A-C generated from PDB(3H4E; 3P0A) using Chimera; D and E adapted from [82, 83]. Not to scale.

1.1.3.2.1. HIV-1 CA monomer

The CA monomer is 231 amino acids in length and contains 11 α -helices, a 3-10 helix and a β -hairpins [84]. The overall arrangement of CA protein is comprised of two independently folded domains, an amino-terminal domain (CA_{NTD}) and a carboxy-terminal domain (CA_{CTD}) that are linked together by a highly flexible linker (**Fig. 1.3.A**, top). The CA_{NTD} (amino acid 1-144) starts with two short β -hairpins and contains 7 α -helices (H1-H7). The residues 85-93 between H4 and H5 form a highly hydrophobic loop known as the CypA-binding loop, which is named after its interaction with host protein CypA [85]. Residues 145-149 form a linker between the CA_{NTD} and CA_{CTD} domain, which is highly flexible in solution [84]. The CA_{CTD} domain (amino acid 150-221) starts with a short 3-10-helix and contains 4 α -helices (H8-H11) [84]. The residues 222-231 at the tail of CA_{CTD} are usually not detectable in crystal structure [86]. Within H8 there is a 20-residue motif (amino acid 153-172), known as the major homology region (MHR), that is reported to be highly conserved among retrovirus and important for particle assembly [87, 88]. The linker region and CTD domain are more mobile than the NTD, which might account for the curvature of the capsid lattice [82].

1.1.3.2.2. HIV-1 CA hexamers and pentamers

The CA hexamer and pentamer assemblies, both of which are formed by CA monomers, serve as the basic structural units of the capsid lattice (**Fig. 1.3.B-E**). Hexamer and pentamer formation are mediated by the NTD-NTD interactions (**Fig. 1.3.B-C**). Intermolecular interactions between H1, H3 from one CA monomer and H2 from the neighboring CA monomer within a hexamer form an 18-helix bundle (15 for pentamer) oriented towards the center, thus forming the 6-fold (5-fold for pentamer) axis [82, 83, 89]. Aliphatic amino acids on these helices face towards the middle of the helices triplets and generate a small hydrophobic pocket [82]. A highly positively charged R18 ring at the center of the hexamer, which is formed by the six Arg18 residues, has been suggested to import dNTPs (deoxy-ribonucleotide triphosphates) and ATP into the closed capsid [70]. This observation, along with other *in vitro* data [90], supports the possibility of reverse transcription

happening within an intact capsid. Studies have also suggested that the CTD-NTD interaction between contiguous CA monomers within the hexamer/pentamer, involving H4, H7, H8 and H11, is critical for capsid stability [91, 92]. However, this interface is more generally recognized as a binding pocket for some host proteins and small molecule antiviral compounds (see **1.1.3.4.3**).

1.1.3.2.3. HIV-1 capsid lattice

The HIV-1 capsid lattice is maintained by interactions both within and between the subunits (**Fig. 1.3.B-E**). Adjacent subunits (hexamer-hexamer or hexamer-pentamer) are held together by CTD-CTD interactions (**Fig. 1.3.C**). H9 and 3-10 helix are responsible for interactions at the 2-fold axis, which is the dimeric interface between 2 CA monomers from 2 adjacent hexamers [89, 93, 94] (**Fig 1.3.E**, black eclipse). The amino acids Trp184 and Met185 play important roles in defining the interaction at the 2-fold interface. H10 and H11 are responsible for interaction at 3-fold axis, which is the trimeric interface formed by 3 CA monomers from 3 adjacent hexamers [93-95] (**Fig 1.3.E**, black triangle). The 6-fold axis contains the R18 ring, which is suggested to be a destabilizing feature that is tolerated by the capsid for efficient recruitment and import of cellular molecules like dNTPs and ATP (**Fig 1.3.E**, hexagon). Although an intact HIV-1 capsid commonly presents a conical architecture, it can also adopt tubular or polyhedral morphologies based on the incorporation site of pentamers within the capsid lattice [35, 96]. It is although worth noting that not all CA proteins are incorporated into capsid lattice within a virion; ~5000 gag precursors are packaged while the capsid consists of only ~1500 CA [42, 89]. These non-incorporated CA molecules have been speculated to assist in maintaining the organization of capsid [97].

To expand our understanding of HIV-1 infection, it is critical to investigate the factors that regulate capsid structure and stability, as well as further characterize the interactions between HIV-1 capsid lattice and host factors [98-100]. *In vivo* and *in vitro* assays serve as top-down and bottom-up strategies that are co-operatively exploited to study these questions. *In vivo* infection assays represent a fundamental technique for identifying capsid-dependent host factors and validating their physiological relevance in HIV-1 infection [101-103]. *In vitro* assays utilizing isolated native viral cores [35, 104], virus-like particles (VLPs) [105, 106], and *in vitro* capsid assemblies [70, 83, 95] are useful platforms for studying capsid structure, stability, and the capsid-host interactions. Viral cores and VLPs, which are isolated from cells and therefore contain the host factors that normally bind to the capsid, represent a more physiologically relevant substrate for examining capsid structure and the capsid-host interactions. However, there are distinct advantages to investigating these

questions using *in vitro* capsid assemblies: 1) it is a minimal, defined system that allows us to focus on specific aspects of capsid biology in the absence of these host factors; 2) these reagents are easier to obtain in large quantities. Therefore, we use *in vitro* capsid assemblies for all the investigations throughout this thesis.

Using recombinant CA protein, *in vitro* capsid assemblies can be induced by high ionic strength (usually 1 M NaCl) [107]; capsids assembled in this fashion adopt long, tubular shapes that are quite different from the native capsid [108]. The addition of host protein CypA at high molar ratio during assembly can reverse the morphology of capsid to native-like [108, 109]. A recent study also demonstrates that capsid assembly can be performed at physiological ionic strength in the presence of host factor IP6 [110]. However, the assembly of WT CA is reversible and requires specific assembly conditions to maintain integrity of the lattice, making it an unideal reagent to use under many experimental conditions. CA-NC tubes, assembled from CA-NC (capsid-nucleocapsid) protein, display an architecture similar to CA tubes and exhibit increased stability [76, 111, 112].

During the past decade, approaches that take advantage of CA with modified cysteine mutations to make crosslinked stabilized capsid assemblies have been more broadly used for generating capsid assemblies for *in vitro* binding assays. Pornillos *et al.* reported a range of crosslinking CA constructs, two of which (A14C/E45C/W184A/M185A and A14C/E45C) have been frequently used [83, 113]. CA protein with the A14C/E45C/W184A/M185A mutations can be assembled into soluble CA hexamer which was used to resolve the first crystal structure of CA hexamer, providing the earliest structural evidence for the inter-hexamer interactions [83]. This construct has proven useful across a range of techniques including crystallization [67, 70, 114, 115], size-exclusion coelution [73, 116], isothermal titration calorimetry [117-120], and surface plasmon resonance [106, 121]. Construct A14C/E45C assembles into WT-like CA tubes and has been widely used in pull-down assays [73, 122, 123]. This construct was also employed to develop as a biosensor where the CA tube is used as substrate in a total internal reflection fluorescence microscopy-based HIV-1 capsid binding assay [124]. Summers *et al.* established a library of construct that forms CA assembly intermediates (from 1/3 hexamer up to heptamer-of-hexamer) [125]. The authors demonstrated that these engineered CA assemblies are easily compatible with techniques including crystallization, size-exclusion coelution and ITC. These constructs could serve as a powerful toolbox although they have not been broadly explored yet. Zhao *et al.* described CA A204C and generated the cryo-EM structure of a fully assembled capsid [95]. Because this construct assembles into a cone-like shape, similar to the native capsid, it is

commonly used. Lau et.al recently used this construct in a confocal fluorescence spectroscopy-based assay [126]. We also combined this construct with the point mutation A92E (to overcome capsid aggregation by reducing the hydrophobicity of capsid surface) to prepare soluble, cone-shaped capsid that are well-suited for a variety of single molecule assays (see **3.3**).

1.1.3.3. HIV-1 capsid uncoating

The spatiotemporal integrity of HIV-1 capsid, which is believed to be modulated by both the nature of capsid and its interactions with host factors, is key to infection. While maintaining a closed capsid is essential to prevent detection of the viral genome by the cellular immune response, to release the viral DNA, the capsid must also open at an appropriate time and location, in a process known as uncoating. The precise timing and location of uncoating are still debatable after almost 30 years of research. Several seemingly contradictory uncoating models have been proposed, including the immediate uncoating model, the cytoplasmic uncoating model, the NPC uncoating model, and the nuclear uncoating model (**Fig. 1.4**).

The immediate uncoating model (**Fig. 1.4.A**) is mainly based on two early studies. An electron-microscopy-based infection assay suggested that no intact capsid can be observed at the viral fusion site upon cell entry [127]. Another biochemical assay quantifying RTC suggests that CA and intact capsid are largely absent from RTC shortly after cell entry [47]. Both assays suggest that uncoating happens concurrently or shortly after cell entry. However, this model is challenged by several observations that viral genome needs the protection of capsid from cytosolic DNA sensors [69, 128], and that CA is needed for integration [129] and for infection of non-dividing cells [130].

The cytoplasmic uncoating model (**Fig. 1.4.B**) suggests that capsid is partly disassembled from RTC while the viral core is transporting to the nucleus. Two live cell imaging assays using GFP incorporated HIV-1 virus, coupled with a Cyclosporin A (CsA) washout assay, suggest that CA is gradually released from capsid within 4h post infection [131, 132]. Another live cell imaging assay using GFP incorporated HIV-1 virus reported that capsid opening occurs approximately 30 min post-infection [133], which is consistent with live cell imaging assays that fluorescently label viral RNA upon capsid opening [134]. The observation that eukaryotic elongation factor 1 (eEF1) is bound to RTC as a reverse transcription cofactor [135] also suggest that capsid is at least partly open in the

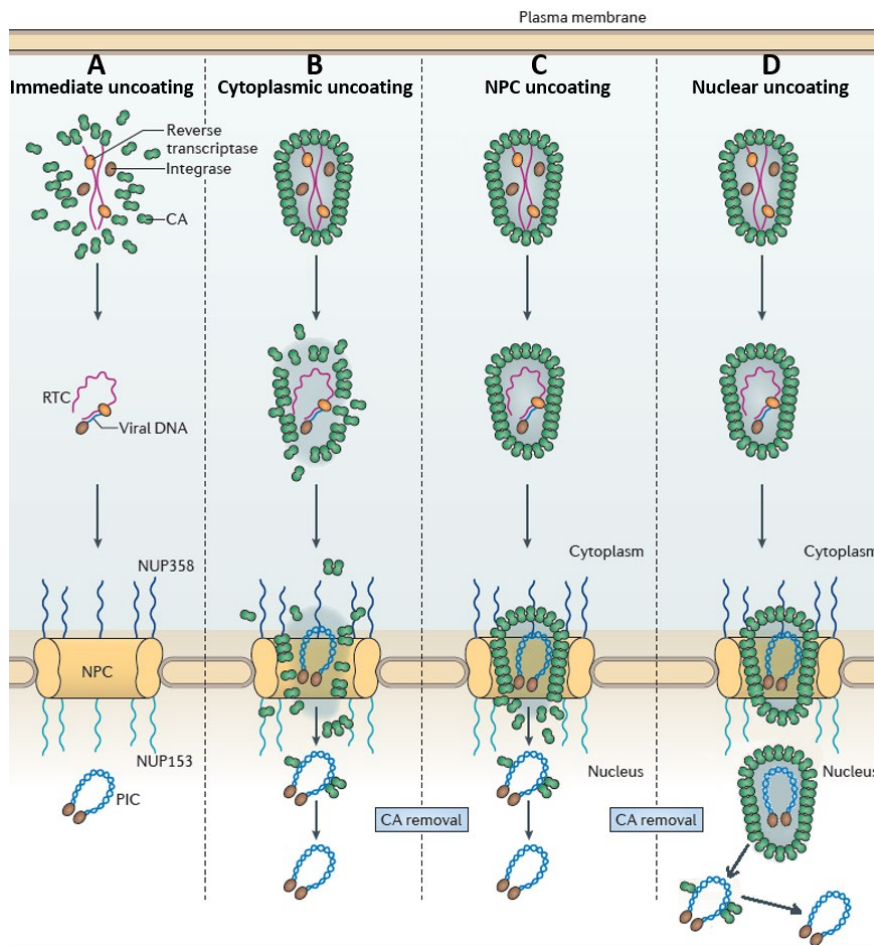


Fig. 1.4. Models of HIV-1 capsid uncoating. **A. Immediate uncoating.** Capsid completely disassembles shortly after cell entry. **B. Cytoplasmic uncoating.** Capsid disassembles gradually during cytoplasmic trafficking towards nucleus. **C. NPC uncoating.** Capsid remains intact during cytoplasmic trafficking and disassembles at NPC. **D. Nuclear uncoating.** Capsid enters the nucleus fully or largely intact and disassembles in the nucleus. Image adapted from [136].

cytoplasm. However, this model is challenged by the question as to how a partially deconstructed capsid is able to protect the viral genome from a host immune response. One speculation is that host cellular factors are recruited in a CA dependent manner to mask and protect viral genome from host immune sensors [137, 138].

The NPC uncoating model (**Fig. 1.4.C**) suggests that the capsid remains intact until it reaches the NPC; this view is primarily supported by the research demonstrating that the viral genome

requires the protection of capsid from cytosolic DNA sensors [69, 128]. Another live cell imaging assay that visualizes capsid uncoating with labelled CypA (CypA-DsRed) suggests that the capsid is needed to facilitate docking of the viral complex at the NPC, and that capsid bound to the nuclear pore displays accelerated uncoating [56]. The observation that the R18 pore at the center of the hexamer can recruit dNTPs and ATP also provide a potential model for how reverse transcription could take place in the enclosed capsid [70]. This model is challenged by observations that early [47] or gradual [131, 132] CA loss is detected during cytoplasmic trafficking of viral complex.

The nuclear uncoating model (**Fig. 1.4.D**) suggests that the capsid remains largely intact when it enters the nucleus. This hypothesis is supported by observations that assembled HIV-1 cores are observed in the nucleus [57, 139-142]. However, a number of physical constraints have called the validity of this model into question. The inner diameter of NPC, which was thought to be ~40 nm [143, 144], i.e. narrower than the diameter of an intact HIV-1 capsid which is usually 45-60 nm in width [95]. It was therefore proposed that the capsid could be remodeled to transport through the NPC [140] or even enter the nucleus in an endocytosis-like pathway independent of NPC transport [145]. However, a recent study has shown that the inner diameter of the NPC is actually wider (~64 nm) than previously estimated allowing the passage of an intact (or nearly intact) HIV-1 capsid [57]. While the nuclear uncoating model has gained considerable support in recent years, more evidence is required to unequivocally test it.

Despite of the controversy of the uncoating model, it has been shown that uncoating is functionally coupled with all steps of HIV-1 early infection including reverse transcription [146, 147], cytoplasmic transport [52, 148-150], nuclear import [151, 152] and integration [139, 141]. Besides, numerous host factors have been reported to modulate capsid uncoating as summarized in reviews [98, 153].

1.1.3.4. Canonical binding interfaces of HIV-1 capsid and interacting host factors

As mentioned previously, interactions between HIV-1 capsid and multiple host factors mediate many critical aspects HIV-1 infection. Significant progress has been made towards understanding capsid structure and capsid-host interactions in the past decades; however, much remains unknown. In this section we will briefly enumerate the canonical binding interfaces on HIV-1 capsid lattice and the host factors that have been shown to directly interact with these motifs.

1.1.3.4.1. The CypA-binding loop and interacting host factors

The CypA-binding loop is a highly hydrophobic loop at N-terminal of CA monomer (aa 85-93) that stretches outwards from the capsid lattice, with G89 and P90A being the key residues for host factor

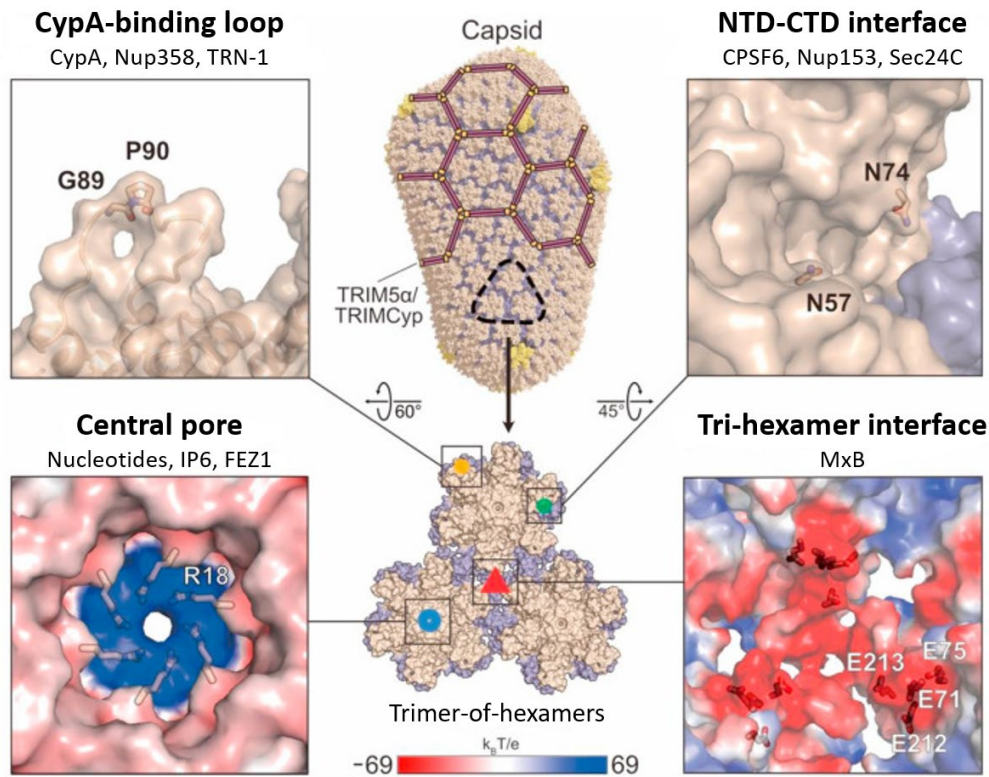


Fig. 1.5. Canonical binding motifs of HIV-1 capsid and known interacting host factors. The CypA binding loop, NTD-CTD interface, central pore, and tri-hexamer interfaces are indicated in a trimer-of-hexamers with yellow, green, red, and blue shapes respectively (middle, bottom). Major motifs of the canonical binding sites are shown in the zoomed in images (corners), with the selected key residues highlighted. The bottom bar indicates the electrostatic surface potential. Schematic display of TRIM5 cage is also indicated (middle, top). Image adapted from [99].

interaction [85, 154] (**Fig. 1.3.A** and **Fig. 1.5**). Host factors that have been identified to interact with the CypA-binding loop so far include Cyclophilin A (CypA), Nucleoporin 358 (Nup358), and β -karyopherin Transportin-1 (TRN-1).

CypA is a peptidyl prolyl cis-trans isomerase that was first demonstrated to bind capsid and modulate HIV-1 infection almost 30 years ago [85, 155]. However, due to the cell-type-dependent effects of CypA on viral infectivity [156-158] and capsid stability [159], the mechanism by which it

functions remains unclear. CypA is able to recognize the G89 and P90 residues of CA monomer, meaning that CypA-capsid interaction does not require an assembled capsid lattice [154]. Recent studies suggested that one CypA molecule can simultaneously bind to two [109] or three [160] CA molecules from adjacent CA hexamer to stabilize the HIV-1 capsid. However, these additional binding sites, if they exist, are quite weak based on the observations that CypA binds to CA monomer, hexamer, or capsid lattice with highly similar affinities [77, 106, 121, 154]. A complete understanding of how CypA modulates HIV-1 infection remains elusive due to the fact that CypA could either promote or restrict HIV-1 infection in a cell-type dependent manner [158, 159, 161, 162]. One popular speculation is that CypA binding enhances the ability of the HIV-1 virus to evade the host immune response. This model is supported by a number of observations: 1) the CypA-capsid interaction inhibits immune responses towards HIV-1 infection in TE71 cell line [163]; 2) loss of CypA binding triggers type-I interferon response which restricts HIV-1 infection in human monocyte-derived macrophages [68]; 3) CypA protects HIV-1 infection by shielding the capsid from restriction factor tripartite motif 5 α (TRIM5 α) binding in lymphocytes [164]. In addition, it is also known that CypA indirectly modulate HIV-1 infection by regulating the interactions of capsid with other host factors [77, 161, 165, 166].

Nup358 is the largest component of the nuclear pore complex (NPC) and is functionally involved in cellular processes like nuclear pore translocation and cell cycle progression [167]. It was first identified as a host factor involved in HIV-1 infection by three independent genomic scale screens [101-103], and depletion of Nup358 has been shown to decrease HIV-1 infectivity [131, 150, 168]. The CTD of Nup358 contains a cyclophilin-like domain which directly binds to the CypA-binding loop of HIV-1 capsid [77, 131, 169, 170]. A crystal structure of this domain in complex with the NTD of HIV-1 CA shows that the residue P90 of the CypA-binding loop is key to the interaction, similar to the CypA-CA interaction [170]. However, in contrast to CypA, Nup358 is insensitive to the inhibition of cyclosporin when binding to HIV-1 capsid suggesting that the Nup358-capsid interaction differs from the CypA-capsid interaction [77]. In line with its role as a component of NPC, Nup358 has been implicated in mediating the docking of HIV-1 cores at NPC and subsequent nuclear entry [75, 131, 150, 171, 172]. It has also been suggested that Nup358 relocates in a Kif5B dependent manner from NPC to the cytoplasm to meet the incoming HIV-1 capsid prior the nuclear entry of the HIV-1 core [75].

TRN-1 is a β -karyopherin that recognizes the nuclear localization signals of target proteins and contributes to their nuclear import [173]. Two early studies reported that TRN-1 is responsible for the recognition and import of HIV-1 Rev protein [172, 174]; however, whether these processes modulated HIV-1 infection were not investigated. A recent study claims that TRN-1 is required for HIV-1 infection in a capsid-dependent manner [175]. The study first demonstrated that TRN-1 binds to the CypA-binding loop primarily via the residue G89 based on infection assays and *in vitro* binding assays. The study then showed that TRN-1 promoted uncoating of HIV-1 cores isolated from infected cells and *in vitro* assembled CA-NC tubes. The study further suggested that TRN-1 promoted the nuclear entry of the HIV-1 core.

1.1.3.4.2. The Central pore and interacting host factors

The central pore is a size-selective channel at the center of each CA hexamer, with a highly positively charged R18 ring formed by 6 arginine each from a CA monomer within the CA hexamer [70] (**Fig. 1.5**). Host factors that have been shown to interact with the R18 ring include nucleotides (dNTPs, ATP, rNTPs), IP6, and FEZ1. In this thesis we demonstrated that BICD2 also binds to the R18 ring (see **4.2.2**).

Cellular dNTPs are used by the HIV-1 virus as substrates for the reverse transcription of the viral genome while ATP hydrolysis is required by reverse transcriptase. Jacques *et al.* reported that HIV-1 capsid can recruit and import dNTPs and ATP through a dynamic pore at the center of the CA hexamer, raising the possibility that reverse transcription could be facilitated within a fully enclosed capsid [70]. This study offered the first description of the size-selective pore at the middle of CA hexamer and the R18 ring as a binding interface on HIV-1 capsid. The authors reported that the interaction between ATP/dNTPs and the R18 ring showed high affinity (6-40 nM), fast on-rate ($> 2 \times 10^8 \text{ M}^{-1} \text{ s}^{-1}$) and fast off-rate ($> 12 \text{ s}^{-1}$). These observations suggest that HIV-1 capsid could recruit ATP/dNTPs from cytoplasm and import them into the interior of HIV-1 capsid, thereby providing substrates and energy for reverse transcription. CA hexamers lose binding with nucleotides when the positive charge of R18 ring is removed by mutation R18A or R18G, confirming that the positively charged R18 ring is important for recruiting nucleotides. In addition, the authors observed that dNTPs and rNTPs (ribonucleoside triphosphates) bind to R18 ring equally well while other polyanions like hexacarboxybenzene or inorganic phosphate (when tested at a concentration 5 times higher than its cellular concentration) could also compete with nucleotides for the R18 ring. These results imply that the R18 ring potentially could non-selectively interact with polyanions in

cells. A recent study which reconstitutes HIV-1 reverse transcription *in vitro* also confirmed that reverse transcription can take place in an enclosed HIV-1 capsid [90].

IP6 is a strongly negatively charged metabolite that is highly abundant in a range of organisms including humans [176]. IP6 was first reported to be recruited to the R18 ring to stabilize capsid and promote DNA synthesis by Mallery *et al.* [67]. Co-crystallization of IP6 with CA hexamer reveals that IP6 binds to the R18 ring. Addition of IP6 dramatically stabilizes HIV-1 capsid based on an *in vitro* uncoating assay, likely because the binding of IP6 neutralizes the potential destabilizing effect coming from the electric repulsion of the six arginine in the R18 ring. The authors further demonstrated that high concentrations of IP6 and ATP promoted DNA synthesis, which was proposed to result from the stabilized HIV-1 capsid. An independent study from Dick *et al.* confirmed that IP6 binds to the R18 ring based on a crystal structure of IP6 and CA hexamer [110]. The authors also show that IP6 is a vital host factor for the assembly of both immature HIV-1 gag lattice and mature capsid lattice based on a combination of *in vitro* structural and functional analyses. Both studies estimated that IP6 is incorporated into HIV-1 capsid lattice at a ratio of roughly one IP6 molecule per CA hexamer [67, 110]. The enhancement of reverse transcription by increased capsid stability was also confirmed by a recent study reconstituting HIV-1 reverse transcription *in vitro* [90]. Mallery *et al.* further reported that viruses unable to package IP6 were deficient in maturation, capsid stability, and infectivity, indicating that IP6 is required for viral production in the producer cell and for viral infectivity in target cell [177].

FEZ1, the mammalian homologue of *Caenorhabditis elegans* protein UNC-76, is functionally associated with axonal outgrowth [178] and neuronal development [179]. It is also recognized as an adaptor protein of kinesin-1 motor [180-182]. Based on cellular infection assays, early studies reported that overexpression of FEZ1 restricted HIV-1 infection in fibroblast cell line [183] and in neurons [184]. However, more recent studies have demonstrated that endogenous levels of FEZ1 are required for HIV-1 infection [53, 73, 185]. Malikov *et al.* first reported that FEZ1 is the adaptor protein for the kinesin-dependent transport of the HIV-1 viral core in the cytoplasm [53]. The study showed that FEZ1, kinesin-1, as well as the interaction between FEZ1 and kinesin-1, were all necessary for HIV-1 infection and the overall retrograde transport of the HIV-1 viral core. The authors also demonstrated that FEZ1 directly bound to *in vitro* assembled CA-NC tube. In a subsequent study, Malikov *et al.* suggested that FEZ1 is also involved in HIV-1 capsid uncoating based on the observations that depletion of FEZ1 delayed uncoating [186]. Huang *et al.* reported

that FEZ1 binds to the R18 ring of HIV-1 capsid via its negatively charged motifs [73]. The authors proposed that a cluster of glutamic acid residues (aa182-186) form the primary HIV1-capsid-binding motif on FEZ1, based on observations that truncations including this region co-pellet with capsid in pull-down assays using assembled CA tubes, while truncations excluding this region do not. Truncations including this region are observed in co-elutes with CA hexamer but not CA assemblies reproducing other canonical binding interfaces on capsid, suggesting that FEZ1 specifically binds to the R18 ring of CA hexamer.

1.1.3.4.3. The NTD-CTD interface and interacting host factors

The NTD-CTD interface is orientated between two adjacent CA monomers in a CA hexamer (**Fig. 1.5**). Residues within helices 3 and 4 from NTD in the first CA monomer, helices 2 and 7 from NTD of the second CA monomer, and helices 8 and 9 from CTD of the second CA monomer together form the NTD-CTD interface [82, 92]. Numerous host factors have been shown to interact with the NTD-CTD interface, including cleavage and polyadenylation specific factor 6 (CPSF6), nucleoporin 153 (Nup153), and Sec24 homolog C (Sec24C).

CPSF6 is a pre-mRNA processing protein that dynamically shuttles between the cytoplasm and nucleus [187], while a truncated CPSF6 lacking the C-terminal nuclear targeting domain that is confined to the cytoplasm has also been identified [188]. Overexpression of this truncated CPSF6-358, prevents nuclear entry and inhibits HIV-1 infection [112, 189-191]. This effect is likely due to the inability of the truncated CPSF6-358 to facilitate the nuclear entry of the HIV-1 viral core, in line with the observation that the inhibition of infection is released when CPSF6-358 is targeted to the nucleus by fusion of a heterologous nuclear localization signal [190]. CPSF6₃₁₃₋₃₂₇ has been identified as the minimum binding motif that interacts with CA protein via its phenylalanine-glycine (FG) motif, with N74 of HIV-1 CA being a key residue for the interaction [118, 189, 192]. Different studies have reported different K_D values for the interaction between CPSF₃₁₃₋₃₂₇ and CA proteins, with an overall trend that CPSF₃₁₃₋₃₂₇ binds more tightly to CA hexamer [118, 120, 193] compared to CA monomer or CA_{NTD} [118, 189, 194]. Crystal structures of CPSF6₃₁₃₋₃₂₇ in complex with HIV-1 capsid confirmed that CPSF₃₁₃₋₃₂₇ binds to the NTD-CTD interface [118, 119]. An *in vitro* binding study observed that CPSF6-358 destabilizes CA tubes, which counters previous reports that CPSF6-358 lead to abnormally stabilized HIV-1 core [190, 191]. Two recent studies using the full-length CPSF6 provide direct evidence that CPSF6 facilitates the nuclear entry of the HIV-1 viral core based on data showing

that disruption of either the full-length CPSF6 or the interaction between HIV-1 capsid and the full-length CPSF6 leads to deficient nuclear entry of the HIV-1 core.

Nup153 is an essential component of the nuclear pore complex (NPC) that is localized to the nucleoplasmic side of the NPC [195]. It was first identified as a host factor involved in HIV-1 infection by three independent screens [101-103]. Nup153 is required for the nuclear entry [131, 165, 196, 197], and likely nuclear targeting [117, 165, 198], of the HIV-1 viral core. Co-crystallization of CA hexamer and the FG-motif containing Nup153₁₄₀₇₋₁₄₂₃ revealed that NUP₁₅₃ binds to the NTD-CTD interface of HIV-1 capsid lattice [119]. The same study also suggested that Nup153₁₄₀₇₋₁₄₂₃ binds to CA hexamer much more tightly than to CA monomer based on isothermal titration calorimetry (ITC) binding assays. The crystal structure of Nup153₁₄₀₇₋₁₄₂₉ and CA hexamer from a separate study confirmed that Nup153 binds to the NTD-CTD interface [197]. The residue N57, rather than N74, is key for the interaction between Nup153 and HIV-1 CA hexamer [119, 197], indicating that while both Nup153 and CPSF6 bind to the NTD-CTD interface, the structural bases for these interactions are distinct.

A recent study reported that Sec24C, a component the coat protein complex II (COPII) involved in vesicle trafficking [199], is required for HIV-1 infection in a capsid dependent manner [114]. The study identified Sec24C in a mass spectrometry-based proteomics as a capsid binder and then confirmed the interaction *in vitro* using isolated viral cores and *in vivo* based on a proximity ligation assay (PLA). Knockdown of Sec24C decreased capsid stability, reverse transcription, and nuclear entry but not entry of the virus into the cell. The binding motif was narrowed down to Sec24C₁₉₆₋₃₁₄ using a Trim-fusion-based restriction assay and then further narrowed down to a Sec24C₂₂₈₋₂₄₂ which contains similar FG motifs compared to CPSF6₃₁₃₋₃₂₇ and Nup153₁₄₀₉₋₁₄₂₃. Co-crystallization of CA hexamer and Sec24C₁₉₆₋₃₁₄ showed that the interaction is via the NTD-CTD interface, with N57 and N74 both vital for the interaction.

1.1.3.4.4. The tri-hexamer interface and interacting host factors

The tri-hexamer interface is located at the junction of three adjacent CA hexamers (**Fig. 1.5**) and is formed by residues within helices 10 and 11 from 3 neighboring CA monomers (each from one of the three adjacent CA hexamers) [96]. It is comprised of 12 glutamate residues (E71, E72, E212, and E213 from 3 monomers) that form a highly negatively charged groove [200]. The host factor myxovirus resistance protein B (MxB) has been identified to bind to this interface.

MxB is a dynamin-like GTPase serving as an interferon-inducible antiviral protein [201]. MxB is recognized as an HIV-1 inhibitor by restricting nuclear entry integration [200, 202-206]. Fribourgh *et al.* first showed that MxB directly binds to capsid assemblies, but not to CA monomers, pentamers or hexamers, to restrict HIV-1 infection, suggesting that the interaction requires a capsid lattice at least larger than a hexamer [206]. Schulte *et al.*, later showed that an N-terminal 25 aa region containing a triple arginine motif is necessary for the MxB-capsid interaction [205]. A recent study revealed that MxB binds to the tri-hexamer interface based on biochemical/biophysical characterizations and molecular dynamics simulations [200]. The study showed that mutations of CA at the tri-hexamer interface disrupted both the MxB-capsid interaction and the restriction of MxB towards HIV-1 infection. This result was confirmed by a separate study based on the observations that MxB only co-elute with CA assemblies bearing the tri-hexamer interface in a SEC co-elution assay using engineered CA assemblies which mimic various sizes of capsid lattice [125].

In this section (**1.1.3.4**) we only mentioned the host factors that have been demonstrated to directly interact with the canonical binding sites of HIV-1 capsid. Capsid binders that exhibit a more complicated binding pattern (e.g., TRIM5 [207, 208]), whose binding interfaces have not been identified, (e.g., BICD2 [52, 74]), and infection-relevant host factors which may indirectly associate with the capsid (e.g., TRN-3 [209], Kif5B [52, 150]), have not been discussed.

1.2. HIV-1 retrograde transport

Many viruses utilize the host cytoskeleton and motor protein complexes to transport in the cytoplasm [210, 211]. As a lentivirus, HIV-1 virus needs to traverse the cytoplasm prior to nuclear entry and integration. Considering the size of the HIV-1 viral core and the crowded nature of the cytoplasm, this process is assumed to occur via active transport rather than by free diffusion. This view is supported by the fact that cytoplasmic transport of HIV-1 particle requires the microtubule network [51]. Cytoplasmic dynein and kinesin are the two main cytoplasmic motor complexes that facilitate retrograde and anterograde transport of cargoes along microtubules [212]. Recent studies provide evidence that HIV-1 capsid exploits both dynein [52, 74] and kinesin-1 [53, 73, 186] motor complexes for the active transport of the HIV-1 viral core towards the nucleus during the early stages of viral infection. In this section we will discuss the basics of microtubule structure and dynamics followed by several current models for how HIV-1 capsid is transported through the cytoplasm.

1.2.1. Microtubules

Microtubules, together with actin and intermediate filaments, constitute the multifunctional cytoskeleton network in all eukaryotic cells which is involved in multiple important cellular

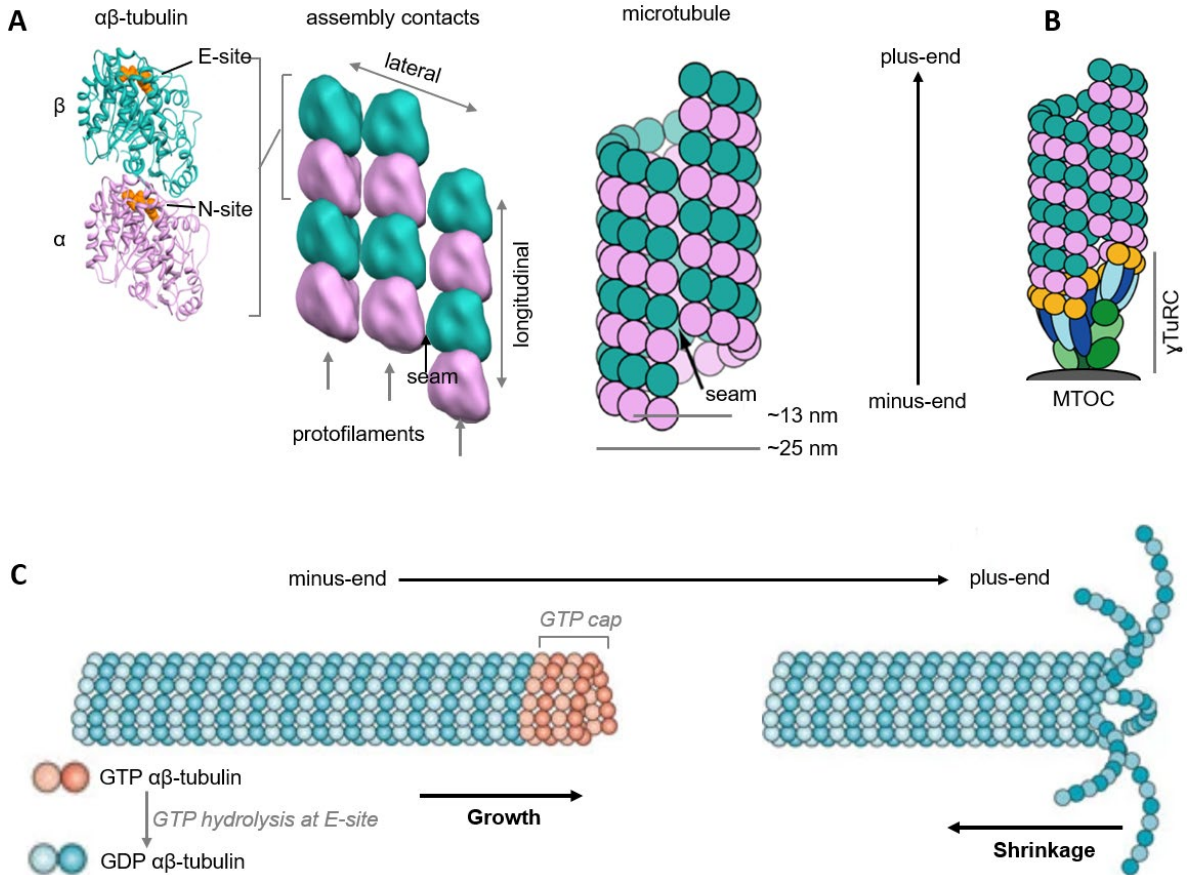


Fig. 1.6. Microtubule structure and plus-end dynamics. **A.** Arrangement of $\alpha\beta$ -tubulin heterodimer, which is the building block of microtubule, into protofilament and further into microtubule. GTP/GDP binding site in α - and β -tubulin is colored in yellow. **B.** Microtubule anchors at the MTOC with its minus-end while grows towards the cell periphery with its plus-end. **C.** Microtubules plus-end grows when GTP hydrolysis is slower than the incorporation of $\alpha\beta$ -tubulin into the lattice (i.e, the GTP cap is present). When GTP hydrolysis is faster than the incorporation of $\alpha\beta$ -tubulin, microtubule undergoes rapid disassembly. Images adapted from [213, 214].

processes including cell division, cell morphology, and intracellular transport [215-217]. The $\alpha\beta$ -tubulin heterodimers, which are the building blocks of microtubule, polymerize head-to-tail into a polar protofilament (PF) with β -tubulin exposed on the plus end and α -tubulin exposed on the minus end. Each $\alpha\beta$ -tubulin has two guanosine triphosphates (GTPs) binding sites: an E-site (exchangeable)

in β -tubulin which can exchange guanosines diphosphates (GDP) with GTP when an un-incorporated tubulin dimer is free in solution, and a N-site (non-exchangeable) in α -tubulin which is constitutively occupied by GTP [218-220]. Typically, 13 PFs associate laterally into a hollow microtubule where the seam describes the lateral contacts between α - and β -tubulins [213, 221] (**Fig. 1.6.A**). Microtubules have an outer/inner diameter of approximately 25/13 nm (**Fig. 1.6.A**), and a length ranging from sub-micrometer to more than 100 μ m [222, 223]. Within the cell, the more stable, minus end of microtubules are anchored at the microtubule-organizing center (MTOC) via γ -tubulin ring complex (γ TuRC), while the dynamic plus end radiates outwards towards the cell periphery (**Fig. 1.6.B**) [213, 215, 223]. A cluster of acidic residues at the C-terminal tail of α - and β -tubulin make the surface of microtubule highly negatively charged, which is key for the interactions between microtubule and many microtubule associated proteins (MAPs) [224, 225]. Microtubule undergoes various post-translational modifications, which is another key feature that contributes to microtubule regulations and functions [226-228].

Microtubules exhibit dynamic instability, meaning that microtubules frequently switch between rapid growth and shrinking phases [214, 229]. Microtubule dynamics are regulated by multiple factors including the concentration of soluble tubulin, MAPs [223, 230, 231], and mechanical forces [232-234]. On a basic level, microtubule growth simply represents the addition of $\alpha\beta$ -tubulin dimers onto existing protofilaments [233, 235]. The GTP bound at the E-site of β -tubulin is hydrolyzed soon after the tubulin dimer is incorporated into the microtubule lattice; hydrolysis of the GTP at E-site of β -tubulin is assembly-dependent because the incoming subunit functions as a GTPase activating protein (GAP) which complete the binding site to enable hydrolysis [220, 236, 237]. Upon GTP hydrolysis, the 'GTP $\alpha\beta$ -tubulin' turns into 'GDP $\alpha\beta$ -tubulin', gradually forming a GDP lattice. When the incorporation rate of $\alpha\beta$ -tubulin dimer is faster than the GTP hydrolysis rate, a GTP cap presents at the plus-end and the microtubule keeps growing (**Fig. 1.6.C**, left); when the GTP hydrolysis rate is faster than the incorporation rate of $\alpha\beta$ -tubulin dimer, the microtubule undergoes rapid disassembly (**Fig. 1.6.C**, right) [214, 229, 237-240].

In this thesis, we will use microtubules only as the track along which motor protein complexes transport HIV-1 capsid. However, given the dynamic nature of microtubules, they need to be stabilized to prevent disassembly over the time range of our experiments. GMPCPP [241-244] and paclitaxel (taxol) [245-250] are commonly used microtubule stabilizing agents to prepare stabilized microtubules for *in vitro* assays. GMPCPP is a slowly hydrolyzing analog of GTP, that stabilizes

microtubules by slowing down the hydrolysis rate since GTP hydrolysis, leading to microtubules that are bound exclusively in the GTP state [241, 242, 244]. In contrast, taxol is a compound that was first reported to stabilize microtubules in late 1970s [247, 251] and is widely used as a chemotherapeutic drug for cancer by targeting cell division [252]. It binds to the microtubule lattice and stabilizes it through a mechanism that remains unclear.

1.2.2. Dynein dependent transport

Dynein is a microtubule motor responsible for retrograde transport and numerous studies have implicated its involvement in HIV-1 infection [253-255]. The earliest direct evidence of HIV-1 virus utilizing cytoskeleton for transport was reported by McDonald *et al.* in 2002, who proposed that HIV-1 relies on microtubule and dynein to deliver the viral genome towards the nucleus [51]. Other studies have identified the interactions between dynein subunits and components within the viral core including Vpr [256] and IN [254, 257] that contribute to the transport of HIV-1 core. However, these observations are difficult to reconcile with several models for uncoating, because dynein would not be able to access Vpr or IN while the capsid core remains fully intact in the cytoplasm. Nevertheless, these initial studies clearly demonstrate the involvement of dynein in HIV-1 infection.

Dharan *et al.* reported that the HIV-1 viral core recruits the dynein motor complex for retrograde transport via BICD2 [74], a known adaptor protein for dynein [258, 259] that had also been shown to be required for HIV-1 infection [102]. The study showed that BICD2 associates with HIV-1 capsid during infection based on a proximity ligation assay; direct interactions between BICD2 and capsid were confirmed using *in vitro* pull-down experiments with CA-NC (capsid-nucleocapsid) tubes. The study further suggested that capsid binds BICD2 via its C-terminal CC3 (coiled-coil 3) domain, which is the canonical cargo binding domain of BICD2 [260].

Carnes *et al.* presented a systematic analysis of the interplay between HIV-1 virus and the dynein motor complex, further supporting the notion that the viral core engages dynein-dynactin-BICD2 complex for transport to the nucleus [52]. The authors performed knock-down experiments disrupting subunits of dynein or dynactin, as well as BICD2, followed by cell-based HIV-1 infection assays. Reduced infection and nuclear import, but not reverse transcription, were observed after knock-down of dynein heavy chain, BICD2, or dynactin subunits. The proportion of non-motile viral cores significantly increased upon the knock-down of dynein heavy chain or BICD2. For the viral cores that were still motile, the average distance of their retrograde transport decreased. Taken

together, the authors suggested that the dynein-dynactin-BICD2 motor complex is recruited by the viral core to mediate its transport to the nucleus. The study also confirmed that BICD2 directly binds to capsid based on an *in vitro* pull-down assay using CA-NC tube. Surprisingly, the study showed that both the N-terminal CC1 (coiled-coil 1) domain and CC3 domain of BICD2 bind to HIV-1 capsid, which is unexpected since CC1 is generally recognized as the dynein-dynactin binding domain of BICD2 [261, 262]. Together, these two studies suggest a model in which HIV-1 capsid recruits dynein via BICD2, thus forming a dynein-dynactin-BICD2-capsid complex that facilitates the retrograde transport of the HIV-1 viral core.

1.2.3. Kinesin-1 dependent transport

Multiple studies have shown that kinesin-1, an anterograde motor that transports cargoes to the cell periphery, also contribute to the retrograde transport of HIV-1 capsid [53, 73, 75, 150, 186, 263]. While these results initially seem contradictory, it is in line with the current thinking of how cargo transport is implemented in the cell [264, 265]. Specifically, many systems have demonstrated that the net movement in one direction depends upon the action of both retro- and anterograde motors. Consistent with this idea, bi-directional movement of the HIV-1 viral core in the cytoplasm during early infection has been demonstrated by early live cell imaging [51]. However, a clearer picture of how kinesin direct the transport of HIV-1 core has only recently become available.

Malikov *et al.* in 2015 reported that HIV-1 capsid could recruits kinesin-1 via the adaptor protein FEZ1 to support the retrograde transport of the viral core [53]. This study first showed that FEZ1, kinesin-1, as well as the interaction between these factors are required for HIV-1 infection. FEZ1 was confirmed to directly bind to HIV-1 capsid by *in vitro* pull-down assay using CA-NC tubes. Disruption of FEZ1 or kinesin inhibited overall retrograde transport without affecting dynein, suggesting that kinesin and FEZ1 actively contribute to the retrograde transport of the HIV-1 viral core. Based on knock-down assays, Malikov *et al.* further reported that the kinesin-1 heavy chain, but not the light chain, was responsible for the retrograde transport of HIV-1 core [186]. Both studies from Malikov *et al.* suggest that phosphorylation of FEZ1 at residue serine 58 is important for the formation of a kinesin-FEZ1-capsid complex, in line with previous reports that the interaction between FEZ1 and kinesin-1 depends upon this phosphorylation event [182]. While FEZ1 had previously been shown to be involved in HIV-1 infection [183, 184], as well as a known kinesin adaptor [180-182], these two studies linked these observations together and presented a more complete model in which FEZ1 is the adaptor protein for the kinesin dependent transport of HIV-1 capsids.

Huang *et al.* reported that FEZ1 binds to HIV-1 capsid via the electrostatic interaction between the R18 ring of capsid and the negatively charged motifs on FEZ1 [73]. The authors proposed that a cluster of glutamic acid (aa 182-186) form the primary HIV1-capsid-binding motif on FEZ1, based on observations that truncations including this region co-pellet with CA tubes, while truncations excluding this region do not. Furthermore, truncation fragments containing this region are observed to co-elute with CA hexamer but not CA assemblies resembling other canonical binding interfaces on capsid, suggesting that FEZ1 specifically binds to the R18 ring of CA hexamer. However, mutations of this motif do not significantly inhibit the transport of HIV-1 core in cells, although they do cause a moderate reduction in HIV-1 infection. This study provided the earliest evidence for the capsid-FEZ1 interaction at a molecular level. These three studies together suggest a model where HIV-1 hijacks kinesin via FEZ1, thus forming a dynein-dynactin-BICD2-capsid complex to contribute to the overall retrograde transport of the HIV-1 viral core.

1.2.4. Model of HIV-1 retrograde transport

Evidence to date suggests that HIV-1 capsid utilizes both dynein and kinesin motor complexes, via the adaptor proteins BICD2 and FEZ1, to facilitate retrograde transport of the HIV-1 viral core during early infection [52, 53, 73, 74, 186]. Disruption of dynein-dynactin-BICD2 complex or kinesin-1 result in the accumulation of HIV-1 core at the cell periphery [51-53, 186] while depletion of FEZ1 leads to a failure of HIV-1 to reach the nucleus [53, 186]. In short, while HIV-1 cores exhibit net retrograde transport in the cytoplasm, this process requires both dynein and kinesin motors, whereby anterograde transport by kinesin is presumably required to bypass obstacles and/or transport the capsid from the microtubule organizing centre (MTOC) to the nuclear pore complex. Based on these observations, Dharan and Edward proposed a model for HIV-1 cytoplasmic transport that dynein transports the viral core towards the nucleus while kinesin contributes as a mechanism to bypass obstacles by pulling the viral core back a few steps or switching the HIV-1 core to neighboring microtubules [266]. The authors further speculate that the kinesin-1 motor can be turned on or off based on the phosphorylation state of FEZ1 serine 58; such a mechanism could limit the contribution of kinesin to the transport only when HIV-1 core needs to bypass obstacles. In addition, it has been suggested that HIV-1 capsid could interact with multiple microtubules associated proteins (MAPs) to modulate microtubule stability, adding another level of possible regulation to the transport process [267].

I present a fictional model for the retrograde transport of the HIV-1 viral core (**Fig. 1.7**) based on the model proposed by Dharan and Edward [266] as well as a number of other considerations: 1) dynein confers the ability to slightly rotate while walking owing to its relative flexible motile behavior [268, 269]; 2) intracellular cargoes could rotate at microtubule intersection [270]; 3) cargoes with multiple motors could efficiently rotate while walking [269], 4) the HIV-1 capsid lattice is large enough to recruit multiple sets of adaptors/motors (to be discussed in Chapter 4 and Chapter 5).

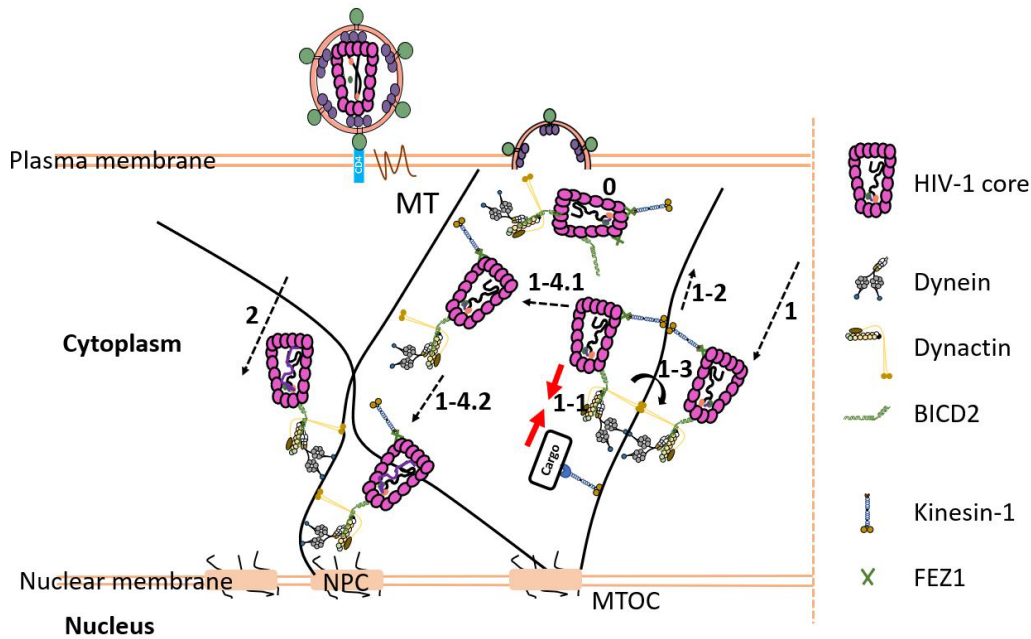


Fig. 1.7. Fictional model of the retrograde transport of HIV-1 viral core. **0)** Upon cell entry, HIV-1 core is released into the cytoplasm and HIV-1 capsid recruits multiple BICD2 and FEZ1 molecules for tethering to motor complexes. **1)** The HIV-1 core is transported inwards by dynein-dynactin-BICD2 complex while encounters a cellular cargo which is transported outward by kinesin complex. Possible scenarios contains: **1-1)** Both complexes pause until one of them falls off, or one complex pushes the other into its own direction; **1-2)** The viral core takes few steps back, as facilitated by kinesin-1, until there is no more conflict; **1-3)** The viral core rotates to bypass obstacle; **1-4.1)** The viral core released from the microtubule and landed onto another microtubule by kinesin-1, or dynein, or both; **1-4.2)** Dynein takes charge and continue to transport the viral core towards the nucleus; **2)** The viral core is transported by dynein alone without coming across obstacles. The fictional model was adapted referring to [266]. Not to scale.

1.3. Motor protein complexes

Motor proteins are defined as biological molecules that transform chemical energy into mechanical forces to assist a range of biological processes, and are broadly classified into cytoskeleton motor proteins, nucleic motor proteins and rotary motors [271]. Cytoskeleton motors include dynein and kinesin which move along microtubules, and myosin which moves along actin filaments [272]. Each motor belongs to a superfamily that are comprised of multiple sub-families. Dynein can be subdivided into cytoplasmic dynein and axonemal dynein [273]. The kinesin super-family contains at least 45 kinesins which can be classified into 15 subfamilies from kinesin-1 family to kinesin-14B family [274]. Both dynein and kinesin are controlled by complicated auto-inhibition and activation mechanisms to ensure that the motors are only active when engaged in cellular activities, such as cargo transport, in order to avoid unnecessary consumption of cellular ATP.

In this thesis we will only discuss cytoplasmic dynein and kinesin-1, the motors primarily responsible for driving retrograde and anterograde transport in the cytoplasm. We focused on these two motor complexes because they have been demonstrated to regulate HIV-1 infection [51, 53, 73, 186, 253-255, 275]. Throughout the text, we will refer to cytoplasmic dynein as dynein and kinesin-1 as kinesin in following paragraphs unless otherwise specified.

1.3.1. Dynein motor complexes

The dynein motor complex is responsible for the retrograde transport of cargoes [273, 276, 277]. Dynein is auto-inhibited by itself and exhibits static interactions or small diffusive movements along microtubules *in vitro* [262, 278, 279]. Dynactin is an essential co-factor of dynein for almost all functions [280, 281]. Both dynein and dynactin are large, multi-subunit complexes which together form the main body of dynein motor complex. Dynactin itself cannot be efficiently coupled to dynein unless an adaptor protein links them together [262, 280, 282]. An adaptor protein can link dynein-dynactin on one end and tethers a cargo to dynein-dynactin on the other end, thus forming an activated dynein-dynactin-adaptor-cargo complex for cargo transport [283-286]. However, the binding of the adaptor alone to dynein and dynactin is not sufficient to release the auto-inhibition until a cargo is attached. On the other hand, truncated adaptor proteins lacking the cargo binding domains can activate dynein-dynactin and give rise to motility *in vitro* [262, 287, 288].

1.3.1.1. Dynein

Dynein is a large motor protein complex (~1.4MDa) which presents as dimer with each monomer consisting of 6 subunits (**Fig. 1.8. A**). A dynein dimer consists of 2 heavy chains (DHC, ~520 KDa each), 2 intermediate chains (DIC, ~74 KDa each), 2 light intermediate chains (DLIC, ~55 KDa each), and 2 sets of light chains (DLC, each set contains RB1, LC8 and Tctex1; all ~ 10 KDa) [276, 286] (**Fig. 1.8. A**).

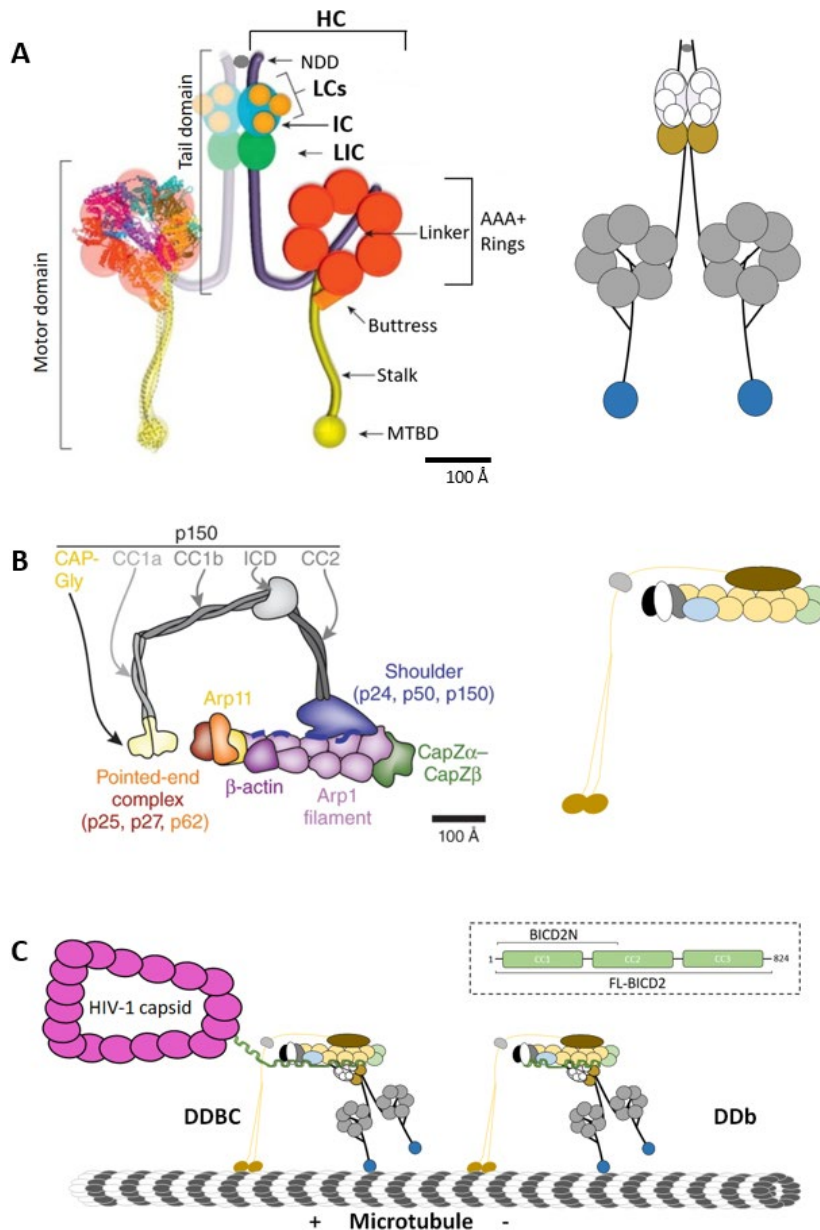


Fig. 1.8. Dynein, dynactin, and dynein motor complexes. A. Schematic displays of dynein.

Subunits are indicated in bold text and important structures are indicated and dynactin (**B**)

Schematic displays of dynactin. Both dynein and dynactin complex are adapted as cartoons on the right for animation of DDB and DDBC. **C.** Schematic displays of active DDB (dynein-dynactin-

BICD2N) and DDBC (dynein-dynactin-BICD2-capsid) complexes transporting towards the minus end of the microtubule. Not to scale. The protein arrangement of BICD2N and FL-BICD2 are indicated in the dashed box. Images adapted from [276, 280].

As the largest subunits, the DHC dimer forms the structural and functional core of dynein. The DHC contains a C-terminal motor domain and a N-terminal tail domain. The N-terminal tail domain contains a dimerization domain (NDD) followed by a region that associates with the DLCs, DIC and DLIC [289, 290]. The end of the tail domain joins the motor domain. The motor domain contains a ring-shaped ATPase head, a stalk with the microtubule binding domain (MTBD), and a linker. Six AAA+ (ATPase associated with various cellular activities) modules form the ring-shaped ATPase head. Of the six AAA+ modules, AAA1 is thought to be the primary ATP hydrolysis site, AAA2-4 are thought to be subsidiary sites for ATP hydrolysis and nucleotide binding, while AAA5 and AAA6 are proposed to be structural components since they lack nucleotide binding motif [291, 292]. The motor domain connects to the tail domain via the linker, which also spans across the AAA+ ring and undergoes conformational changes coupled with the dynein powerstroke cycle [292, 293]. The stalk protrudes out of the AAA+ ring and contains the MTBD on its tip for interacting with microtubule. The buttress, which contacts the stalk on one end and AAA5 on the other end, is speculated to regulate the conformation of the stalk during the dynein powerstroke cycle (**Fig. 1.8.A, Fig. 1.9.A**) [294].

Dynein motility occurs via cyclical conformational changes of dynein coupled with ATP hydrolysis, resulting in the movement of dynein motor complex towards the minus end of microtubule. This process, which is often referred to as the dynein powerstroke cycle, can be attributed to changes of the relative position between the AAA+ ring and the linker domain [291-294]. The C-terminal end of the linker is anchored with AAA1 while the N-terminal alters its positioning relative to the AAA+ ring during the dynein powerstroke cycle. In the absence of nucleotide binding, dynein is in its post-powerstroke conformation where the MTBD binds tightly to microtubule while the N-terminal of the linker contacts AAA4 or AAA5 depending on dynein isoform (**Fig. 1.9.A, right; B, a**). ATP binding to AAA1 triggers a chain of conformational changes which weakens the MTBD-microtubule interaction leading to the detachment of dynein from the microtubule. Shortly after detachment, dynein adopts its pre-powerstroke-I conformation where the AAA+ ring and the stalk rotate away from microtubule towards the MT-minus-end while the N-terminal of the linker rotates to near AAA2/AAA3 (**Fig. 1.9.B, b**). Coupled with ATP hydrolysis, dynein transits from pre-powerstroke-I to

pre-powerstroke-II conformation by rotating back near to microtubule thus allowing the MTBD to weakly bind a new site on the microtubule lattice (**Fig. 1.9.B, c**). Upon release of phosphate and ADP, the powerstroke brings the N-terminal of the linker to AAA4 again thus dragging the dynein motor complex and its cargo one-step-nearer to the minus end of microtubule. Meanwhile, dynein transits back to the post powerstroke conformation and MTBD binds tightly to microtubule again (**Fig. 1.9.B, d**).

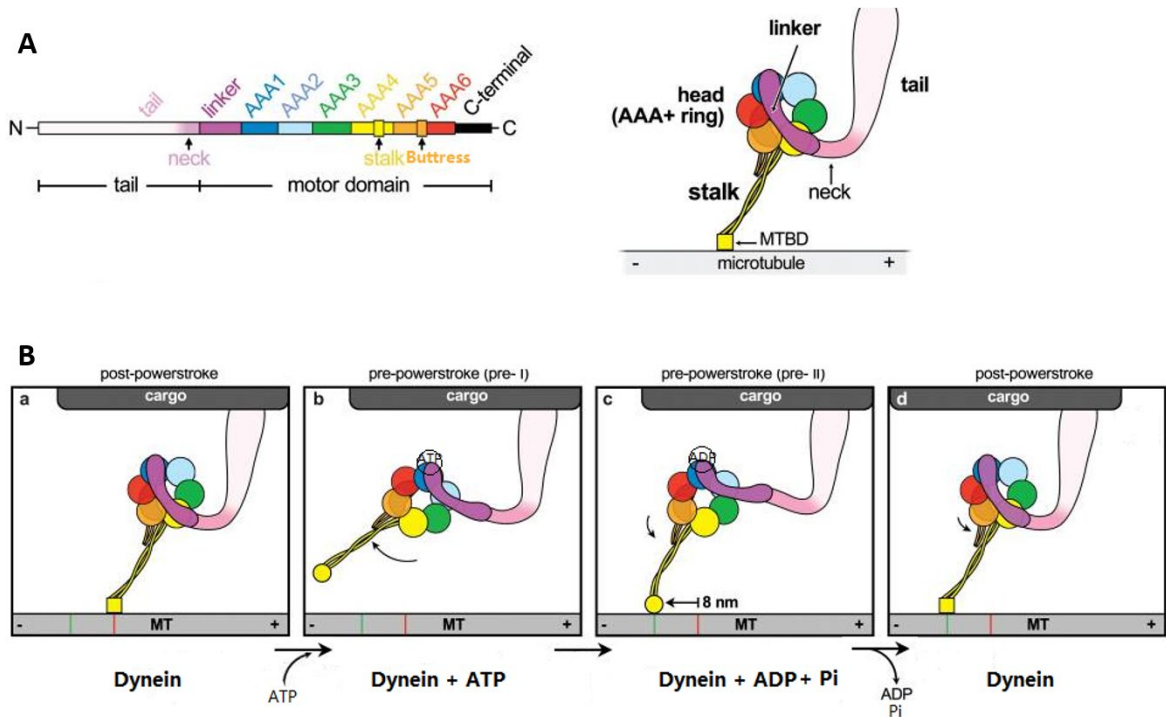


Fig. 1.9. Dynein heavy chain and the dynein powerstroke cycle. **A.** Sequence (left) and arrangement (right) of dynein heavy chain. **B.** In the absence of nucleotide, MTBD binds to microtubule tightly and dynein adopts its post-powerstroke conformation with the linker contacting AAA4 or AAA5. ATP binding to AAA1 cause conformational rearrangement and weakens the MTBD-microtubule interaction, resulting in the releases of dynein from microtubule by tilting away into its pre-I conformation. Upon or after ATP hydrolysis, dynein tilts near to microtubule into its pre-II conformation and MTBD binds weakly onto microtubule. Release of ADP then rest the cycle and the MTBD binds tightly to microtubule again. Images adapted from [293].

1.3.1.2. Dynactin

Dynactin is also a large protein complex (~1.2MDa) comprised of 23 subunits (11 different proteins) [280, 281], which was first identified as a co-factor for dynein motility *in vitro* [295, 296]. Dynactin can be structurally divided into 3 major domains: the Arp1 (Actin-related protein 1) filament, the point end complex, and the shoulder complex (**Fig. 1.8.B**, left) [280]. The Arp1 filament is composed of 8 copies of Arp1 (light purple), 1 copy of β -actin (dark purple), 1 copy of CapZ α - β dimer (green), and 1 copy of Arp11 (yellow) [289]. The scaffold of the Arp1 filament is arranged into 2 protofilaments, with 5 copies of Arp1 in one protofilament and 3 copies of Arp1 plus 1 copy of β -actin on the other protofilament [289, 297]. The Arp1 filament, like an actin filament, is polar with CapZ α - β dimer capping its barbed end and Arp11 capping its pointed end. The Arp1 filament serves as the backbone of the dynactin complex. The pointed end complex, which is made up of 3 subunits (p25, p27 in red and p62 in orange), binds to Arp11 on the pointed end of the Arp1 filament. The pointed end complex is suggested to be involved in cargo targeting [298, 299]. The shoulder complex contains 2 copies of p24, 4 copies of p50, and 2 copies of p150 which together form the shoulder region (blue) and the p150^{Glued} arm (grey) [280, 289]. The shoulder region, which contacts the Arp1 filament, is predominantly formed by p24 and p50. The p150^{Glued} arm is a dimer of the p150 subunit, which is the largest subunit of dynactin complex. The C termini of the p150^{Glued} arm joins the shoulder region while its N termini forms the CAP-Gly (cytoskeleton-associated protein glycine-rich; light yellow) domain which mediates docking of dynactin complex onto microtubule [300, 301]. In between the N and C terminus are 3 coiled-coil domains (CC1a, CC1b and CC2) and an intercoiled domain (ICD) [280]. The projection of these coiled-coil domains is not resolvable when dynactin is not bound to a microtubule [289, 297], suggesting that it could adopt multiple conformations.

1.3.1.3. Dynein-dynactin-BICD2N (DDb) and dynein-dynactin-BICD2-capsid (DDBC) complexes

As mentioned above, an adaptor protein tethers a cargo to dynein and dynactin, thereby forming an activated dynein-dynactin-adaptor-cargo complex to transport the cargo [283-286]. BICD2 is a well-known adaptor protein that facilitates intracellular transport [258, 259] and has been suggested to mediate the interaction of HIV-1 capsid to the dynein-dynactin complex [52, 74]. The binding of BICD2 to dynein and dynactin is not sufficient to release auto-inhibition until a cargo is recruited. However, a truncated BICD2 N-terminal (BICD2N) that lacks the cargo binding C terminus has been shown to efficiently recruit dynein and dynactin to form the active but cargo-free dynein-dynactin-BICD2N complex (hereafter termed as DDb) [262, 287]. In Chapter 4 of this thesis, we present our efforts to reconstitute the dynein-dynactin-BICD2-capsid complex (referred to as DDBC)

complex and examine its motility along microtubule *in vitro*. We have also reproduced the DDb motility assay as means to confirm the production of functional dynein and dynactin for downstream experiments. The organization of DDBC and DDb are schematically shown, where 'b' in 'DDb' refers to the truncated BICD2N, distinguishing it from the uppercase 'B' which refers to FL-BICD2 in 'DDBC' (**Fig. 1.8.C**).

1.3.2. Kinesin-1 motor complexes

Kinesin-1 is responsible for the anterograde transport of cargoes. Kinesin-1 motor exists as either a dimer consisting of two copies of kinesin heavy chain (KHC) or a tetramer consisting of two copies of KHC with two copies of kinesin light chain (KLC) bound. Both the kinesin-1 dimer [302-304] and the kinesin-1 tetramer [305, 306] [307] have been demonstrated to facilitate the transport of cellular cargoes. Kinesin-1 can be divided into three isotypes based on the differences in KHC (Kif5A, Kif5B, Kif5C), with Kif5B being ubiquitously expressed while Kif5A and Kif5C are enriched in neurons [274]. The auto-inhibition and activation mechanisms of kinesin are less understood compared to dynein, although it has been shown that KHC is autoinhibited by itself in a head-to-tail manner [308-310] while KLC contributes to another layer of auto-inhibition [311, 312]. Existing evidence suggest that the transport of HIV-1 capsid is facilitated in a kinesin dimer dependent manner [53, 73, 186]. Therefore, we will focus on KHC in this section followed by a brief discussion of the proposed model for the kinesin-FEZ1-capsid complex.

All 3 isotypes share a similar structure consisting of a N-terminal motor domain, a neck linker, a stalk domain containing several coiled-coil regions connected by flexible hinges, and a tail domain (**Fig. 1.10.A-B**) [274, 313]. The full length Kif5 is autoinhibited in a tail-to-head manner which requires the binding of adaptor and cargo for activation (**Fig. 1.10.B**) [308-310]. In comparison, the N-terminal truncations of kinesin including Kif₄₂₀ and Kif₅₆₀ are not autoinhibited and show motility in *in vitro* assays with similar characteristics to the motility of full-length kinesin *in vivo* [308, 314]. Therefore, these truncated kinesins have been extensively studied for understanding the activity of kinesin motors on a mechanistic level [308, 314-316]. The motor domain contains both the microtubule binding site and the ATPase site [313, 317-320]. Kinesin motor head binds to the groove of between α - and β -tubulin, with α - and β -tubulin equally contributing to the interaction which is primarily facilitated by the electrostatic interaction between the positively charged residues on kinesin and the strong negative charge on the microtubule lattice [319, 321]. The ATP binding site in kinesin is formed by three motifs: a phosphate binding loop (P-loop), a switch-1 motif, and a

switch-2 motif. In the absence of microtubule, both motor heads of kinesin recruits ADP. When one motor head binds to a microtubule, it undergoes a conformational change at the ATP binding site which favors ADP release and ATP recruitment to initiate a mechanochemical cycle [318, 322]. In short, binding of the leading head (i.e., the motor head that is nearer to the plus end of microtubule) to a microtubule drives ADP release and the leading head switches into an apo state where it opens its

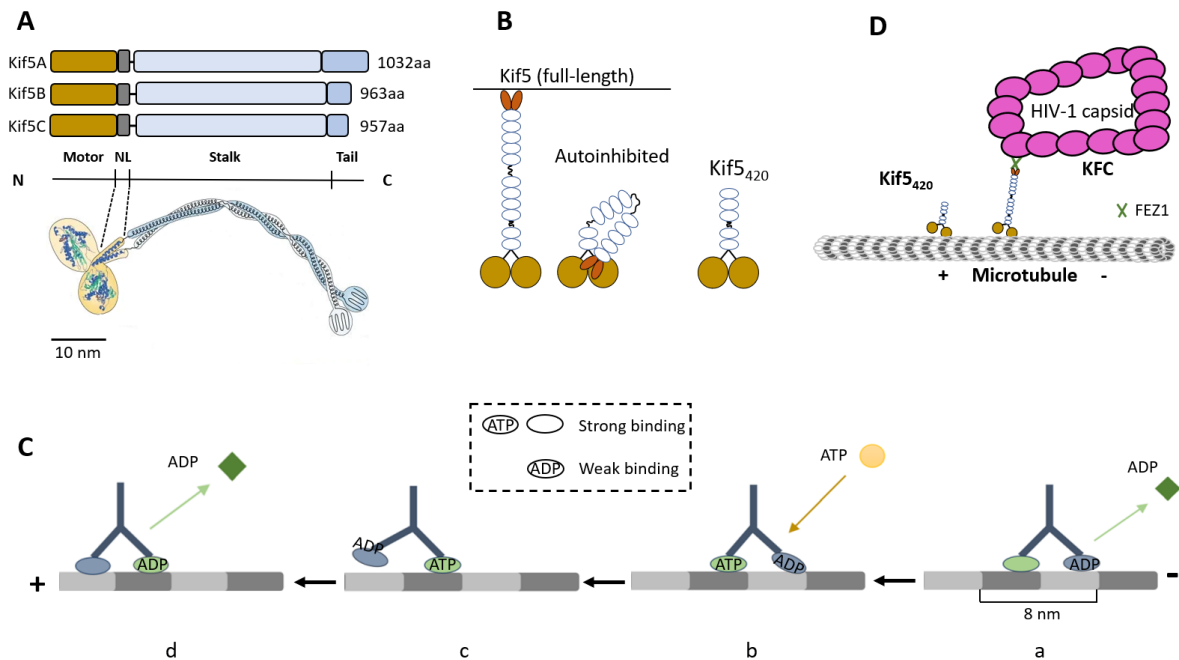


Fig. 1.10. Kif5 structure, autoinhibition, activation, and mechanochemical cycle. **A.** Kif5 consists of a N-terminal motor domain, a neck linker (NL), a stalk domain containing 3 coiled-coil regions connected by flexible hinges, and a C terminal tail domain. **B.** Full length Kif5 is autoinhibited in a tail-to-head manner while a N-terminal truncation (Kif5₄₂₀) is an active motor by itself. **C.** Mechanochemical cycle of kinesin demonstrated with an Kif5₄₂₀. **D.** Cartoons showing an active Kif5₄₂₀ and Kif5-FEZ1-capsid (KFC) complex walking towards the plus end of the microtubule. Not to scale. Images adapted from [313, 323].

binding site for ATP while remaining tightly bound to the microtubule (**Fig. 1.10.C, a**). Subsequent ATP binding to the leading head results in a structural change in the neck linker region that forces the lagging head to search for a next forward binding site (**Fig. 1.10.C, b-c**). Upon binding, the lagging head now becomes the leading head as it releases ADP and switches to the apo state (**Fig. 1.10.C,**

d), marking the start of the next mechanochemical cycle. The step size of kinesin is roughly 8 nm while the frequency is roughly 100 steps per second [324].

As mentioned earlier, full length Kif5B is autoinhibited while the binding of appropriate adaptor and cargo at the tail region may release the autoinhibition. In Chapter 5, we will test whether FEZ1 and HIV-1 capsid could bind to Kif5B and form an active Kif5B-FEZ1-capsid complex (KFC) complex, as schematically shown (**Fig. 1.10.D**).

1.4. Research proposal and research aims

To achieve successful early infection, the HIV-1 capsid interacts with host factors to execute multiple viral activities including evading innate immune responses, reverse transcription, retrograde transport, uncoating, nuclear entry, and integration site targeting. As such, the capsid has emerged as an attractive therapeutic target; however, a more comprehensive understanding of the interactions between capsid and host cell proteins is required.

In this thesis we aim to expand our understanding of how interactions between the capsid and host cell factors regulate viral activities, specifically focusing on the cytoplasmic transport process. It has been shown that HIV-1 viral core exploits the microtubule network and motor complexes to promote its transport to the nucleus. Recent evidence has also suggested that HIV-1 capsid is linked to dynein and kinesin motors via the adaptor proteins BICD2 [52, 74] and FEZ1 [53, 73, 186]. These initial observations have led to a model that HIV-1 capsid could recruit dynein and kinesin motors to form motor-adaptor-cargo complexes (dynein-dynactin-BICD2-capsid (DDBC) and kinesin-FEZ1-capsid (KFC)) for active transport along microtubules. In this thesis we will present our work to reconstitute these complexes and show that they are capable of walking along the microtubule lattice, providing more direct evidence to support these models.

Research Aims

The overall aim of this thesis is to contribute to our understandings of how the interactions between HIV-1 capsid and host factors modulate viral activities, specifically focusing on the cytoplasmic transport process. Chapter 3 will describe the initial work of my PhD where we expanded our understanding of the capsid-host interaction. This chapter will first present our published study [121] which focuses on the CypA-capsid interaction to investigate a previously proposed secondary binding motif on the host protein CypA [109]. More importantly, this chapter describes an optimized

method for *in vitro* assembly of HIV-1 capsid, which allows the generation of capsid assemblies that are well-suited for single molecule assays.

Chapter 4 and Chapter 5 will describe our investigation of the cytoplasmic transport process of HIV-1 capsid using *in vitro* approaches as schematically shown (**Fig. 1.11**). The focus of Chapter 4 is to reconstitute dynein-dependent transport of HIV-1 capsid. We will first examine the interaction between HIV-1 capsid and the adaptor protein BICD2 and provide a quantitative characterization and initial dissection of the binding. We also present initial results that illustrate the reconstitution of the DDBC complex and visualize its motility along microtubules *in vitro*.

The aim of Chapter 5 is to reconstitute kinesin-dependent transport of HIV-1 capsid. To do so, we will first examine the interaction between HIV-1 capsid and the adaptor protein FEZ1, emphasizing a quantitative characterization of this association and describing the protein motifs that mediate the binding. Next, we reconstitute the KFC complex and visualize its motility along microtubule *in vitro*, along with characterization and statistical analysis of the motile behaviors of the KFC complex. We will examine the quantifications while altering certain features (e.g., disruption of the R18 ring on capsid) to better understand the properties of the KFC complex and investigate the requirements for the kinesin-dependent transport of HIV-1 capsid. We will further examine the role that capsid plays in the formation of an active KFC complex.

Chapter 6 will discuss main conclusions and future directions.

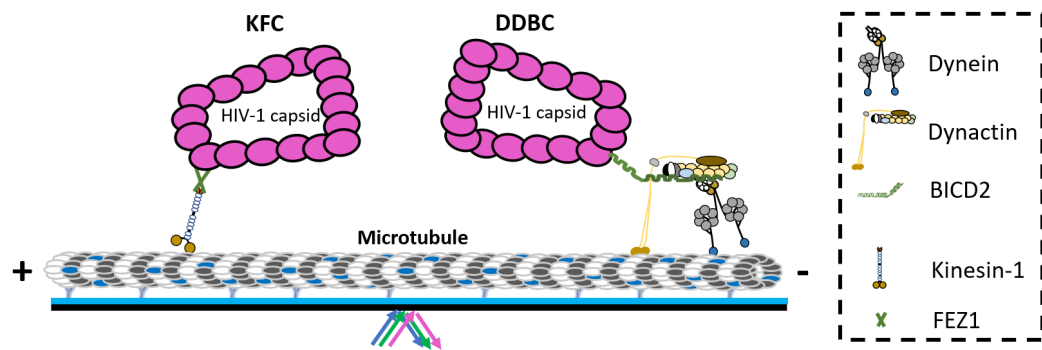


Fig. 1.11. Cartoon showing the experimental design for the *in vitro* reconstitution and visualization of dynein- and kinesin-dependent transport of HIV-1 capsid.

Chapter 2

Materials and methods

2. Materials and methods

2.1. TIRFM (total internal fluorescence microscopy)

2.1.1. Microscope set up

The binding assays between HIV-1 capsid and capsid binders were imaged using a 2-camera TIRF microscope while the motility assays were imaged using a 3-camera TIRF microscope. The photobleaching assays were imaged using both microscopes.

The 2-camera TIRF microscope was equipped with 2 Andor iXon 888 EMCCD cameras (Andor Technology Ltd), and a Nikon 100x CFI Apochromat TIRF oil immersion objective (1.49 NA) based on an ASI-RAMM frame (Applied Scientific Instrumentation), and a Nicolase laser system [325]. Images acquired by this system had a field of view of $88.68\ \mu\text{m} \times 88.68\ \mu\text{m}$ (1024×1024 pixel).

The 3-camera TIRF microscope was equipped with 3 Prime BSI Scientific CMOS cameras (Teledyne Photometrics Ltd), and a Nikon 100x CFI Apochromat TIRF oil immersion objective (1.49 NA) based on an ASI-RAMM frame (Applied Scientific Instrumentation), and a Nicolase laser system [325]. Images acquired by this system had a field of view of $177.48\ \mu\text{m} \times 177.48\ \mu\text{m}$ (2048×2048 pixel).

2.1.2. Microfluidic device set up

The microfluidic device used in this thesis contains a poly-dimethylsiloxane (PDMS) top and a coverslip base. The PDMS blocks and the coverslips were prepared separately and annealed together to form 5 flow channels ($10 \times 0.8 \times 0.06\ \text{mm}$, $L \times W \times H$).

The PDMS blocks were prepared using the Sylgard 184 silicone elastomer kit (Dow Corning) following the standard protocol for soft lithography, with the silicon base and the curing agent mixed at a 10:1 ratio (w/w). The mold generates 5 flow channels on one side of the PDMS block. Upon the separation of the PDMS blocks from the mold, inlet and outlet were created at each end of a flow channel using 0.75mm and 1mm Harris Uni-Core punchers. The PDMS blocks were then cleaned by 3 steps of sonication (ultrapure water-100% isopropyl alcohol-ultrapure water, 10min for each step), dried, and then stored in a double container.

Round coverslips (Australian Scientific, 0117650, 25mm diameter) were cleaned by 3 steps of sonication (100% ethanol, 1M NaOH, ultrapure water, 10min for each step), dried, and stored in a vacuum desiccator.

The cleaned PDMS blocks and coverslips were glow-discharged for 3 min (Harrick Plasma, PDC-32G) prior to annealing, with the channel side of PDMS block adhered to the coverslip. The annealed microfluidic devices were further baked at 70°C for ≥ 1 h to enhance annealing.

2.1.3. Surface chemistry in the microfluidic flow channels

To allow specific immobilization of either HIV-1 capsid (see **2.2.5**) or microtubules (see **2.3.4**), the coverslip surfaces inside the microfluidic channels were functionalized with a monolayer of PLL-g-PEG-biotin followed by a layer of streptavidin. Biotinylated anti-tubulin antibodies were captured by the streptavidin layer for immobilizing the microtubules (see **2.3.4**). A double-antibody-mixture containing anti-CA antibody was captured by the streptavidin layer for immobilizing HIV-1 capsid (see **2.2.5**).

The annealed microfluidic device was plasma cleaned for 3 min to glow discharge the coverslip surfaces within the microfluidic channels. Then 0.1 mg/ml of PLL(20)-g[3.5]-PEG(3.4)-biotin(20%) (SuSoS AG, dissolved in PBS) was loaded into each channel by pipetting and incubated for 30min. The channels were rinsed with ultrapure water and air dried before incubation with 0.2 mg/ml streptavidin (SNN1001, Life Technologies Australia; in buffer 20 mM Tris pH7.5, 2 mM EDTA, 50 mM NaCl, 0.025% Tween 20, 0.2 mg/ml BSA) for 20 min. The device was then mounted in a chamslide chamber (Live Cell Instrument). At this point, inlets and outlets tubing were connected to the microfluidic device so that a sample pump can be incorporated to precisely control volume and flow speed for the binding assay between HIV-1 capsid and capsid binders (see **2.2.6**). For the motility assay, the microtubule immobilization was not compatible with the inlet-outlet setting so the microfluidic device was not connected to tubing (see **2.1.5** and **2.3.4**).

2.1.4. TIRFm binding assay

Upon immobilization of fluorescent HIV-1 capsid onto surfaces (see **2.2.4** and **2.2.5**), 30 μ l of fluorescent binder was introduced into the flow channel at different concentrations within the ranges indicated in table 2.1. as below. The binding assays were performed in either buffer 1 (50

mM Tris, pH8; 150 mM NaCl) or buffer 2 (30 mM HEPES, pH7; 20 mM KCl, 1 mM MgCl₂, 1 mM EDTA, 0.5% pluronic-127, 0.2 mg/ml BSA). 10 frames of capsid channel and binder channel were acquired using Andor iXon 888 EMCCD cameras during sequential excitation with a 491 nm laser and a 639 nm laser.

Binder	Capsid mutant	Buffer	Concentration (s)
CypA-AF647	A14C/E45C:K158C-AF488	Buffer 1	1-50 μ M
	A92E/A204C:K158C-AF488		
ATP-atto488	A92E/A204C:K158C-AF647	Buffer 1	5-500 nM
	R18G/A92E/A204C:R18G/K158C-AF647		200 nM
dATP-atto488	A92E/A204C:K158C-AF647	Buffer 1	400 nM
	R18G/A92E/A204C:R18G/K158C-AF647		400 nM
HCB-bodipy493	A92E/A204C:K158C-AF647	Buffer 1	0.1-500 nM
	R18G/A92E/A204C:R18G/K158C-AF647		100 nM, 500 nM
sfGFP-hFEZ1	A92E/A204C:K158C-AF647	Buffer 2	1-400 nM
	R18G/A92E/A204C:R18G/K158C-AF647		
sfGFP-mBICD2	A92E/A204C:K158C-AF647	Buffer 2	1-400 nM
	R18G/A92E/A204C:R18G/K158C-AF647		

Table 2.1. Summary of HIV-1 capsid binders examined in the TIRFm binding assays. Note: For CypA, any sample of [CypA] > 1 μ M was prepared with 1 μ M CypA-AF647 and unlabeled CypA (added to make the desired final concentration).

2.1.5. TIRFm motility assay

Upon immobilization of fluorescent microtubules onto surfaces (see **2.3.3** and **2.3.4**), 10 μ l of solution containing motor complex in a motility buffer (30 mM HEPES, pH7; 20 mM KCl, 1 mM MgCl₂, 1 mM EDTA, 0.5% pluronic F-127, 0.2 mg/ml BSA, 10 μ M Taxol, 1 mM Mg-ATP supplemented with a PCA-PCD-Trolox oxygen scavenging system) was introduced into the flow cell by manual pipetting. The mixture containing reconstituted KFC complex (see **2.6.4**) was diluted (1:1000 fold to 1:100 fold, see **Table 5.1**) in the motility buffer prior to imaging. The mixture containing reconstituted KFC

complex (see **2.6.5**) was diluted (1:2000 fold to 1:500 fold, see **Table 5.3**) in the motility buffer prior to imaging. The mixture containing reconstituted DDBC (see **2.6.3**) or DDB (see **2.6.2**) complex was used for imaging directly without dilution, while the mixture containing the DDb complex was diluted 1:100 fold to 1:10 fold (see **4.3**). The motility assay was performed at either 25°C or 30°C. The motor complexes imaged in this thesis are listed in **Table 2.2**. One reference frame of the microtubule channel was acquired with a 561 nm laser using Andor iXon 888 EMCCD. 120 frames (either 1 sec/frame or 0.5 sec/frame) of capsid channel and FEZ1/BICD2 channel were acquired using Andor iXon 888 EMCCD cameras during sequential excitation with appropriate lasers (combinations of a 491 nm laser and a 639 nm laser based on the components used).

Motor complexes		Components
KFC (5.3)	KFC combinations	Dark-Kif5B + sfGFP-hFEZ1 + AF647 labelled HIV-1 capsid
		Dark-Kif5B + dark-hFEZ1 + AF647 labelled HIV-1 capsid
		Dark-Kif5B + dark-hFEZ1 + AF488 labelled HIV-1 capsid
		AF647 labelled Kif5B + dark-hFEZ1 + AF488 labelled HIV-1 capsid
		Dark-Kif5B + sfGFP-hFEZ1 + AF647 labelled HIV-1 capsid (R18G)
		Dark-Kif5B + dark-hFEZ1 + AF647 labelled HIV-1 capsid (R18G)
		Dark-Kif5B + dark-hFEZ1 + AF488 labelled HIV-1 capsid (R18G)
	KFC negative controls	KFC without K, or F, or C
KF (5.4)		Kif5B + sfGFP-hFEZ1
DDBC (4.3)		Dynein-dynactin + sfGFP-mBICD2 + AF647 labelled HIV-1 capsid
DDB		Dynein-dynactin + sfGFP-mBICD2
DDb (4.2)		DDb: dynein-dynactin + sfGFP-mBICD2N (25-400)

Table 2.2. Summary of motor complexes examined in the TIRFm motility assays.

2.1.6. Single molecule photobleaching

Single molecule photobleaching experiments were performed to calculate the single molecule intensity of the fluorescent protein used in these experiments. A clean coverslip was glow-discharged for 3 min (see **2.1.2**), mounted into a camlide chamber, and then incubated with a

solution of the fluorescent protein (~5nM CA, ~10pM FEZ1, ~20pM BICD2 for optimal density) for 3 min in the buffer used in the corresponding assay. Unbound molecules were removed by washing the chamber 3 times with buffer. Molecules bound onto coverslip were photobleached for 200 frames until most molecules are photobleached. 4 FOVs of images were acquired with the corresponding laser (same laser power, 5-10x exposure time compared to conditions used in the corresponding binding assay or motility assay).

2.1.7. Image analysis

Images from the single molecule photobleaching and the binding assay were analyzed using a Matlab-based software JIM (<https://github.com/lilbutsa/JIM-Immobilized-Microscopy-Suite>, developed by James Walsh). Images from the motility assay were analyzed using both TrackMate, an ImageJ Fiji plugin [326], and a custom MATLAB script.

Single molecule photobleaching analysis:

For the single molecule photobleaching analysis, the images were first analyzed using the JIM script (Generate-Single_Channel_Traces) to generate fluorescent traces. The images were drift-corrected and fluorescent molecules were selected based on appropriate filtering parameters to avoid background speckles and large aggregates. The fluorescent traces were then analyzed using the JIM script (Single_Molecule_Photobleaching_Generic) to classify traces based on the steps taken before the selected particle was completely photobleached. Single-step traces were fitted with a Gaussian distribution to estimate the single molecule intensity of the fluorescent molecule.

Binding assay analysis:

For the binding assay analysis, the images were analyzed using the JIM script (Generate-Multi_Channel_Traces). The capsid channel and the binder channel were aligned based on either automatic alignment or manual alignment with user-added parameters. The capsid channel was detected to select and localize desired capsid particles based on appropriate parameters to avoid background speckles of background and aggregates. The fluorescent intensities of a selected capsid and its binders were measured in the capsid channel and the binder channel. The fluorescent traces were then analyzed using the JIM script (Arbitrary_Shape_Kd_Measurement). The fluorescent intensities of a capsid and its binders were translated into the number of CA monomers and binders

based on their single molecule intensities obtained from single molecule photobleaching, thus generating a molar ratio of binder/CA. For each concentration of the binder, the median binder/CA-ratio of all selected capsid particles were determined at equilibrium. The median ratios from all concentrations of the binder were then fit against the concentrations of the binder based on a 'One-site-specific-binding' model: $K_D = (B_{\max} \times [\text{binder}]) / B_{\text{eq}} - [\text{binder}]$, where $[\text{binder}]$ is the concentration of binder, B_{eq} is the binder/CA ratio for a given binder concentration, K_D is the dissociation constant, and B_{\max} is the binder/CA ratio at saturation.

Motility assay analysis:

For the motility assay of DDBC, DDb(pu) DDb(po), and DDb(rec), representative kymographs were generated using Fiji software. No statistical analyses were performed on these data because we have not observed enough processive DDBC particles.

For the motility assay of KFC and KF complexes, the images were analyzed using the Fiji plugin TrackMate [326] in conjunction with a custom MATLAB script. Spots were detected in the capsid channel (estimated blob diameter set as 0.8 μm , threshold set as 0.6-0.8) for the KFC motility assay and in the FEZ1 channel (estimated blob diameter set as 0.6 μm , threshold set as 1-1.5) for KF motility assay. Spots near to edges were excluded based on x/y position. After spot detection, tracks were generated based on defined parameters (Linking max distance set as 0.8 μm ; Gap-closing max distance set as 0.4 μm ; Gap-closing max frame gap set as 2), and filtered using defined parameters (only tracks longer than 0.4 μm in length and longer than 3 steps (3 seconds) were selected). The set of generated tracks were manually screened and false tracks were excluded. Three csv files ("Track statistics", "Spots in tracks statistics", and "Links in tracks statistics") were exported from the Trackmate analysis. The "Track statistics" file contains basic analysis of track behavior, including average speed and run length of all the tracks, but this readout was not sufficient to accurately describe our data. We therefore further analyzed the "Spots in tracks statistics" file, which contains the X-Y coordinates of every spot in the tracks, using a custom MATLAB script. This approach allows us to exclude the 'pause' time when calculating average speed of a track (see Chapter 5 and **Fig. 8.4**). In short, the workflow went as follows: 1) calculate the displacement of each step along microtubule; 2) define a step as "pause" if its speed was below a certain threshold (30 nm/s); 3) classify steps into pause or walking categories; 4) calculate average speed by dividing the total run length by the duration of walking phases. Wherever applicable, the numbers of CA-per-particle and FEZ1-per-

particle were quantified based on the background-subtracted fluorescent intensities of the particles and the single molecule intensities of FEZ1 or CA obtained from single molecule photobleaching. From this analysis, the average speeds and run lengths of all the processive particles within the analyzed image stack were calculated. The number of the processive particles was divided by the total length of microtubules within the image (determined using the JIM script Generate-Multi_Channel_Traces), the total time, and the concentration of Kif5B to estimate landing rate of the complex for the analyzed image.

2.2. HIV-1 capsid

2.2.1. Plasmid constructs

Plasmids encoding HIV-1 CA mutants used in this thesis are outlined in **Table 2.3**.

Plasmid	Source	Comment
pET21a-CA-A92E/A204C	Cloned by Vaibhav Shah	For making crosslinking-stabilized, soluble, and conical HIV-1 capsid
pET21a-CA-R18G/A92E/A204C	Cloned by Andrew Tuckwell	For making R18-ring-null HIV-1 capsid on top of A92E/A204C
pET11a-CA-A204C	Zhao <i>et al.</i> [95]	For making crosslinking-stabilized, conical HIV-1 capsid
pET11a-CA-K158C	Cloned by Vaibhav Shah	Cysteine introduced at residue K158 for biotinylating or fluorescent labelling
pET11a-CA-R18G/K158C	Cloned by Andrew Tuckwell	For making the R18-ring-null version of K158C
pET11a-CA-A14C/E45C	Pornilos <i>et al.</i> [113]	For making crosslinking-stabilized, tubular HIV-1 capsid
pET11a-CA-N21C/A22C/W184A/M185A	Pornilos <i>et al.</i> [82]	For making crosslinking-stabilized, HIV-1 pentamer subunit
pET11a-CA-A14C/E45C/W184A/M185A	Pornilos <i>et al.</i> [113]	For making crosslinking-stabilized, HIV-1 hexamer subunit

Table 2.3. HIV-1 CA protein constructs.

2.2.2. CA protein expression and purification

Plasmid constructs containing the HIV-1 CA mutants listed in Table 2.1 were transformed into *E. coli* strain Rosetta(DE3)pLysS and cultured in Luria-Bertani media containing either 100 µg/ml Ampicillin and 32 µg/ml Chloramphenicol (for constructs in pET11a vector), or 50 µg/ml Kanamycin and 32 µg/ml Chloramphenicol (for constructs in pET21a vector) at 37°C with shaking at 180rpm. When the culture reached an OD_{600nm} of approximately 0.6, protein expression was induced by addition of 1mM IPTG (Isopropyl β-d-1-thiogalactopyranoside; GoldBio, I2481C50) to the bacteria culture. Cells were then incubated at 18°C overnight with shaking at 180rpm prior harvesting by centrifugation.

For CA proteins A92E/A204C, R18G/A92E/A204C, A204C, K158C, R18G/K158C, and A14C/E45C, we used two protocols for the purification:

Method 1: Bacteria pellets were resuspended in buffer (50 mM Tris, pH8; 50 mM NaCl, 1X EDTA-free protease inhibitor; 40 mM β-mercaptoethanol) and then lysed by sonication. The cell lysate was centrifuged at 43,000 g for 1h at 4 °C and the supernatant was clarified by filtering through a 0.22µm filter. The clarified supernatant was precipitated with ammonium sulfate (20% w/v, g/ml) for 30 min at 4 °C prior centrifugation at 42,000 g, 4 °C for 20 min. The pellet was resuspended in buffer (100 mM citric acid, pH 4.5; 40 mM β-mercaptoethanol) and dialyzed 4 times against the same buffer to remove ammonium sulfate. The mixture was clarified by centrifugation at 42,000 g for 20 min at 4°C and the supernatant was further dialyzed twice into 50 mM Tris, pH8, 2mM DTT. The resulting solution was filtered through a 0.22 µm filter and then applied onto Hitrap Capto Q Impres column pre-equilibrated with 50 mM Tris, pH8, 40 mM NaCl. Bound CA was eluted with 0-1 M NaCl gradient in 50 mM Tris, pH8. Appropriate fractions in the elution were identified by reducing SDS page to examine protein purity and then concentrated to ≥ 10mg/ml (OD₂₈₀ measured by DeNovix) using centrifugal concentrator (Amicon Ultra-15, 10 MWCO, Merck-UFC901008). The concentrated protein was centrifuged (18,000 g, 5min, 4°C) to remove aggregates prior to flash-freezing in liquid N₂ and storage at -80°C.

Method 2: Bacteria pellets containing CA protein were resuspended in lysis buffer (50 mM Tris, pH8; 200 mM β-mercaptoethanol; 1X-EDTA-free protease inhibitor) and lysed by sonication for 6 mins on ice (cycles of 15s on/off). Cell lysate was clarified by centrifugation at 43,000 g for 1h at 4°C and the supernatant was passed through a 0.22µm filter. CA protein was isolated from this supernatant by

two rounds of precipitation and re-solubilization. For each round, CA protein in solution was assembled into capsid in resuspension buffer (50 mM Tris, pH8; 200 mM β -mercaptoethanol) containing 2.5M NaCl (incubated on ice for 15 min) and pelleted at 4,000 g at 4°C for 45 min. Pelleted capsid was resuspended and disassembled into CA protein in resuspension buffer for the 1st round (incubated on ice for 15 min). For the 2nd round, pelleted capsid was resuspended and disassembled into CA protein in buffer A (50 mM Tris, pH8; 50 mM NaCl, 2mM DTT), filtered through a 0.22 μ m filter and further purified by subtractive anion exchange chromatography using a Hitrap Capto Q Impres column (5ml, GE Healthcare, 17-5470-55) mounted on ÄKTA pure protein purification system (GE Healthcare). sample was loaded onto the Q column pre-equilibrated with buffer A and CA protein was collected in the flowthrough. Appropriate fractions in the flowthrough were identified by reducing SDS page to examine protein purity and concentrated to ≥ 10 mg/ml. The concentrated protein was centrifuged (18,000 g, 5min, 4°C) to remove aggregates prior to flash-freezing in liquid N₂ and storage at -80°C. HIV-1 CA protein R18G/A92E/A204C and R18G/K158C was purified by Andrew Tuckwell.

For CA protein N21C/A22C/W184A/M185A or A14C/E45C/W184A/M185A. Bacteria pellets containing CA protein were resuspended in buffer (50 mM Tris, pH8; 50 mM NaCl, 1X EDTA-free protease inhibitor; 20 mM β -mercaptoethanol) and then lysed by sonication. The crude lysate was centrifuged at 43,000 g for 1h at 4 °C and the supernatant was clarified by filtering through a 0.22 μ m filter, followed by ammonium sulfate precipitation (20% w/v, g/ml) for 30 min at 4 °C prior to centrifugation at 42,000 g, 4 °C for 20 min. The pellet was resuspended in buffer (100 mM citric acid, pH 4.5; 20 mM β -mercaptoethanol) and dialyzed 4 times against the same buffer to remove ammonium sulfate. The mixture was clarified by centrifugation at 42,000 g for 20 min at 4°C and the supernatant containing CA protein was collected. The supernatant was dialyzed against 3 buffers sequentially (twice for each buffer). Buffer 1: 50 mM Tris, pH 8.0, 1M NaCl, 20 mM β -mercaptoethanol. Buffer 2: 50 mM Tris, pH 8.0, 1M NaCl. Buffer 3: 50 mM Tris, pH 8.0. The dialyzed mixture was clarified by centrifugation at 42,000 g for 20 min at 4°C. The supernatant containing soluble HIV-1 pentamer (for mutant N21C/A22C/W184A/M185A) or soluble hexamer (for mutant A14C/E45C/W184A/M185A) was further purified by anion exchange chromatography (AIEX) and size-exclusion chromatography (SEC). For AIEX, the supernatant was applied onto a Hitrap Capto Q Impres column pre-equilibrated with 50 mM Tris, pH8, 40 mM NaCl. Bound pentamer/hexamer was eluted with a 0-1 M NaCl gradient in 50 mM Tris, pH8 (soluble HIV-1 CA pentamer or hexamer eluted

around 200-300 mM NaCl). The protein collected from ALEX was further purified by SEC in buffer 20 mM Tris, pH 8, 40 mM NaCl using HiLoad 16/600 Superdex 200 pg (GE Healthcare, 28989335). Peak fractions were pooled together and concentrated to around 40mg/ml (OD₂₈₀ measured by DeNovix). The concentrated protein was centrifuged (18,000 g, 5min, 4°C) to remove aggregate prior to flash-freezing in liquid N₂ and storage at -80°C. Throughout the purification process, appropriate fractions were identified by non-reducing SDS page to examine protein purity and the formation of crosslinking-stabilized HIV-1 CA pentamer/hexamer.

2.2.3. Fluorescent labelling of HIV-1 CA protein

Both CA K158C and R18G/K158C were labelled with Alexa Fluor 488-C5-maleimide or Alexa Fluor 647-C2-maleimide dyes (Thermo Fisher) at the engineered cysteine after assembly into tubular capsid to avoid modifying native cysteine residues. CA K158C or R18G/K158C (≥5mg/ml) was assembled into tubular capsid on ice for 15min by addition of NaCl powder to a final concentration of 2.5M. Assembled capsid was pelleted (18,000 g, 5min, 4°C) and resuspended in labelling buffer (50 mM Tris, pH8; 2.5M NaCl; 0.1mM TCEP). The pelleting/resuspension process was repeated twice. Two-fold molar excess of Alexa Fluor 488-C5-maleimide or Alexa Fluor 647-C2-maleimide was added to the resuspended tubular capsid and reacted for 1 min before quenching the unreacted dye by adding β-mercaptoethanol (final 25mM). The labelled CA tubes were washed 4 times via the pelleting/resuspension process to remove free dye. Finally, the labelled tubes were pelleted (18,000 g, 5min, 4°C) and resuspended in storage buffer (50 mM Tris, pH8; 0.1mM TCEP). The resuspension was incubated o/n at 4°C to induce capsid disassembly into CA protein. The labelled CA protein was then centrifuged (18,000 g, 5min, 4°C) to remove aggregates prior to flash-freezing aliquots in liquid N₂ and storage at -80°C.

2.2.4. *In vitro* assembly of HIV-1 capsid

2.2.4.1. *In vitro* assembly of HIV-1 CA to produce cones that are stabilized, remain soluble, and are labelled with fluorophores

Four assembly mixtures containing 80 μM CA (76 μM A92E/A204C + 4 μM K158C-AF647) in assembly buffer (50 mM MES, pH6, 30 mM NaCl, 2.5 mM IP6), or 80 μM CA (76 μM A92E/A204C + 4 μM K158C-AF488) in assembly buffer (50 mM MES, pH6, 30 mM NaCl, 2.5 mM IP6), or 80 μM CA (76 μM R18G/A92E/A204C + 4 μM R18G/K158C-AF647) in assembly buffer (50 mM MES, pH6, 750 mM NaCl), or 80 μM CA (76 μM R18G/A92E/A204C + 4 μM R18G/K158C-AF488) in assembly buffer (50 mM

MES, pH6, 750 mM NaCl) were prepared. For all assembly mixtures, CA A92E/A204C or R18G/A92E/A204C were used to make crosslinking stabilized and soluble capsid, while K158C or R18G/K158C were included to incorporate fluorescence into the assembled capsid. All assembly mixtures were incubated at 4°C o/n before pelleting the assembled capsid by centrifugation at 4°C, 18,000 g for 10 min. The resulting pellet was gently resuspended in a resuspension buffer (50 mM HEPES, pH7; 150 mM NaCl) and then centrifuged again at 4°C, 5,000 g for 5 min to remove large aggregates. The resulting supernatant containing the self-assembled, -stabilized, fluorescent, and soluble capsid particles was aliquoted, flash-frozen in liquid N₂ and stored at -80°C. Negative staining electron micrographs showed that the capsid particles assembled following this protocol were mostly conical (>90%) but also contained some spheres and short tubes(see **Fig. 3.1.d-e**) and were used throughout in this thesis for both capsid binding assay and motility assay except for section **3.2**.

2.2.4.2. *In vitro* assembly of CA tubes on coverslip

See the material & methods section of **3.2** (taken from 'Functional analysis of the secondary HIV-1 capsid binding site in the host protein cyclophilin A') for CA tubes assembly and immobilization.

2.2.5. Immobilization of self-assembled HIV-1 capsids on a modified coverslip

Upon the connection of inlets and outlets (at this stage the coverslip surface inside the microfluidics channels were immobilized with PLL-g-PEG-biotin-streptavidin already, see 2.1.3), the microfluidic device mounted in a chamliide chamber was connected to a sample pump and 30 µl of buffer (either buffer 1 or buffer 2 based on experiment, see 2.1.4.) was used to rinse the flow channel. 15 µl of solution containing 1:3000 dilution of biotinylated α -mouse F(AB')₂ (Jackson ImmunoResearch, 115-066-071) and α -CA Ab (Advanced Biotechnologies, 13-102-100) was drawn into the flow channel and incubated for 15 min. Unbound antibody was washed away with 30 µl of buffer and 15 µl of solution containing 1:500 dilution of capsid (see 2.2.4.1.) was pulled into the flow channel and incubated for 10 min. Unbound capsid was washed away with 30 µl of buffer and the flow channel was ready for the binding assay.

2.3. Microtubule

2.3.1. Tubulin purification

Tubulin was isolated from mouse brains following either a TOG-affinity protocol [327] or a high-molarity buffer protocol [328].

2.3.1.1. The TOG-affinity protocol

In short, GST-TOG1/2 (TOG1/2 domains of STU2 protein of *Saccharomyces cerevisiae*) protein was conjugated to GSH resin (GOLDBIO, G-250-5) to serve as an affinity bait for isolating tubulin from mouse brain lysate [327].

GST-TOG1/2 in pGEX-6p-1 vector was transformed and expressed in Rosetta(DE3)pLysS following standard *E. coli* expression protocol (similar to HIV-1 CA expression in **2.2.2**). The bacterial pellet from a 2L culture was resuspended in GST lysis buffer (50 mM Tris, pH8; 150 mM NaCl; 0.1 mM EDTA; 1 mM DTT; 1x protease inhibitor) and then lysed by sonication. The crude cell lysate was centrifuged at 43,000 g for 1h at 4 °C and the supernatant was clarified by filtering through a 0.22µm filter. The clarified lysate was mixed with 2.5 mL of GSH resin equilibrated with GST wash buffer (50 mM Tris, pH8; 150 mM NaCl; 0.1 mM EDTA; 1 mM DTT) and rotated at 4°C for 1 h. The mixture was packed into an Econo-Pac column (Biorad, 7321010) and further washed with 5 CV of GST wash buffer, thus forming a TOG column.

The TOG column was equilibrated with 5 CV of BRB80. Meanwhile, mouse brains were lysed using mortar and pestle in brain lysis buffer (1X BRB80, 1mM DTT, 1 mM EGTA, 1 mM PMSF, 0.1% NP-40), clarified by centrifugation (4°C, 100,000 g, 30 min) and filtered through a 0.22 µm filter. The clarified brain lysate was mixed into the TOG column and rotated at 4°C for 1 h. The tubulin-bound-TOG column was washed with 10 CV of tubulin wash buffer 1 (1X BRB80, 10 µM GTP), 3 CV of tubulin wash buffer 2 (1X BRB80, 100 µM GTP, 10 mM MgCl₂, 5 mM ATP), and 5 CV of tubulin wash buffer 1 prior tubulin elution with 5 CV of tubulin elution buffer (1X BRB80, 500 mM ammonium sulfate). Peak fractions were pooled, concentrated to a volume of 2.5 ml, desalted into tubulin wash buffer 1 using PD10 column (GE Healthcare, GE17-0851-01), and concentrated again to approximately 20 µM (1.1 mg/ml, quantified by OD280). 5% glycerol was added prior flash-freezing in liquid N₂ and storage at -80°C.

2.3.1.2. The high-molarity buffer protocol

Mouse brains were lysed using a dounce homogenizer in depolymerization buffer (50 mM MES, pH6.6; 1 mM CaCl₂) at a ratio of 1 g/ml before clarification by centrifugation (4°C, 29,000 g, 60 min)

and filtration through a 0.22 μm filter. The 1st-round of polymerization-depolymerization was performed as follows. Supernatant was mixed a high-molarity PIPES buffer (1M pipes, pH6.9; 10 mM MgCl_2 , 20 mM EGTA) and glycerol at a volume ratio of 1:1:1, supplemented with 1 mM ATP and 0.37 mM GTP, and then incubated in a 37 °C water bath for 1 h to polymerize tubulin. Polymerized tubulin was harvested (37°C, 151,000 g, 30 min) and resuspended in 1/10 volume of the lysate supernatant in cold depolymerization buffer to promote microtubule depolymerization. The polymerization-depolymerization cycle was repeated for a 2nd-round, and the final volume of purified tubulin was concentrated to 100 μM (11 mg/ml, quantified by OD280), flash-frozen in liquid N_2 and stored at -80°C.

2.3.2. Fluorescent labelling of tubulin

Tubulin was labelled with Alexa Fluor 568 or 647 NHS Ester (Thermo Fisher A20003 or A37573), following an established protocol [329]. Tubulin (minimum 10 mg) was polymerized in buffer (0.5X BRB80, 3.5 mM MgCl_2 , 1mM GTP, 33% glycerol) for 1 h at 37°C before centrifugation (100,000 g, 37°C, 10min) through a high pH cushion (0.1 M HEPES, pH 8.6, 1 mM MgCl_2 , 1mM EGTA, 60% glycerol; warmed to 37°C) to harvest the polymerized microtubule. Discard the supernatant above the cushion, rinse the cushion interface twice with labelling buffer (0.1 M HEPES, pH 8.6, 1 mM MgCl_2 , 1mM EGTA, 40% glycerol; warmed to 37°C), and discard the cushion. The pellet containing microtubules was resuspended gently in labelling buffer, 2 x molar excess of dye was added to the resuspension, mixed well, and labelled for 10 min at 37°C. The reaction was quenched with the addition of 1M glycine before centrifugation (100,000 g, 37°C, 10min) through a low pH cushion (1X BRB80, 60% glycerol) to harvest the labelled microtubules. The supernatant above the cushion was aspirated off, the cushion interface was rinsed twice with ice-cold BRB80, and the cushion was discarded. The pellet containing labelled microtubules was resuspended gently in ice-cold 1X BRB80 to depolymerize the microtubules. The labelled tubulin dimer was cycled through another round of polymerization-depolymerization to remove assembly-deficient tubulin dimer. A final tubulin concentration of 5-15 mg/ml was generated by adjusting the volume of buffer used for solubilization in the last step. The final labelled tubulin dimer was centrifuged (18,000 g, 5min, 4°C) to remove aggregates prior to flash-freezing in liquid N_2 and storage at -80°C. Tubulin concentration and labelling ratio was determined by UV-VIS.

2.3.3. Polymerization of microtubules

Labelled and dark tubulin were mixed (~1/200 labelled tubulin) to a final concentration of 20 μ M tubulin in buffer (1X BRB80, 1 mM GTP). 5ul aliquots were prepared, and flash-frozen in liquid N₂ and stored at -80°C as our stock tubulin assembly mix.

One aliquot of tubulin mix was incubated at 37°C for 30 min to promote the polymerization of fluorescent microtubules. 95 μ l of microtubule storage buffer (1X BRB80, 10 μ M Taxol) was added followed by an additional incubation at 37°C for 30 min before centrifugation (100,000 g, 37°C, 10min) through a cushion (1X BRB80, 10 μ M Taxol, 40% glycerol) to harvest the stabilized, fluorescent microtubules. The resulting pellet was gently resuspended in 100 μ l of microtubule storage buffer. The taxol stabilized microtubules were used within 2 days after being prepared.

2.3.4. Immobilization of microtubules on modified coverslip

The flow channels of the microfluidics device (immobilized with PLL-g-PEG-biotin-streptavidin, see **2.1.3**) were incubated with 10 μ l of biotinylated anti- α -tubulin (Thermo Fisher #A21371) at a dilution of 1:100 in 1X BRB80 for 30 min by pipetting. Then the flow channels were further rinsed with 20 μ l of blocking buffer (1X BRB80, 0.5% Pluronic F-127, 0.6 mg/ml casein) for \geq 1h until being used. Pipet 10 μ l of a solution containing microtubules (1:10 dilution of the sample from **2.3.3**) and incubate for 10 min. Unbound microtubules were washed away by 10 μ l of the microtubule storage buffer.

2.4. Other recombinant proteins

2.4.1. Cyclophilin A

See the material & methods section of **3.2** (taken from 'Functional analysis of the secondary HIV-1 capsid binding site in the host protein cyclophilin A').

2.4.2. hFEZ1 (human Fasciculation and elongation protein zeta-1) protein

2.4.2.1. Plasmid constructs

Plasmid constructs bearing sfGFP-hFEZ1 and hFEZ1 were cloned by Jeff Stear. The cDNA encoding hFEZ1 was obtained from DNASU (HsCD00042980). The arrangement of the sequences, together with the restriction sites used for cloning, are indicated in **Fig. 2.1**.

For sfGFP-hFEZ1 cloning, cDNA of hFEZ1 was amplified with primers (Forward: 5'-CATGGATGAGCTCTACAAAGGATCCATGGAGGCCCACTGGTG-3'; Reverse: 5'-TGGTGGTGGTGCTCGAGTGCCTAGGTAGGGCAGAGCACTTTTAAATG-3') and inserted into a sfGFP-

mFEZ1 construct (gifted by Richard James Mckenney) by digestion-ligation between restriction sites *BamHI*/*NotI* (therefore replacing the mFEZ1 with hFEZ1 while the precision site was gone too).

For dark hFEZ1 cloning, cDNA of hFEZ1 was amplified with primers (Forward: 5'-GGGGAATTCATGGAGGCCCACTGGTGAG-3'; Reverse: 5'-

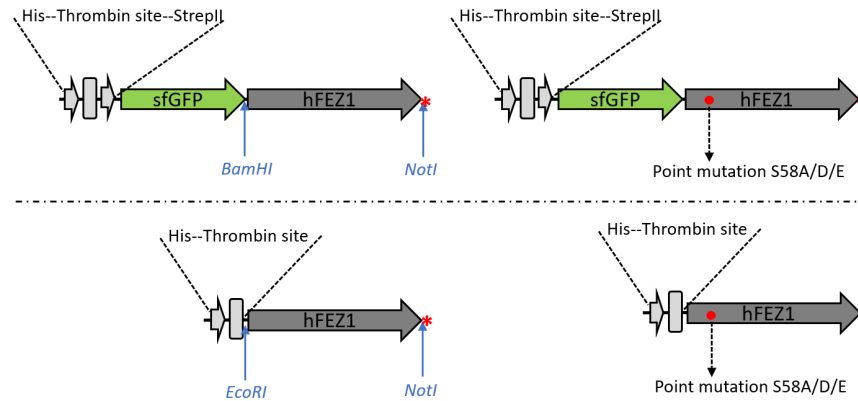


Fig. 2.1. Schematic display of hFEZ1 constructs. Full length hFEZ1 proteins (1-392) and point mutations: sfGFP-hFEZ1, dark hFEZ1, and both proteins with the point mutations S58A, S58D, or S58E. Positions of restriction sites used for cloning are indicated with blue arrow. Positions of point mutagenesis are indicated with red dot.

and inserted into pET28a vector by digestion-ligation between restriction sites *EcoRI*/*NotI*. The arrangements of the recombinant proteins are schematically shown in **Fig. 2.1**. The point mutation S58A mimics the unphosphorylated state of S58 while S58D/E mimics the phosphorylated state of S58. Point mutations were introduced by QuickChange Site-Directed Mutagenesis using the primers listed in **Table 2.4**.

Mutation	Primer sequence
hFEZ1 S58A	Forward: 5'-GAATTTTCTTCGAAATAATCAGCTTCAAGGCCATGGAGGAC-3' Reverse: 5'-CTCATCAAATTCATTTACGAGGTCCTCCATGGCCTTGAAGCT-3'
hFEZ1 S58D	Forward: 5'-GAATTTTCTTCGAAATAATCAGCTTCAAGGACATGGAGGAC-3' Reverse: 5'-CTCATCAAATTCATTTACGAGGTCCTCCATGTCCTTGAAGCT-3'
hFEZ1 S58E	Forward: 5'-GAATTTTCTTCGAAATAATCAGCTTCAAGGAGATGGAGGAC-3' Reverse: 5'-CTCATCAAATTCATTTACGAGGTCCTCCATCTCCTTGAAGCT-3'

Table 2.4. Primers for FEZ1 point mutagenesis.

2.4.2.2. hFEZ1 protein expression and purification

Plasmid constructs bearing sfGFP-hFEZ1 or dark hFEZ11 were transformed and expressed in the *E. coli* strain Rosetta(DE3)pLysS following standard bacterial expression protocol (similar to HIV-1 CA expression in 2.2.2.).

Bacteria pellets containing hFEZ1 proteins were resuspended in buffer A (50 mM HEPES, pH7.4; 50 mM NaCl, 2 mM PMSF [Thermo Fisher, 36978], 1 mM EDTA, 10% glycerol) containing 300 mM NaCl and 1x protease inhibitor cocktail, and then lysed by sonication. The cell lysate was centrifuged at 43,000 g for 1h at 4 °C and the supernatant was clarified by filtering through a 0.22µm filter. The clarified lysate was applied onto a 5 ml StrepTrap column (Cytiva, 28907546) pre-equilibrated with Strep-wash-buffer (Buffer A + 300 mM NaCl). The column was washed with 5 CV of Strep-wash-buffer prior eluting the bound protein with 5 CV of Strep-elution-buffer (buffer A + 2.5 mM dethiobiotin [Sigma-Aldrich, D1411]). Peak fractions from the elution were pooled together and applied to a Hitrap Capto Q Impres column pre-equilibrated with buffer A prior eluting bound protein with 0-1 M NaCl gradient in buffer A (20 CV in total). All the FEZ1 constructs seemed prone to degradation therefore generating several truncations. The full-length FEZ1 (and one of the truncations) was eluted at ~650-750 mM NaCl while the other truncations were eluted at lower concentrations of NaCl. Fractions containing the full-length FEZ1 were further purified by SEC in SEC-buffer (buffer A + 50 mM) using a HiLoad 26/600 Superdex 75 pg (GE HealthCare, GE28-9893-34) column. Appropriate fractions were pooled together, concentrated, centrifuged (18,000 g, 5min, 4°C) to remove potential aggregates, prior to flash-freezing in liquid N₂ and storage at -80°C.

2.4.3. mBICD2 (mouse protein bicaudal D homolog 2)

2.4.3.1. Plasmid constructs

The plasmid construct expressing sfGFP-mBICD2 in pFastBac vector, and the plasmid construct expressing sfGFP-mBICD2N (aa 25-400) in pET28a vector, were gifted by Richard J McKenney (UC Davis, CA, USA). The arrangements of the sequences are schematically shown in **Fig. 2.2.**

2.4.3.2. mBICD2 protein expression and purification

The plasmid construct bearing sfGFP-mBICD2 was transformed into DH10Bac competent cells (Invitrogen,10361012). The transformation mixture was plated onto LB agar plates containing 50 µg/ml kanamycin (Sigma-Aldrich, 60615), 7 µg/ml gentamicin (GoldBio, G-400-1), 15 µg/ml

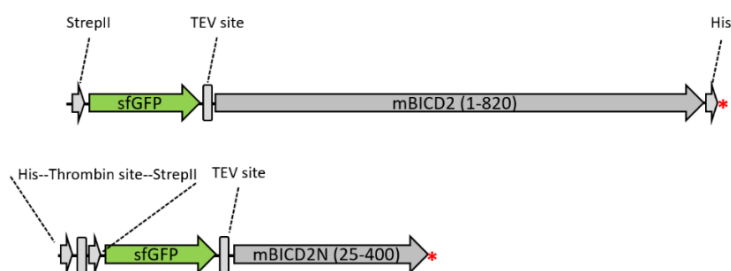


Fig. 2.2. Schematic display of mBICD2 constructs. Full length and truncated mBICD2 proteins: sfGFP-mBICD2 (aa 1-820) and sfGFP-mBICD2N (aa 25-400).

tetracycline (Sigma-Aldrich, 64-75-5), 200 µg/ml X-Gal (Thermo Fisher, R0404), 1 mM IPTG and incubated at 37 °C for 2 days. The recombinant BACmid containing the desired DNA sequence formed white colonies while the native BACmid formed blue colonies. The presence of BACmid from picked white colonies was confirmed by PCR. Positive clones were selected to isolate BACmid DNA using a standard isopropanol DNA precipitation. A positive clone was inoculated into LB media containing 50µg/ml kanamycin, 3µg/ml gentamycin and 10µg/ml tetracycline and incubated o/n. Bacterial cells from 1.5ml of the o/n culture was harvested by centrifugation (5000 g, 1 min) and resuspended in 300µl of Sol1 (15mM Tris-HCl pH8.0, 10mM EDTA 100µg/ml RnaseA). The resuspension was gently mixed with 300µl of Sol2 (0.2N NaOH, 1% SDS), incubated at room temperature for less than 5 min, topped-up with 300µl of 3M Kac (pH 5.5) while mixing, and then incubated on ice for 10 min. The mixture was clarified by centrifugation (5000 g, 10 min) and the supernatant was mixed with 800µl isopropanol (mix by inversion) in a new tube before incubated on ice for 10 min to precipitate DNA. DNA in the mixture was harvested by centrifugation (5000 g, 15 min) and the resulting pellet was washed with 70% ethanol, dried, and then resuspended in 40µl of ultrapure water.

To produce baculovirus from the BACmid DNA, Sf9 cells in Insect-XPRESS media (BELN12-730Q, LONZA) at a density of 0.5×10^6 cells/ml were seeded into each well of a 6-well plate (2 ml/well) and incubated at 27°C for 1 h to allow cell attachment. A mixture containing polyethylenimine (PEI) and BACmid (containing 2 µg of BACmid and 8 µg of PEI in 200 µl of optimum media) was vortexed, incubated for 30 min, and added dropwise into each of the 6-well plate. The cells were incubated at 27°C for 5 to 7 days to allow viral transfection. Successful transfection was determined based on GFP signal (in the cases of GFP recombinant proteins), SDS-PAGE analysis, or the morphology of the

Sf9 cell (transfected cells should show signs of lysis and should have a much larger diameter compared to un-transfected cells). At this point most cells had been lysed and the infectious baculovirus were released into the culture. The supernatant was collected, spun (4000 g, 5min) to remove cell debris and dead cells, and then used to infect Baculovirus Infected Cells (BIC) stocks.

To amplify the virus and freeze down BIC stocks, the supernatant was used to inoculate 50 ml of Sf9 cells (density around 1×10^6 cells/ml), which were cultured at 27°C for 2 days. At this point most cells had produced new baculovirus but had not yet lysed. Cells were harvested by centrifugation (4000 g, 5min) and resuspended in 4 ml of media containing 10% DMSO (Dimethyl sulfoxide, Thermo Fisher, D12345) and 10% FBS (Fetal Bovine Serum, Thermo Fisher, A4766801). The resuspension was distributed into 1 ml aliquots and slowly frozen in polystyrene boxes at -80°C.

For the final step in protein expression, 1 liter of Sf9 cell culture was grown to a density of $1.5-2 \times 10^6$ cells/ml. The BIC stock was added to the prepared culture and incubated for an additional 3 days (27°C, 120 rpm). Cells subsequently were harvested by centrifugation (4000 g, 5min), resuspended in 20 ml of buffer (30 mM HEPES, pH7.4, 300 mM NaCl, 5% glycerol, 20 mM Imidazole, 1mM DTT, 1 X protease inhibitor), pipetted dropwise into liquid N₂, then stored at -80°C.

Sf9 cell pellet expressing mBICD2 protein was dissolved and lysed using a dounce homogenizer, then clarified by centrifugation (43,000 g, 1 h, 4 °C) and filtered through a 0.22 µm filter. The clarified solution was applied onto a 5 ml HisTrap column (Merck, GE17-5255-01) pre-equilibrated with His-wash-buffer (30 mM HEPES, pH7.4, 300 mM NaCl, 10% glycerol, 20 mM Imidazole, 1mM DTT). The His column was washed with 5 CV of His-wash-buffer and bound protein was eluted by 5 CV of His elution buffer (30 mM HEPES, pH7.4, 300 mM NaCl, 10% glycerol, 250 mM Imidazole, 1mM DTT). Fractions containing the desired protein were pooled and applied onto a 5 ml StrepTrap column pre-equilibrated with Strep-wash-buffer (30 mM HEPES, pH7.4, 300 mM NaCl, 10% glycerol, 1mM DTT). The Strep column was washed with 5 CV of Strep-wash-buffer and bound protein was eluted by 5 CV of Strep-elution-buffer (30 mM HEPES, pH7.4, 300 mM NaCl, 2.5 mM dethiobiotin, 10% glycerol, 1mM DTT). Fractions containing the desired protein were pooled, concentrated to around 4 ml, and further purified by SEC in SEC-buffer (30 mM HEPES, pH7.4, 150 mM NaCl, 10% glycerol, 1mM DTT) using a HiLoad 26/600 Superdex 200pg (Cytiva, 28-9893-36) column. Appropriate fractions from SEC were pooled together, concentrated, centrifuged (18,000 g, 5 min, 4°C) to remove potential aggregation, and flash frozen in liquid N₂ before storage at -80°C.

2.4.3.3. mBICD2N (aa 25-400) protein expression and purification

Plasmids containing the sfGFP-mBICD2N construct were transformed and expressed in *E. coli* strain Rosetta(DE3)pLysS following standard bacterial expression protocol (similar to HIV-1 CA expression in 2.2.2.). The resulting pellets containing sfGFP-mBICD2N were resuspended in lysis buffer (30 mM HEPES, pH7.4, 300 mM NaCl, 10% glycerol, 20 mM Imidazole, 1mM DTT, 1X protease inhibitor). The lysate was clarified by centrifugation (43,000 g, 1h, 4 °C) and filtered through a 0.22µm filter. The clarified lysate was applied onto a 5 ml HisTrap column pre-equilibrated with His-wash-buffer (30 mM HEPES, pH7.4, 300 mM NaCl, 10% glycerol, 20 mM Imidazole, 1mM DTT). The column was washed with 5 CV of His-wash-buffer prior eluting the bound protein with 5 CV of His-elution-buffer (30 mM HEPES, pH7.4, 300 mM NaCl, 10% glycerol, 250 mM Imidazole, 1mM DTT). Peak fractions from His elution were pooled together, concentrated to around 500 µl, and further purified by SEC in SEC-buffer (30 mM HEPES, pH7.4, 150 mM NaCl, 10% glycerol, 1 mM DTT) using Superdex 200 Increase 10/300 GL (GE HealthCare, GE28-9909-44) column. Appropriate fractions were pooled together, prior to flash-freezing in liquid N₂ and storage at -80°C.

2.4.4. hKif5B (human kinesin-1 heavy chain)

2.4.4.1. Plasmid constructs

The hKif5B-Scarlet-pACEBac1 vector provided by Richard J McKenney (UC Davis, CA, USA). The construct expressing dark hKif5B was cloned by Jeff Stear. cDNA of hKif5B was amplified with primers (Forward: 5'-GGGGCGGCCGCATGGCGGACCTGGCCGAGTG-3'; Reverse: 5'-GGGCTCGAGCACTTGTTCCTCCTCC-3') from the plasmid bearing hKif5B-Scarlet and inserted back to the same plasmid by digestion-ligation between restriction sites *NotI*/*XhoI*. The arrangements of the sequences, together with restriction sites used for cloning, are schematically shown in **Fig. 2.3**.

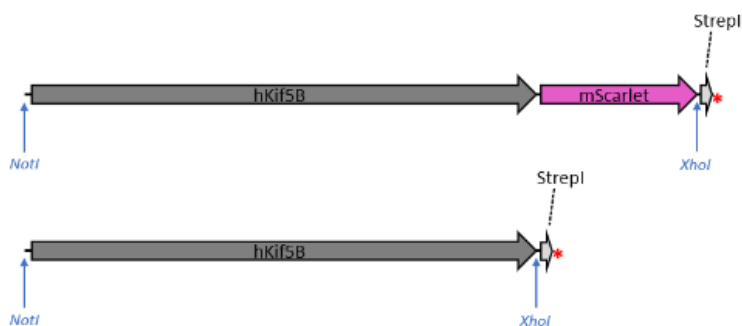


Fig. 2.3. Schematic display of hKif5B constructs. Both the proteins hKif5B and hKif5B-mScarlet were used for examining the reconstitution of KFC complexes. Data with hKif5B-mScarlet were not shown due to poor efficiency of reconstitution.

2.4.4.2. hKif5B proteins expression and purification

hKif5B-Scarlet or dark hKif5B was expressed in Sf9 insect cells following the baculovirus expression protocol described above. Sf9 cell pellets bearing hKif5B-Scarlet and hKif5B protein were dissolved and lysed using an Emulsiflex C5 (ATA Scientific), then clarified by centrifugation (43,000 g, 1 h, 4 °C) and filtered through a 0.22 µm filter. The clarified solution was applied onto a 5 ml StrepTrap column pre-equilibrated with Strep-wash-buffer (30 mM HEPES, pH7.4, 300 mM NaCl, 10% glycerol, 1mM DTT). The Strep column was washed with 5 CV of Strep-wash-buffer and bound protein was eluted by 5 CV of Strep-elution-buffer (30 mM HEPES, pH7.4, 300 mM NaCl, 2.5 mM dethiobiotin, 10% glycerol, 1mM DTT). Fractions containing the desired protein were pooled, concentrated to around 500 µl, and further purified by SEC in SEC-buffer (30 mM HEPES, pH7.4, 150 mM NaCl, 10% glycerol, 1mM DTT) using a Superdex 200 Increase 10/300 GL column. Appropriate fractions from SEC were pooled together, concentrated, centrifuged (18,000 g, 5min, 4°C) to remove potential aggregation, prior to flash-freezing in liquid N₂ and storage at -80°C.

2.4.4.3. Fluorescent labelling of dark hKif5B and purification

A fluorescent labelling step was introduced into the purification protocol of dark hKif5B (**2.4.5.2.**) between the Strep step and the SEC step; otherwise, the protocols were identical. For the labelling step, the elution fractions from the Strep step were pooled together and mixed with dyes (either an ATTO 643 NHS-ester dye (AD643, ATTO-TEC) or an Alexa Fluor 647 C2 Maleimide dye (A20347, Thermo Fisher)) at a molar ratio of 1:1 (Kif5B-dierm: dye), incubated at room temperature in dark (rotating), prior the SEC purification step.

2.4.5. hMAP7 (human microtubule associated protein 7)

2.4.5.1. Plasmid constructs

The pFastBac vector containing sfGFP-hMAP7 was provided by Richard J McKenney (UC Davis, CA, USA). Jeff Stear generated an untagged version of MAP7 by PCR amplifying the MAP7 ORF and the vector backbone (excluding the GFP sequence), using primers that included overlapping ends for

both products (Forward: 5'- GACGACGATAAGTAATCTAGAGCCTGCAGTCTCGAG -3'; Reverse: 5'- CGCCAGCTCCTAGCTCCGCCATACTGCCTTTTCGAACTGCGGG -3'). The resulting PCR bands were gel-purified and assembled using a Gibson cloning reaction (Forward: 5'- CGCAGTTCGAAAAAGGCAGTATGGCGGAGCTAGGAGCTGGCG -3'; Reverse: 5'- CTCGAGACTGCAGGCTCTAGATTACTTATCGTCGTC -3'). The arrangements of the sequences, together with restriction sites used for cloning, are schematically shown in **Fig. 2.4**.

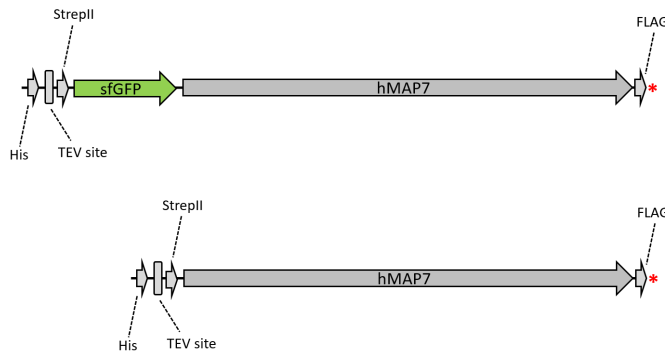


Fig. 2.4. Schematic display hMAP7 constructs.

2.4.5.2. hMAP7 proteins expression and purification

sfGFP-hMAP7 or hMAP7 expressed in Sf9 insect cells the standard baculovirus expression protocols described above. Sf9 cell pellet bearing sfGFP-hMAP7 or hMAP7 protein was dissolved and lysed using Emulsiflex C5 (ATA Scientific), then clarified by centrifugation (43,000 g, 1 h, 4 °C) and filtration through a 0.22 µm filter. The clarified solution was applied onto a 5 ml HisTrap column (Merck, GE17-5255-01) pre-equilibrated with Strep-wash-buffer (30 mM HEPES, pH7.4, 300 mM NaCl, 10% glycerol, 1mM DTT). The His column was washed with 5 CV of His-wash-buffer and bound protein was eluted by 5 CV of Strep-elution-buffer (30 mM HEPES, pH7.4, 300 mM NaCl, 10% glycerol, 2.5 mM dethiobiotin, 1mM DTT). Fractions containing the desired protein were pooled, concentrated to around 500 µl, and further purified by SEC in SEC-buffer (30 mM HEPES, pH7.4, 150 mM NaCl, 10% glycerol, 1mM DTT) using Superdex 200 Increase 10/300 GL. Appropriate fractions from SEC were pooled together, concentrated, prior to flash-freezing in liquid N₂ and storage at -80°C.

2.5. Isolated protein complexes from brain

The protocols for isolating DDb and DD were reported by McKenney *et.al* in 2014 [262]. The protocols for preparing DDb(rec), DDB, and DDBC were adapted based on the published methods

(**Fig. 2.5**). Mouse brains were lysed using a dounce homogenizer in equal amount (g/ml) of buffer A (30 mM Hepes, pH 7.4, 50 mM KCl, 1mM MgCl₂, 1mM EGTA, 1 mM PMSF, 10% glycerol, 2mM DTT), and then clarified by centrifugation (30,000 g, 30 min, 4°C) followed by another round of centrifugation (100,000 g, 10 min, 4°C). 250 nM of sfGFP-mBICD2N (from **2.4.5.2.**) was added into the supernatant and incubated (1 h, 4°C, rotating) to allow for the formation of DDb (Dynein-dynactin_sfGFP-mBICD2N). The mixture was clarified by filtration through a 0.22 µm filter and then applied onto a 1 ml StrepTrap column (GE HealthCare, GE29-0486-53) pre-equilibrated with buffer A. The column was washed with 5 CV of buffer A prior to elution of DDb (**2.5.1**) or DD (**2.5.2**).

2.5.1. DDb (dynein-dynactin-BICD2N)

The bound DDb complex was eluted by 5 CV of buffer A containing 2.5 mM desthiobiotin. Fractions containing the DDb complex (should be the first 2 CV of elution fractions) were pooled together, flash frozen and stored at -80°C. To distinguish this DDb pulled out from brain compared to the DDb reconstituted using isolated DD and BICD2N (**2.6.1**), we term them as DDb(pu) and DDb(rec) hereinafter.

2.5.2. DD (dynein-dynactin)

Dynein and dynactin were eluted by 5 CV of buffer A containing 300 mM NaCl. Fractions containing a mixture of dynein and dynactin (should be the first 2 CV of elution fractions) were pooled together, flash frozen and stored at -80°C.

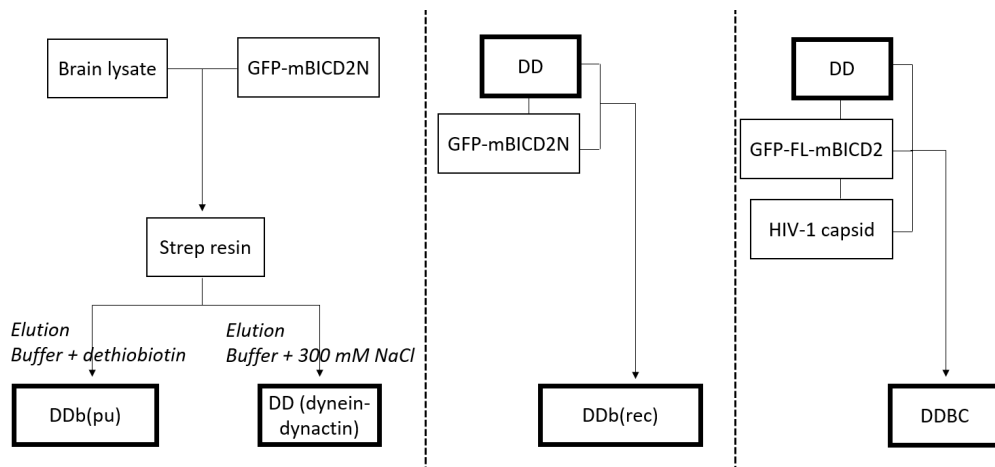


Fig. 2.5. Schematic display of the purification processes for DDb(pu), DD, and reconstitution of DDb(rec), DDBC complexes.

2.6. Reconstitution of motor-adaptor-(capsid) complexes

The DDb(rec), DDB, DDBC, KFC, KF motor complexes were reconstituted by incubating the required components in the motility buffer (30 mM HEPES, pH7; 20 mM KCl, 1 mM MgCl₂, 1 mM EDTA, 0.5% pluronic F-127, 0.2 mg/ml BSA, 10 µM Taxol, 1 mM Mg-ATP) for 3 h at 4°C. The mixture was either used straight away or diluted to a desired concentration prior imaging as specified. The motility assay for these complexes were carried out in the motility buffer supplemented with a PCA-PCD-Trolox oxygen scavenging system at 30°C.

2.6.1. DDb(rec)

DDb(rec) was examined to validate whether the isolated DD is still competent for further forming active complex. The isolated DD (~10 nM) was mixed with 250 nM sfGFP-mBICD2N in the motility buffer, incubated for 3 h at 4°C for the formation of DDb(rec), and then diluted 100-fold or 10-fold prior imaging.

2.6.2. DDB (dynein-dynactin-BICD2)

DDB (Dynein-dynactin-BICD2) was examined as a control for DDBC motility assay (data not shown in this thesis). The isolated DD (~10 nM) was mixed with 50 nM sfGFP-mBICD2 (bearing full length BICD2) in the motility buffer, incubated for 3 h at 4°C, and then used for imaging.

2.6.3. DDBC (Dynein-dynactin-BICD2-capsid)

The DDBC complex was reconstituted by incubating a mixture of isolated DD (~10 nM), 50 nM sfGFP-mBICD2 (bearing full length BICD2) and pre-assembled HIV-1 capsid containing 2 µM CA monomer (concentration of CA monomer) in the motility buffer for 3 h at 4°C. The mixture was used directly for imaging.

2.6.4. KFC (Kif5B-FEZ1-capsid)

The KFC complex was reconstituted by incubating a mixture of 250 nM Kif5B, 250 nM FEZ1, and pre-assembled HIV-1 capsid containing 10 µM CA monomer in the motility buffer for 3 h at 4°C. The mixture was then diluted prior imaging (see **Table 5.1**). A range of KFC combinations containing slightly different components were examined in this thesis (see section **5.3**). Samples serving as negative controls of the KFC motility assay were prepared in the same way as KFC complex

reconstitution while excluding one or more components during the sample preparation (e.g., KF, KC, FC).

2.6.5. KF (Kif5B-FEZ1)

The KF complex was reconstituted by incubating a mixture of 250 nM Kif5B and 250 nM sfGFP-FEZ1 in the motility buffer for 3 h at 4°C. The mixture was then diluted before imaging (see **Table 5.3**).

2.7. Negative staining electron microscopy

The HIV-1 capsid assembled at various assembly conditions were imaged by EM to determine the morphologies. A carbon and formvar coated Cu grid (TED Pella, 01811) was plasma cleaned (PELCP EasiGLOW). 5 µl of sample containing the assembled HIV-1 capsid (1 in 10 dilution) was applied onto the grid and incubated for 5 min at room temperature. Excess sample was drained off (by touching the grid edge onto a piece of filter paper) and the grid was washed 3 times by applying 5 µl of milli Q H₂O (dried immediately after each wash). The grid was then stained with 2% (w/v) uranyl acetate (ProSciTech, C079) for 10 sec, dried and stored at room temperature for EM imaging. A Tecnai G20 20 electron microscope (set up at Electron Microscope Unit) was used to acquire images with objective aperture set to 1 and condenser aperture set to 3. Images for HIV-1 capsid assembly was acquired at 9900X and 19500X folds of magnification while the motor complexes were acquired at 19500X, 38000X and 97000X.

2.8. SPR (surface plasmon response)

SPR was used only for section **3.2** (taken from 'Functional analysis of the secondary HIV-1 capsid binding site in the host protein cyclophilin A'). See details in the materials & methods within this section.

Chapter 3

HIV-1 capsid serves as a lattice
that interacts with host factors

3. HIV-1 capsid serves as a lattice that interacts with host factors

3.1. Introduction

The HIV capsid is an interaction platform for competing sets of proteins from the host cells. The virus has evolved to hijack host proteins as cofactors for infection, whereby sites required for host cofactor binding represent an appealing drug target. On the other hand, proteins from the innate immune system have evolved to recognise viral capsids and target them for degradation. Assembled HIV-1 capsid structures, such as CA tubes, spheres, and cones, have served as a useful tool for investigating capsid-host interactions [107, 124, 125, 330, 331]. A better understanding of these interactions at a molecular level is prerequisite for developing antiviral strategies that target the capsid. Optimizing the methods for *in vitro* assembly of CA to resemble native cones as closely as possible, and thus more suitable for interaction assays, would provide advantageous in addressing these questions.

Section 3.2 contains a published study focused on investigating a previously proposed non-canonical binding site between host protein CypA and HIV-1 capsid [109]. Our study suggested that the proposed binding site, if present, was of low affinity. The content of section 3.2 was published in a peer-reviewed journal, and I was a co-first author of the paper [121]. I would like to thank the co-authors' contribution to the paper, and for their consents for the incorporation of this paper into my thesis Chapter 3.

Wang Peng, Jiong Shi, Chantal L. Márquez, Derrick Lau, James Walsh, K. M. Rifat Faysal, Chang H. Byeon, In-Ja L. Byeon, Christopher Aiken & Till Böcking, "Functional analysis of the secondary HIV-1 capsid binding site in the host protein cyclophilin A", *Retrovirology*, 16(1), 10. doi:10.1186/s12977-019-0471-4.

The following work from the paper was undertaken as part of my PhD thesis:

1. Demonstration of assembled HIV-1 capsid as a lattice that interacts with the host protein CypA
2. Quantitative description of the CypA-capsid interaction to determine affinity and stoichiometry
3. Comparing the capacity of different capsid lattice assemblies and capsid subunits to interact with CypA

Sections **3.3** and **3.4** describe an optimized method for assembly of HIV-1 capsid for the production of stabilized particles that are soluble, conical, and easily labeled by fluorescent dyes. This method improves upon existing methods, thereby generating HIV-1 capsid assemblies that are well-suited for our investigation of capsid-host interaction as well as the motility assays described in Chapter 4 and Chapter 5.

3.2. HIV-1 capsid interacts with CypA: Publication - 'Functional analysis of the secondary HIV-1 capsid binding site in the host protein cyclophilin A'

Peng et al. *Retrovirology* (2019) 16:10
<https://doi.org/10.1186/s12977-019-0471-4>


Retrovirology

RESEARCH

Open Access



Functional analysis of the secondary HIV-1 capsid binding site in the host protein cyclophilin A

Wang Peng^{1†}, Jiong Shi^{2†}, Chantal L. Márquez¹, Derrick Lau¹, James Walsh¹, K. M. Rifat Faysal¹, Chang H. Byeon^{3,4}, In-Ja L. Byeon^{3,4}, Christopher Aiken^{2,3*‡} and Till Böcking^{1*‡} 

Abstract

Background: Efficient HIV-1 replication depends on interaction of the viral capsid with the host protein cyclophilin A (CypA). CypA, a peptidylprolyl isomerase, binds to an exposed loop in the viral CA protein via the enzyme's active site. Recent structural analysis of CypA in complex with CA tubes in conjunction with molecular dynamics simulations identified a secondary CA binding site on CypA that allows a bridging interaction with two hexameric subunits of the assembled CA lattice, leading to capsid stabilization (Liu et al. in Nat Commun 7:10714, 2016).

Results: We performed mutational analysis of residues that have been proposed to mediate CA binding at the secondary binding site on CypA (A25, K27, P29 and K30) and tested the effects of the amino acid substitutions using interaction assays and HIV-1 infection assays in cells. The binding of recombinant CypA to self-assembled CA tubes or native HIV-1 capsids was measured *in vitro* using a quantitative fluorescence microscopy binding assay revealing that affinity and stoichiometry of CypA to the CA lattice was not affected by the substitutions. To test for functionality of the CypA secondary CA-binding site in HIV-1 infection, mutant CypA proteins were expressed in cells in which endogenous CypA was deleted, and the effects on HIV-1 infection were assayed. In normal HeLa-P4 cells, infection with HIV-1 bearing the A92E substitution in CA is inhibited by endogenous CypA and was inhibited to the same extent by expression of CypA mutants in CypA-null HeLa-P4 cells. Expression of the mutant CypA proteins in CypA-null Jurkat cells restored their permissiveness to infection by wild type HIV-1.

Conclusions: The amino acid changes at A25, K27, P29 and K30 did not affect the affinity of CypA for the CA lattice and did not impair CypA function in infection assays suggesting that these residues are not part of a secondary CA binding site on CypA.

Keywords: HIV-1, Capsid, Cyclophilin A, Non-canonical binding site

Background

The HIV-1 capsid is composed of about 1200–1500 copies of the viral CA protein arranged into a predominantly

hexameric lattice with exactly 12 pentamers to form a closed conical shell that houses the viral RNA [1, 2]. After cell entry the capsid serves as a transport and reaction container that recruits a series of host co-factors to coordinate steps during the early stage of the HIV-1 life cycle [1, 3, 4] including reverse transcription [5, 6], cytoplasmic transport [7, 8], nuclear import [9, 10], and integration targeting of the viral DNA [9, 11–13]. Somewhere on its journey from the cell periphery into the nucleus, the capsid undergoes a disassembly process (termed uncoating) that releases the viral DNA for integration into the host chromosome. While there is controversy about the

*Correspondence: chris.aiken@vanderbilt.edu; till.boecking@unsw.edu.au

[†]Wang Peng and Jiong Shi are co-first authors

[‡]Christopher Aiken and Till Böcking are co-senior authors

¹ EMBL Australia Node in Single Molecule Science and ARC Centre of Excellence in Advanced Molecular Imaging, School of Medical Sciences, UNSW, Sydney, NSW 2052, Australia

² Department of Pathology, Microbiology and Immunology, Vanderbilt University Medical Center, Nashville, TN, USA

Full list of author information is available at the end of the article



© The Author(s) 2019. This article is distributed under the terms of the Creative Commons Attribution 4.0 International License (<http://creativecommons.org/licenses/by/4.0/>), which permits unrestricted use, distribution, and reproduction in any medium, provided you give appropriate credit to the original author(s) and the source, provide a link to the Creative Commons license, and indicate if changes were made. The Creative Commons Public Domain Dedication waiver (<http://creativecommons.org/publicdomain/zero/1.0/>) applies to the data made available in this article, unless otherwise stated.

precise location and timing of uncoating in the cell, it is likely that capsid stability is also controlled by interaction of the capsid with proteins and small molecules that the virus collects from the producer cell and/or the host cell.

The peptidylprolyl isomerase cyclophilin A (CypA) is an abundant cytosolic protein that binds via its active site to the CypA binding loop located on the N-terminal domain of CA (CA-NTD). The CypA binding loop comprises CA residues 85 to 93 with G89 and P90 being the primary binding motif for CypA [14, 15] (Fig. 1b). The interaction of CypA molecules with multiple of these loops exposed on the outside of the capsid in the cytoplasm of the target cell modulates HIV infection in a cell type-specific manner [16, 17], possibly by regulating capsid stability and uncoating [18, 19]. For example, inhibition of this interaction in myeloid cells, either by using the competitive inhibitor cyclosporin A (CsA) or by mutation of residues in the CypA binding loop on CA, results in HIV-1 induction of host cell immune responses, which has been attributed to premature uncoating and release of viral DNA in the cytoplasm [20, 21]. The molecular mechanisms underlying modulation of infection are not fully understood but may involve dynamic allostery [22].

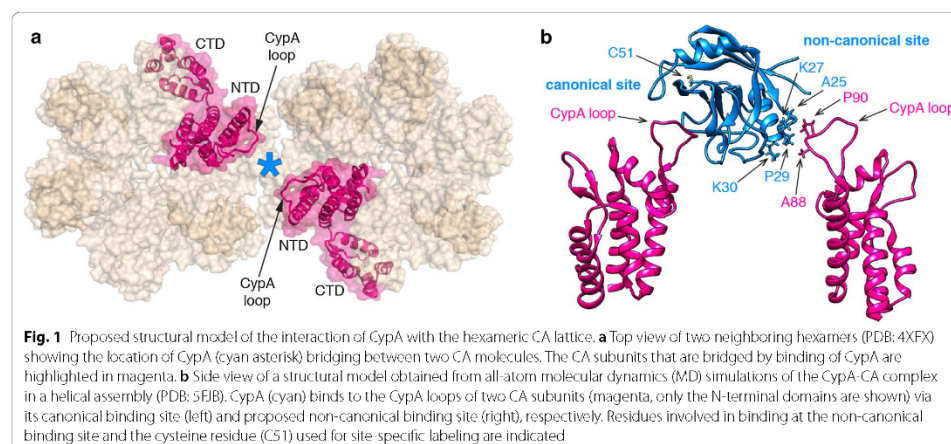
A recent cryoelectron microscopy structure of CypA in complex with self-assembled CA tubes revealed that CypA binds preferentially between CA hexamers along the direction of highest curvature [23]. The authors proposed that CypA bridges between the hexamers by binding to a CypA loop of one hexamer via the CypA active site (canonical site) and contacting a CypA loop of the second hexamer via a previously unidentified second

(non-canonical) binding site (Fig. 1b). Molecular dynamics simulations suggested that the contact was mediated by A88, G89 and P90 from CA and A25, P29 and K30 from CypA [23]. The bridging interaction afforded by the second binding site is predicted to strengthen the interaction between CypA and the capsid as a result of avidity, stabilize the capsid in the cytoplasm and facilitate the effects of CypA in HIV-1 infection. Validation of this new site is therefore crucial for further dissecting the molecular mechanisms by which CypA affects the capsid during the early stages of the HIV-1 life cycle. Here we show that amino acid substitutions at CypA residues A25, K27, P29 and K30, which are proposed to mediate binding at the second site, did not affect the interaction of CypA with self-assembled CA tubes or native viral capsids *in vitro* nor the function of CypA in HIV-1 infection in HeLa-P4 or Jurkat cells. Our results suggest that these residues do not form a non-canonical capsid binding site.

Materials and methods

CypA expression and purification

The coding sequence for human CypA (wild type and mutants A25D, K27D, P29K and K30D) was amplified from the corresponding constructs for mammalian expression (see below) by PCR and cloned into a pET-21 vector using the XhoI and NdeI restriction sites to generate a construct for expression of CypA without purification tags. CypA was expressed in *E. coli* Rosetta (DE3) cultured in LB medium containing 100 µg/ml ampicillin and 32 µg/ml chloramphenicol at 37 °C with shaking to an optical density of 0.5. After induction with 1 mM IPTG and expression at 37 °C for 3 h, the cells were



harvested by centrifugation, resuspended in cold purification buffer, whereby the buffer composition depended on the mutations because these result in changes of the isoelectric point of the protein: 25 mM HEPES, pH 7.6 [wild type CypA] or pH 7.2 [CypA A25D]; 50 mM MES, pH 6.8 [CypA K27D and CypA K30D]; 50 mM Bicine, pH 8.9 [CypA P29K]; each buffer was supplemented with 1 mM DTT, 0.02% NaN₃, 1 mg/mL lysozyme and “Complete” protease inhibitor. The cells were then lysed by sonication on ice for 6 min (cycles of 15 s on/15 s off). The lysate was centrifuged at 43,000g, 4 °C for 1 h and the supernatant was filtered through a 0.22 µm membrane. All CypA variants were then partially purified by subtractive anion exchange chromatography using two HiTrap Q HP columns (2 × 5 mL connected in series, GE Healthcare) equilibrated with the corresponding purification buffer supplemented with 1 mM DTT and 0.02% NaN₃. In subtractive anion exchange chromatography, the protein of interest elutes in the flow through during sample loading while contaminating proteins bind to the column and are thus removed. The next purification step differed for the CypA variants. Wild type CypA and mutants A25D and P29K were further purified by cation exchange chromatography. Pooled fractions containing CypA were adjusted in pH (pH 5.8 [wild type CypA]; pH 5.1 [CypA A25D]; pH 6.1 [CypA P29K]) using 1% v/v acetic acid prior to centrifugation at 43,000g, 4 °C for 1 h. The supernatant was injected onto HiTrap SP HP columns (2 × 5 mL connected in series, GE Healthcare) equilibrated with SP buffer, whereby the buffer composition depended on the mutation: 25 mM sodium phosphate, pH 5.8 [wild type CypA]; 50 mM sodium acetate, pH 5.1 [CypA A25D]; 50 mM BIS-TRIS, pH 6.1 [CypA P29K]; each buffer supplemented with 1 mM DTT, 0.02% NaN₃. CypA was eluted using a linear gradient from 0 to 1 M NaCl in the corresponding SP buffer. CypA mutants K27D and K30D were further purified by gel filtration. Fractions containing CypA were combined, concentrated to yield a volume of approximately 600 µL and purified using a Superdex 200 Increase 10/300 GL column (GE Healthcare) equilibrated with gel filtration buffer (10 mM HEPES, pH 8, 2 mM EDTA, 100 mM NaCl). All CypA variants were dialyzed into CypA storage buffer (25 mM HEPES, pH 8, 1 mM DTT, 0.02% NaN₃, 20% glycerol) prior to flash-freezing with liquid N₂ and storage at −80 °C.

CypA fluorescence labeling

Recombinant CypA was labeled with a twofold excess of Alexa Fluor 647-C2-maleimide (Thermo Fisher, A20347) in PBS (pH 7.4) containing 0.1 mM TCEP at room temperature for 10 min in the dark before quenching with DTT. Unconjugated dye was removed using Zeba

desalting columns (ThermoFisher) equilibrated with AF647-CypA storage buffer (50 mM Tris, pH 7.9, 1 mM DTT, 20% glycerol). Under these conditions, CypA is quantitatively labeled at residue C51. Wild type CypA labeled at C51 binds in surface plasmon resonance measurements to immobilized CA or CA hexamers with the same affinity as unlabeled CypA [24]. Labeled CypA was frozen in liquid nitrogen and stored at −40 °C.

CA expression and purification for assembly of tubes on surfaces

Expression and purification of CA mutants with engineered cysteine residues for cross-linking tubes (CA A14C/E45C) and for site-specific labeling (CA K158C) was carried out using published methods for the purification of CA [25].

CA fluorescence labeling

CA K158C was labeled with Alexa Fluor 488-C5-maleimide at the engineered cysteine residue (Thermo Fisher) after assembly into CA tubes to avoid modification of native cysteine residues. CA K158C (7.36 mg/mL in 25 mM sodium phosphate buffer, pH 7, 0.02% NaN₃, 2 mM DTT) was assembled for 15 min on ice after addition of solid NaCl to a final concentration of 2.5 M. The resulting CA tubes were collected by centrifugation (18,000g, 5 min) and resuspended in high salt buffer (50 mM Tris pH 8, 2.5 M NaCl, 0.1 mM TCEP, 0.02% NaN₃). This centrifugation/resuspension process was repeated twice. A twofold molar excess of Alexa Fluor 488-C5-maleimide was then added to the resuspended CA K158C tubes, allowed to react for 1 min and unreacted dye was then quenched by the addition 2-mercaptoethanol to a final concentration of 25 mM. The labeled tubes were washed by four cycles of centrifugation and resuspension in high salt buffer as above. Finally, the tubes were collected by centrifugation, resuspended in buffer without salt to induce disassembly (50 mM Tris, pH 8, 0.1 mM TCEP, 0.02% NaN₃). The solution was then centrifuged at 18,000g, 10 min, 4 °C to remove aggregates. The supernatant containing labeled CA was flash frozen in aliquots with liquid N₂ and stored at −40 °C in dark.

NMR experiments

Uniform ¹⁵N/¹³C labeling of wild type CypA and CypA mutants A25K, P29D and P29K was performed by growth in modified minimal medium using ¹⁵NH₄Cl and ¹³C₆ glucose as the sole nitrogen and carbon sources, respectively. Expression, purification and uniform ¹⁵N/¹³C labeling of wild type CA-NTD for NMR was performed as described previously [26]. NMR experiments were conducted at 25 °C on ¹⁵N/¹³C wild type

CA-NTD in the absence or presence of CypA (wild type or mutants), or $^{15}\text{N}/^{13}\text{C}$ CypA (wild type or mutants) in the absence and presence of wild type CA-NTD in NMR buffer (25 mM sodium phosphate buffer, pH 6.5, 1 mM DTT, 0.02% NaN_3). A Bruker 600 MHz spectrometer equipped with a 5 mm triple resonance and z-axis gradient cryoprobe was used to obtain one-dimensional (1D) ^1H and two-dimensional (2D) ^1H - ^{15}N heteronuclear single quantum coherence (HSQC) spectra.

Surface plasmon resonance (SPR) measurements

SPR measurements were performed on a Biacore S200 (GE Healthcare) as described previously [24]. Briefly, biotinylated CA K158C and biotinylated CA hexamer (assembled from CA A14C/E45C/W184A/M185A) were immobilized in separate flow channels of a CM5 sensor chip modified with streptavidin. Flow channels modified with streptavidin only were used as reference cells. CypA was exchanged into SPR running buffer (10 mM HEPES, pH 8, 0.005% Tween 20, 2 mM EDTA, 150 mM NaCl) using a Zeba desalting column and injected into the flow channels at a range of concentrations (1.1–72.8 μM) for 20 s followed by wash-out with SPR running buffer for 30 s at a flow speed of 100 $\mu\text{L}/\text{min}$ while measuring the SPR response at a frequency of 40 Hz. SPR data were analyzed using the Biacore S200 Evaluation software and GraphPad Prism 7. Data for all background-corrected SPR traces are available in Additional file 2: Tables S1–S10.

Fabrication of microfluidic flow cells

Glass coverslips were sonicated in ethanol for 30 min before sonication in 1 M NaOH for 30 min, and then rinsed with ddH₂O and dried. PDMS devices with five flow channels (height 60 μm , width 800 μm) were prepared following standard soft lithography protocols. Both PDMS device and glass coverslip were exposed to an air plasma inside a plasma cleaner for 3 min before they were assembled into microfluidic flow cells. The microfluidic flow cell was then heated at 70 °C for at least 5 min to enhance bonding.

Surface chemistry and CA tube assembly on surfaces

The surface of the glass cover slip forming the bottom of the microfluidic flow cell was coated with a co-polymer composed of poly-L-lysine (PLL) and biotinylated poly(ethylene glycol) (PEG) (Susos AG, PLL(20)-g[3.5]-PEG(2)/PEG(3.4)-biotin(20%)) by incubating each flow channel with a solution of PLL-PEG (1 mg/mL in PBS) for 30 min at room temperature before washing the channels with water and drying. The flow channels were then incubated with a solution of streptavidin (0.2 mg/mL) in blocking buffer (20 mM Tris, pH 7.5, 0.2 mg/mL BSA,

50 mM NaCl, 2 mM EDTA, 0.03% NaN_3 , 0.025% Tween 20) for 30 min at room temperature before rinsing the flow channels with 50 μL of washing buffer (50 mM Tris, pH 8). The flow channels were connected to inlet and outlet tubing and the entire flow cell mounted onto the microscope stage. The outlet tubing of the channel in use was connected to a syringe pump operated in withdraw mode at a flow speed of 100 $\mu\text{L}/\text{min}$ unless otherwise specified. The flow channel was filled with an antibody mixture (20 μL , delivered at 100 $\mu\text{L}/\text{min}$) containing biotinylated anti-mouse IgG F(Ab')₂ fragment (Jackson ImmunoResearch, 115-066-071; 1:800 dilution) and mouse anti-HIV-1 p24 monoclonal antibody (Advance Biotechnologies, 13-102-100; 1:800 dilution) and incubated for 1 min before rinsing with 100 μL of washing buffer. Then the flow cell was filled with CA tube assembly mixture (15 μL , delivered at 30 $\mu\text{L}/\text{min}$) containing CA-K158C-AF488 (4 μM), CA A14C/E45C (76 μM) in assembly buffer (50 mM Tris, pH 8, 500 mM NaCl; NaCl was added just before flowing the mixture into the flow channel) and incubated for 25 min to allow the growth of CA tubes on the modified surface.

TIRF imaging of CypA binding to self-assembled CA tubes

The microfluidic flow cell was flushed with 100 μL of imaging buffer (50 mM Tris, pH 8, 150 mM NaCl, 2 mM trolox (Sigma-Aldrich) and 2.5 mM protocatechuic acid (Sigma-Aldrich)). CypA solutions (1–50 μM) were prepared with AF647-CypA (1 μM) and unlabeled CypA (added to make up the desired final concentration) in imaging buffer supplemented with protocatechuic acid (0.25 U/mL, Sigma-Aldrich) shortly before injection into the flow channel. The CypA solution (30 μL) was flowed into the microfluidic channel and images were collected in both channels (CA and CypA) in four different fields of view. Subsequently the CypA solution was washed out with 100 μL of imaging buffer. This procedure was used to image CypA binding for a randomized sequence of different CypA concentrations in the same flow channel. TIRF images (5 frames per channel) were acquired with sequential excitation with a 491 nm laser (CA channel) and a 639 nm (CypA channel) with an exposure time of 10 ms using Andor iXon 888 EMCCD cameras. Images were analyzed using home-written image analysis software (<https://github.com/lilbutsa/JIM-Immobilized-Microscopy-Suite>). Regions of images containing capsid tubes were detected using the CA channel. The fluorescence intensity (sum of pixel values minus background intensity) for each tube was determined in each channel. Background fluorescence was determined from pixels surrounding the regions containing tubes.

The intensities of the two fluorophores were determined by single molecule photobleaching of labeled proteins adsorbed onto the surface of a coverslip. The absolute intensities of the two fluorophores were used to convert the fluorescence ratio of each region between the two channels (CypA:CA) to a molar binding ratio.

Binding curves were obtained by plotting the best fit molar binding ratio as a function of CypA concentration. The following equation was used for model fitting to obtain estimates for the dissociation constant and the maximum binding ratio: $R(\text{eq}) = [\text{CypA}] \times R(\text{max}) / ([\text{CypA}] + K_D)$, where $R(\text{eq})$ is the CypA:CA ratio at equilibrium for a given CypA concentration, $[\text{CypA}]$ is the concentration of CypA, $R(\text{max})$ is the CypA:CA ratio at saturation and K_D is the dissociation constant.

TIRF imaging of CypA A25D binding to capsids in permeabilized viral particles

The protein–capsid interaction assay with viral particles immobilized inside the microfluidic flow channel was carried out as described previously. Briefly, HIV-1 particles were produced by transfecting HEK-293T cells with a mixture of pNL4.3-iGFP-ΔEnv and psPAX2 (1.4:1, mol/mol) using polyethylenimine (PEI Max) reagent (Polysciences, 9002-98-6). Supernatant containing viral particles was collected 48 h after transfection. The viral particles were biotinylated with EZ-Link Sulfo-NHS-LC-LC-Biotin (Thermo Scientific, 21338) and purified by size exclusion chromatography using a HiPrep 16/60 Sephacryl S-500 HR column (GE Healthcare) equilibrated with HBS (50 mM HEPES, pH 7.5, 100 mM NaCl). For imaging, viral particles were bound inside a microfluidic channel to the surface of a cover slip modified with PLL-PEG and streptavidin as described above. AF647-CypA A25D binding was imaged by time-lapse total internal reflection fluorescence microscopy (sequential acquisition, 491 nm and 561 nm laser, 20 ms exposure time, one frame per second) after injecting perfringolysin O (200 nM) in VLP imaging buffer (50 mM HEPES pH 7.0, 100 mM NaCl) supplemented with an oxygen quenching system to reduce photobleaching (2 mM trolox, 2.5 mM protocatechuic acid, 0.25 U mL⁻¹ protocatechuate-3,4-dioxygenase). CypA solutions (0.1–20 mM) were prepared with AF647-CypA (1 μM) and unlabeled CypA (added to make up the desired final concentration) in VLP imaging buffer were assessed, whereby the concentration of the AF647-CypA A25D was used at a maximum concentration of 1 μM. Images were analysed with software written in MATLAB (The MathWorks, Inc.) as previously described [24].

Generation of cells expressing mutant CypA proteins

Hela-P4 cells [27] were cultured in Dulbecco's modification of Eagle's medium (DMEM) containing 10% fetal bovine serum and antibiotics. Jurkat cells were cultured in RPMI1640 medium with the same supplements. The *PPIA* gene, encoding cyclophilin A, was disrupted in Hela-P4 cells by transduction with a pLentiCRISPRv2 lentiviral vector [28] encoding guide RNA sequence 5'-GTTCTTCGACATTGCGTCTCGA-3'. The vector was packaged by cotransfecting 293T cells with psPAX2 (AddGene 12260) and pHCMV-G [29]. Transduced cells were selected in puromycin; single-cell clones were obtained by limiting dilution, expanded, and analyzed for CypA expression by immunoblotting. A cell clone lacking detectable CypA expression was reconstituted with wild type and mutant CypA proteins. For CypA reconstitution, pEF-IRES-bsd, a lentiviral vector containing the eEF1 promoter upstream of an IRES-Bsd cassette, was constructed from the EF.CMV.RFP lentiviral vector (Addgene plasmid # 17619; a gift from Linzhao Cheng) by substituting the IRES-Bsd cassette region, amplified by PCR from pMXs-IRES-Bsd (Cell Biolabs, cat. RTV-016), for the CMV-RFP region. Mutant CypA cDNAs with an upstream consensus Kozak sequence (CCACC) were created by site-directed mutagenesis via overlap PCR and inserted into the unique EcoRV site in pEF-IRES-Bsd. The orientation of the inserts was tested by restriction digestion, and the CypA cDNA inserts were confirmed by DNA sequencing. The resulting lentiviral vector constructs were packaged and transduced into the CypA-disrupted Hela-P4 cell clone. Transduced cells were selected with blasticidin, and the resulting populations were analyzed by immunoblotting for CypA expression. For Jurkat cell lines, Jurkat *PPIA*^{-/-} cells [30] obtained from the NIH AIDS Reagent Program, were reconstituted by transduction with EF-CypA-IRES-Bsd vectors. Blasticidin-resistant populations were selected and used in HIV-1 infection assays.

Infection assays

Cells were assayed for permissiveness to HIV-1 infection by flow cytometric analysis of infected cells expressing GFP following inoculation with HIV-1 reporter viruses encoding GFP. VSV-G-pseudotyped reporter particles were produced by co-transfection of 293T cells with pHIV-GFP [31] and pHCMV-G. Culture supernatants were harvested and clarified by centrifugation, assayed for p24 by ELISA, and frozen in aliquots at -80 °C. Jurkat cells were suspended at 200,000 per ml and distributed into 96-well plates (100 μL per well), and dilutions of the reporter viruses were added (100 μL volumes) with polybrene at a final concentration of 5 μg/ml in the presence

and absence of cyclosporin A (5 μ M). Virus stocks were diluted to achieve infection levels from 1–30% to ensure accurate quantification. Two days after inoculation, cells were fixed overnight with 2% paraformaldehyde. For Hela-P4 infection assays, 10,000 cells were seeded overnight in wells of 96-well plates (100 μ L volumes). Monolayers were inoculated with viruses in the presence of polybrene for 48 h, after which cells were detached with trypsin and fixed in paraformaldehyde. Fixed cell populations were analyzed for GFP expression with an Accuri C6 flow cytometer. The extent of infection was expressed as %GFP+ cells. Infection assays were performed in duplicate and the average values determined.

Immunoblotting

Cells were detached with trypsin and complete medium was added. Cells were pelleted, washed once in PBS, and cytoplasmic extracts prepared by lysis in 100 mM Tris-HCl pH 8.0, 100 mM NaCl, 0.5% NP-40. Protein concentrations were determined by the bicinchoninic acid method (Pierce). Normalized quantities of total protein were subjected to SDS-PAGE on 4–20% polyacrylamide gradient gels (GenScript). After separation, the proteins were transferred to nitrocellulose membranes (Perkin Elmer) and probed with polyclonal antibody to cyclophilin A (Millipore, Cat. #07-313) at a 1:2000 dilution and antibody to GAPDH (Thermo Fisher, Cat. #A21994; 5 μ g/ml). Antibody complexes were detected with the appropriate IR dye-conjugated secondary antibodies (LI-COR Biosciences) and detected by scanning with a LI-COR Odyssey imaging system. Bands were quantified using the Odyssey imaging software.

Results

We generated single site CypA mutants (A25D, K27D, P29K and K30D) at four residues located at the secondary CA contact site (Fig. 1b) and tested their ability to disrupt CA binding biochemically and affect HIV-1 infection in cells. Additional mutants at these residues (A25K, K27A and P29D) were also tested in the infection assays. Introduction of a charged amino acid (lysine or aspartic acid) at residues A25 and P29 was designed to disrupt possible hydrophobic interactions with CA. The mutation at P29 (located at the N-terminal side of an α -helix) may also lead to localised main-chain displacement. Mutating K27 and K30 to an aspartic acid residue replaces a hydrogen bond donor with a hydrogen bond acceptor. In addition, these mutations, as well as K27A, change the steric configuration at these sites. K30D would also be expected to locally destabilise the structure by breaking the interaction of K30 with E83 that is apparent in the crystal structure of wild type CypA [32].

To test for avidity arising from the bridging binding mode of CypA with CA lattices (Fig. 1a), we compared the affinity of recombinant wild type and mutant CypA (A25D, K27D, P29K and K30D) for unassembled CA, cross-linked CA hexamers and self-assembled CA tubes. Biophysical characterization of purified proteins by differential scanning fluorimetry and circular dichroism (Additional file 1: Figure S1) showed that mutants A25D, K27D and P29K were similar to wild type CypA with respect to melting point and secondary structure content, whereas CypA K30D was destabilized, possibly as a result of removing the interaction of K30 with E83 as discussed above. 1D 1 H spectra of CypA A25K and P29D mutants (not shown) and 2D 1 H- 15 N HSQC NMR spectrum of 15 N/ 13 C-labeled CypA P29K mutant (Additional file 1: Figure S2B) reveal that the structures of the mutants are essentially the same as for wild type protein (Additional file 1: Figure S2A), whereby perturbations were confined to the mutated site and neighbouring residues while the active site was intact. Moreover, the binding property of CypA P29K (Additional file 1: Figure S2D) to CA-NTD, studied by 1 H- 15 N HSQC, was the same as for wild type protein (Additional file 1: Figure S2C), i.e. the same set of CypA residues were perturbed by CA-NTD. Similarly, the 1 H- 15 N HSQC spectral perturbations of 15 N/ 13 C-labeled CA-NTD upon adding unlabeled CypA P29K, P29D and A25K were similar (not shown). In summary, the binding data by NMR indicate that these CypA residues are not involved in the interaction with monomeric CA in solution.

We first used surface plasmon resonance (SPR) to determine the dissociation constant (K_D) for all CypA variants interacting with CA immobilized on the surface of the SPR chip (Fig. 2 and Table 1, Additional file 1: Figure S3). The K_D for the interaction of wild type CypA with unassembled CA ($K_D \sim 27 \mu$ M) was in the range of values determined previously by a range of techniques (7 μ M [9] or $16 \pm 4 \mu$ M [14] measured by isothermal titration microcalorimetry; 30 μ M [33] or 21.8 μ M [24] measured by SPR). As expected, the affinity of the interaction was essentially the same when using cross-linked CA hexamers (Fig. 2) because the bridging binding mode is not available within a single hexamer but only available between hexamers in a lattice (Fig. 1a). The K_D values for mutants A25D, K27D and P29K interacting with unassembled or hexameric CA were similar to the values observed for wild type CypA (Table 1) confirming that these mutations did not affect the integrity of the active site. The destabilized mutant K30D showed only a minor defect in binding via the active site with a 1.5–twofold increase in K_D compared to the other variants.

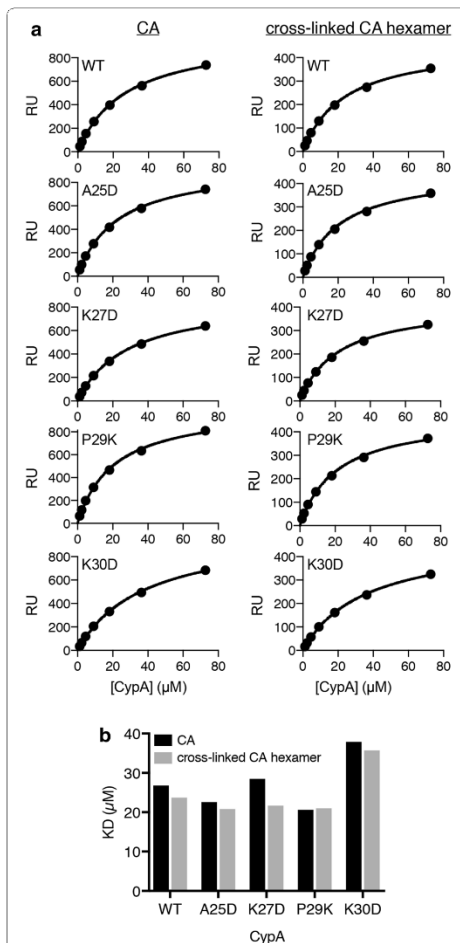


Fig. 2 Binding affinity of wild type and mutant CypA for CA and cross-linked CA hexamers. **a** Equilibrium analysis of surface plasmon resonance (SPR) curves of CypA binding on surfaces modified with CA K158C (reacted with a maleimide derivative of biotin) or cross-linked CA A14C/I45C/W184A/M185A hexamers (reacted with an NHS ester derivative of biotin). The SPR curves are shown in Additional file 1: Figure S2. **a** SPR response at equilibrium as a function of CypA concentration and fit of a binding model to the data (black line) to obtain the dissociation constant of the CypA interaction. **b** Equilibrium dissociation constants (K_D) determined for wild type CypA and mutant interacting with CA and CA hexamers from the single experiments shown in **a**

Next, we investigated the interaction of wild type and mutant CypA with the CA lattice. Capsid binding of host proteins is commonly investigated using co-sedimentation with CA (or CA-NC) tubes as surrogates for the native capsid lattice. Recombinant CA self-assembles into tubular lattices made up of CA hexamers in the presence of high salt in the buffer. These tubes can be stabilized to prevent disassembly at physiological salt concentrations by using a double cysteine mutant (CA A14C/E45C) that forms disulfide cross-links between adjacent CA subunits in each hexamer. Here we used a quantitative fluorescence imaging assay to measure the affinity and stoichiometry of CypA variants binding to cross-linked CA tubes, as illustrated in Fig. 3a. CA tubes were grown inside a microfluidic flow-channel in a high salt solution by co-assembly of CA A14C/E45C and CA K158C modified with AlexaFluor 488 (for fluorescence labeling of the tubes) and immobilized onto the modified surface of the glass cover slip via an antibody directed against the CypA loop of CA. We then measured binding and dissociation of CypA labeled at Cys51 with Alexa Fluor 647 (Fig. 1b) flowed into the channel at a range of concentrations and then washed out while imaging the fluorescence signals of the CA tubes and bound CypA by total internal reflection fluorescence (TIRF) microscopy. CA tubes were detected as lines in the fluorescence image (Fig. 3b, top). The signal of AF647-CypA co-localized with the tubes and rapidly reached a constant level after injection into the flow channel (Fig. 3b, bottom). Wash-out with buffer led to complete disappearance of the AF647-CypA signal indicating rapid dissociation (Fig. 3b, bottom). The ratio of the fluorescence intensity for each tube in the CA channel to the corresponding intensity in the CypA channel was converted to a molar binding ratio (see Materials and Methods). Analysis of the binding curves measured for tubes in multiple fields of view at a range of CypA concentrations with an equilibrium binding model (Fig. 3c) then yielded an estimate of K_D . There was no statistically significant difference in the affinity of the interaction between CypA and CA tubes for wild type ($K_D \sim 15 \mu\text{M}$) and mutant CypA ($K_D \sim 16\text{--}18 \mu\text{M}$), including the destabilized mutant K30D (Fig. 3d and Table 1). The binding curves further revealed that CypA binding to the CA lattice saturated when $\sim 40\%$ of CypA loops on the lattice are occupied with a CypA molecule irrespective of mutation (Fig. 3e). This binding ratio is close to the maximum ratio that is expected when taking steric hindrance between CypA molecules interacting with neighboring CypA loops on the lattice into account [23]. We conclude that substitutions of residues at the proposed secondary binding site on CypA do not affect the affinity or stoichiometry of CypA binding to the hexameric lattice of cross-linked CA tubes.

Table 1 Dissociation constants ($K_D/\mu\text{M}$) for the CypA–CA interaction determined by SPR for CA and cross-linked CA hexamers (single experiments) and by fluorescence imaging for cross-linked CA tubes and native capsids (mean \pm standard deviation)

	CA	CA hexamer	CA tube	Native capsid
WT	26.8	23.7	14.5 \pm 5	10.7 \pm 0.7
A25D	22.6	20.8	17.2 \pm 4.8	8.7 \pm 2.1
K27D	28.5	21.7	17.7 \pm 6.7	n.d.
P29K	20.6	21	16.4 \pm 3.8	n.d.
K30D	37.9	35.7	17 \pm 9.2	n.d.

n.d. Not determined

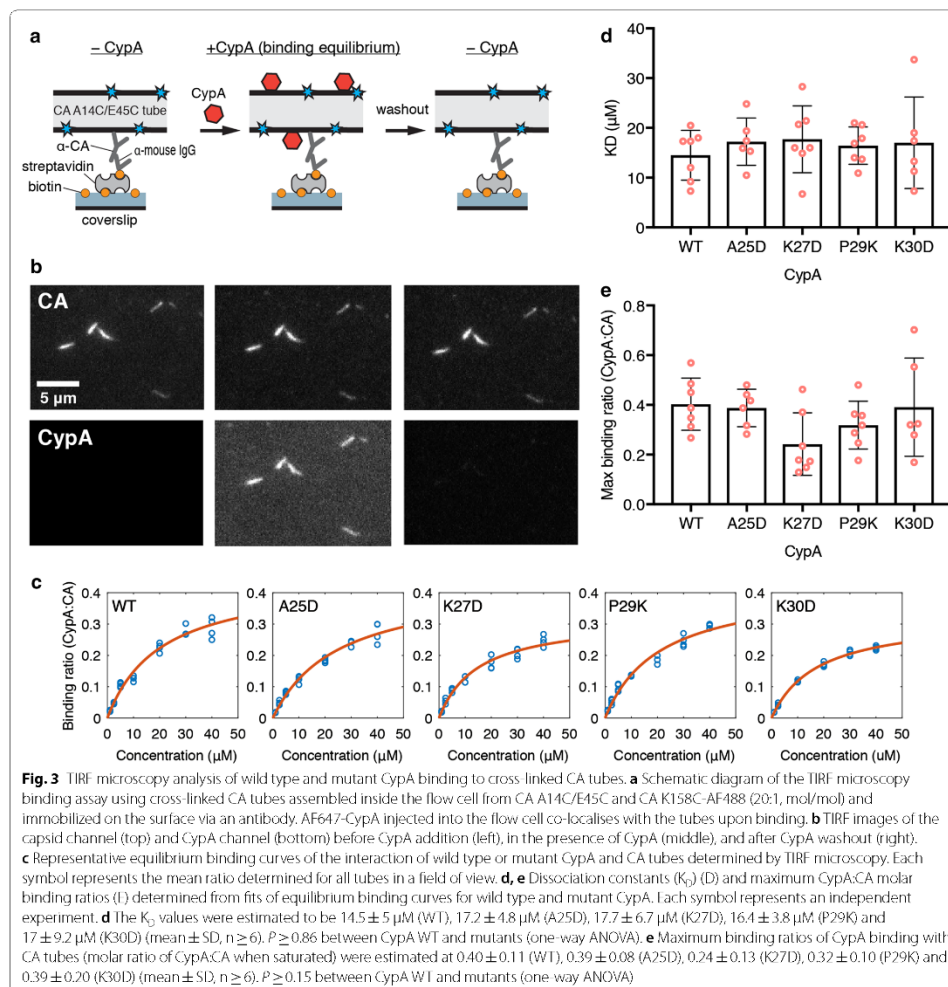
Finally, we chose CypA A25D as one of the secondary site mutants without folding defects to determine whether its interaction with the wild type CA lattice of authentic viral cores was impaired compared to wild type CypA. The binding affinity and the number of CypA loops that can be occupied simultaneously on the assembled capsid were determined using our recently developed *in vitro* single-molecule fluorescence imaging assay (Fig. 4a) [24]. Viral particles containing GFP as a solution phase marker were immobilized on the glass surface of a cover slip and permeabilized with a pore-forming protein to allow access of CypA to the capsid. Permeabilized virions with intact capsids retain encapsidated GFP molecules and were detected as diffraction-limited spots in the GFP channel. The fluorescence intensity of AF647-CypA injected into the flow channel was then monitored by TIRF microscopy at each location corresponding to an intact capsid, reaching a rapid equilibrium level. The AF647-CypA fluorescence intensity was then converted to the number of CypA molecules bound using a calibration value obtained by single molecule photobleaching. Representative equilibrium binding curves obtained by plotting the mean number of molecules per capsid as a function of CypA concentration are shown in Fig. 4b for wild type (top) and mutant (bottom). The K_D of CypA A25D binding to intact capsids ($8.7 \pm 2.1 \mu\text{M}$) was not significantly different from the K_D measured for wild type CypA in the same system ($10.7 \pm 0.7 \mu\text{M}$) (Fig. 4c). Likewise, the number of CypA loops occupied at saturation, as determined from the fit of the equilibrium binding curve, was not significantly different for mutant (877 ± 286) and wild type (987 ± 251) CypA (Fig. 4d). Taken together our observations with cross-linked tubes and authentic capsids suggest that mutation of secondary site residues does not affect binding of CypA to the CA lattice *in vitro*.

To test for functionality of the CypA secondary CA-binding site in HIV-1 infection, we expressed mutant

CypA proteins in cells in which endogenous CypA was deleted and assayed the effects of secondary site mutations on HIV-1 infection. In the following sections we present results from infection assays in (1) HeLa-P4 cells (using HIV-1 with CA A92E mutation) and (2) Jurkat cells.

The HIV-1 capsid escape mutant A92E arises during passage of HIV-1 in HeLa-P4 cells during CypA inhibition [34] and is poorly infective in cells expressing high CypA levels such that its replication becomes dependent on the presence of the CypA inhibitor cyclosporin A (CsA) [35]. In HeLa-P4 cells, which express high levels of endogenous CypA, infectivity of an HIV-1 A92E reporter virus in the absence of CsA was less than 10% of the infectivity in the presence of CsA (– CsA/+ CsA infection ratio < 0.1 , Fig. 5a). As expected, removal of CypA expression by disruption of the *PPIA* gene with CRISPR technology resulted in efficient HIV-1 A92E infection without the need for CypA inhibition (– CsA/+ CsA infection ratio > 0.8 , Fig. 5a). Wild type CypA and CypA mutants A25D, A25K, K27A, K27D, P29K and K30D could be expressed in the CypA-null cells at near or above endogenous levels (Fig. 5b) using lentiviral vectors, which inhibited HIV-1 A92E infection and thus restored the CsA dependence to the same extent for all variants (– CsA/+ CsA infection ratio < 0.1 , Fig. 5a).

CypA enhances HIV-1 infection in Jurkat cells [30, 36] and accordingly we found that infection of Jurkat cells with an HIV-1 reporter virus expressing GFP was about twice that in the absence of CsA vs. in the presence of CsA (Fig. 6a). As expected, HIV-1 infection was the same in the absence and presence of CsA in CypA-null Jurkat cells (– CsA/+ CsA infection ratio = 1, Fig. 6a), confirming that the antiviral effect of CsA is via inhibition of CypA. Expression of CypA proteins with mutations in secondary site residues A25 and K27 in CypA-null Jurkat cells restored their permissiveness to infection by wild type HIV-1 close to the level observed for wild type CypA, while the destabilized mutant CypA K30D showed partial enhancement of infectivity (see also Additional file 1: Figure S4). Expression of CypA P29K also enhanced HIV-1 infection close to wild-type levels, while CypA P29D did not restore permissiveness to infection, possibly because the expression level of this mutant was too low in CypA-null Jurkat cells (approximately half of the expression level of wild type CypA in CypA-null Jurkat cells, Fig. 6b). In additional experiments, expression of the P29D and P29K mutants was undetectable, and the phenotype of the corresponding cell lines was identical to that of the CypA-null cells (Additional file 1: Figure S4). Taken together these results suggest that the second capsid binding site on CypA is not functional in the infection

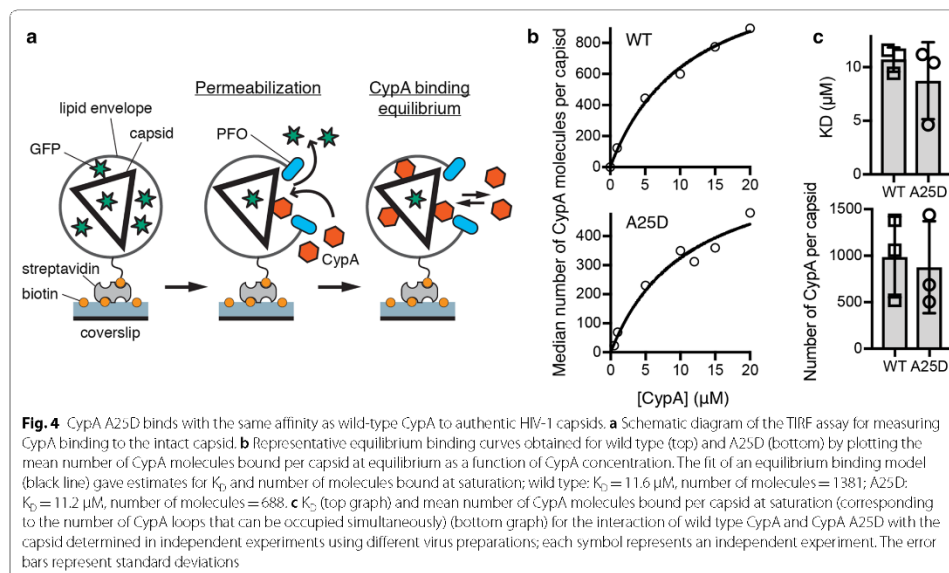


assays we employed or was not affected by the amino acid changes tested thus far.

Discussion and conclusion

Our mutational analysis of CypA residues at the proposed second CA binding interface revealed that introduction of a charged residue at A25 or P29, or charge

reversal at K27 or K30, had no effect on: (1) CypA binding affinity or stoichiometry with the CA lattice *in vitro*; (2) the ability of the protein to inhibit infection of HeLa-P4 cells by a HIV-1 CA escape mutant that is dependent on CysA for replication; and (3) the ability of CypA to enhance HIV-1 infection of Jurkat cells. On the basis of these observations we conclude that the



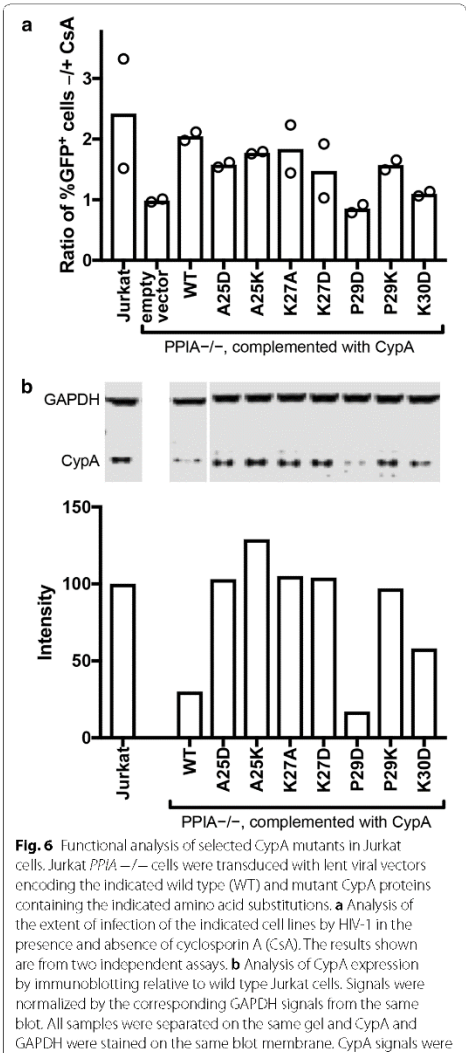
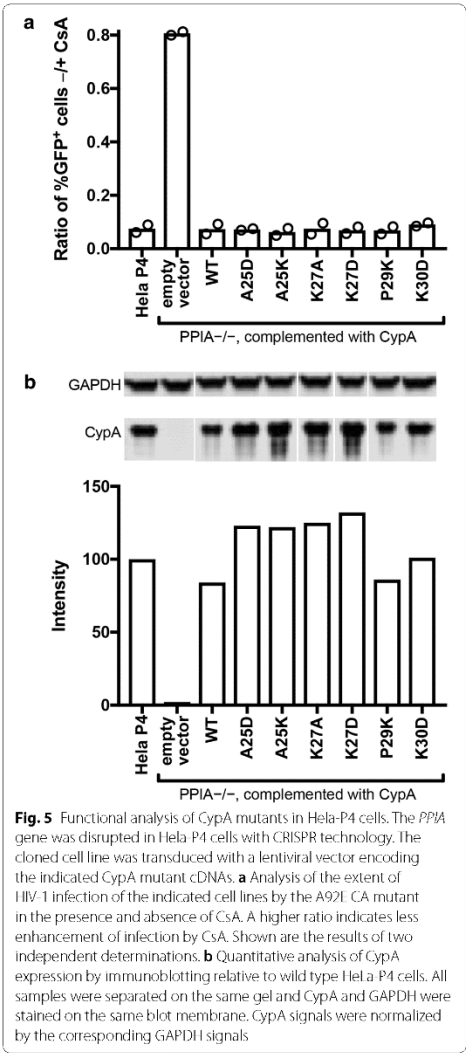
residues investigated here do not constitute a secondary binding interface for CA. Mutational analysis of CA was not carried out because the same residues (A88, G89, P90) implicated in binding to the non-canonical site of CypA also interact with the active (canonical) site of CypA, where they are buried into a hydrophobic groove [15].

Our *in-vitro* measurements of CypA–CA interactions utilized primarily self-assembled CA A14C/E45C tubes, which are similar in structure to the wild type CA tubes used previously to determine the cryoEM structure of the complex [23]. The CypA:CA stoichiometry of ~0.3–0.4 (corresponding to about two CypA molecules per hexamer) we obtained for all CypA variants is consistent with the computationally generated binding models reported for the tubular complex [23]. The additional interaction via the second site for CypA molecules along the most highly curved direction of the tube (corresponding to one CypA molecule per CA hexamer) would be expected to strengthen CypA–CA lattice interaction through avidity. Disabling the second site, e.g. via mutation, should weaken the interaction

of mutant CypA with the tube compared to the wild type protein, which was not observed in our assay. The cross-linked hexamer used here to stabilise tubes at physiological salt concentrations structurally resembles the native hexamer [37] but cross-linking could in principle affect interactions with the lattice, e.g. as a result of lattice rigidification. As an additional test, we used a new fluorescence imaging assay that can quantify the number of CypA molecules interacting with native viral capsids to compare one of the mutants (A25D) to the wild type protein, but we observed no differences in affinity.

Similarly, our HIV-1 infection assays in HeLa-P4 and Jurkat cells revealed no functional differences between wild type CypA and the second site mutants, suggesting that the site was misidentified or does not play a role in the CypA use by HIV-1 capsid during the early life cycle.

The mutational analysis of residues conducted here does not rule out the existence of a secondary CA binding site and future structural studies of the complex at higher resolution may identify a different set of CypA



residues that could constitute such a site. Our observation that the binding of wild type CypA to the CA lattice is only modestly stronger with the CA lattice than with unassembled CA (up to twofold reduction in K_D

for CA tubes and up to threefold reduction in K_D for native capsids) suggests that binding at the second site, if present, is considerably weaker than at the active site

and/or only accessible at few locations on the capsid lattice.

Additional files

Additional file 1. Biochemical and structural characterization of CypA mutants, SPR sensorgrams, additional infection assays in Jurkat cells expressing CypA mutants.

Additional file 2. Tables of SPR sensorgram data.

Abbreviations

CsA: cyclosporine A; CypA: cyclophilin A; NMR: nuclear magnetic resonance; NTD: N-terminal domain; SPR: surface plasmon resonance; TIRF: total internal reflection fluorescence.

Authors' contributions

WP: Investigation (CypA purification and biophysical characterization; SPR, TIRF binding assay with CA tubes), Data analysis, Writing—original draft. JS: Investigation (generation of cell lines, HIV infection assays and immunoblotting), Data analysis. CM: Investigation (TIRF binding assay with viral particles), Data analysis, Writing—review and editing. KMRF: Investigation (TIRF binding assay with viral particles), Data analysis. DL: Investigation (TIRF binding assay with CA tubes), Writing—review and editing. JW: Software, Data analysis. CHB: Investigation (protein purification, NMR data acquisition and analysis). JLB: Conceptualization (design of CypA mutants), Investigation (NMR data acquisition and analysis), Writing—review and editing. CA: Conceptualization, Writing—original draft. TB: Conceptualization, Writing—original draft. All authors read and approved the final manuscript.

Author details

¹ EMBL Australia Node in Single Molecule Science and ARC Centre of Excellence in Advanced Molecular Imaging, School of Medical Sciences, UNSW, Sydney, NSW 2052, Australia. ² Department of Pathology, Microbiology and Immunology, Vanderbilt University Medical Center, Nashville, TN, USA. ³ Pittsburgh Center for HIV Protein Interactions, University of Pittsburgh School of Medicine, Pittsburgh, PA, USA. ⁴ Department of Structural Biology, University of Pittsburgh School of Medicine, Pittsburgh, PA, USA.

Acknowledgements

We thank Manman Lu for expression and purification of unlabeled and ¹⁵N/¹³C-labeled CypA wild type and mutants for NMR studies, Jeremy Luban for Jurkat PPIA α -/- cells (obtained via the NIH AIDS Reagent Program) and Miro Janco (UNSW) for help with acquiring CD data.

Competing interests

The authors declare that they have no competing interests.

Availability of data and materials

Raw data files and materials are available upon request from the corresponding authors.

Consent for publication

Not applicable.

Ethics approval and consent to participate

Not applicable.

Funding

TB received funding from the National Health and Medical Research Council of Australia (NHMRC APP1100771) and the Australian Centre for HIV and Hepatitis Virology Research. CA was supported by the Pittsburgh Center for HIV-Protein Interactions (NIH P50 GM082251 from the NIGMS and the NIAID). WP was supported by a University International Postgraduate Award from

UNSW. CM and DL received an Australian Government Research Training Program Scholarship.

Publisher's Note

Springer Nature remains neutral with regard to jurisdictional claims in published maps and institutional affiliations.

Received: 17 January 2019 Accepted: 23 March 2019

Published online: 04 April 2019

References

- Campbell EM, Hope TJ. HIV-1 capsid: the multifaceted key player in HIV-1 infection. *Nat Rev Microbiol*. 2015;13(8):471–83.
- Ganser BK, Li S, Klishko VV, Finch JT, Sundquist WL. Assembly and analysis of conical models for the HIV-1 core. *Science*. 1999;283(5398):80–3.
- Freed EO. HIV-1 gag proteins: diverse functions in the virus life cycle. *Virology*. 1998;251(1):1–15.
- von Schwedler UK, Stray KM, Garrus JE, Sundquist WL. Functional surfaces of the human immunodeficiency virus type 1 capsid protein. *J Virol*. 2003;77(9):5439–50.
- Hulme AE, Perez Q, Hope TJ. Complementary assays reveal a relationship between HIV-1 uncoating and reverse transcription. *Proc Natl Acad Sci USA*. 2011;108(24):9975–80.
- Jacques DA, McEwan WA, Hilditch L, Price AJ, Towers GJ, James LC. HIV-1 uses dynamic capsid pores to import nucleotides and fuel encapsidated DNA synthesis. *Nature*. 2016;536(7616):349–53.
- Delaney MK, Malikov V, Chai Q, Zhao G, Naghavi MH. Distinct functions of diaphanous-related formins regulate HIV-1 uncoating and transport. *Proc Natl Acad Sci USA*. 2017;114(33):E6932–41.
- Carnes SK, Zhou J, Aiken C. HIV-1 engages a dynein-dynactin-BICD2 complex for infection and transport to the nucleus. *J Virol*. 2018;92:e00358.
- Schaller T, Ocwieja KE, Rasaiyaah J, Price AJ, Brady TL, Roth SL, et al. HIV-1 capsid-cyclophilin interactions determine nuclear import pathway, integration targeting and replication efficiency. *PLoS Pathog*. 2011;7(12):e1002439.
- Di Nunzio F, Danckaert A, Fricke T, Perez P, Fernandez J, Perret E, et al. Human nucleoporins promote HIV-1 docking at the nuclear pore, nuclear import and integration. *PLoS ONE*. 2012;7(9):e46037.
- Koh Y, Wu X, Ferris AL, Matreyek KA, Smith SJ, Lee K, et al. Differential effects of human immunodeficiency virus type 1 capsid and cellular factors nucleoporin 153 and LEDGF/p75 on the efficiency and specificity of viral DNA integration. *J Virol*. 2013;87(1):648–58.
- Sowd GA, Serrao E, Wang H, Wang W, Fadel HJ, Poeschla EM, et al. A critical role for alternative polyadenylation factor CPSF6 in targeting HIV-1 integration to transcriptionally active chromatin. *Proc Natl Acad Sci USA*. 2016;113(8):E1054–63.
- Ocwieja KE, Brady TL, Ronen K, Huegel A, Roth SL, Schaller T, et al. HIV integration targeting: a pathway involving Transportin-3 and the nuclear pore protein RanBP2. *PLoS Pathog*. 2011;7(3):e1001313.
- Yoo S, Myszkowski DG, Yeh C, McMurray M, Hill CP, Sundquist WL. Molecular recognition in the HIV-1 capsid/cyclophilin A complex. *J Mol Biol*. 1997;269(5):780–95.
- Gamble TR, Vajdos FF, Yoo S, Worthylake DK, Houseweart M, Sundquist WL, et al. Crystal structure of human cyclophilin A bound to the amino-terminal domain of HIV-1 capsid. *Cell*. 1996;87(7):1285–94.
- Sokolskaja E, Sayah DM, Luban J. Target cell cyclophilin A modulates human immunodeficiency virus type 1 infectivity. *J Virol*. 2004;78(23):12800–8.
- Berthoux L, Sebastian S, Sokolskaja E, Luban J. Cyclophilin A is required for TRIM5 α -mediated resistance to HIV-1 in old world monkey cells. *Proc Natl Acad Sci USA*. 2005;102(41):14849–53.
- Li Y, Kar AK, Sodroski J. Target cell type-dependent modulation of human immunodeficiency virus type 1 capsid disassembly by cyclophilin A. *J Virol*. 2009;83(21):10951–62.

19. Shah VB, Shi J, Hout DR, Oztop I, Krishnan L, Ahn J, et al. The host proteins transportin SR2/TNPO3 and cyclophilin A exert opposing effects on HIV-1 uncoating. *J Virol*. 2013;87(1):422–32.
20. Rasaiyaah J, Tan CP, Fletcher AJ, Price AJ, Blondeau C, Hilditch L, et al. HIV-1 evades innate immune recognition through specific cofactor recruitment. *Nature*. 2013;503(7476):402–5.
21. Le Sage V, Mouland AJ, Valiente-Echeverria F. Roles of HIV-1 capsid in viral replication and immune evasion. *Virus Res*. 2014;193:116–29.
22. Lu M, Hou G, Zhang H, Suiter CL, Ahn J, Byeon IJ, et al. Dynamic allosteric governs cyclophilin A-HIV capsid interplay. *Proc Natl Acad Sci USA*. 2015;112(47):14617–22.
23. Liu C, Perilla JR, Ning J, Lu M, Hou G, Ramalho R, et al. Cyclophilin A stabilizes the HIV-1 capsid through a novel non-canonical binding site. *Nat Commun*. 2016;7:10714.
24. Marquez CL, Lau D, Walsh J, Shah V, McGuinness C, Wong A, et al. Kinetics of HIV-1 capsid uncoating revealed by single-molecule analysis. *Elife*. 2018;7:e34772.
25. Hung M, Niedziela-Majka A, Jin D, Wong M, Leavitt S, Brendza KM, et al. Large-scale functional purification of recombinant HIV-1 capsid. *PLoS ONE*. 2013;8(3):e58035.
26. Yang R, Shi J, Byeon IJ, Ahn J, Sheehan JH, Meiler J, et al. Second-site suppressors of HIV-1 capsid mutations: restoration of intracellular activities without correction of intrinsic capsid stability defects. *Retrovirology*. 2012;9:30.
27. Charneau P, Alizon M, Clavel F. A second origin of DNA plus-strand synthesis is required for optimal human immunodeficiency virus replication. *J Virol*. 1992;66(5):2814–20.
28. Sanjana NE, Shalem O, Zhang F. Improved vectors and genome-wide libraries for CRISPR screening. *Nat Methods*. 2014;11(8):783–4.
29. Yee JK, Friedmann T, Burns JC. Generation of high-titer pseudotyped retroviral vectors with very broad host range. *Methods Cell Biol*. 1994;43(Pt A):99–112.
30. Braaten D, Luban J. Cyclophilin A regulates HIV-1 infectivity, as demonstrated by gene targeting in human T cells. *EMBO J*. 2001;20(6):1300–9.
31. He J, Chen Y, Farzan M, Choe H, Ohagen A, Gartner S, et al. CCR3 and CCR5 are co-receptors for HIV-1 infection of microglia. *Nature*. 1997;385(6617):645–9.
32. Fraser JS, Clarkson MW, Degnan SC, Erion R, Kern D, Albert T. Hidden alternative structures of proline isomerase essential for catalysis. *Nature*. 2009;462(7273):669–73.
33. Grattinger M, Hohenberg H, Thomas D, Wilk T, Muller B, Krausslich HG. In vitro assembly properties of wild-type and cyclophilin-binding defective human immunodeficiency virus capsid proteins in the presence and absence of cyclophilin A. *Virology*. 1999;257(1):247–60.
34. Aberham C, Weber S, Phares W. Spontaneous mutations in the human immunodeficiency virus type 1 gag gene that affect viral replication in the presence of cyclosporins. *J Virol*. 1996;70(6):3536–44.
35. Ylinen LM, Schaller T, Price A, Fletcher AJ, Noursadeghi M, James LC, et al. Cyclophilin A levels dictate infection efficiency of human immunodeficiency virus type 1 capsid escape mutants A92E and G94D. *J Virol*. 2009;83(4):2044–7.
36. Hatziloannou T, Perez-Caballero D, Cowan S, Bieniasz PD. Cyclophilin interactions with incoming human immunodeficiency virus type 1 capsids with opposing effects on infectivity in human cells. *J Virol*. 2005;79(1):176–83.
37. Mattei S, Glass B, Hagen WJ, Krausslich HG, Briggs JA. The structure and flexibility of conical HIV-1 capsids determined within intact virions. *Science*. 2016;354(6318):1434–7.

Ready to submit your research? Choose BMC and benefit from:

- fast, convenient online submission
- thorough peer review by experienced researchers in your field
- rapid publication on acceptance
- support for research data, including large and complex data types
- gold Open Access which fosters wider collaboration and increased citations
- maximum visibility for your research: over 100M website views per year

At BMC, research is always in progress.

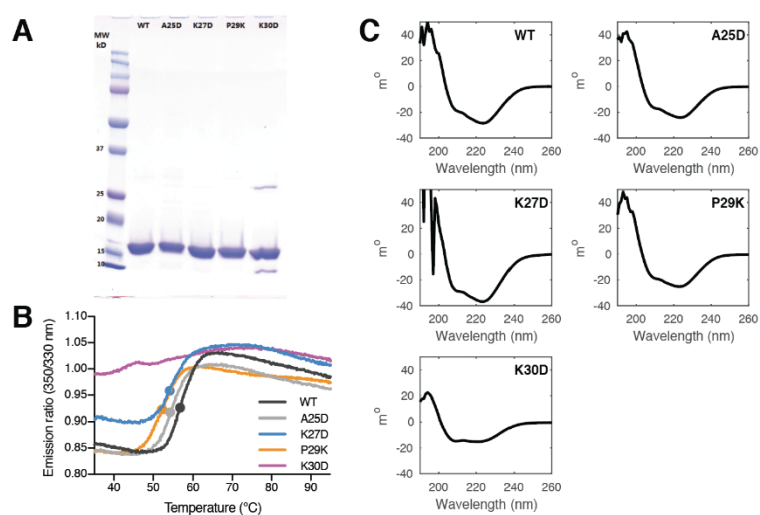
Learn more biomedcentral.com/submissions



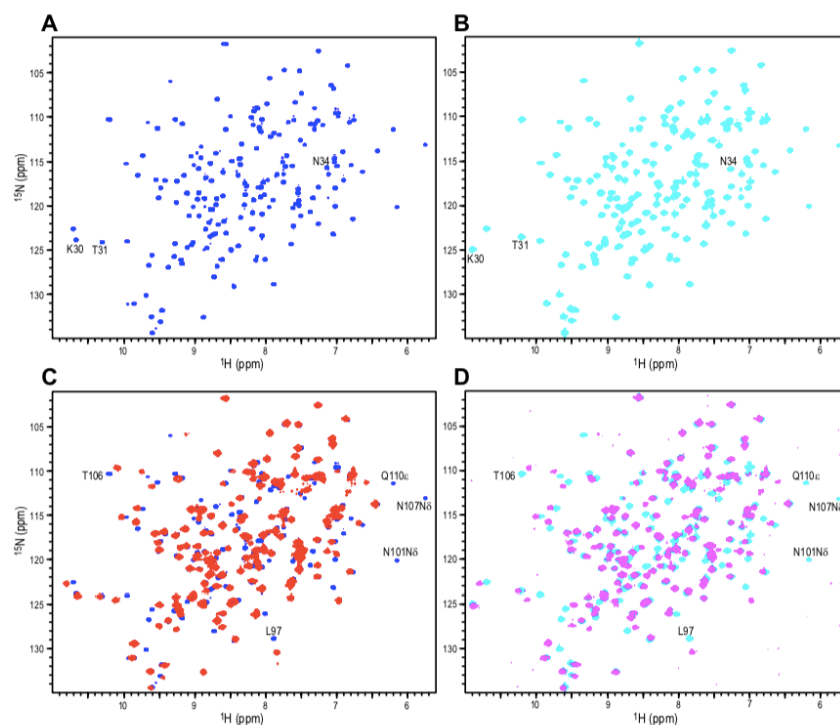
Supplementary information

Functional analysis of the secondary HIV-1 capsid binding site in the host protein cyclophilin A

Wang Peng, Jiong Shi, Chantal Márquez, Derrick Lau, James Walsh, K. M. Rifat Faysal, Chan H. Byeon, In-Ja L. Byeon, Christopher Aiken, Till Böcking



Supplementary Figure S1. Biochemical and structural characterization of recombinant CypA. **A.** SDS PAGE analysis with Coomassie staining of purified wild type and mutant CypA expressed in bacteria. **B.** Melting curves of wild type and mutant CypA measured by differential scanning fluorimetry. Melting temperatures (indicated by the dots) could be estimated for wild type CypA (56.8 °C) and mutants A25D (54.2°C), K27D (54.1°C) and P29K (52.2°C). The melting curve for CypA K30D showed a high fluorescence emission ratio across the entire temperature range (35–95 °C) indicating that this mutant is not properly folded. **C.** Circular dichroism spectra of wild type and mutant CypA.



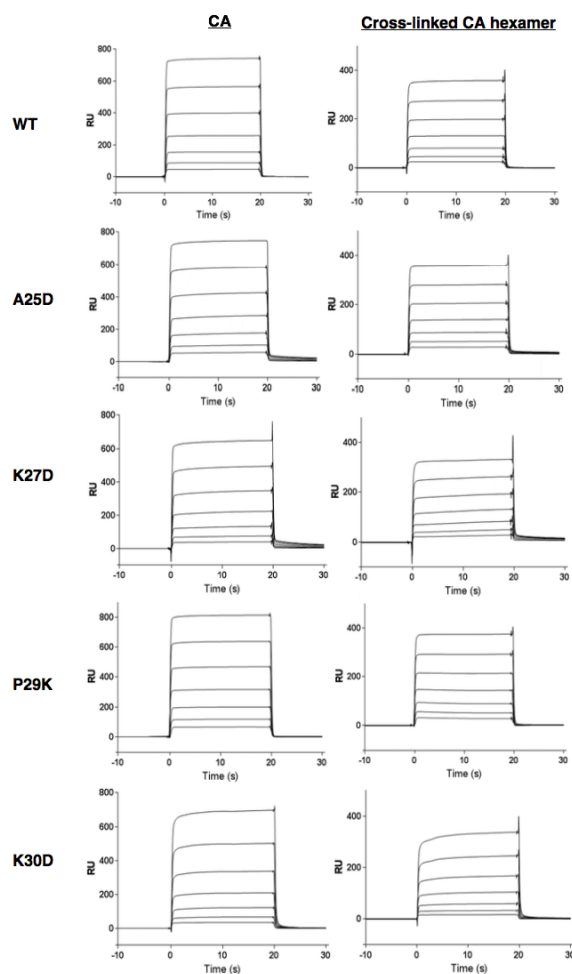
Supplementary Figure S2. ^1H - ^{15}N HSQC spectra show that wild type CypA and CypA P29K have essentially the same structure and CA-NTD-binding property.

A. ^1H - ^{15}N HSQC spectrum of $^{15}\text{N}/^{13}\text{C}$ wild type CypA.

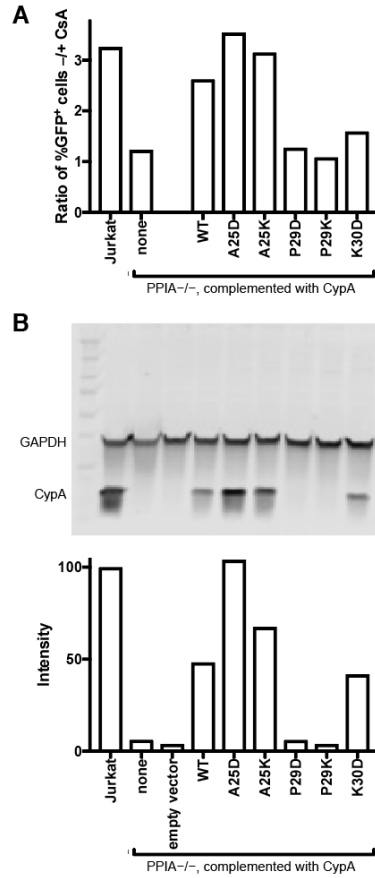
B. ^1H - ^{15}N HSQC spectrum of $^{15}\text{N}/^{13}\text{C}$ CypA P29K.

C. Superimposed ^1H - ^{15}N HSQC spectra of $^{15}\text{N}/^{13}\text{C}$ wild type CypA alone (blue) and with 2-fold molar excess of CA-NTD (red).

D. Superimposed ^1H - ^{15}N HSQC spectra of $^{15}\text{N}/^{13}\text{C}$ CypA P29K alone (cyan) and with 2-fold molar excess of CA-NTD (magenta).



Supplementary Figure S3. Surface plasmon resonance spectroscopy traces of wild type and mutant CypA interacting with CA and cross-linked CA hexamers. CypA WT, A25D, K27D, P29K and K30D at a range of concentrations (1.1, 2.3, 4.5, 9.1, 18.2, 36.4 and 72.8 μ M corresponding to curves from bottom to top) were flowed through SPR chip flow cells for 20s followed by wash-out while SPR response were recorded. SPR responses in CA monomer/hexamer flow cells were corrected from reference responses.



Supplementary Figure S4. Additional functional analysis of selected CypA mutants in Jurkat cells. Jurkat *PPIA*^{-/-} cells were transduced with lentiviral vectors encoding the indicated wild type (WT) and mutant CypA proteins containing the indicated amino acid substitutions. (A) Analysis of the extent of infection of the indicated cell lines by HIV-1 in the presence and absence of cyclosporin A (CsA). The results shown are from one independent assay. (B) Analysis of CypA expression by immunoblotting relative to wild type Jurkat cells. Signals were normalized by the corresponding GAPDH signals from the same blot. All samples were separated on the same gel and CypA and GAPDH were stained on the same blot membrane. CypA signals were normalized by the corresponding GAPDH signals.

3.3. *In vitro* assembly of HIV-1 CA to produce cones that are stabilized, remain soluble, and are labelled with fluorophores

In section 3.2, we used the stabilized and fluorescence labelled CA tube, reported by Lau *et al.* [124], as a tool to investigate the capsid-CypA interaction. This method is based on the established CA mutant A14C/E45C [113], which assembles into CA tubes at high salt similarly to CA WT. Although this tool serves as a powerful platform for studying the interactions between HIV-1 capsid and host factors, it is not compatible with our motility assay due to the propensity of CA tubes to aggregate. To be suitable for the motility assay, the capsid structures must be soluble and ideally assemble into structures that resemble what is observed for the native virus (i.e., cone-like). To overcome this challenge, we combined the established CA stabilizing mutant A204C which preferentially assembles into cone-like capsids [95] and the CA mutant A92E which decreases the hydrophobicity of the capsid exterior [80][74][66], thus generating a CA double mutant A92E/A204C for assembly of conical, soluble, and stabilized HIV-1 capsid particles. Fluorescence was introduced by co-assembly of CA A92E/A204C and CA K158C specifically labelled at the engineered cysteine residue at position 158 (see 2.2.4.1).

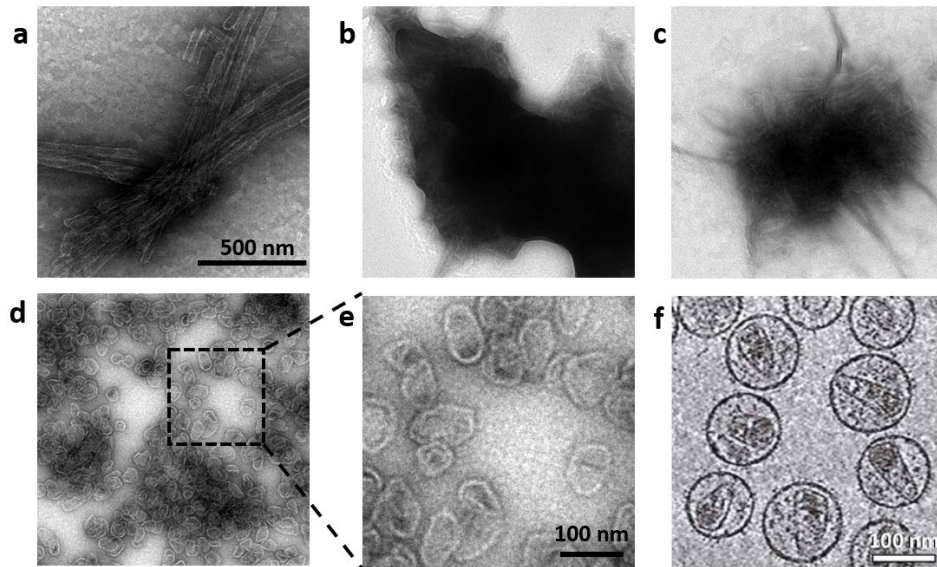


Fig. 3.1 Representative negative stain electron microscope images of HIV-1 capsid assemblies. WT (a), A14C/E45C (b), A204C (c), A92E/A204C (d), zoomed in field of view of A92E/A204C capsid (e), and cryogenic electron microscopy image of HIV-1 virions (f, image from [332]).

HIV-1 capsid structures assembled from CA A92E/A204C (**Fig. 3.1.d**) appeared as separate cones in negative staining electron microscopy images while structures assembled from CA WT, A14C/E45C, and A204C (**Fig. 3.1.a-c**) were aggregated into large clusters containing CA tubes. The morphology of self-assembled A92E/A204C capsids was (**Fig. 3.1.e**) comparable to the HIV-1 capsid within native HIV-1 virions (**Fig. 3.1.f**, image from [332]). Although CA A92E/A204C and A204C preferably assembled into conical structures, they also formed CA tubes depending on assembly conditions. We noticed that pH, ionic strength, and concentration of IP6 during HIV-1 CA assembly all had effects on capsid morphology (data not shown). Therefore, we picked assembly conditions (see **2.2.4.1**) that produced predominantly conical capsids (**Fig. 3.1.d**) for downstream experiments. We further applied a 2-step spin method to isolate soluble capsids from capsid aggregates and unassembled CA protein (**Fig. 3.2.A**). In short, assembled CA (fraction P1) was first separated from unassembled CA (fraction S1) by a fast spin, and then resuspended prior to a slow spin to separate soluble capsids (fraction S2, used for subsequent experiments) from capsid aggregates (fraction P2). Assembly efficiency and fluorescence labelling ratio were estimated based on Coomassie and fluorescence band intensities when the fractions were examined by reducing SDS-PAGE. Solubility of these capsid particles were confirmed by negative stain EM (**Fig. 3.2.C**) and TIRFm (**Fig. 3.2.D**).

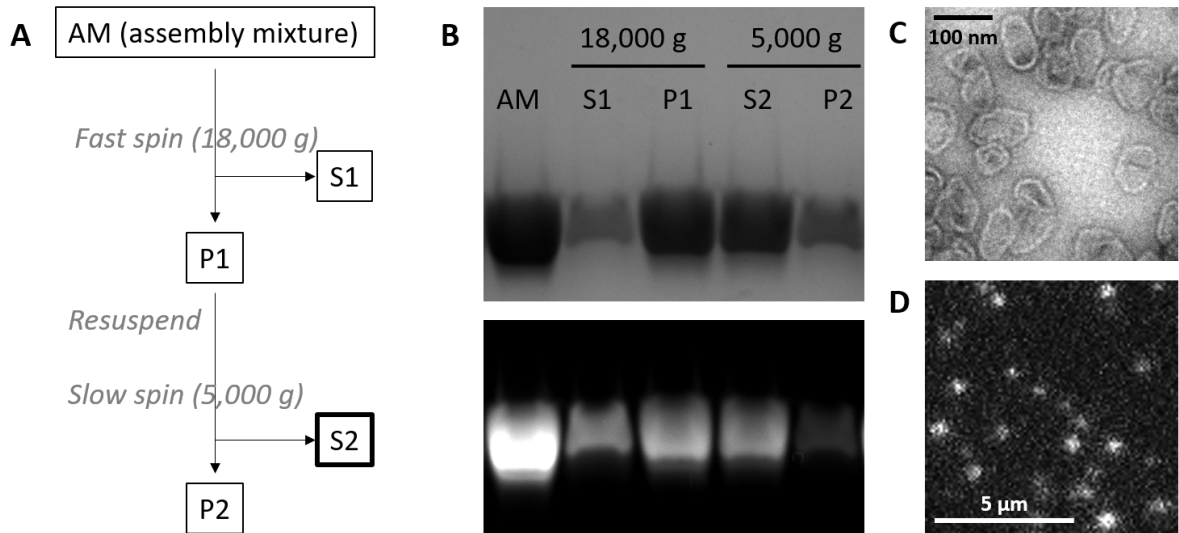


Fig. 3.2. Preparation of pre-assembled, conical, soluble, stabilized, and fluorescence labelled HIV-1 capsid. **A.** Schematic display of a 2-step spin method for separating soluble capsid (S2) from capsid aggregates (P2) and unassembled CA protein (S1). The assembly mixture (76 μ M CA A92E/A204C, 4 μ M K158C-AF647 in 50 mM MES, pH 6, 30 mM NaCl, 2.5 mM IP6) was incubated for > 1h at 4 $^{\circ}$ C

prior to the first spin. **B.** The assembly mixture (AM) and fractions S1, P1, S2, P2 were analyzed by reducing SDS page (top, Coomassie; bottom, fluorescence). **C-D.** Representative negative stain EM image (**C**) and TIRFm image (**D**) of the pre-assembled, conical, soluble, stabilized, and fluorescently labelled HIV-1 capsid.

3.4. The self-assembled HIV-1 CA A92E/A204C capsids interact with known capsid binders

We demonstrated that the capsids self-assembled as described in section 3.3 were able to interact with known capsid binders (**Fig. 3.3**) using a TIRFm binding assay. Fluorescent capsids captured onto the surface of a chemically modified glass coverslip appeared as diffraction-limited fluorescence spots in the TIRF image of the capsid channel. Addition of capsid-binding molecules labelled with a different fluorophore to the solution resulted in the appearance of fluorescence spots in the binder channel that co-localised with the signals in the capsid channel, as demonstrated for CypA-AF488, which binds to the CypA loop on the N-terminal domain of CA and for a range of Atto488-labelled polyanions that bind to the R18 pore in the centre of CA hexamers including ATP, dATP and hexacarboxybenzene (**Fig. 3.3**). These observations confirmed that the self-assembled CA A92E/A204C capsids could serve as a lattice for interaction with known capsid-binding host factors.

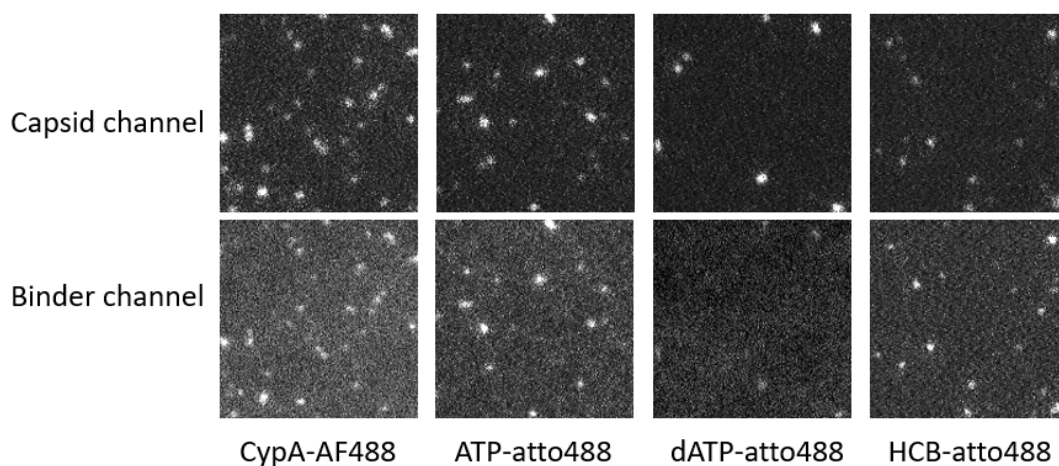


Fig. 3.3. The self-assembled HIV-1 capsids (from CA A92E/A204C) interact with known capsid binders. Representative TIRFm images of binding assays using fluorescent versions of known capsid binders including CypA, ATP, dATP, and hexacarboxybenzene (HCB) were demonstrated to interact with the self-assembled CA A92E/A204C structures prepared as described in section 3.3.

3.5. Summary

This chapter describes the property of HIV-1 capsid as a lattice that interacts with host factors.

Section 3.2 contains a published study showing that amino acid substitutions in CA at a proposed secondary binding site between the host protein CypA and HIV-1 capsid did not affect the binding affinity or ability to support infection, suggesting that the proposed residues do not participate in a potential secondary binding site [109]. A recent study from the same group suggests that CypA senses specific geometries of capsid lattice and that one CypA could interact with up to three CA molecules simultaneously [160]. However, our data do not provide strong evidence for the existence of non-canonical binding site(s) based on the observations that CypA binds to CA monomer, hexamer, and capsid lattice with highly similar affinities [121].

Section 3.3 and 3.4 describe an optimized method for assembly of soluble, stabilized HIV-1 capsids that are fluorescently labeled and retain the shape of native viral capsids. Compared to existing methods, our method greatly improves capsid solubility, providing an optimized reagent to investigate the interactions between HIV-1 capsid and host factors at a molecular level. More importantly, this method yields HIV-1 capsids suitable for single molecule assays, which is a prerequisite for the downstream motility assays described in Chapter 4 and Chapter 5.

Chapter 4

In vitro reconstitution of dynein-
dependent transport of HIV-1
capsid

4. *In vitro* reconstitution of dynein-dependent transport of HIV-1 capsid

4.1. Introduction

Multiple studies have demonstrated that the dynein-dynactin complex (hereafter referred to as dynein complex unless discussion of dynactin is necessary) is required for HIV-1 infection [149]. Disrupting components of this complex inhibits the transport of the HIV-1 viral core towards the nucleus, consistent with the role of dynein as the canonical retrograde motor [51, 149, 256, 257]. While other studies have implicated the involvement of dynein in additional steps of HIV-1 infection including uncoating [150] and reverse transcription [253, 333], it is likely that these effects are related to defects in cytoplasmic HIV-1 capsid transport. These initial studies clearly demonstrate a role for dynein in the early life cycle of HIV-1 infection; however, two important questions remained unaddressed. First, how is the interaction between the HIV-1 core and the dynein motor complex regulated? Second, if the ability of dynein to transport HIV-1 core is governed by the conventional dynein-dynactin-adaptor-cargo model [283-285], is HIV-1 capsid sufficient to drive the formation of a dynein-dynactin-adaptor-cargo complex?

As noted above, the assembly of a processive dynein motor complex requires adaptor proteins that have been activated through the binding of cargo. BICD2 is a well-known adaptor protein of dynein [258, 259] and it has been shown to be required for HIV-1 infection in a genome-wide RNAi screen [102]. Dharan *et al.* reported that BICD2 is the adaptor protein which links HIV-1 capsid to dynein for the dynein-dependent transport of the HIV-1 viral core [74]. This study demonstrated that depletion of BICD2 or disruption of the BICD2-dynein interaction led to defects in HIV-1 infection. Using proximity ligation assays the authors showed that BICD2 associates with HIV-1 capsid during infection, suggesting that BICD2 binds to HIV-1 capsid directly. The direct interaction between BICD2 and HIV-1 capsid was confirmed using a pulldown assay with CA-NC (capsid-nucleocapsid) tubes. These results indicated that the C-terminal CC3 (coiled-coil 3) domain of BICD2, which contains the cargo binding domain [260], is responsible for mediating the interaction with the HIV-1 capsid. Lastly, the study showed that depletion of BICD2 led to a decrease in both the speed and the net displacement of the HIV-1 viral core towards the nucleus, indicating that the retrograde transport of the HIV-1 core is dependent on BICD2.

Carnes *et al.* reported a systematic analysis of the interactions between the HIV-1 core and the dynein motor complex, suggesting that the HIV-1 core engages the dynein-dynactin-BICD2 complex for transport to the nucleus [52]. The authors performed extensive knock-down experiments of the dynein-dynactin-BICD2 complex including BICD2, and subunits of dynein or dynactin in a cell-based HIV-1 infection assay. Decreases in infection and nuclear import, but not reverse transcription, were observed upon knock-down of dynein heavy chain, BICD2, or dynactin subunits. A significant increase was observed for the percentage of non-motile HIV-1 cores upon the knock-down of dynein heavy chain or BICD2. In addition, the average distance of retrograde transport for the viral cores that remained motile decreased too. Using pull-down experiments with assembled CA tubes or CA-NC tubes, the study also confirmed that BICD2 binds to HIV-1 capsid via the CC3 domain of BICD2. Additionally, the study showed that the N-terminal CC1 (coiled-coil 1) domain also contributed to the BICD2-capsid interaction, which is surprising since CC1 is generally recognized as the dynein-dynactin binding domain of BICD2 [261, 262] rather than the cargo binding domain. Taken together, the authors suggested that HIV-1 engages dynein-dynactin-BICD2 complex for the retrograde transport of the HIV-1 core.

The results from Dharan *et al.* and Carnes *et al.* together present a model in which HIV-1 capsid hijacks the dynein complex via the adaptor protein BICD2, forming a dynein-dynactin-BICD2-capsid complex which facilitates the retrograde transport of HIV-1 core [74]. The first aim of this chapter is to characterise the BICD2-capsid interaction on a molecular level, including quantitative description of the BICD2-capsid interaction and initial dissection of the interfaces on HIV-1 capsid that are responsible for the interaction. The second aim is to investigate whether a complex containing dynein-dynactin-BICD2-capsid is sufficient to reconstitute capsid transport along microtubules.

4.2. BICD2 interacts with HIV-1 capsid

4.2.1. Quantitative analysis of the BICD2-capsid interaction

We used the TIRFm-based capsid binding assay, as described in Chapter 3, to quantitatively investigate the interaction between HIV-1 capsid and BICD2. A solution containing self-assembled HIV-1 capsids (see **2.4.1.1** A92E/A204C + K158C-AF647) was flowed into a microfluidic flow-channel and HIV-1 capsids were captured onto the modified surface of a glass coverslip. The captured HIV-1 capsids can be visualized when excited by a 637 nm laser (**Fig. 4.1.A**, left) as mostly diffraction-

limited spots as well as elongated objects, presumably corresponding to cones and short tubes, respectively. The variation in brightness, which relates to the total number of labelled CA in each particle, could be a result of both variation in capsid size as well as capsid clustering. A solution containing sfGFP-mBICD2 was introduced into the flow-channel to examine whether sfGFP-mBICD2 could bind to the HIV-1 capsid. When excited using a 491 nm laser, sfGFP-mBICD2 signal was observed to colocalize to the HIV-1 capsid spots (**Fig. 4.1.A**, right), demonstrating that sfGFP-mBICD2 directly binds to the HIV-1 capsid. The signal of bound sfGFP-mBICD2 rapidly reached a constant level upon the injection of the solution.

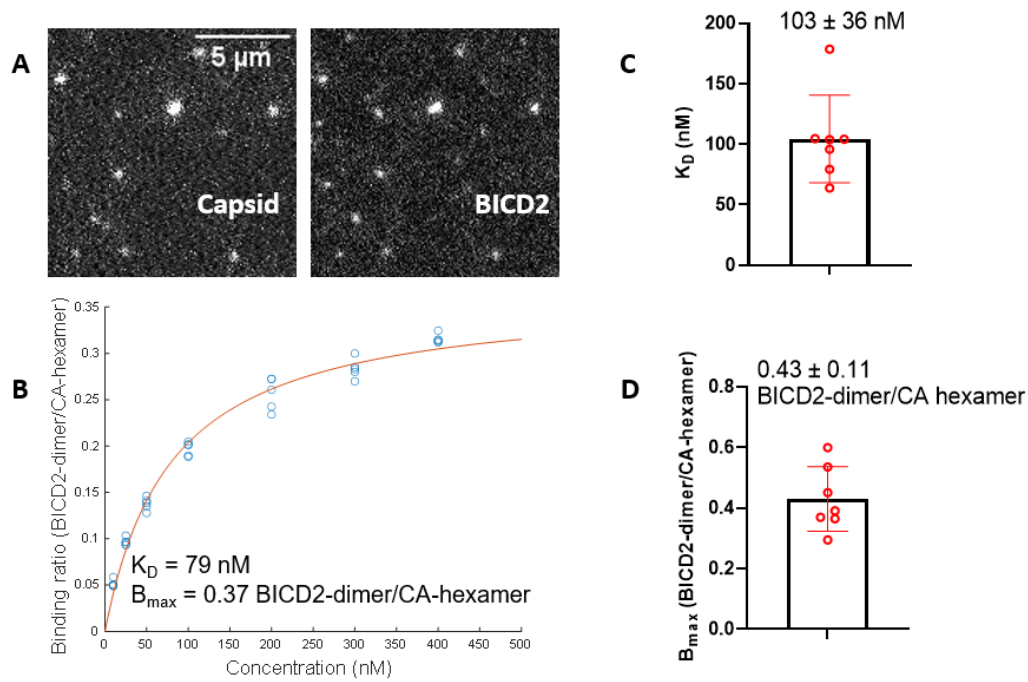


Fig.4.1. Quantitative analysis of BICD2-capsid interaction based on a TIRFm binding assay. A. Representative TIRFm image of the capsid channel (left) and the BICD2 channel (right). **B.** Representative equilibrium binding curve of the interaction between HIV-1 capsid and BICD2 determined by the TIRFm capsid binding assay. Each data point represents the average BICD2 dimer:CA hexamer binding ratio determined from a different field of view. **C-D.** Dissociation constant (K_D) (**C**) and maximum molar binding ratio (B_{max} , BICD2-dimer:CA-hexamer) (**D**) determined from fits of the equilibrium binding curves. Each red circle represents an individual repeat. K_D and B_{max} were estimated to be $103 \pm 36 \text{ nM}$ and $0.43 \pm 0.11 \text{ BICD2-dimer per CA-hexamer}$ (mean \pm SD, $n = 7$), respectively.

We then performed a titration assay by injecting solutions containing sfGFP-mBICD2 at a range of concentrations into a flow-channel while sequentially imaging the signals of capsid particles and bound sfGFP-mBICD2 after the injection of each concentration. The ratio of fluorescent intensity for each capsid particle to the intensity of bound sfGFP-mBICD2 was calculated and converted to a molar ratio (see **2.1.4**). The concentrations of sfGFP-mBICD2 were plotted against corresponding binding ratios to generate a binding curve (**Fig. 4.1.B**), which was then fitted with an equilibrium binding model to yield an estimation of K_D and B_{max} (**Fig. 4.1.B**). K_D and B_{max} were estimated to be 103 ± 36 nM (**Fig. 4.1.C**) and 0.43 ± 0.11 BICD2-dimer per CA-hexamer (**Fig. 4.1.D**), respectively, based on 7 independent repeats. The B_{max} could also be presented as 107 ± 27 BICD2 dimers per HIV-1 capsid, meaning that on average 107 ± 27 BICD2 could be bound to a single HIV-1 capsid at saturation.

4.2.2. BICD2 binds to HIV-1 capsid primarily via the R18 ring

As previously reported, the CC3 domain [52, 74], or both CC3 and CC1 domains [52], of BICD2 were responsible for the BICD2-capsid interaction. However, the motifs on HIV-1 capsid that mediate the interaction with BICD2 remain unknown. We investigated this question by testing whether any of the canonical binding interfaces of HIV-1 capsid (see **1.1.3.4**) are responsible for the BICD2-capsid interaction. The amino acid sequence of BICD2, similar to FEZ1 [73], contains multiple negatively charged aspartate and glutamate residues and several clusters of the negatively charged residues, raising the possibility that BICD2 binds to the positively charged R18 ring of HIV-1 capsid. To investigate this hypothesis, we compared the binding level of sfGFP-mBICD2 to HIV-1 capsid when the R18 ring was unaffected (capsid A92E/A204C), when the charged residues of this feature were disrupted by the mutation R18G (capsid R18G/A92E/A204C), or when the R18 ring binding pocket was occupied by other known R18 ring binders like hexacarboxybenzene and IP6 (**Fig. 4.2**). Two concentrations (500 nM and 15 nM) of sfGFP-mBICD2, which are ~ 5 folds higher or lower than the K_D , were examined. The level of BICD2 bound to capsid declined, but was not abolished, when the R18 ring was mutated (capsid R18G/A92E/A204C vs A92E/A204C). This observation was confirmed by the competition assay; while the levels of BICD2 associated with HIV-1 capsid decreased in the presence of an excess of hexacarboxybenzene or IP6, some binding was still detected (**Fig. 4.2**). Taken together, these observations suggested that BICD2 bound to HIV-1 capsid primarily, but not exclusively, via the R18 ring of HIV-1 capsid.

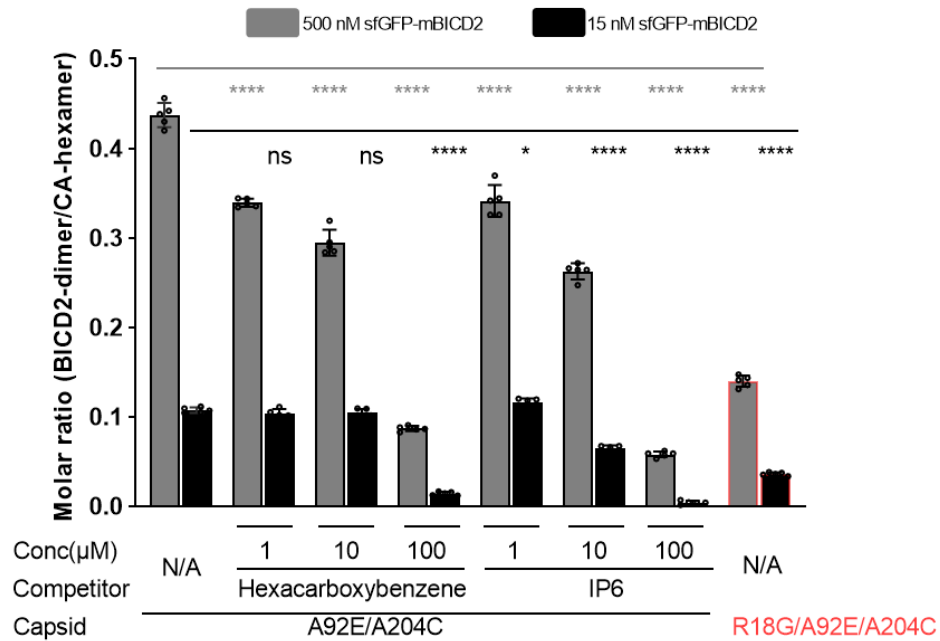


Fig. 4.2. BICD2 binds to HIV-1 capsid primarily, but not solely, via the R18 ring of capsid. Bar chart showing the decreased, but not abolished, binding of sfGFP-mBICD2 to HIV-1 capsid when the R18 ring was mutated (capsid R18G/A92E/A204C) or competed out by other known R18 ring binders (hexacarboxybenzene and IP6). Two concentrations (500 nM and 15 nM) of sfGFP-mBICD2, which are > 5 folds higher or lower than the K_D respectively, were examined and similar trends were observed. Each bar represented a particular assay condition and dots on the bar represent different fields of view from the TIRF binding assay. For both concentrations, the mutant condition and each competition condition were compared to the no-treatment condition using one-way ANOVA, Tukey's multiple comparisons test (****, $p < 0.0001$; *, $0.01 \leq p < 0.1$; ns, not significant, $p \geq 0.05$).

4.3. Reconstitution and visualization of the DDBC complex walking along microtubules

To investigate whether reconstituted DDBC complexes were able to walk along microtubules, it was essential to first isolate functional dynein and dynactin. As previously discussed, both dynein and dynactin are massive protein complexes comprising multiple subunits (~1.4 and 1.2 MDa respectively, see **1.3.1.1** and **1.3.1.2**). Schlager *et.al* established a protocol to recombinantly produce dynein [287], but there is currently no published method to recombinantly produce dynactin. As such, the conventional approach for these experiments is to isolate active complexes directly from brain tissue [334]. In short, dynein and dynactin were pulled out of brain lysate using a Strep-tagged N-terminal truncation fragment of murine BICD2 fused with sfGFP (sfGFP-mBICD2N) to form an active tripartite complex dynein-dynactin-mBICD2N (DDb). The DD complex (dynein-dynactin) could be separated from the complex later (see **2.5**) [262].

To confirm whether the isolated DD complex was still active, we measured the activities of DDb(pu) and DDb(rec) using TIRFm motility assays. DDb(pu) was the DDb complex pulled out of the brain lysate, while DDb(rec) was the DDb complex formed from sfGFP-mBICD2N and the isolated DD complex (see **2.5**, **2.6.1**, and **Fig. 2.5**). Both DDb(pu) and DDb(rec) showed processive movement along microtubules, as shown by the representative kymographs (**Fig. 4.3.A**, left for DDb(pu), right for DDb(rec)). These results confirmed that we were able to isolate functional DDb and DD complexes.

To fully reconstitute the dynein-dynactin-BICD2-capsid (DDBC) complex and examine its motility, functional dynein complex was purified as described above. It was combined with full-length, recombinant sfGFP-BICD2 and fluorescently labeled HIV-1 capsid. A representative example of active DDBC complex walking along a microtubule is shown (**Fig. 4.3.B**). The sample for this image contained 0.33 nM of AF647 labelled HIV-1 capsid (obtained from an assembly reaction containing 500 nM CA), 100 nM of sfGFP-mBICD2, and ~10 nM of isolated DD complex. The DDBC particle moved for 8 μ m in 60 s as evident from the co-migration of the diffraction-limited signals in the sfGFP-mBICD2 channel and the HIV-1 capsid (AF647 labelled) channel. In total, approximately 20 DDBC particles were observed moving along microtubules. Further optimization of the assay is needed before a more detailed description of this motile behaviour is possible. Nevertheless, these preliminary results are encouraging, and clearly demonstrate the feasibility of reconstituting and visualizing the transport of the DDBC complex along microtubules. Furthermore, this data supports

the proposed model in which interactions between the cargo adaptor BICD2 and HIV-1 capsid are sufficient to drive the assembly of an active dynein-motor complex.

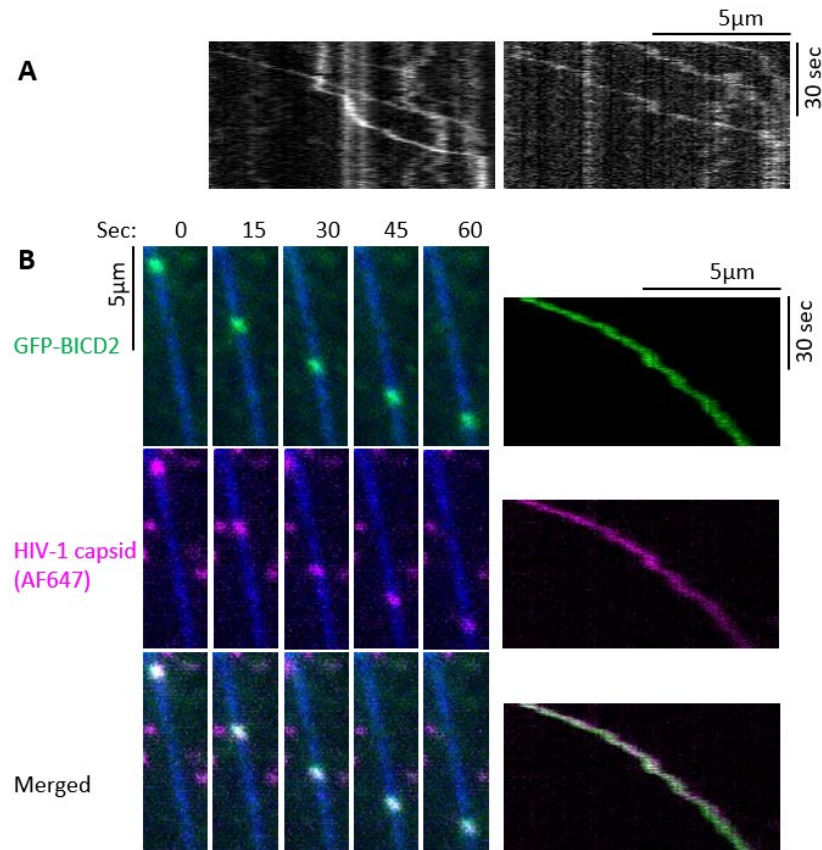


Fig. 4.3. Dynein-dependent transport of HIV-1 capsid: DDBC motility assay. **A.** Representative kymographs of DDb(pu) and DDb(rec) showing that the isolated DD complex is competent to further form active complexes. The signal represents sfGFP-BICD2N within the tripartite complex dynein-dynactin-BICD2N. **B.** Successive frames at time points 0/15/30/45/60 s showing a processive DDBC complex moving along a microtubule (blue). sfGFP-mBICD2 channel is colored in green while capsid (AF647 labelled) channel is colored magenta. BICD2 and HIV-1 capsid co-migrated with the DDBC complex for 8 µm in 60 s. Right: corresponding kymographs.

4.4. Discussion

The first aim of this chapter was to investigate the interaction between BICD2 and HIV-1 capsid. We have quantitatively measured the interactions (4.2.1) and demonstrated that the R18 ring of HIV-1 capsid is part of the binding motifs responsible for the interaction (4.2.2). However, our data suggested that BICD2 could also bind to other motifs of HIV-1 capsid apart from the R18 ring. Further investigations are needed to identify these additional motifs, which might be other canonical binding sites of HIV-1 capsid (CypA binding loop, FG-binding pocket, Tri-hexamer interface) or even unexplored sites.

The second aim of this study was to test the previously proposed model that interactions between HIV-1 capsid and BICD2 promote the assembly of an active DDBC complex. We demonstrated the dynein-dependent transport of HIV-1 capsid along microtubules, which confirmed the DDBC model suggested by recent studies. While it is exciting to demonstrate DDBC transport, rigorously characterization will need more data with better quality. Potential optimizations of the DDBC motility assay include: 1) improve the quality and increase the concentration of the DD complex isolated from brain tissue; 2) optimize the protocol for reconstituting of the DDBC complex and 3) optimize assay conditions of the motility assay for the DDBC complex.

While the DD complex was isolated from mouse brains (see 2.5) following an established protocol [262], performing the quality control for the purified complex was a challenge. Firstly, activity testing of the isolated DD complex required reconstituting the DDb(rec) or DDBC complexes for TIRFm motility assays. Secondly, it was unclear to what extent the activity of the DDb(rec) or DDBC complexes was affected by other factors, including the efficiency of the reconstitution and conditions of the motility assay. We also observed that the activity of the DDb(pu) complex was dependent on the freshness of the mouse brains. Therefore, the quality of the DD complex could potentially be improved by freezing brains as soon as possible after sacrificing the animal in future attempts. Another option is to scale up the protein isolation by using more brains, which would yield the DD complex at a higher concentration, which would increase the efficiency and flexibility for the reconstitution process downstream. Finally, we could consider recombinant methods to purify dynein [287] and dynactin (unpublished method from Carter lab and Musacchio lab), which could improve production compared to the conventional methods.

Another option is to optimize the protocol for DDBC reconstitution; the protocol (see **2.6.3**) employed here was limited by the concentration of the DD complex available. A comparison of the conditions for reconstituting the DDBC complex and the KFC complex () shows that the concentration of BICD2 (limited by the yields from the isolation procedure) was below the K_D of BICD2-capsid interaction (0.5-fold difference) while the concentration of FEZ1 was above the K_D of FEZ1-capsid interaction (13-fold difference) (Table **4.1**). Lastly, we can consider optimizing the buffer condition for the DDBC motility assay.

	DDBC	KFC
Concentration of motor (DD complex or Kif5B)	~10 nM	250 nM
Concentration of adaptor (BICD2 or FEZ1)	50 nM	250 nM
Capsid concentration (expressed as the CA monomer)	2 μ M	10 μ M
Molar ratio (motor:adaptor:CA-hexamer)	1:5:33	1:1:7
K_D of the adaptor:capsid interaction	104 \pm 34 nM	19 \pm 8 nM
Concentration of adaptor/ K_D	0.5	13

Table 4.1. Comparison of the concentrations of components used for reconstituting the DDBC and KFC complexes. The concentrations were chosen to maintain the molar ratio of the components (motor: adaptor: CA-hexamer) Concentrations of the components, molar ratios among the components, fold difference between the concentration of the adaptor (BICD2/FEZ1) and K_D of the adaptor-capsid interaction were indicated.

These potential optimizations should improve the efficiency and reproducibility of DDBC reconstitution to allow a systematic investigation of the behaviours of the DDBC complex. We can then further combine both the dynein- and kinesin-dependent transport of HIV-1 capsid to start investigating the bi-directional transport of HIV-1 capsid, thereby coming closer to reconstituting the interplay between motors that defines the transport of HIV-1 core *in vivo*.

Chapter 5

In vitro reconstitution of kinesin-dependent HIV-1 capsid transport

5. *In vitro* reconstitution of the kinesin-dependent HIV-1 capsid transport

5.1. Introduction

After cell entry, HIV-1 virus hijacks the microtubule network and motor protein complexes to facilitate transport to the nucleus. Multiple studies have shown that kinesin-1 is required for successful HIV-1 infection [53, 73, 75, 150, 186, 263], which seems contradictory to the fact that kinesin-1 conventionally transports cargoes away from the nucleus. However, early studies based on live cell imaging demonstrated that HIV-1 virus shows bi-directional movement in the cytoplasm during the early phase of infection, with an overall directionality toward the nucleus [51, 275], suggesting that kinesin also contributes to the overall transport of HIV-1 core. In fact, bi-directional cargo transport along microtubules is a common behavior of cellular organelles and vesicles [264, 335, 336] as well as viruses [337-339], because this is overall a more effective mechanism which allows error correction and overcomes crowdedness during cytoplasmic transport.

Similar to dynein dependent cargo transport, the formation of a processive kinesin motor complex also requires adaptor proteins. FEZ1 is a known kinesin adaptor [180-182] and has been shown to be involved in HIV-1 infection [183, 184] before Malikov *et al.* first reported that FEZ1 is the adaptor protein for the kinesin-dependent transport of the viral core [53]. This study demonstrated that FEZ1, kinesin-1, as well as the interaction between FEZ1 and kinesin-1, were all required for HIV-1 infection and the overall retrograde transport of the HIV-1 viral core based on cellular assays. This study provided the earliest evidence for a model that a kinesin-1, FEZ1, and HIV-1 capsid could form a complex for the cytoplasmic transport of the HIV-1 viral core. In a later study Malikov *et al.* further reported that kinesin-1 heavy chain, but not light chain, was responsible for the retrograde transport of HIV-1 core. [186] Both reports suggest that phosphorylation of FEZ1 at residue serine 58 is important for the formation of a kinesin-FEZ1-capsid complex, in line with previous reports that the interaction between FEZ1 and kinesin 1 is strictly dependent on this phosphorylation [182].

Huang *et al.* expanded upon these results, demonstrating that FEZ1 binds to HIV-1 capsid via the electrostatic interaction between R18 ring on capsid hexamer and negatively charged motifs on FEZ1 [73]. The authors proposed that a cluster of glutamic acid residues (aa182-186) form the primary HIV1-capsid-binding motif on FEZ1, based on observations that truncated forms of FEZ1 that include this region co-pellet with capsid in pull-down assays using assembled CA tubes, while truncations

excluding this region do not. Truncated FEZ1 containing this region are observed in co-elutes with CA hexamer but not CA assemblies resembling other canonical binding interfaces on capsid, suggesting that FEZ1 specifically binds to the R18 ring of CA hexamer. This study provided the earliest evidence for FEZ1-capsid interaction at a molecular level.

Taken together, these three studies proposed a model that kinesin-1 heavy chain, FEZ1, and HIV-1 capsid form a complex for the cytoplasmic transport of the HIV-1 viral core along microtubules. Out of the three isoforms of kinesin-1 (Kif5A, Kif5B, Kif5C), Kif5B is the most relevant because it has been reported to be involved in HIV-1 infection in multiple studies [53, 75, 150, 186]. The aim of this chapter is to reconstitute Kif5B-FEZ1-capsid complex *in vitro* and examine its motility along microtubules.

5.2. FEZ1 interacts with HIV-1 capsid

5.2.1. Quantitative analysis of the FEZ1-capsid interaction

We used the TIRFm-based capsid binding assay, similar to the capsid binding assay of BICD2 as described in Chapter 4, to quantitatively investigate the interaction between HIV-1 capsid and FEZ1. Immobilized HIV-1 capsid (see **2.4.1.1** A92E/A204C + K158C-AF647) was imaged using a 639 nm laser (**Fig. 5.1.A**, left) while sfGFP-FEZ1 was imaged using a 491 nm laser (**Fig. 5.1.A**, right). The colocalization between capsid and FEZ1 demonstrated that FEZ1 binds directly to HIV-1 capsid. We then performed and analyzed the titration binding assay to generate a K_D curve from which affinity and stoichiometry were calculated (**Fig. 5.1.B**). K_D (19 ± 4 nM (**Fig. 5.1.C**)) and B_{max} (0.38 ± 0.06 FEZ1 per CA-hexamer (**Fig. 5.1.D**)) were calculated from only 2 repeats. We also performed binding assays between sfGFP-FEZ1 and HIV-1 capsid assembled from CA A204C (**Fig. 5.1.E-G**), providing a value for K_D (70 ± 28 nM (**Fig. 5.1.F**)) and B_{max} (0.75 ± 0.15 FEZ1 per CA-hexamer (**Fig. 5.1.G**)), which were ~4-fold and 2-fold higher, respectively, than the values determined for CA A92E/A204C capsids. While capsid assembled from CA A204C or CA A92E/A204C showed differences in affinity and stoichiometry (**Fig. 8.3**), both binding assays clearly demonstrated that full-length sfGFP-FEZ1 directly binds to the cross-linked CA lattice with a higher affinity but lower stoichiometry than determined for the interaction between the minimal capsid-binding region of FEZ1 (residues 178-188) and cross-linked CA hexamers (K_D 190 ± 40 nM and B_{max} 1 ± 0.2 FEZ1 per CA-hexamer [73]). This

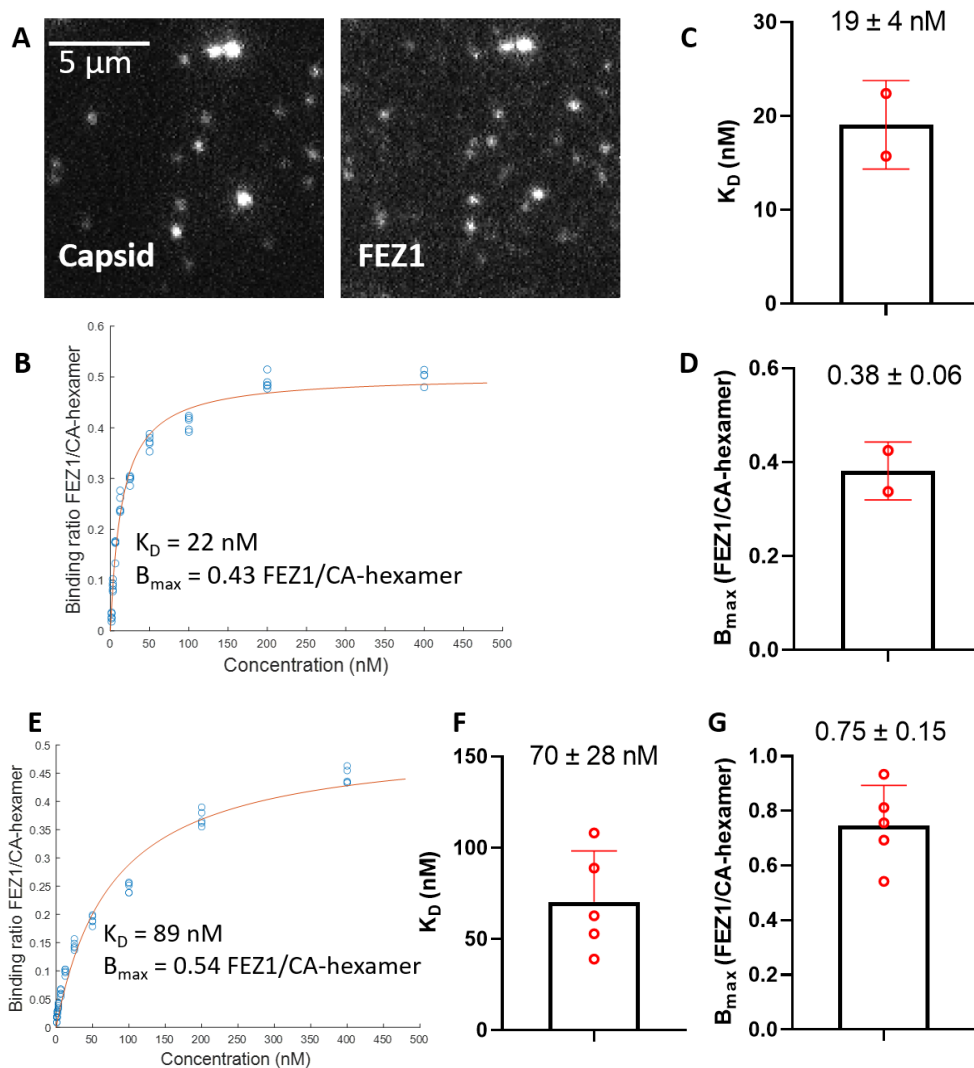


Fig. 5.1. Quantitative analysis of FEZ1-capsid interaction based on a TIRFm binding assay. A-D. Binding assays between sfGFP-FEZ1 and HIV-1 capsid assembly with CA A92E/A204C. **A.** Representative TIRFm image of capsid channel (left) and FEZ1 channel (right). **B.** Representative equilibrium binding curve of the interaction between HIV-1 capsid and FEZ1 determined by the TIRFm capsid binding assay. Various concentrations of sfGFP-FEZ1 (12-fold dilution series, 1.6–400 nM) **C-D.** Dissociation constant (K_D) (**C**) and maximum molar binding ratio (B_{max} , FEZ1:CA-hexamer) (**D**) determined from fits of equilibrium binding curves. Each red circle represents an individual repeat. K_D and B_{max} were calculated to be $19 \pm 4 \text{ nM}$ and $0.38 \pm 0.06 \text{ FEZ1 per CA-hexamer}$ (mean \pm SD, $n = 2$), respectively. B_{max} corresponds to $95 \pm 15 \text{ FEZ1 per capsid}$ **E-G.** Summary of binding assay between sfGFP-FEZ1 and HIV-1 capsid assembled with CA A204C.

difference is consistent with the proposed multivalent interaction between negatively charged regions of full-length FEZ1 and the R18 pores of multiple hexamers of the capsid [73].

5.2.2. FEZ1 binds to HIV-1 capsid primarily via the R18 ring

As previously reported, FEZ1 binds to the R18 ring of HIV-1 hexamer [73]. We confirmed this result based on the observation that FEZ1 binding to HIV-1 capsid decreased in the presence of excessive hexacarboxybenzene, a known R18 ring binder (**Fig. 5.2**). However, we noticed that FEZ1 binding was not abolished even in presence of excessive HCB competition, as shown in the bar chart (**Fig. 5.2.A**) and illustrative TIRFm images (**Fig. 5.2.B**). These observations implied that, similar to BICD2, FEZ1 binds to HIV-1 capsid primarily, but not exclusively, via the R18 ring of HIV-1 capsid. Due to background binding issues in subsequent experiments, we were unable to generate more data to confirm these observations by either competition or mutation of R18 ring in the FEZ1-capsid TIRFm binding assay.

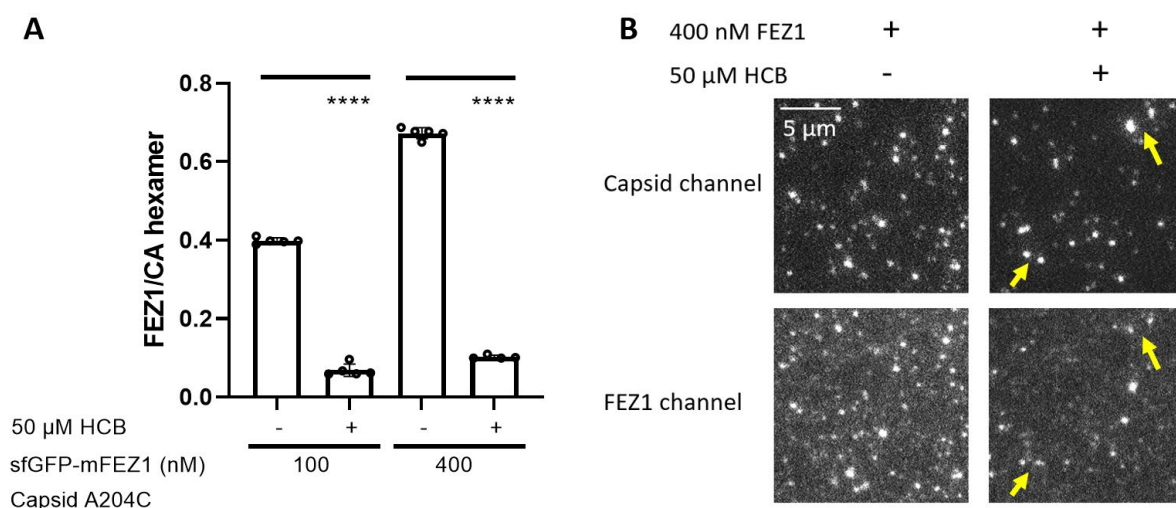


Fig. 5.2. FEZ1 binds to HIV-1 capsid primarily, but not exclusively, via the R18 ring. **A.** Bar chart showing the decreased, level of sfGFP-FEZ1 binding to HIV-1 capsid when the R18 ring was occupied by the known R18 ring binder hexacarboxybenzene (HCB). Each bar represented a particular assay condition and dots on the bar represent different fields of interest from the assay condition (****, $p < 0.0001$; one-way ANOVA, Tukey's multiple comparisons test). **B.** Illustrative TIRFm images showing FEZ1-capsid interaction in the absence (left) and presence (right) of excessive HCB competition. In comparison, the level of FEZ1 binding largely decreased while residual binding could still be observed (yellow arrows).

5.3. Reconstitution and visualization of the KFC complex walking along microtubules

To reconstitute the KFC (Kif5B-FEZ1-capsid) complex, we combined Kif5B, FEZ1, and pre-assembled HIV-1 capsid as a mixture in buffer M (see 2.1.5). The mixture was subsequently examined in motility assays to investigate whether the reconstituted KFC complexes were able to walk along microtubules. Given that a KFC complex is comprised of 3 components (Kif5B, FEZ1, and capsid), two considerations immediately came to mind. First, what are the optimal set of concentrations and molar ratios of the individual components to efficiently reconstitute the KFC complex? Second, because fluorescent microtubules occupy one channel out of the three-color TRIFm system only two channels remain available. Which component(s) of the KFC complex should be fluorescent -i.e, what color combinations of KFC should we examine?

We first examined this question using a KFC combination made up of dark Kif5B, sfGFP-FEZ1 and AF647 labelled HIV-1 capsid (see 5.3.1). We initially focused on this permutation because we had previously demonstrated the interaction between sfGFP-FEZ1 and AF647 labelled HIV-1 capsid (see 5.2). After successfully demonstrating the motility of this KFC combination, we subsequently investigated other KFC combinations to better understand the properties of the KFC complex (see 5.3.1-5.3.2).

To find an optimal condition, we tested the KFC reconstitution at various concentrations and molar ratios of the components while evaluating the frequency of KFC walking events (data not shown). **Table 5.1** describes the condition that yielded the best results; the KFC complex was reconstituted at high concentrations of the components (250 nM Kif5B, 250 nM FEZ1, and pre-assembled HIV-1 capsid containing 10 μ M of CA monomer) for 3 h and the sample was then diluted and added to surface-bound microtubules on a microscope coverslip for image acquisition in the motility assay. In this mixture, the molar ratio of Kif5B:FEZ1:CA-hexamer was 1:1:6.7. Compared to the calculated K_D and B_{max} between FEZ1 and HIV-1 capsid (19 ± 4 nM and 1 FEZ1 per 2-3 hexamers, see 5.2), the concentrations of the components were above the K_D of the FEZ1-capsid interaction but FEZ1 was substoichiometric relative to the number of binding sites on the capsid. The sample was diluted 100-fold to 1000-fold before image acquisition to achieve a sufficiently low surface density of complexes that allows for the imaging of single motor complexes. This sample preparation approach was used for all the KFC combinations examined in following sections (see 5.3.1-5.3.2).

	[Kif5B-dimer]/nM	[FEZ1]/nM	Capsid	
			[CA]/ μ M	[Capsid particle]/nM
Sample (KFC)	250	250	10	6.7
1:100 dilution	2.5	2.5	0.1	6.7E-02
1:250 dilution	1	1	0.04	2.7E-02
1:500 dilution	0.5	0.5	0.02	1.3E-02
1:1000 dilution	0.25	0.25	0.01	6.7E-03

Table 5.1. Sample preparation for KFC complex reconstitution and KFC motility assay. 250 nM Kif5B, 250 nM FEZ1, and pre-assembled HIV-1 capsid containing 10 μ M of CA monomer were mixed and incubated in the motility buffer (see **2.1.5**) for the formation of the KFC complex. The sample was diluted 100-fold to 1000-fold prior image acquisition for the KFC motility assay and the theoretical concentrations of the components were specified. In most cases, the motility assays were performed using samples at 500-fold or 1000-fold dilution to avoid overcrowding of particles on the surface. The KFC complexes were apparently sufficiently long-lived such that intact complexes were observed to bind to microtubules after dilution.

5.3.1. Reconstitution of KFC motility

We first examined the KFC combination comprising dark Kif5B, sfGFP-FEZ1 and AF647-labelled HIV-1 capsid. Selected frames from a TIRF movie of KFC particles walking along microtubules are shown in **Fig. 5.3.A**. There were two KFC particles that showed almost overlapping trajectories in the movie while their movements were only distinguishable at certain time points (e.g., time points 60 and 80 second). One of the KFC particles contained a brighter capsid signal (time points 60 s and 80 s), consistent with a larger capsid (or aggregate of more than one capsid). The KFC particle with the brighter capsid walked for around 10 μ m in 73 s (8–81 s) with a pause of 12 s (62–74 s, top white arrow in the kymograph) in middle of the run. The KFC particle with the dimmer capsid walked for around 11 μ m in 103 s (1–104 s) with a pause of 6 s (78–84 s, bottom white arrow in the kymograph) in middle of the run. Both particles reached the end of the microtubule before the movie ended and still stayed associated with the microtubule when the movie ended, with FEZ1 and HIV-1 capsid

exhibited clear co-migration. (**Fig. 5.3.A**). Motile behavior made up of both walking and pause phases was frequently observed for processive KFC particles.

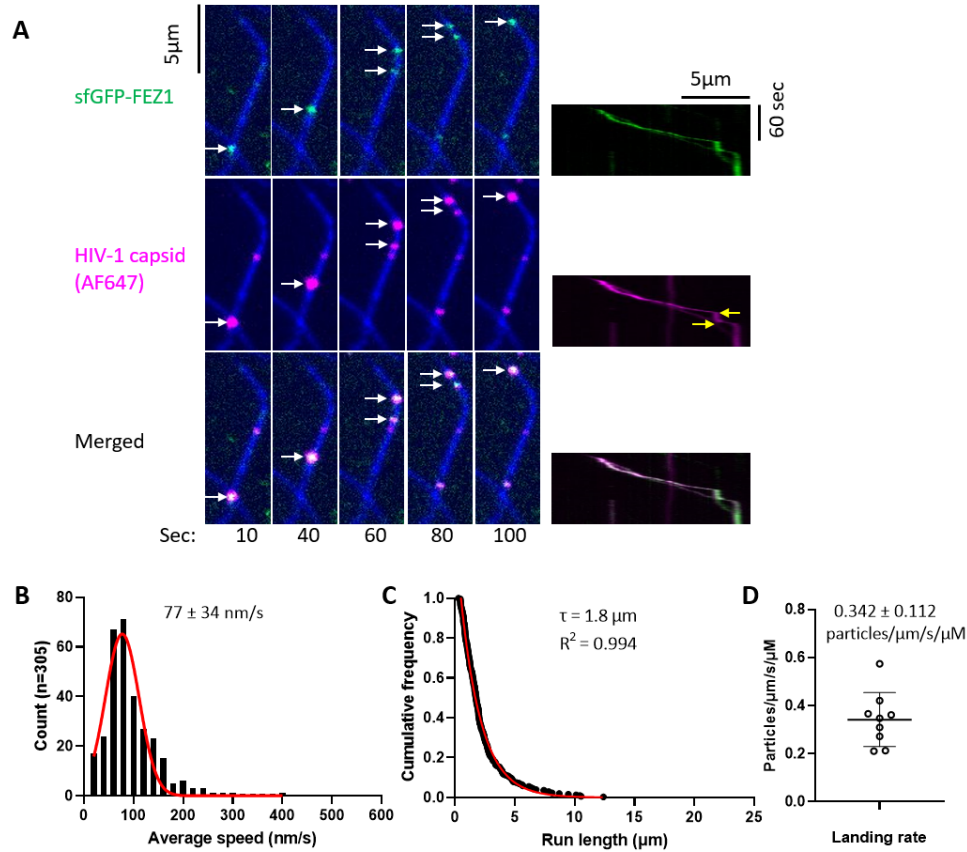


Fig. 5.3. Kinesin (Kif5B)-dependent transport of HIV-1 capsid: KFC combination with dark Kif5B, sfGFP-FEZ1 and AF647-labelled HIV-1 capsid. A. Movie frames showing two processive KFC particles moving along a microtubule (blue). The sfGFP-FEZ1 channel is colored in green while the capsid channel is colored in magenta. The two walking particles mostly co-migrated and were only distinguishable at certain time points (e.g., 60 s and 80 s). Right: Corresponding kymograph of the KFC particles. **B-D.** Statistical analysis of the speed (**B**), run length (**C**), and landing rate (**D**) of the processive KFC particles based on 305 processive KFC particles from 9 image stacks.

To detect and analyze all the processive KFC particles in an image stack, we established a semi-automated approach (see **2.1.7** and **8.4**) which employed Trackmate, an Image J single particle tracking plugin [326], to generate trajectories for all motile capsid particles based on user-defined

parameters and manual filtering. The trajectories of particle positions (X-Y coordinates) generated in Trackmate were then further analysed using a home-written MATLAB script to detect walking and pausing phases and calculate average speed, run length, and landing rate of moving KFC particles. The average speed was calculated to be 77 ± 34 nm/s (mean \pm SD) based on a histogram analysis with a Gaussian fit (**Fig. 5.3.B**). Run length (τ) was calculated to be $1.8 \mu\text{m}$ based on a cumulative frequency distribution analysis followed by a one-phase exponential decay fit (**Fig. 5.3.C**). Both average speed and run length were calculated based on 305 processive KFC particles from 9 image stacks. For each independent image stack, the landing rate was calculated by dividing the total number of processive KFC particles against the total length of microtubules, time, and concentration of Kif5B. Based on the 9 image stacks, landing rate was calculated to be 0.342 ± 0.112 particles/ $\mu\text{m/s}/\mu\text{M}$ (**Fig. 5.3.D**). Preliminary data suggested that no processive KFC particles could be detected when any of the components (Kif5B, FEZ1, capsid) were excluded during the KFC reconstitution (data not shown), suggesting that Kif5B-FEZ1-capsid serves as the minimum requirement for the formation of a processive KFC complex.

To test whether the GFP tag of FEZ1 affected motility, we examined two additional KFC combinations comprising dark Kif5B, dark FEZ1, and HIV-1 capsid labelled with either AF647 (**Fig. 5.4.A-D**, 943 processive KFC particles from 9 image stacks) or AF488 (**Fig. 5.4.E-H**, 975 processive KFC particles from 16 image stacks). The average speed (AF647: 80 ± 37 nm/s; AF488: 71 ± 47 nm/s), run length (AF647: $2 \mu\text{m}$; AF488: $1.8 \mu\text{m}$), and landing rate (AF647: 0.578 ± 0.474 particles/ $\mu\text{m/s}/\mu\text{M}$; AF488: 0.288 ± 0.188 particles/ $\mu\text{m/s}/\mu\text{M}$) were essentially the same as for the KFC combination with sfGFP-tagged FEZ1 examined above (**Fig. 5.3.B-D**), indicating that neither the GFP tag of FEZ1 nor the different fluorescent labels (AF647 vs AF488) of HIV-1 capsid introduced artefacts to the KFC motility assay. A detailed comparison among different KFC combinations is discussed in a later section (see **5.3.3**).

Finally, we reconstituted a KFC combination containing fluorescence labels on capsid and Kif5B to directly observe the co-migration of Kif5B and HIV-1 capsid. To prepare fluorescent Kif5B, we labeled Kif5B either via lysine residues using an ATTO 643 NHS-ester dye or via cysteine residues using an Alexa Fluor 647 C2 maleimide dye. Both versions of fluorescent Kif5B performed similarly in the KFC motility assays (data not shown). We then examined the KFC combination comprising AF647-

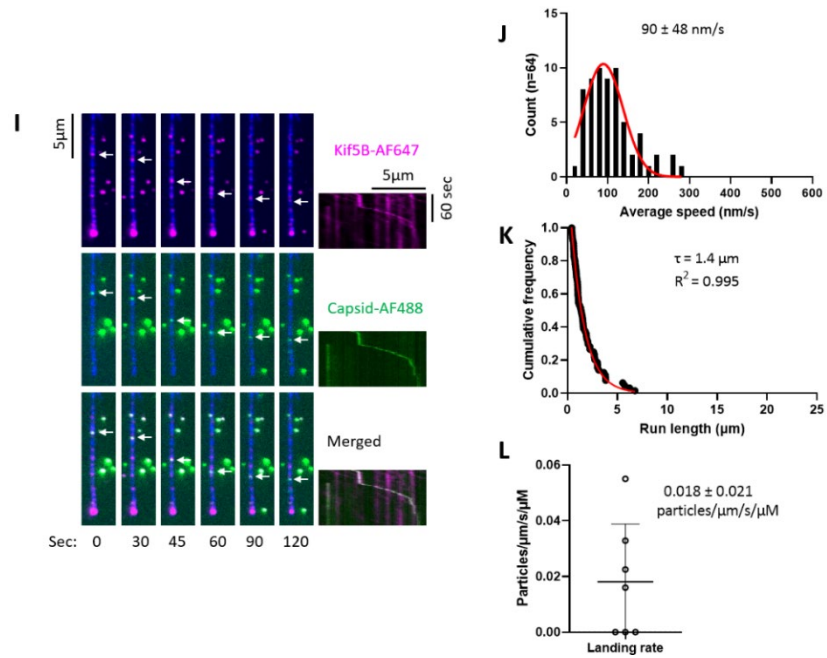
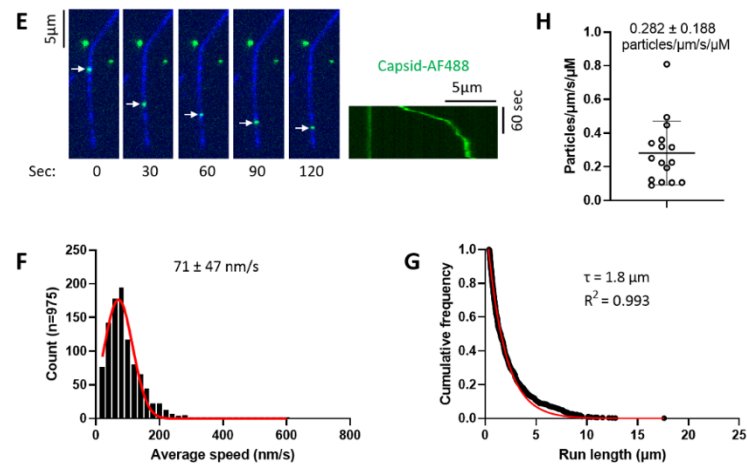
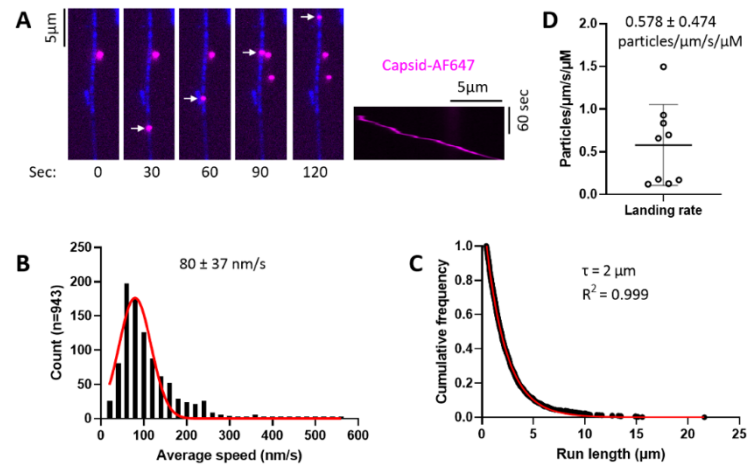


Fig. 5.4. KFC motility assays of additional KFC combinations. **A-D.** Representative frames and kymograph (**A**), average speed (**B**), run length (**C**) and landing rate (**D**) of the KFC combination comprising dark Kif5B, dark FEZ1 and AF647-labelled HIV-1 capsid. In total, 943 processive KFC particles from 9 image stacks were analyzed. **E-H.** Representative frames and kymograph (**E**), average speed (**F**), run length (**G**) and landing rate (**H**) of the KFC combination comprising dark Kif5B, dark FEZ1 and AF488-labelled HIV-1 capsid. In total, 975 processive KFC particles from 16 image stacks were analyzed. **I-L.** Representative frames and kymograph (**I**), average speed (**J**), run length (**K**) and landing rate (**L**) of the KFC combination comprising AF647-labelled Kif5B, dark FEZ1 and AF488-labelled HIV-1 capsid. In total, 64 processive KFC particles from 8 image stacks were analyzed. In the representative images (**A**, **E**, **I**), the microtubule channel is shown in blue while the color of capsid channel and Kif5B (if applicable) are indicated by the colors of the corresponding text next to the kymographs.

labelled Kif5B (labelled via cysteines), dark FEZ1 and AF488-labelled HIV-1 capsid in more detail (**Fig. 5.4.I-L**). Selected frames from an example image stack of a KFC particle walking along a microtubule is shown in **Fig. 5.4.I** with white arrows indicating the positions of the KFC particle, demonstrating a clear co-migration of Kif5B and HIV-1 capsid. This KFC particle contained ~ 25 Kif5B dimers and a HIV-1 capsid with ~ 400 CA molecules as quantified by normalizing the particle intensity against single-molecule intensities of Kif5B and CA, respectively. This observation suggests that a single capsid (cargo) can recruit multiple motors, as expected for the multiple binding sites on the CA lattice, whereby not all of the associated Kif5B molecules would engage with the microtubule at the same time. The average speed, run length, and landing rate (**Fig. 5.4.J-K**) were calculated based on only 64 processive KFC particles from 7 image stacks. Whilst the average speed of KFC complexes with labelled (90 ± 48 nm/s) and dark Kif5B (71 ± 47 nm/s) were similar, we noticed a >10-fold decrease in landing rate (0.018 ± 0.021 particles/ μ m/s/ μ M versus 0.282 ± 0.188 particles/ μ m/s/ μ M). The decrease in landing rate suggested that AF647-labelled Kif5B was attenuated in forming processive KFC complexes. One possible explanation was that the modifications of certain cysteine residues affected the structure of Kif5B, thereby disrupting its ability to form active complexes. We did not further investigate the fluorescently labelled Kif5B because of this defect. However, the observation that we can directly detect capsids walking along microtubules in conjunction with

kinesin is nevertheless an important result which confirms that a processive KFC complex is indeed formed and all the components (Kif5B, FEZ1, capsid) co-migrate to contribute to the processivity of the KFC complex.

5.3.2. The R18 ring of HIV-1 capsid is required to form a processive KFC complex

We previously showed that FEZ1 interacts with the HIV-1 capsid primarily, but not exclusively, via the R18 ring of HIV-1 capsid (see **5.2.2**). Having successfully demonstrated the motility of the KFC complex, we asked whether the residual level of FEZ1-capsid interaction would be sufficient to promote the formation a processive KFC complex. To investigate this question, we reconstituted KFC complexes with HIV-1 capsid bearing the R18G mutation (capsid assembled from CA R18G/A92E/A204C, see **2.2.4.1**). We examined the following three KFC combinations: 1) dark Kif5B, dark FEZ1, with AF488-labelled HIV-1 capsid-R18G (**Fig.5.5.A-D**); 2) dark Kif5B, dark FEZ1, with AF647-labelled HIV-1 capsid-R18G (**Fig.5.5.E-H**); 3) dark Kif5B, sfGFP-FEZ1, with AF647-labelled HIV-1 capsid-R18G (**Fig.5.5.I-L**).

In all three combinations, capsids bearing the R18G mutation strongly reduced the efficiency of forming a processive complex. For example, only 68 processive particles out of 7 image stacks were observed for the KFC combination comprising dark Kif5B, dark FEZ1 and AF488-labelled HIV-1 capsids with R18G mutation (**Fig 5.5.A-D**). This was reflected in a ~20-fold reduction in the landing rate compared to wild type capsids. We further observed a modest (2–3-fold) reduction in run length, suggesting that these complexes might be less stable. However, the average speed was essentially the same for KFC complexes formed with R18G or wild type capsids. These observations indicate that a processive KFC particle containing HIV-1 capsid with R18G is less likely to form, although it could still walk along microtubule at an unaffected speed once it is formed. Similar trends were observed when comparing the other two KFC combinations with their corresponding KFC combinations containing HIV-1 capsid bearing wild-type R18 ring (**Fig. 5.5.E-H** and **Fig. 5.5.I-L**). A detailed comparison among different KFC combinations is discussed below.

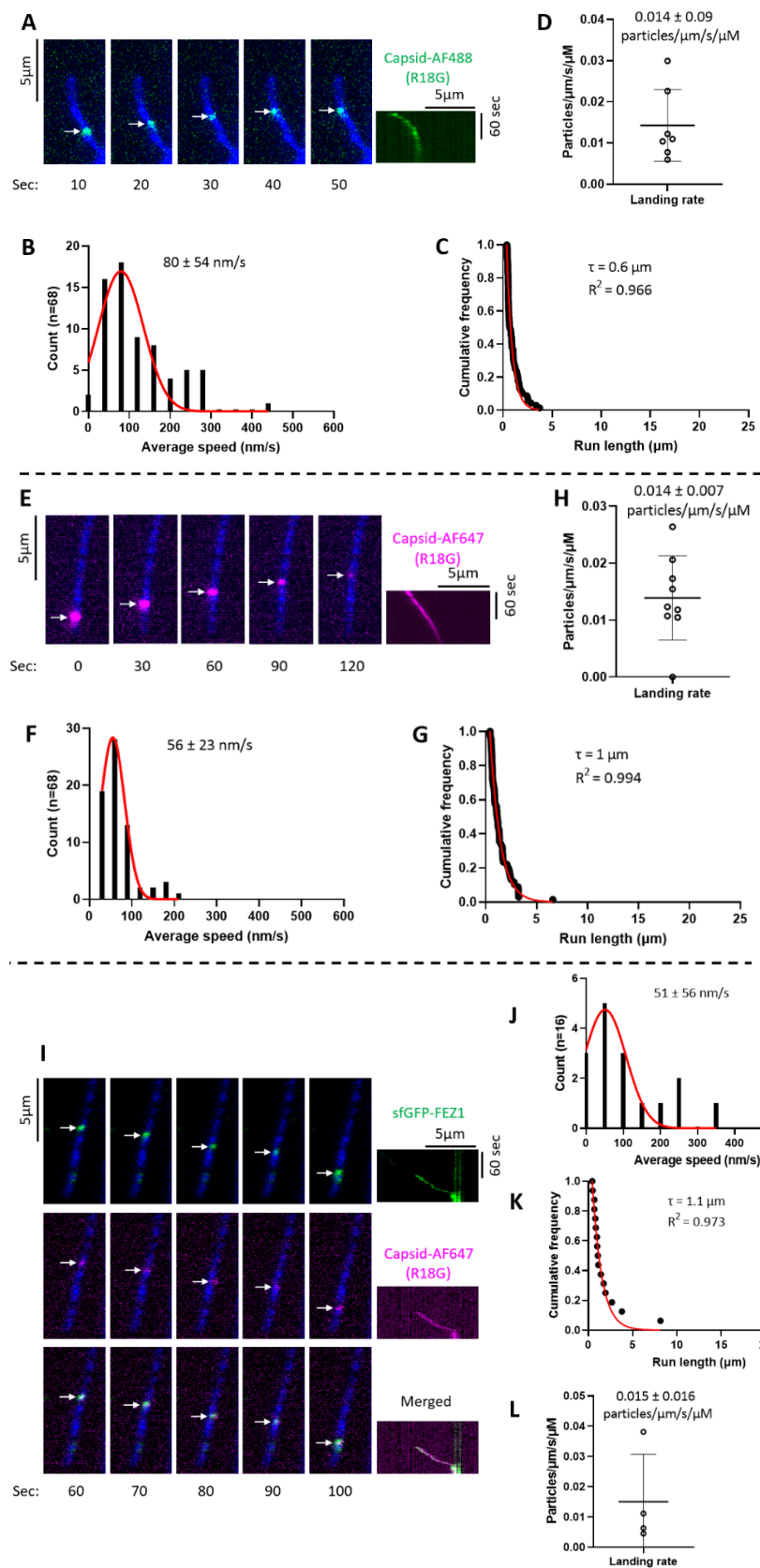


Fig. 5.5. KFC motility assays of KFC combinations containing HIV-1 capsid lacking the R18 ring. A-D. Representative frames and kymograph (A), average speed (B), run length (C) and landing rate (D) of the KFC combination comprising dark Kif5B, dark FEZ1 and AF488-labelled HIV-1 capsid-R18G. In total, 68 processive KFC particles from 7 image stacks were analyzed. **E-H.** Representative frames and kymograph (E), average speed (F), run length (G) and landing rate (H) of the KFC combination comprising dark Kif5B, dark FEZ1 and AF647 labelled HIV-1 capsid-R18G. In total, only 68 processive KFC particles from 9 image stacks were analyzed. **I-L.** Representative frames and kymograph (I), average speed (B), run length (K) and landing rate (L) of the KFC combination comprising dark Kif5B, sfGFP-FEZ1 and AF488-labelled HIV-1 capsid-R18G. In total, only 16 processive KFC particles from 4 image stacks were analyzed. In the representative images (A, E, I), the microtubule channel is shown in blue while the color of capsid channel and Kif5B (if applicable) are indicated by the colors of the corresponding text next to the kymographs.

5.3.3. Effects of fluorescent labels and the CA R18G mutation on motility parameters

This section summarizes the average speed, run length, and landing rate of KFC complexes with the different compositions examined in this thesis (**Table 5.2**). This analysis is then extended to a comparison of the following three groups obtained by combining data from complexes with similar composition: (1) dark Kif5B + FEZ1 (GFP label or dark) + wild type capsid (AF488 or AF647 label); (2) AF647-labelled Kif5B + dark FEZ1 + wild type capsid (AF488 label); (3) dark Kif5B + FEZ1 (GFP label or dark) + R18G capsid (AF488 or AF647 label).

KFC combination	Abbreviation	Abbreviation (combined experiments)	
Dark Kif5B + sfGFP-FEZ1 + AF647-labelled capsid (5.3.1)	K-dark_F-gfp_C-647		K-dark_F_C
Dark Kif5B + dark FEZ1 + AF647-labelled capsid (5.3.1)	K-dark_F-dark_C-647	K-dark_F-dark_C	
Dark Kif5B + dark FEZ1 + AF488-labelled capsid (5.3.1)	K-dark_F-dark_C-488		

AF647 labelled Kif5B + dark FEZ1 + AF488-labelled capsid (5.3.1)	K-647_F-dark_C-488		K-647_F_C
Dark Kif5B + dark FEZ1 + AF488-labelled capsid R18G (5.3.2)	K-dark_F-dark_C-r18g-488	K-dark_F-dark_C-r18g	K-dark_F_C-r18g
Dark Kif5B + dark FEZ1 + AF647-labelled capsid R18G (5.3.2)	K-dark_F-dark_C-r18g-647		
Dark Kif5B + sfGFP-FEZ1 + AF647-labelled capsid R18G (5.3.2)	K-dark_F-gfp_C-r18g-647		

Table 5.2. Summary of the KFC combinations examined in sections 5.3.1-5.3.2.

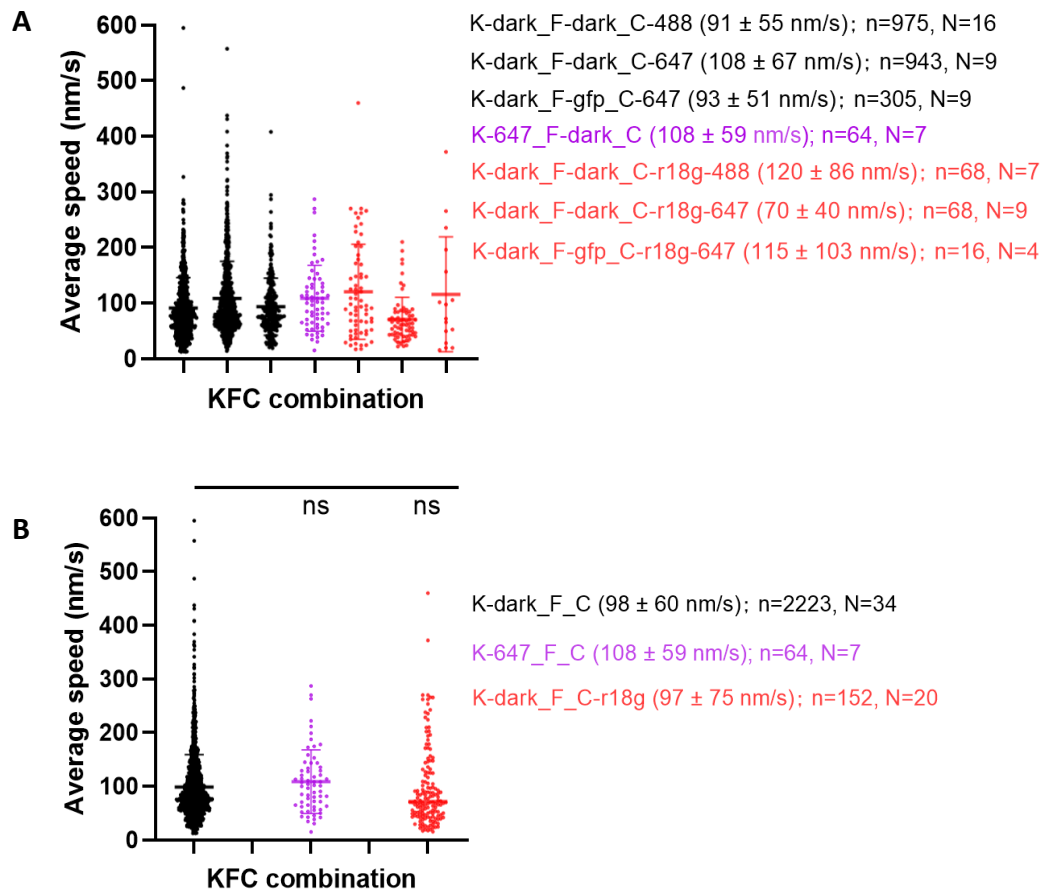


Fig. 5.6. Average speed comparison of the KFC combinations. Legend entries from top to bottom correspond to the data sets from left to right. Legend indicates the KFC combination and its average speed (mean \pm SD). “n” and “N” represents number of KFC particles and number of independent image stacks for the analysis. Each dot in the bar represents a KFC particle. Different groups were tested by One-way ANOVA, Tukey’s multiple comparisons. **A.** Comparison of average speed of all the KFC combinations examined in sections 5.3.1-5.3.2. **B.** Comparison after combining the data from complexes with similar composition (ns, not significant, $p>0.05$).

The average speed of all complexes with different compositions were within less than a factor of 2 of each other (**Fig. 5.6.A**), and there were no statistically significant differences between the three groups (**Fig. 5.6.B**). These data suggest that neither the GFP tag on FEZ1, the type of fluorescent labelling of capsid, the fluorescent labelling of Kif5B, nor the R18G mutation on HIV-1 capsid affected the speed of a processive KFC complex once it is formed.

We next compared run lengths of the different KFC complexes. Neither the GFP tag on FEZ1 nor the different fluorescent labelling of capsid affected the run length of KFC particles (**Fig. 5.7, C vs B vs A**). In contrast, KFC combinations containing the R18G mutant showed shorter run lengths compared to similar KFC combinations containing capsid with a wild-type R18 ring (**Fig. 5.7, D vs A, E vs B, F vs C**). This difference is also apparent when we combine the data sets of the complexes with wild type capsid (**Fig. 5.7.H**) or R18G capsid (**Fig. 5.7.I**). Finally, the KFC combination containing AF647 labelled Kif5B showed shorter (by ~20%) run length compared to complexes containing dark Kif5B (**Fig. 5.7, G vs A**), suggesting that the fluorescent labelling of Kif5B might inhibit the processivity of KFC complexes. However, more data of this KFC complex with labelled Kif5B (K-647_F-dark_C-488, **Fig. 5.7.G**, 64 particles) is needed for a more robust comparison. Overall, we conclude that: (1) neither the GFP tag on FEZ1 nor the different fluorescent labelling of capsid introduced noticeable artefacts to the processivity of the KFC complexes; (2) the R18 ring on HIV-1 capsid is an important feature for the processivity of KFC complexes; (3) fluorescent labelling of Kif5B at random cysteine residues might lead to a mild inhibition of the KFC complex processivity.

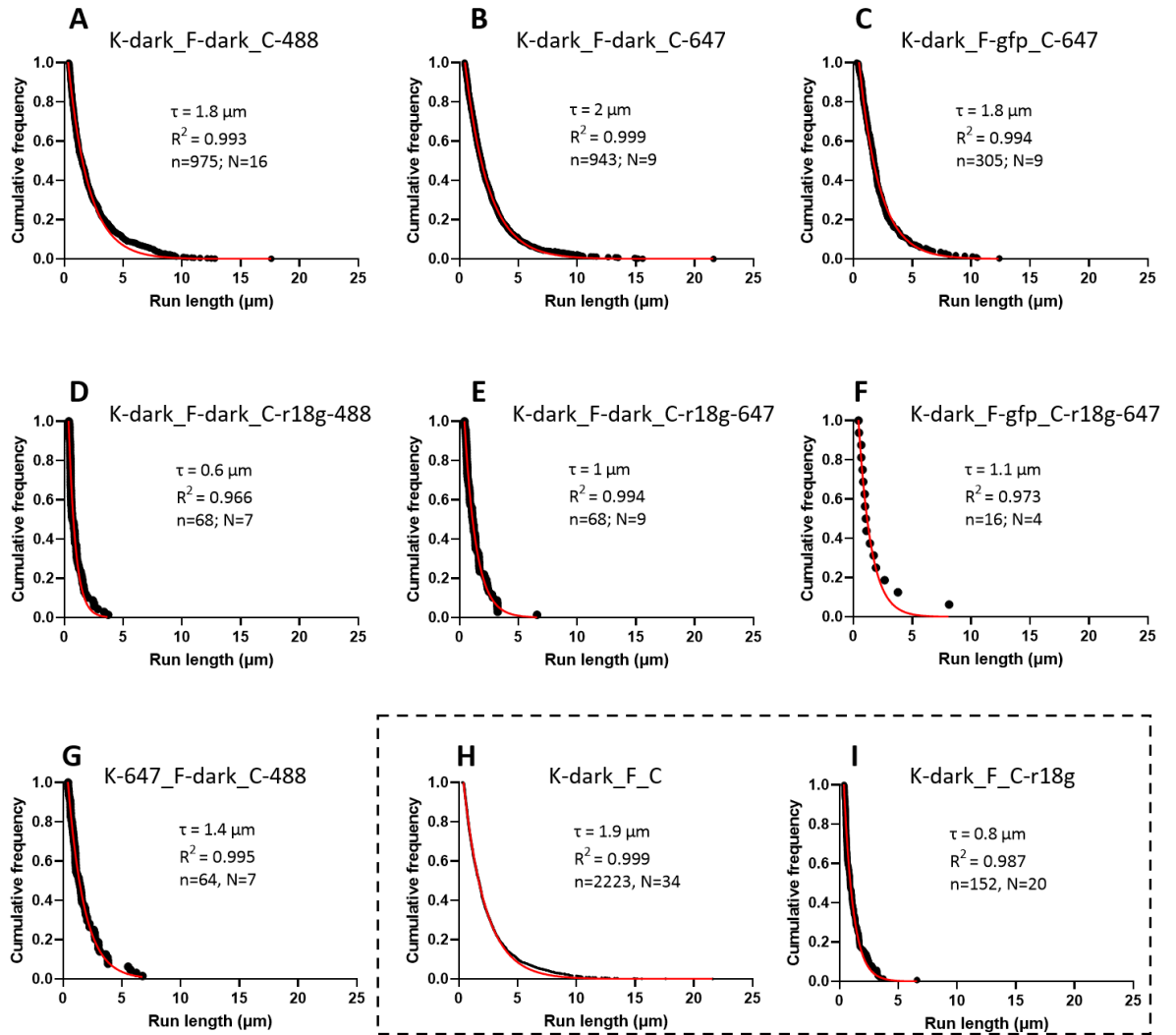


Fig. 5.7. Run length comparison of the KFC combinations. Each panel represents the run length distribution of the corresponding KFC complex as indicated. Run length (τ , decay constant) and R^2 are shown. “n” and “N” represents the number of KFC particles and the number of independent image stacks, respectively. Data from **A-C** were combined to yield the distribution in **H**, **D-F** were combined to yield the distribution in **I**.

Finally, we compared landing rates of the different KFC complexes to determine whether their composition would affect the probability of forming functional (processive) complexes. Neither the GFP tag on FEZ1 nor the difference in the fluorescent labelling of capsid affected the landing rate of processive KFC particles (**Fig. 5.8.A**). In contrast, KFC complexes containing R18G capsids exhibited

a decreased landing rate compared to similar KFC combinations containing capsid with wild-type R18 ring (**Fig. 5.8.A**, red data sets vs black data sets). Overall, the landing rate decreased by ~27-fold when comparing combined data sets of wild type or R18G capsids (**Fig. 5.8.B**). Similarly, the KFC complex containing AF647-labelled Kif5B showed >20 folds lower landing rate compared to similar KFC complexes containing dark Kif5B (**Fig. 5.8.A**, K-647_F-dark_C-488 vs K-dark_F-dark_C-488), suggesting that the fluorescent labelling of Kif5B affected the formation of processive KFC complexes, e.g., because of the reduced motor-adaptor/cargo interaction, and/or inactivation of the motor, and/or motor aggregation as a result of modification of functionally important cysteine residues.

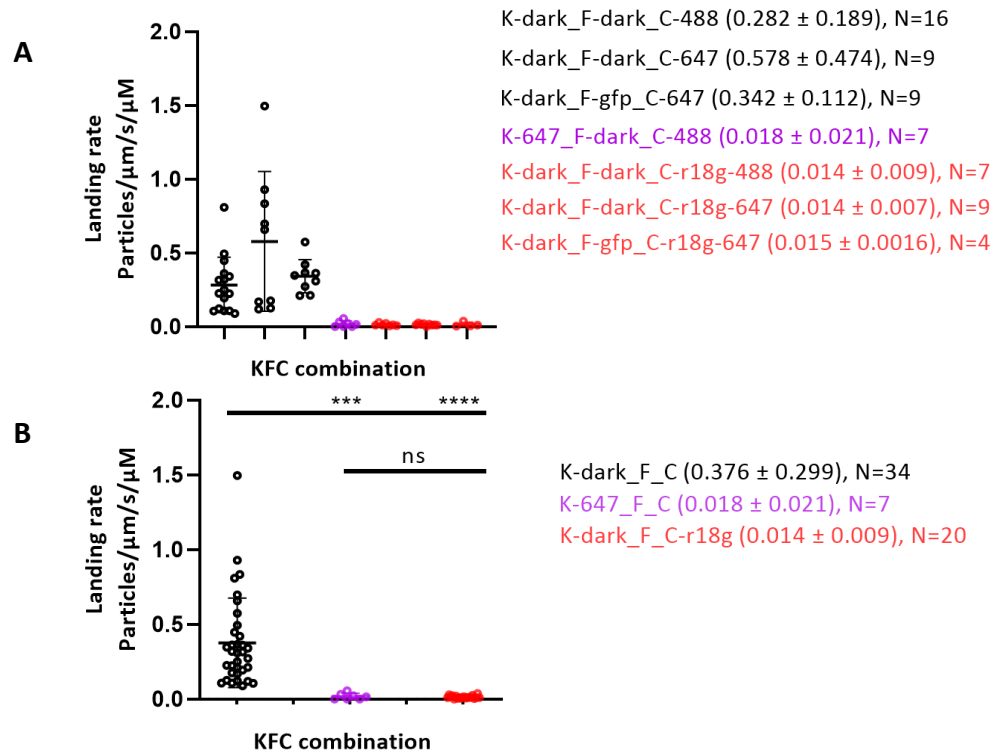


Fig. 5.8. Landing rate comparison of the KFC combinations. Legend entries from top to bottom correspond to the data sets from left to right. Legend indicates the KFC complex composition and corresponding landing rate (mean \pm SD). “N” represents the number of independent image stacks for the analysis. Different groups were tested by One-way ANOVA with Tukey’s multiple comparisons. **A.** Landing rate comparison of all the KFC combinations examined in sections 5.3.1-5.3.2 (see **Table 8.1** for statistical tests). **B.** Landing rate comparison of the combined data for KFC complexes.

Taken together, this analysis leads to the following conclusions. First, neither the GFP tag on FEZ1 nor the fluorescent labelling of capsid introduced artefacts in the KFC motility assay. This ability to label different components allows for flexibility in experimental design. In contrast, labelling of Kif5B with reactive derivatives of fluorophores, can lead to inactivation and/or interfere with complex formation as reflected by significantly lower landing rate. Second, disruption of the R18 ring leads to major defects in the formation of processive KFC complexes, as evidenced by a significantly lower landing rate and shorter run length. This is consistent with the observation that the R18 ring is required for FEZ1-capsid interaction. Finally, whilst certain features (e.g., R18G mutation of HIV-1 capsid or fluorescent labelling of Kif5B) reduce the efficiency of forming processive KFC complexes, they do not affect the speed of the KFC complex once it is formed.

5.4. HIV-1 capsid is a passenger of the Kif5B-FEZ1 complex

While analyzing the KFC complexes comprising dark Kif5B, sfGFP-FEZ1 and AF647-labelled HIV-1 capsid, we noticed a population of processive particles that showed fluorescent signal only in the FEZ1 channel but not in the capsid channel. Potential explanations include: 1) The self-assembled HIV-1 capsids within these KFC particles incorporated too little labelled CA such that their fluorescence signals were too dim to be detected under our experimental conditions; 2) HIV-1 capsids dissociated from KFC particles but the remaining KF particles remained processive; 3) Kif5B and FEZ1 were sufficient to form a processive complex (KF complex) without needing a cargo.

5.4.1. Kif5B and FEZ1 can form a processive KF complex without a cargo

	[Dark Kif5B-dimer]/nM	[sfGFP-FEZ1]/nM
Sample (KF)	250	250
1in100_dilution	2.5	2.5
1in250_dilution	1	1
1in500_dilution	0.5	0.5
1in1000_dilution	0.25	0.25
1in2000_dilution	0.0125	0.0125

Table 5.3. Sample preparation for KF complex reconstitution and KF motility assay. 250 nM Kif5B and 250 nM FEZ1 were mixed and incubated in the motility buffer (see 2.1.5) for the formation of KF complex. The sample was diluted 100-fold to 2000-fold prior to addition to the coverslip with

immobilized microtubules. The motility assays were typically performed using samples at 500-fold to 2000-fold dilution to obtain a sufficiently low particle density on the surface to facilitate tracking of single particles on microtubules.

To investigate whether processive KF complexes could form in the absence of capsids, we incubated dark Kif5B dimers and sfGFP-FEZ1 in a 1:1 molar ratio (**Table 5.3**) and analysed the resulting complexes in the TIRF motility assay by tracking the movement of GFP-positive particles on microtubules. **Fig. 5.9.A** shows an example set of successive frames showing two KF particles (indicated by white and yellow arrows) walking along microtubules and the corresponding kymographs. The dim KF particle (white arrow) remained stationary on the microtubule for 10 s,

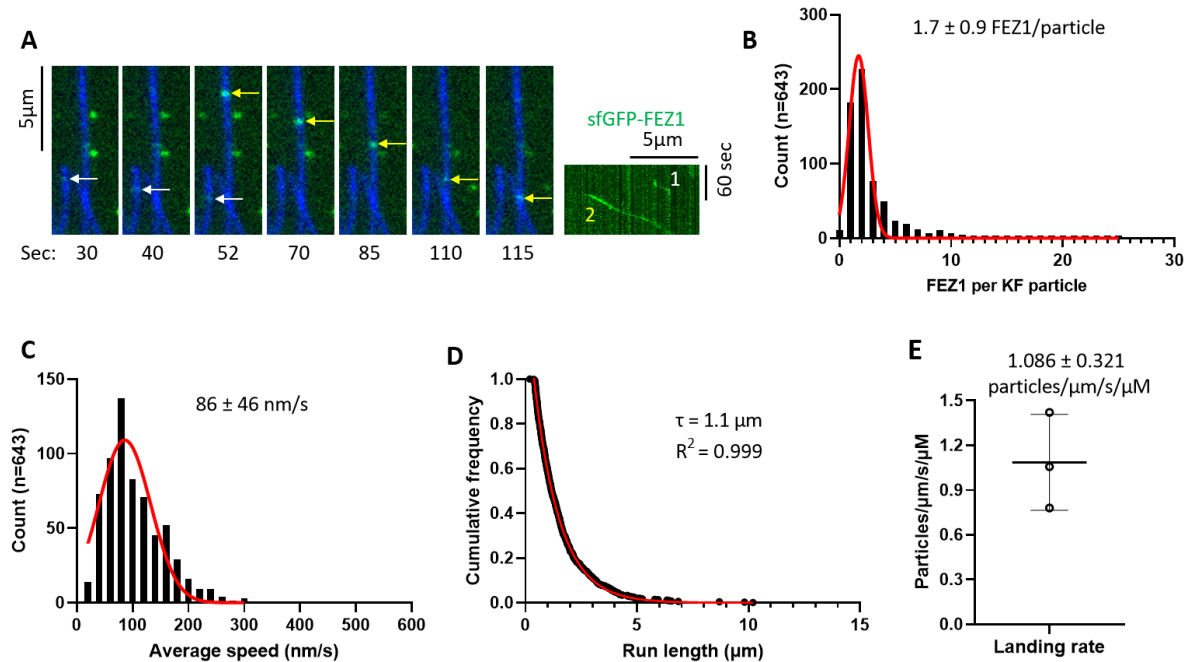


Fig. 5.9. Kif5B and FEZ1 can form a processive KF complex. **A.** Movie frames showing two processive KF particles (white arrows indicate a dim KF particle, yellow arrows indicate a bright KF particle) moving along microtubules. The two KF particles contained ~ 1 and 9 FEZ1 molecules, respectively. **B-E.** Distribution of the number of FEZ1 molecules per particle (1.7 ± 0.9 FEZ1/particle; mean \pm SD), average speed (86 ± 46 nm/s; mean \pm SD), run length ($1.1 \mu\text{m}$, τ , decay constant), and landing rate (1.086 ± 0.321 particles/ $\mu\text{m/s}/\mu\text{M}$) of processive KF particles (643 particles from 3 image stacks were analyzed).

then walked for 1 μm during the next 7 s and finally pauses again for 13 s before the FEZ1 signal was no longer detectable. The bright KF particle (yellow arrow) landed on the microtubule at the 52 s time point and walked continuously for 6.1 μm during the final 69 s of the movie. Next, we calculated the number of FEZ1 molecules per KF particle by dividing the FEZ1 intensity of each processive GFP-positive spot by the single molecule intensity of FEZ1 determined by photobleaching. Most KF particles contained 1–2 FEZ1 molecules (average of 1.7 ± 0.9 , mean \pm SD, **Fig. 5.9.B**), but the tail of the distribution contained particles with up to ~ 10 FEZ1 molecules, possibly due to aggregation (of either FEZ1 and/or Kif5B). The average speed, run length, and landing rate of processive KFC particles were calculated to be 86 ± 46 nm/s (mean \pm SD), 1.1 μm , and 1.086 ± 0.321 particles/ μm /s/ μM respectively (**Fig. 5.9.C-E**).

5.4.2. Comparison between KF and KFC complexes

The observation that Kif5B and FEZ1 form a processive complex in the absence HIV-1 capsid, calls into question the generally accepted model that the kinesin motors require cargo binding to actively walk along microtubules. In other words, does the HIV-1 capsid play a role in activating the KFC complex or is it just a passenger on an already active motor complex? To investigate this, we measured the average speed, run length and landing rate between KF (dark Kif5B + sfGFP-FEZ1) and KFC (dark Kif5B + sfGFP-FEZ1 + AF647 labelled HIV-1 capsid) complexes reconstituted under otherwise identical conditions to determine whether the capsid affected the motile behaviors of the KFC complexes.

The average speed of both complexes was indistinguishable (**Fig. 5.10.A**), suggesting that capsid neither accelerated nor slowed down the complex. The run length of KFC particles was ~ 1.4 -fold higher than that of KF particles (**Fig. 5.10.B**, 1.1 μm vs 1.5 μm), suggesting that capsid might lead to a modest increase of the complex processivity. KFC particles contained a larger number of FEZ1 molecules than KF particles, as expected for the large number of FEZ1 binding sites on the capsid (~ 100 FEZ1 molecules at saturation, see **Fig. 5.1.D**). Each FEZ1 molecule bound to the capsid could in principle recruit a Kif5B motor, whereby the presence of multiple motors might lead to the observed increase in processivity of the KFC complex. Finally, we observed more processive events in KF samples compared to KFC samples, as seen from the 2–3-fold higher landing rate (**Fig. 5.10.C**). It should be noted that this increase might simply be a reflection of the higher concentration of KF complexes compared to KFC complexes given that the latter contained 2–3 times more FEZ1

molecules per complex than the former.

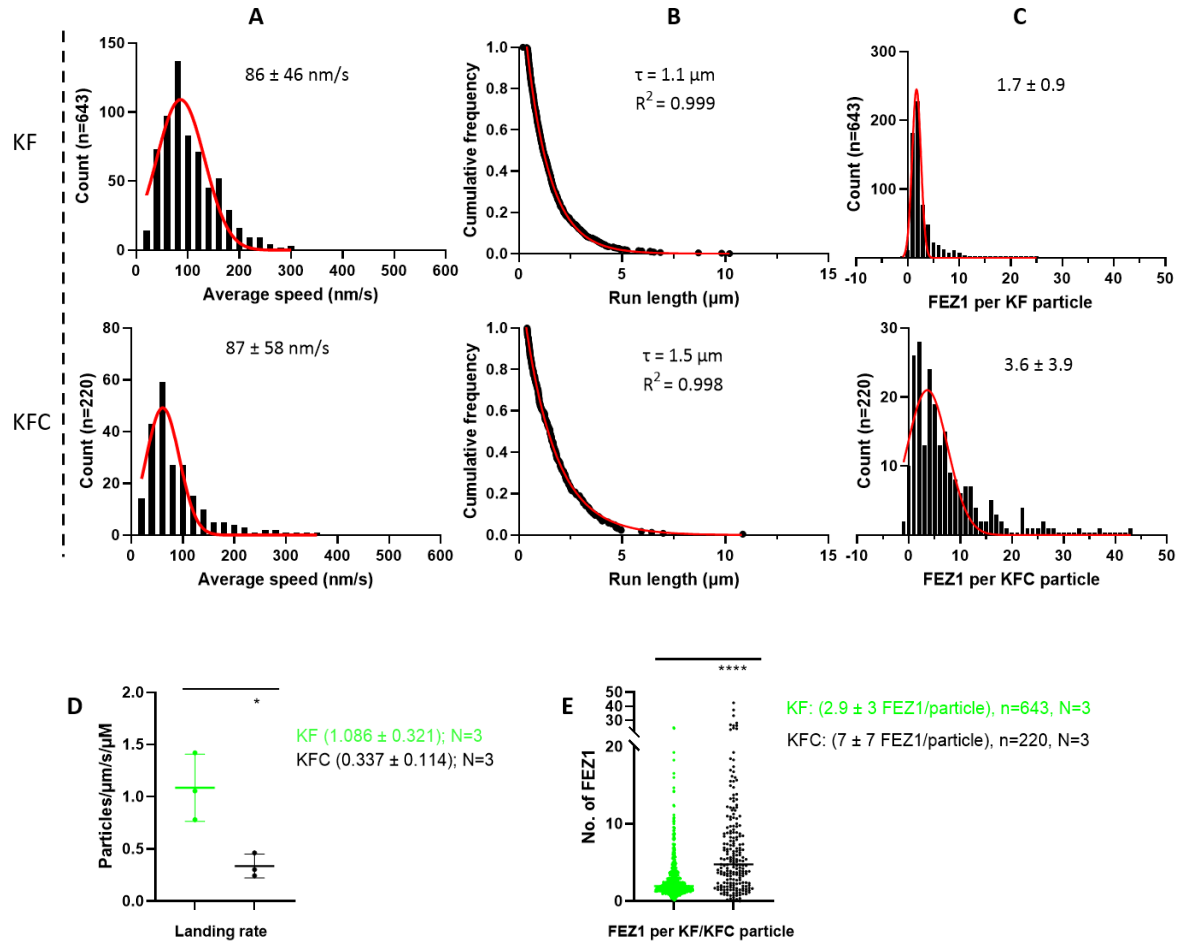


Fig. 5.10. Comparison of KF and KFC motile behaviors. 643 KF particles from 3 image stacks and 220 KFC particles from 3 image stacks were analyzed. The data for the KF complex is the same as in **Fig 5.9**. **A-C**. Distribution of average speed (**A**), run length (**B**) and number of FEZ1 molecules per particle (**C**) for KF (top) and KFC (bottom) complexes. **D-E**. Comparison of the landing rate (**D**) and the number of FEZ1 molecules per particle (**E**, same data as in panel C) using unpaired T tests (****, $p < 0.0001$; *, $0.01 < p < 0.05$). “N” and “n” represent the number of image stacks and processive particles analyzed, respectively.

Taken together, we conclude that HIV-1 capsid does not increase the average speed or the landing rate of a processive Kif5B-containing complexes but may slightly increase the run length, possibly due to binding of multiple motors. These results indicate that the HIV-1 capsid does not play an

important role in activating the kinesin motor. This was surprising since the binding of cargo to kinesin via adaptors is typically believed to be necessary to release the autoinhibition of kinesin [284, 309, 310, 340], although there are reports about the activation of kinesin by adaptors only [181, 341, 342].

5.5. Discussion

The first aim of this chapter was to investigate the interaction between full-length FEZ1 and HIV-1 capsids formed by self-assembly of CA bearing the A204C substitution for disulfide cross-linking at the trimer interface. We observed a slight increase in affinity (~ 3 – 15 -fold lower K_D) and 3 – 15 -fold decrease in the FEZ1:hexamer stoichiometry compared to the previously characterized interaction between FEZ1 truncations and cross-linked HIV-1 CA hexamers [73] (**Table 5.4**). This observation is consistent with the proposed model in which FEZ1 binds to a hexameric subunit of the capsid via its minimal binding motif (aa 178-188) but makes additional weak interactions with neighboring CA hexamers via other stretches of negatively charged residues located in the unstructured regions of FEZ1 [73]. In addition, we confirmed that FEZ1 directly binds to the R18 ring at the center of HIV-1 CA hexamer (**5.2.1**), in line with the previous study [73]. However, residual binding of FEZ1 was still detected in presence of the competitive binding inhibitor hexacarboxybenzene (**5.2.2**). Similarly, capsids assembled with CA R18G showed residual formation of processive KFC complexes in motility assays (**5.3.2**). These observations suggest that additional FEZ1 binding sites might be present on the capsid; further studies are needed to identify these interfaces.

Method	FEZ1	CA assembly	K_D (nM)	B_{\max} (FEZ1/CA hexamer)
TIRF microscopy	Full length	cone (A92E/A204C)	19 ± 4	0.38 ± 0.06
		cone (A204C)	70 ± 28	0.75 ± 0.15
Isothermal titration calorimetry [73]	aa 92-198	hexamer (A14C/E45C/W184A/M185A)	300 ± 60	1.3 ± 0.1
	aa 178-188		190 ± 40	1.0 ± 0.2

Table 5.4. Quantifications of the FEZ1-capsid interaction compared to literature. Measurements in our assay (grey rows) compared to previous report [73].

The second aim of this chapter was to reconstitute the KFC complex *in vitro* for TIRF imaging of its movement on surface-immobilized microtubules in real time. We have successfully demonstrated this process and measured parameters of the KFC complex motility including average speed, run length, and landing rate (5.3). We also demonstrated that the R18 ring of HIV-1 capsid facilitated assembly of a processive KFC complex (5.3.2). Overall, our observations provide strong evidence that the recruitment of FEZ1 and Kif5B by HIV-1 capsid serves as the minimum requirement for the kinesin-dependent transport of HIV-1 capsid, whereby the capsid is primarily a passenger rather than an activator of this machinery (5.4). Below we discuss these findings and potential limitations of our assays in more detail.

First, the average speed of the KFC complex calculated in our assay (~ 100 nm/s, Fig. 5.6.B) was significantly slower than the conventionally reported speed of kinesin-1 (~ 400 - 1000 nm/s) either *in vitro* [181, 343-345] or *in vivo* [344, 346, 347]. However, these comparisons are not straightforward due to the major differences in the experimental designs. In our assay, we use Kif5B, a full-length kinesin-1 heavy chain (KHC), which requires adaptor and cargo binding to release auto-inhibition, together with FEZ1 and capsid to reconstitute the motility of the KFC complex. The measurements from the existing *in vitro* studies are based on truncated, constitutively active forms of KHC. The measurements from the existing *in vivo* studies, on the other hand, are complicated by the presence of KLC (Kinesin-1 heavy chain) and other potential kinesin regulators. A recent study reported the *in vitro* reconstitution of mitochondria transport along microtubule at a speed of ~ 250 nm/s [341]. This study provides the first description of kinesin dependent transport of physiological cargo *in vitro*; however, the complex is transported by a truncated rather than a full length KHC. While assay conditions (e.g., temperature, pH, ionic strength) might also play roles in the slow speed of the KFC complex in our assay, we speculate the slow speed might represent the nature of the complex. Supporting evidence come from an early single-molecule study, which demonstrates that full length Kif5B also shows processive movement along microtubule although the frequency is much lower compared to truncated Kif5B [308]. More importantly, full length Kif5B exhibits motile behavior composed of frequent pauses intersected with bursts of movements at varied velocities, with an overall average speed of ~ 100 nm/s. Both the average speed and the motile behaviors of the KFC complexes in our assay highly match these of the full length Kif5B alone. Therefore, we suggest that

while the KFC complex is not fully activated but it is clearly sufficient to reconstitute the kinesin dependent transport of HIV-1 capsid.

Second, the run lengths determined for both the KF and KFC complexes might misrepresent an underestimate (**Fig. 8.5**) as a subset of particles remained associated with the microtubule at the end of the experiment (i.e. had not completed their run). As such, experiments with an extended imaging period are required to validate the run lengths. It is also worth noting that the stoichiometry of the KFC complex varies, whereby the average number of motors per capsid depends on the concentrations of the different components. As such the landing rate of this complex (calculated relative to the Kif5B concentration) depends on the conditions used for reconstitution and is not directly comparable to the landing rate calculated for complexes with well-defined stoichiometry.

Lastly, we have shown here that the KFC complex is sufficient to mediate the kinesin-dependent transport of HIV-1 capsid. As mentioned above, additional factors or post-translational modifications could further regulate this complex. The phosphorylation of FEZ1 and the microtubule binding protein MAP7 are two of the potential regulatory factors which we are in the process of examination. Phosphorylation of FEZ1 at residue serine 58 has been suggested to be essential for the kinesin-dependent transport of HIV-1 capsid [53, 186]; similarly, other reports claim that the interaction between FEZ1 and kinesin-1 is strictly dependent on the phosphorylation of FEZ1 at serine 58 [182, 185]. In our assay, FEZ1 is recombinantly produced from *E. coli* therefore not phosphorylated. Although we demonstrated that the non-phosphorylated FEZ1 is sufficient to interact with Kif5B and form processive complexes, we do not rule out the possibility that the phosphorylation of FEZ1 might further affect the activity of the KF and KFC complexes. We plan to investigate this by using both FEZ1 recombinantly produced from insect cell expression system (phosphorylated), as well as phosphomimetic mutants of FEZ1 (S58D, S58E) recombinantly produced from *E. coli*. We also tested MAP7, a known kinesin activator [345, 348, 349], in our assay once without seeing a significant effect when this thesis was written (data not shown). These experiments will be pursued in the future to identify additional factors that regulate the transport of HIV-1 capsid by the kinesin motor complex.

Chapter 6

Conclusions and future directions

6. Conclusions and future directions

A key to understanding the multifaceted role of the capsid during HIV infection is to better understand the varied interactions it has with host cell molecules. On one hand, the capsid serves as a protective shell that shields the virus from the host cell immune response. On the other hand, the capsid is required to interface with numerous cellular components during early infection including reverse transcription, retrograde transport, uncoating, nuclear entry, and integration site targeting in a precisely controlled manner. These processes are actively regulated by the interactions between HIV-1 capsid and multiple host factors. The aim of this thesis is to further our understanding of how the interplay between capsid and host factors modulate HIV-1 viral activities, specifically focusing on the cytoplasmic transport process.

Chapter 3 contains our published study [121] which focuses on the CypA-capsid interaction and investigates a previously proposed secondary capsid binding motif on the host protein CypA [109]. Mutational analysis of the residues comprising the proposed showed that they were not involved in capsid binding; and suggested that if a secondary binding site does exist, it is very weak. In addition, the chapter describes an optimized method for the assembly of soluble, stabilized HIV-1 capsids that are fluorescently labeled and retain the shape of native viral capsids. This method allows for the generation of capsid assemblies that are well-suited for the investigation of capsid-host interactions as well as the motility assays in Chapter 4 and Chapter 5.

The focus of this thesis then turned to a different set of host proteins required for the cytoplasmic transport of the viral core to the nucleus. It has been shown that the HIV-1 viral core exploits microtubule motor complexes; however, the details of how the viral core assembles into a functional transport complex remained unclear. Based on cellular knock-down assays and biochemical characterizations, recent studies proposed a model whereby the HIV-1 capsid hijacks dynein via the adaptor protein BICD2 [52, 74] and kinesin via the adaptor protein FEZ1 [53, 73, 186] to form motor-adaptor-cargo complexes (dynein-dynactin-BICD2-capsid (DDBC) and kinesin-FEZ1-capsid (KFC)) for active transport along microtubules. The aim of Chapter 4 and Chapter 5 is to investigate the cytoplasmic transport of the HIV-1 viral core by reconstituting the DDBC and KFC complexes *in vitro* and demonstrating their motilities along microtubule. One important

achievement of this thesis is to establish the enabling technologies for imaging motor-driven capsid transport, including protein expression, purification and labelling for formation of functional complexes; surface chemistry for deposition of microtubules while resisting non-specific adsorption of proteins to the surface; sample delivery on the microscope and optimization of imaging conditions; semi-automated analysis of TIRF movies and single-particle trajectories.

Chapter 4 examined the interaction between BICD2 and the HIV-1 capsid using a novel TIRF imaging-based biosensor developed as part of this thesis to measure the dissociation constant (K_D) and stoichiometry of this interaction. The biosensor builds on previous designs [124, 350] but uses self-assembled, stabilized CA cones (instead of CA tubes or spheres) immobilized at the bottom surface of a microfluidic channel device. BICD2 binding was strongly reduced with capsids bearing the R18G substitution, revealing the positively charged R18 pore as a major BICD2 binding site while the residual level of binding suggested the existence of additional binding sites. The molecular dissection of the BICD2-capsid interaction facilitated the main aim of this chapter, namely the reconstitution of the DDBC complex for TIRF microscopy-based imaging of its motility along microtubules in real time. The DDBC complex was reconstituted from the dynein-dynactin complex isolated from tissues, recombinant GFP-tagged BICD2 produced in insect cells and cross-linked CA cones labelled with a chemical dye. These complexes bound to and moved along fluorescence-labelled microtubules immobilized on the surface of glass coverslips. Imaging of this process by multi-color TIRF microscopy provided the first evidence that this minimal machine comprising dynein-dynactin-BICD2-capsid is sufficient for the dynein-dependent transport of HIV-1 capsid along microtubules while single-particle tracking provided the first insight into the characteristics of this process. The establishment of the DDBC motility assay in this chapter will underpin future experiments to study the movement of the DDBC complex, providing a platform for the molecular dissection of dynein-dependent transport of the HIV-1 core.

Chapter 5 examined the FEZ1-capsid interaction. Quantitative biosensor measurements yielded the dissociation constant (K_D) and stoichiometry of the complex between full-length FEZ1 and self-assembled CA cones, expanding upon previous characterization of this interaction using FEZ1 truncations and the HIV-1 CA hexamer [73]. Mutational analysis confirmed that FEZ1 binds to the R18 ring of HIV-1 capsid, as reported previously [73]. However, like BICD2, low level FEZ1 binding

to R18G capsids suggested the existence of additional binding sites. For molecular dissection of its function *in vitro*, the KFC complex was reconstituted using recombinant full length Kif5B produced in insect cells, recombinant FEZ1 produced with or without GFP-tag in bacteria and cross-linked CA cones labelled with a chemical dye. When imaged in the TIRF-microscopy motility assay, the fluorescent signals of different components from this complex were observed to move together along microtubules, confirming the model that a complex comprising kinesin-FEZ1-capsid is sufficient to mediate the kinesin-dependent transport of the HIV-1 viral core. This also provided the first observation of the transport of physiological cargo by full-length kinesin heavy chain *in vitro*. Single-particle tracking and statistical analysis of the trajectories of hundreds of processive KFC particles showed that runs were interspersed with pauses and provided the average speed, run length, and landing rate of the KFC complex. The CA R18G substitution strongly reduced the formation of processive KFC particles indicating that the R18 ring is an important feature for the kinesin-dependent transport of HIV-1 capsid, consistent with its importance for mediating the FEZ1-capsid interaction. Unexpectedly, the complex consisting of Kif5B and FEZ1 exhibited motility with the same speed and run length as the KFC complex, suggesting that the HIV-1 capsid in this minimal system did not activate the complex. Future work will focus on identifying and characterizing additional components and post-translational modification that control the motility of the KFC complex. Since the capsid can recruit multiple motors simultaneously, the system developed here could also be extended to study whether multiple motors coordinate their activities to move the same cargo, whereby it is possible that mechanical coupling of the motors may synchronise their motions.

Taken together, this work established an *in vitro* TIRF microscopy assay to image the cytoplasmic transport of HIV-1 capsid in real time for single-particle tracking, providing a new tool for molecular dissection of a vital process for early HIV-1 infection post cell entry. The observations from this assay validate the proposed models for the cytoplasmic transport of HIV-1 viral core by demonstrating that the DDBC and KFC complexes are sufficient for capsid transport, providing direct evidence that the HIV-1 capsid hijacks these motor protein complexes. Motor activation induced by cargo attachment has been an extremely challenging subject to study despite of the efforts in the past years. This study, together with two studies of dynein-dependent mRNA transport [351, 352] and a recent study of kinesin-dependent transport of mitochondria (which

uses a truncated kinesin heavy chain for the reconstitution) [341], are among the first *in vitro* systems using authentic cargo for mechanistic insight into this process.

Despite enormous progress in understanding HIV-1 capsid transport, a range of exciting research questions relevant for the fields of both HIV infection and motor proteins remain, including:

- 1) How do the capsid (cargo) and FEZ1 (adaptor) regulate kinesin activity?
- 2) How do the other components (e.g., MAP7 or kinesin light chain) and modification (e.g., phosphorylation of FEZ1) regulate the kinesin-dependent transport of capsid?
- 3) What are the mechanisms that determine the directionality of movement when both dynein and kinesin motor are recruited to the same capsid?

The approaches to analyze capsid transport at the single-particle level in a defined system developed as part of this thesis will be instrumental in addressing these questions and identifying strategies to target this essential process for HIV therapy.

Chapter 7

References

7. References

- [1] R. C. Gallo *et al.*, "Frequent detection and isolation of cytopathic retroviruses (HTLV-III) from patients with AIDS and at risk for AIDS," (in eng), *Science*, vol. 224, no. 4648, pp. 500-3, May 4 1984.
- [2] World Health Organization, "HIV/AIDS," 2021, Nov 8th.
- [3] G. M. Shaw and E. Hunter, "HIV transmission," (in eng), *Cold Spring Harb Perspect Med*, vol. 2, no. 11, Nov 1 2012.
- [4] R. Marlink *et al.*, "Reduced rate of disease development after HIV-2 infection as compared to HIV-1," (in eng), *Science*, vol. 265, no. 5178, pp. 1587-90, Sep 9 1994.
- [5] M. Essex and Y. Lu, "HIV/AIDS: Lessons from a New Disease Pandemic," (in eng), *Emerging Infections in Asia*, pp. 133-142, 2008.
- [6] J. Hemelaar, "The origin and diversity of the HIV-1 pandemic," (in eng), *Trends Mol Med*, vol. 18, no. 3, pp. 182-92, Mar 2012.
- [7] D. Klatzmann *et al.*, "Selective tropism of lymphadenopathy associated virus (LAV) for helper-inducer T lymphocytes," (in eng), *Science*, vol. 225, no. 4657, pp. 59-63, Jul 6 1984.
- [8] P. U. Cameron *et al.*, "Susceptibility of dendritic cells to HIV-1 infection in vitro," (in eng), *J Leukoc Biol*, vol. 56, no. 3, pp. 257-65, Sep 1994.
- [9] V. Gill *et al.*, "Macrophages are the major target cell for HIV infection in long-term marrow culture and demonstrate dual susceptibility to lymphocytotropic and monocytotropic strains of HIV-1," (in eng), *Br J Haematol*, vol. 93, no. 1, pp. 30-7, Apr 1996.
- [10] C. J. Lopez Angel and G. D. Tomaras, "Bringing the path toward an HIV-1 vaccine into focus," (in eng), *PLoS Pathog*, vol. 16, no. 9, p. e1008663, Sep 2020.
- [11] Y. Mu, S. Kodidela, Y. Wang, S. Kumar, and T. J. Cory, "The dawn of precision medicine in HIV: state of the art of pharmacotherapy," (in eng), *Expert opinion on pharmacotherapy*, vol. 19, no. 14, pp. 1581-1595, 2018.
- [12] B. S. Taylor, S. A. Olender, H.-V. Tieu, and T. J. Wilkin, "CROI 2016: Advances in Antiretroviral Therapy," (in eng), *Topics in antiviral medicine*, vol. 24, no. 1, pp. 59-81, May-Jun 2016.
- [13] A. Dutta, C. Barker, and A. Kallarakal, "The HIV Treatment Gap: Estimates of the Financial Resources Needed versus Available for Scale-Up of Antiretroviral Therapy in 97 Countries from 2015 to 2020," (in eng), *PLoS medicine*, vol. 12, no. 11, pp. e1001907-e1001907, 2015.
- [14] J. M. Cuevas, R. Geller, R. Garijo, J. López-Aldeguer, and R. Sanjuán, "Extremely High Mutation Rate of HIV-1 In Vivo," (in eng), *PLoS biology*, vol. 13, no. 9, pp. e1002251-e1002251, 2015.
- [15] L. Ratner *et al.*, "Complete nucleotide sequence of the AIDS virus, HTLV-III," *Nature*, vol. 313, no. 6000, pp. 277-284, 1985/01/01 1985.
- [16] J. M. Watts *et al.*, "Architecture and secondary structure of an entire HIV-1 RNA genome," (in eng), *Nature*, vol. 460, no. 7256, pp. 711-6, Aug 6 2009.
- [17] K. A. Wilkinson *et al.*, "High-throughput SHAPE analysis reveals structures in HIV-1 genomic RNA strongly conserved across distinct biological states," (in eng), *PLoS Biol*, vol. 6, no. 4, p. e96, Apr 29 2008.
- [18] H. G. Göttlinger, J. G. Sodroski, and W. A. Haseltine, "Role of capsid precursor processing and myristoylation in morphogenesis and infectivity of human immunodeficiency virus type 1," (in eng), *Proc Natl Acad Sci U S A*, vol. 86, no. 15, pp. 5781-5, Aug 1989.

- [19] M. Bryant and L. Ratner, "Myristoylation-dependent replication and assembly of human immunodeficiency virus 1," (in eng), *Proc Natl Acad Sci U S A*, vol. 87, no. 2, pp. 523-7, Jan 1990.
- [20] R. Craigie, "The molecular biology of HIV integrase," (in eng), *Future virology*, vol. 7, no. 7, pp. 679-686, 2012.
- [21] M. Hill, G. Tachedjian, and J. Mak, "The packaging and maturation of the HIV-1 Pol proteins," (in eng), *Curr HIV Res*, vol. 3, no. 1, pp. 73-85, Jan 2005.
- [22] L. K. Nicholson *et al.*, "Flexibility and function in HIV-1 protease," *Nature Structural Biology*, vol. 2, no. 4, pp. 274-280, 1995/04/01 1995.
- [23] S. G. Sarafianos *et al.*, "Structure and function of HIV-1 reverse transcriptase: molecular mechanisms of polymerization and inhibition," (in eng), *Journal of molecular biology*, vol. 385, no. 3, pp. 693-713, 2009.
- [24] T. Jacks, M. D. Power, F. R. Masiarz, P. A. Luciw, P. J. Barr, and H. E. Varmus, "Characterization of ribosomal frameshifting in HIV-1 gag-pol expression," (in eng), *Nature*, vol. 331, no. 6153, pp. 280-3, Jan 21 1988.
- [25] C. JM, H. SH, and V. HE, C. JM, H. SH, and V. HE, Eds. *Retroviruses* (Synthesis of Gag and Gag-Pro-Pol Proteins). Cold Spring Harbor Laboratory Press, 1997.
- [26] C. D. Rizzuto *et al.*, "A conserved HIV gp120 glycoprotein structure involved in chemokine receptor binding," (in eng), *Science*, vol. 280, no. 5371, pp. 1949-53, Jun 19 1998.
- [27] F. D. Veronese, A. L. DeVico, T. D. Copeland, S. Oroszlan, R. C. Gallo, and M. G. Sarngadharan, "Characterization of gp41 as the transmembrane protein coded by the HTLV-III/LAV envelope gene," (in eng), *Science*, vol. 229, no. 4720, pp. 1402-5, Sep 27 1985.
- [28] C. Brigati, M. Giacca, D. M. Noonan, and A. Albin, "HIV Tat, its TARgets and the control of viral gene expression," (in eng), *FEMS Microbiol Lett*, vol. 220, no. 1, pp. 57-65, Mar 14 2003.
- [29] T. J. Hope, "The ins and outs of HIV Rev," (in eng), *Arch Biochem Biophys*, vol. 365, no. 2, pp. 186-91, May 15 1999.
- [30] E. L. Evans, 3rd, J. T. Becker, S. L. Fricke, K. Patel, and N. M. Sherer, "HIV-1 Vif's Capacity To Manipulate the Cell Cycle Is Species Specific," (in eng), *J Virol*, vol. 92, no. 7, Apr 1 2018.
- [31] A. Heigele, D. Sauter, J. Münch, and F. Kirchhoff, "HIV-1 accessory proteins: Nef," (in eng), *Methods Mol Biol*, vol. 1087, pp. 115-23, 2014.
- [32] M. H. Malim and M. Emerman, "HIV-1 accessory proteins--ensuring viral survival in a hostile environment," (in eng), *Cell Host Microbe*, vol. 3, no. 6, pp. 388-98, Jun 12 2008.
- [33] E. N. Pawlak, B. S. Dirk, R. A. Jacob, A. L. Johnson, and J. D. Dikeakos, "The HIV-1 accessory proteins Nef and Vpu downregulate total and cell surface CD28 in CD4(+) T cells," (in eng), *Retrovirology*, vol. 15, no. 1, p. 6, Jan 12 2018.
- [34] R. Y. Zhao and M. I. Bukrinsky, "HIV-1 accessory proteins: Vpr," (in eng), *Methods Mol Biol*, vol. 1087, pp. 125-34, 2014.
- [35] J. A. Briggs, T. Wilk, R. Welker, H. G. Kräusslich, and S. D. Fuller, "Structural organization of authentic, mature HIV-1 virions and cores," (in eng), *Embo j*, vol. 22, no. 7, pp. 1707-15, Apr 1 2003.
- [36] J. A. Briggs, K. Grünewald, B. Glass, F. Förster, H. G. Kräusslich, and S. D. Fuller, "The mechanism of HIV-1 core assembly: insights from three-dimensional reconstructions of authentic virions," (in eng), *Structure*, vol. 14, no. 1, pp. 15-20, Jan 2006.

- [37] E. O. Freed, "HIV-1 assembly, release and maturation," (in eng), *Nat Rev Microbiol*, vol. 13, no. 8, pp. 484-96, Aug 2015.
- [38] P. Zhu *et al.*, "Distribution and three-dimensional structure of AIDS virus envelope spikes," (in eng), *Nature*, vol. 441, no. 7095, pp. 847-52, Jun 15 2006.
- [39] M. R. Tardif and M. J. Tremblay, "Presence of host ICAM-1 in human immunodeficiency virus type 1 virions increases productive infection of CD4+ T lymphocytes by favoring cytosolic delivery of viral material," (in eng), *J Virol*, vol. 77, no. 22, pp. 12299-309, Nov 2003.
- [40] J. Benjamin, B. K. Ganster-Pornillos, W. F. Tivol, W. I. Sundquist, and G. J. Jensen, "Three-dimensional structure of HIV-1 virus-like particles by electron cryotomography," (in eng), *J Mol Biol*, vol. 346, no. 2, pp. 577-88, Feb 18 2005.
- [41] A. Bukrinskaya, "HIV-1 matrix protein: a mysterious regulator of the viral life cycle," (in eng), *Virus Res*, vol. 124, no. 1-2, pp. 1-11, Mar 2007.
- [42] J. A. Briggs *et al.*, "The stoichiometry of Gag protein in HIV-1," (in eng), *Nat Struct Mol Biol*, vol. 11, no. 7, pp. 672-5, Jul 2004.
- [43] J. G. Levin, M. Mitra, A. Mascarenhas, and K. Musier-Forsyth, "Role of HIV-1 nucleocapsid protein in HIV-1 reverse transcription," (in eng), *RNA biology*, vol. 7, no. 6, pp. 754-774, Nov-Dec 2010.
- [44] A. C. Francis *et al.*, "HIV-1 replication complexes accumulate in nuclear speckles and integrate into speckle-associated genomic domains," *Nature Communications*, vol. 11, no. 1, p. 3505, 2020/07/14 2020.
- [45] J. P. Moore, A. Trkola, and T. Dragic, "Co-receptors for HIV-1 entry," (in eng), *Curr Opin Immunol*, vol. 9, no. 4, pp. 551-62, Aug 1997.
- [46] R. Blumenthal, S. Durell, and M. Viard, "HIV entry and envelope glycoprotein-mediated fusion," (in eng), *The Journal of biological chemistry*, vol. 287, no. 49, pp. 40841-40849, 2012.
- [47] A. Fassati and S. P. Goff, "Characterization of intracellular reverse transcription complexes of human immunodeficiency virus type 1," (in eng), *J Virol*, vol. 75, no. 8, pp. 3626-35, Apr 2001.
- [48] W. S. Hu and S. H. Hughes, "HIV-1 reverse transcription," (in eng), *Cold Spring Harb Perspect Med*, vol. 2, no. 10, Oct 1 2012.
- [49] S. Iordanskiy and M. Bukrinsky, "Reverse transcription complex: the key player of the early phase of HIV replication," (in eng), *Future virology*, vol. 2, no. 1, pp. 49-64, 2007.
- [50] N. Levy *et al.*, "Structural and functional studies of the HIV-1 pre-integration complex," (in eng), *Retrovirology*, vol. 10, no. Suppl 1, pp. P76-P76, 2013.
- [51] D. McDonald *et al.*, "Visualization of the intracellular behavior of HIV in living cells," (in eng), *The Journal of cell biology*, vol. 159, no. 3, pp. 441-452, 2002.
- [52] S. K. Carnes, J. Zhou, and C. Aiken, "HIV-1 Engages a Dynein-Dynactin-BICD2 Complex for Infection and Transport to the Nucleus," (in eng), *J Virol*, vol. 92, no. 20, Oct 15 2018.
- [53] V. Malikov *et al.*, "HIV-1 capsids bind and exploit the kinesin-1 adaptor FEZ1 for inward movement to the nucleus," (in eng), *Nat Commun*, vol. 6, p. 6660, Mar 30 2015.
- [54] R. Gaudin, B. C. de Alencar, N. Arhel, and P. Benaroch, "HIV trafficking in host cells: motors wanted!," (in eng), *Trends Cell Biol*, vol. 23, no. 12, pp. 652-62, Dec 2013.
- [55] M. I. Bukrinsky *et al.*, "Active nuclear import of human immunodeficiency virus type 1 preintegration complexes," (in eng), *Proceedings of the National Academy of Sciences of the United States of America*, vol. 89, no. 14, pp. 6580-6584, 1992.

- [56] A. C. Francis and G. B. Melikyan, "Single HIV-1 Imaging Reveals Progression of Infection through CA-Dependent Steps of Docking at the Nuclear Pore, Uncoating, and Nuclear Transport," (in eng), *Cell Host Microbe*, vol. 23, no. 4, pp. 536-548.e6, Apr 11 2018.
- [57] V. Zila *et al.*, "Cone-shaped HIV-1 capsids are transported through intact nuclear pores," (in eng), *Cell*, vol. 184, no. 4, pp. 1032-1046.e18, Feb 18 2021.
- [58] A. R. Schröder, P. Shinn, H. Chen, C. Berry, J. R. Ecker, and F. Bushman, "HIV-1 integration in the human genome favors active genes and local hotspots," (in eng), *Cell*, vol. 110, no. 4, pp. 521-9, Aug 23 2002.
- [59] M. Lusic and R. F. Siliciano, "Nuclear landscape of HIV-1 infection and integration," (in eng), *Nat Rev Microbiol*, vol. 15, no. 2, pp. 69-82, Feb 2017.
- [60] F. B. Hamid, J. Kim, and C. G. Shin, "Distribution and fate of HIV-1 unintegrated DNA species: a comprehensive update," (in eng), *AIDS Res Ther*, vol. 14, no. 1, p. 9, Feb 16 2017.
- [61] J. Karn and C. M. Stoltzfus, "Transcriptional and posttranscriptional regulation of HIV-1 gene expression," (in eng), *Cold Spring Harbor perspectives in medicine*, vol. 2, no. 2, pp. a006916-a006916, 2012.
- [62] M. A. Checkley, B. G. Luttge, and E. O. Freed, "HIV-1 envelope glycoprotein biosynthesis, trafficking, and incorporation," (in eng), *J Mol Biol*, vol. 410, no. 4, pp. 582-608, Jul 22 2011.
- [63] A. Seelamgari *et al.*, "Role of viral regulatory and accessory proteins in HIV-1 replication," (in eng), *Front Biosci*, vol. 9, pp. 2388-413, Sep 1 2004.
- [64] L. Hermida-Matsumoto and M. D. Resh, "Localization of human immunodeficiency virus type 1 Gag and Env at the plasma membrane by confocal imaging," (in eng), *J Virol*, vol. 74, no. 18, pp. 8670-9, Sep 2000.
- [65] E. Poole, P. Strappe, H. P. Mok, R. Hicks, and A. M. Lever, "HIV-1 Gag-RNA interaction occurs at a perinuclear/centrosomal site; analysis by confocal microscopy and FRET," (in eng), *Traffic*, vol. 6, no. 9, pp. 741-55, Sep 2005.
- [66] E. K. Franke, H. E. Yuan, and J. Luban, "Specific incorporation of cyclophilin A into HIV-1 virions," (in eng), *Nature*, vol. 372, no. 6504, pp. 359-62, Nov 24 1994.
- [67] D. L. Mallery *et al.*, "IP6 is an HIV pocket factor that prevents capsid collapse and promotes DNA synthesis," (in eng), *Elife*, vol. 7, May 31 2018.
- [68] J. Rasaiyaah *et al.*, "HIV-1 evades innate immune recognition through specific cofactor recruitment," (in eng), *Nature*, vol. 503, no. 7476, pp. 402-405, Nov 21 2013.
- [69] X. Lahaye *et al.*, "The capsids of HIV-1 and HIV-2 determine immune detection of the viral cDNA by the innate sensor cGAS in dendritic cells," (in eng), *Immunity*, vol. 39, no. 6, pp. 1132-42, Dec 12 2013.
- [70] D. A. Jacques, W. A. McEwan, L. Hilditch, A. J. Price, G. J. Towers, and L. C. James, "HIV-1 uses dynamic capsid pores to import nucleotides and fuel encapsidated DNA synthesis," (in eng), *Nature*, vol. 536, no. 7616, pp. 349-53, Aug 18 2016.
- [71] J. Jennings, J. Shi, J. Varadarajan, P. J. Jamieson, and C. Aiken, "The Host Cell Metabolite Inositol Hexakisphosphate Promotes Efficient Endogenous HIV-1 Reverse Transcription by Stabilizing the Viral Capsid," (in eng), *mBio*, vol. 11, no. 6, Dec 1 2020.
- [72] C. Aiken and I. Rousso, "The HIV-1 capsid and reverse transcription," (in eng), *Retrovirology*, vol. 18, no. 1, p. 29, Sep 25 2021.
- [73] P. T. Huang *et al.*, "FEZ1 Is Recruited to a Conserved Cofactor Site on Capsid to Promote HIV-1 Trafficking," (in eng), *Cell Rep*, vol. 28, no. 9, pp. 2373-2385.e7, Aug 27 2019.

- [74] A. Dharan *et al.*, "Bicaudal D2 facilitates the cytoplasmic trafficking and nuclear import of HIV-1 genomes during infection," (in eng), *Proc Natl Acad Sci U S A*, vol. 114, no. 50, pp. E10707-e10716, Dec 12 2017.
- [75] A. Dharan *et al.*, "KIF5B and Nup358 Cooperatively Mediate the Nuclear Import of HIV-1 during Infection," (in eng), *PLoS Pathog*, vol. 12, no. 6, p. e1005700, Jun 2016.
- [76] K. A. Matreyek, S. S. Yücel, X. Li, and A. Engelman, "Nucleoporin NUP153 phenylalanine-glycine motifs engage a common binding pocket within the HIV-1 capsid protein to mediate lentiviral infectivity," (in eng), *PLoS Pathog*, vol. 9, no. 10, p. e1003693, 2013.
- [77] T. Schaller *et al.*, "HIV-1 capsid-cyclophilin interactions determine nuclear import pathway, integration targeting and replication efficiency," (in eng), *PLoS Pathog*, vol. 7, no. 12, p. e1002439, Dec 2011.
- [78] K. E. Ocwieja *et al.*, "HIV integration targeting: a pathway involving Transportin-3 and the nuclear pore protein RanBP2," (in eng), *PLoS Pathog*, vol. 7, no. 3, p. e1001313, Mar 2011.
- [79] S. J. Rihn *et al.*, "Extreme genetic fragility of the HIV-1 capsid," (in eng), *PLoS Pathog*, vol. 9, no. 6, p. e1003461, 2013.
- [80] S. Li, C. P. Hill, W. I. Sundquist, and J. T. Finch, "Image reconstructions of helical assemblies of the HIV-1 CA protein," (in eng), *Nature*, vol. 407, no. 6802, pp. 409-13, Sep 21 2000.
- [81] B. K. Ganer, S. Li, V. Y. Klishko, J. T. Finch, and W. I. Sundquist, "Assembly and analysis of conical models for the HIV-1 core," (in eng), *Science*, vol. 283, no. 5398, pp. 80-3, Jan 1 1999.
- [82] O. Pornillos, B. K. Ganer-Pornillos, and M. Yeager, "Atomic-level modelling of the HIV capsid," (in eng), *Nature*, vol. 469, no. 7330, pp. 424-7, Jan 20 2011.
- [83] O. Pornillos *et al.*, "X-ray structures of the hexameric building block of the HIV capsid," (in eng), *Cell*, vol. 137, no. 7, pp. 1282-92, Jun 26 2009.
- [84] R. Shin, Y.-M. Tzou, and N. R. Krishna, "Structure of a monomeric mutant of the HIV-1 capsid protein," (in eng), *Biochemistry*, vol. 50, no. 44, pp. 9457-9467, 2011.
- [85] T. R. Gamble *et al.*, "Crystal structure of human cyclophilin A bound to the amino-terminal domain of HIV-1 capsid," (in eng), *Cell*, vol. 87, no. 7, pp. 1285-94, Dec 27 1996.
- [86] A. Lampel, O. Yaniv, O. Berger, E. Bacharach, E. Gazit, and F. Frolow, "A triclinic crystal structure of the carboxy-terminal domain of HIV-1 capsid protein with four molecules in the asymmetric unit reveals a novel packing interface," (in eng), *Acta Crystallogr Sect F Struct Biol Cryst Commun*, vol. 69, no. Pt 6, pp. 602-6, Jun 2013.
- [87] A. I. Chien, W. H. Liao, D. M. Yang, and C. T. Wang, "A domain directly C-terminal to the major homology region of human immunodeficiency type 1 capsid protein plays a crucial role in directing both virus assembly and incorporation of Gag-Pol," (in eng), *Virology*, vol. 348, no. 1, pp. 84-95, Apr 25 2006.
- [88] Y. F. Chang, S. M. Wang, K. J. Huang, and C. T. Wang, "Mutations in capsid major homology region affect assembly and membrane affinity of HIV-1 Gag," (in eng), *J Mol Biol*, vol. 370, no. 3, pp. 585-97, Jul 13 2007.
- [89] B. K. Ganer-Pornillos, A. Cheng, and M. Yeager, "Structure of full-length HIV-1 CA: a model for the mature capsid lattice," (in eng), *Cell*, vol. 131, no. 1, pp. 70-9, Oct 5 2007.
- [90] D. E. Christensen, B. K. Ganer-Pornillos, J. S. Johnson, O. Pornillos, and W. I. Sundquist, "Reconstitution and visualization of HIV-1 capsid-dependent replication and integration in vitro," (in eng), *Science*, vol. 370, no. 6513, Oct 9 2020.

- [91] I. J. Byeon *et al.*, "Structural convergence between Cryo-EM and NMR reveals intersubunit interactions critical for HIV-1 capsid function," (in eng), *Cell*, vol. 139, no. 4, pp. 780-90, Nov 13 2009.
- [92] E. L. Yufenyuy and C. Aiken, "The NTD-CTD intersubunit interface plays a critical role in assembly and stabilization of the HIV-1 capsid," (in eng), *Retrovirology*, vol. 10, p. 29, Mar 6 2013.
- [93] T. R. Gamble *et al.*, "Structure of the carboxyl-terminal dimerization domain of the HIV-1 capsid protein," (in eng), *Science*, vol. 278, no. 5339, pp. 849-53, Oct 31 1997.
- [94] A. T. Gres, K. A. Kirby, V. N. KewalRamani, J. J. Tanner, O. Pornillos, and S. G. Sarafianos, "STRUCTURAL VIROLOGY. X-ray crystal structures of native HIV-1 capsid protein reveal conformational variability," (in eng), *Science*, vol. 349, no. 6243, pp. 99-103, Jul 3 2015.
- [95] G. Zhao *et al.*, "Mature HIV-1 capsid structure by cryo-electron microscopy and all-atom molecular dynamics," (in eng), *Nature*, vol. 497, no. 7451, pp. 643-6, May 30 2013.
- [96] S. Mattei, B. Glass, W. J. Hagen, H. G. Kräusslich, and J. A. Briggs, "The structure and flexibility of conical HIV-1 capsids determined within intact virions," (in eng), *Science*, vol. 354, no. 6318, pp. 1434-1437, Dec 16 2016.
- [97] G. B. Mortuza, L. F. Haire, A. Stevens, S. J. Smerdon, J. P. Stoye, and I. A. Taylor, "High-resolution structure of a retroviral capsid hexameric amino-terminal domain," (in eng), *Nature*, vol. 431, no. 7007, pp. 481-5, Sep 23 2004.
- [98] M. Yamashita and A. N. Engelman, "Capsid-Dependent Host Factors in HIV-1 Infection," (in eng), *Trends Microbiol*, vol. 25, no. 9, pp. 741-755, Sep 2017.
- [99] J. Temple, T. N. Tripler, Q. Shen, and Y. Xiong, "A snapshot of HIV-1 capsid-host interactions," (in eng), *Curr Res Struct Biol*, vol. 2, pp. 222-228, 2020.
- [100] E. Rossi, M. E. Meuser, C. J. Cunanan, and S. Cocklin, "Structure, Function, and Interactions of the HIV-1 Capsid Protein," (in eng), *Life (Basel)*, vol. 11, no. 2, Jan 29 2021.
- [101] R. König *et al.*, "Global analysis of host-pathogen interactions that regulate early-stage HIV-1 replication," (in eng), *Cell*, vol. 135, no. 1, pp. 49-60, Oct 3 2008.
- [102] H. Zhou *et al.*, "Genome-scale RNAi screen for host factors required for HIV replication," (in eng), *Cell Host Microbe*, vol. 4, no. 5, pp. 495-504, Nov 13 2008.
- [103] A. L. Brass *et al.*, "Identification of host proteins required for HIV infection through a functional genomic screen," (in eng), *Science*, vol. 319, no. 5865, pp. 921-6, Feb 15 2008.
- [104] V. B. Shah and C. Aiken, "In vitro uncoating of HIV-1 cores," (in eng), *J Vis Exp*, no. 57, Nov 8 2011.
- [105] W. Hübner, P. Chen, A. Del Portillo, Y. Liu, R. E. Gordon, and B. K. Chen, "Sequence of human immunodeficiency virus type 1 (HIV-1) Gag localization and oligomerization monitored with live confocal imaging of a replication-competent, fluorescently tagged HIV-1," (in eng), *J Virol*, vol. 81, no. 22, pp. 12596-607, Nov 2007.
- [106] C. L. Márquez *et al.*, "Kinetics of HIV-1 capsid uncoating revealed by single-molecule analysis," (in eng), *Elife*, vol. 7, Jun 7 2018.
- [107] L. S. Ehrlich, B. E. Agresta, and C. A. Carter, "Assembly of recombinant human immunodeficiency virus type 1 capsid protein in vitro," (in eng), *J Virol*, vol. 66, no. 8, pp. 4874-83, Aug 1992.
- [108] M. Grättinger, H. Hohenberg, D. Thomas, T. Wilk, B. Müller, and H. G. Kräusslich, "In vitro assembly properties of wild-type and cyclophilin-binding defective human immunodeficiency virus capsid proteins in the presence and absence of cyclophilin A," (in eng), *Virology*, vol. 257, no. 1, pp. 247-60, Apr 25 1999.

- [109] C. Liu *et al.*, "Cyclophilin A stabilizes the HIV-1 capsid through a novel non-canonical binding site," (in eng), *Nat Commun*, vol. 7, p. 10714, Mar 4 2016.
- [110] R. A. Dick *et al.*, "Inositol phosphates are assembly co-factors for HIV-1," (in eng), *Nature*, vol. 560, no. 7719, pp. 509-512, 2018.
- [111] S. Campbell and V. M. Vogt, "Self-assembly in vitro of purified CA-NC proteins from Rous sarcoma virus and human immunodeficiency virus type 1," (in eng), *J Virol*, vol. 69, no. 10, pp. 6487-97, Oct 1995.
- [112] K. Lee *et al.*, "Flexible use of nuclear import pathways by HIV-1," (in eng), *Cell Host Microbe*, vol. 7, no. 3, pp. 221-33, Mar 18 2010.
- [113] O. Pornillos, B. K. Ganser-Pornillos, S. Banumathi, Y. Hua, and M. Yeager, "Disulfide bond stabilization of the hexameric capsomer of human immunodeficiency virus," (in eng), *Journal of molecular biology*, vol. 401, no. 5, pp. 985-995, 2010.
- [114] S. V. Rebensburg *et al.*, "Sec24C is an HIV-1 host dependency factor crucial for virus replication," (in eng), *Nat Microbiol*, vol. 6, no. 4, pp. 435-444, Apr 2021.
- [115] S. M. Bester *et al.*, "Structural and mechanistic bases for a potent HIV-1 capsid inhibitor," (in eng), *Science*, vol. 370, no. 6514, pp. 360-364, Oct 16 2020.
- [116] H. Yang *et al.*, "Structural insight into HIV-1 capsid recognition by rhesus TRIM5 α ," (in eng), *Proc Natl Acad Sci U S A*, vol. 109, no. 45, pp. 18372-7, Nov 6 2012.
- [117] N. Y. Chen *et al.*, "HIV-1 capsid is involved in post-nuclear entry steps," (in eng), *Retrovirology*, vol. 13, p. 28, Apr 23 2016.
- [118] A. Bhattacharya *et al.*, "Structural basis of HIV-1 capsid recognition by PF74 and CPSF6," (in eng), *Proc Natl Acad Sci U S A*, vol. 111, no. 52, pp. 18625-30, Dec 30 2014.
- [119] A. J. Price *et al.*, "Host cofactors and pharmacologic ligands share an essential interface in HIV-1 capsid that is lost upon disassembly," (in eng), *PLoS Pathog*, vol. 10, no. 10, p. e1004459, Oct 2014.
- [120] J. Zhou, A. J. Price, U. D. Halambage, L. C. James, and C. Aiken, "HIV-1 Resistance to the Capsid-Targeting Inhibitor PF74 Results in Altered Dependence on Host Factors Required for Virus Nuclear Entry," (in eng), *J Virol*, vol. 89, no. 17, pp. 9068-79, Sep 2015.
- [121] W. Peng *et al.*, "Functional analysis of the secondary HIV-1 capsid binding site in the host protein cyclophilin A," (in eng), *Retrovirology*, vol. 16, no. 1, p. 10, Apr 4 2019.
- [122] S. Rasheedi *et al.*, "The Cleavage and Polyadenylation Specificity Factor 6 (CPSF6) Subunit of the Capsid-recruited Pre-messenger RNA Cleavage Factor I (CFIm) Complex Mediates HIV-1 Integration into Genes," (in eng), *J Biol Chem*, vol. 291, no. 22, pp. 11809-19, May 27 2016.
- [123] A. Selyutina, A. Bulnes-Ramos, and F. Diaz-Griffero, "Binding of host factors to stabilized HIV-1 capsid tubes," (in eng), *Virology*, vol. 523, pp. 1-5, Oct 2018.
- [124] D. Lau *et al.*, "Fluorescence Biosensor for Real-Time Interaction Dynamics of Host Proteins with HIV-1 Capsid Tubes," (in eng), *ACS Appl Mater Interfaces*, vol. 11, no. 38, pp. 34586-34594, Sep 25 2019.
- [125] B. J. Summers *et al.*, "Modular HIV-1 Capsid Assemblies Reveal Diverse Host-Capsid Recognition Mechanisms," (in eng), *Cell Host Microbe*, vol. 26, no. 2, pp. 203-216.e6, Aug 14 2019.
- [126] D. Lau *et al.*, "Rapid HIV-1 Capsid Interaction Screening Using Fluorescence Fluctuation Spectroscopy," (in eng), *Anal Chem*, vol. 93, no. 8, pp. 3786-3793, Mar 2 2021.
- [127] C. Grewe, A. Beck, and H. R. Gelderblom, "HIV: early virus-cell interactions," (in eng), *J Acquir Immune Defic Syndr (1988)*, vol. 3, no. 10, pp. 965-74, 1990.

- [128] D. Gao *et al.*, "Cyclic GMP-AMP synthase is an innate immune sensor of HIV and other retroviruses," (in eng), *Science*, vol. 341, no. 6148, pp. 903-6, Aug 23 2013.
- [129] R. Craigie and F. D. Bushman, "HIV DNA integration," (in eng), *Cold Spring Harb Perspect Med*, vol. 2, no. 7, p. a006890, Jul 2012.
- [130] M. Yamashita, O. Perez, T. J. Hope, and M. Emerman, "Evidence for direct involvement of the capsid protein in HIV infection of nondividing cells," (in eng), *PLoS Pathog*, vol. 3, no. 10, pp. 1502-10, Oct 26 2007.
- [131] F. Di Nunzio *et al.*, "Human nucleoporins promote HIV-1 docking at the nuclear pore, nuclear import and integration," (in eng), *PLoS One*, vol. 7, no. 9, p. e46037, 2012.
- [132] A. E. Hulme, Z. Kelley, E. A. Okocha, and T. J. Hope, "Identification of capsid mutations that alter the rate of HIV-1 uncoating in infected cells," (in eng), *J Virol*, vol. 89, no. 1, pp. 643-51, Jan 2015.
- [133] J. I. Mamede, G. C. Cianci, M. R. Anderson, and T. J. Hope, "Early cytoplasmic uncoating is associated with infectivity of HIV-1," (in eng), *Proc Natl Acad Sci U S A*, vol. 114, no. 34, pp. E7169-e7178, Aug 22 2017.
- [134] H. Xu *et al.*, "Evidence for biphasic uncoating during HIV-1 infection from a novel imaging assay," (in eng), *Retrovirology*, vol. 10, p. 70, Jul 9 2013.
- [135] K. Warren *et al.*, "Eukaryotic elongation factor 1 complex subunits are critical HIV-1 reverse transcription cofactors," (in eng), *Proc Natl Acad Sci U S A*, vol. 109, no. 24, pp. 9587-92, Jun 12 2012.
- [136] E. M. Campbell and T. J. Hope, "HIV-1 capsid: the multifaceted key player in HIV-1 infection," (in eng), *Nat Rev Microbiol*, vol. 13, no. 8, pp. 471-83, Aug 2015.
- [137] L. Li, K. Yoder, M. S. Hansen, J. Olvera, M. D. Miller, and F. D. Bushman, "Retroviral cDNA integration: stimulation by HMG I family proteins," (in eng), *J Virol*, vol. 74, no. 23, pp. 10965-74, Dec 2000.
- [138] C. M. Farnet and F. D. Bushman, "HIV-1 cDNA integration: requirement of HMG I(Y) protein for function of preintegration complexes in vitro," (in eng), *Cell*, vol. 88, no. 4, pp. 483-92, Feb 21 1997.
- [139] R. C. Burdick *et al.*, "HIV-1 uncoats in the nucleus near sites of integration," (in eng), *Proc Natl Acad Sci U S A*, vol. 117, no. 10, pp. 5486-5493, Mar 10 2020.
- [140] G. Blanco-Rodriguez *et al.*, "Remodeling of the Core Leads HIV-1 Preintegration Complex into the Nucleus of Human Lymphocytes," (in eng), *J Virol*, vol. 94, no. 11, May 18 2020.
- [141] T. G. Müller *et al.*, "HIV-1 uncoating by release of viral cDNA from capsid-like structures in the nucleus of infected cells," (in eng), *Elife*, vol. 10, Apr 27 2021.
- [142] C. Li, R. C. Burdick, K. Nagashima, W. S. Hu, and V. K. Pathak, "HIV-1 cores retain their integrity until minutes before uncoating in the nucleus," (in eng), *Proc Natl Acad Sci U S A*, vol. 118, no. 10, Mar 9 2021.
- [143] T. Maimon, N. Elad, I. Dahan, and O. Medalia, "The human nuclear pore complex as revealed by cryo-electron tomography," (in eng), *Structure*, vol. 20, no. 6, pp. 998-1006, Jun 6 2012.
- [144] K. H. Bui *et al.*, "Integrated structural analysis of the human nuclear pore complex scaffold," (in eng), *Cell*, vol. 155, no. 6, pp. 1233-43, Dec 5 2013.
- [145] X. Li *et al.*, "HIV-1 viral cores enter the nucleus collectively through the nuclear endocytosis-like pathway," (in eng), *Sci China Life Sci*, May 14 2020.

- [146] A. E. Hulme, O. Perez, and T. J. Hope, "Complementary assays reveal a relationship between HIV-1 uncoating and reverse transcription," (in eng), *Proc Natl Acad Sci U S A*, vol. 108, no. 24, pp. 9975-80, Jun 14 2011.
- [147] S. Rankovic, J. Varadarajan, R. Ramalho, C. Aiken, and I. Rousso, "Reverse Transcription Mechanically Initiates HIV-1 Capsid Disassembly," (in eng), *J Virol*, vol. 91, no. 12, Jun 15 2017.
- [148] M. K. Delaney, V. Malikov, Q. Chai, G. Zhao, and M. H. Naghavi, "Distinct functions of diaphanous-related formins regulate HIV-1 uncoating and transport," (in eng), *Proc Natl Acad Sci U S A*, vol. 114, no. 33, pp. E6932-e6941, Aug 15 2017.
- [149] P. Pawlica and L. Berthoux, "Cytoplasmic dynein promotes HIV-1 uncoating," (in eng), *Viruses*, vol. 6, no. 11, pp. 4195-211, Nov 4 2014.
- [150] Z. Lukic, A. Dharan, T. Fricke, F. Diaz-Griffero, and E. M. Campbell, "HIV-1 uncoating is facilitated by dynein and kinesin 1," (in eng), *J Virol*, vol. 88, no. 23, pp. 13613-25, Dec 2014.
- [151] D. J. Dismuke and C. Aiken, "Evidence for a functional link between uncoating of the human immunodeficiency virus type 1 core and nuclear import of the viral preintegration complex," (in eng), *J Virol*, vol. 80, no. 8, pp. 3712-20, Apr 2006.
- [152] N. J. Arhel *et al.*, "HIV-1 DNA Flap formation promotes uncoating of the pre-integration complex at the nuclear pore," (in eng), *Embo j*, vol. 26, no. 12, pp. 3025-37, Jun 20 2007.
- [153] D. J. Rawle and D. Harrich, "Toward the "unravelling" of HIV: Host cell factors involved in HIV-1 core uncoating," (in eng), *PLoS Pathog*, vol. 14, no. 10, p. e1007270, Oct 2018.
- [154] S. Yoo, D. G. Myszka, C. Yeh, M. McMurray, C. P. Hill, and W. I. Sundquist, "Molecular recognition in the HIV-1 capsid/cyclophilin A complex," (in eng), *J Mol Biol*, vol. 269, no. 5, pp. 780-95, Jun 27 1997.
- [155] E. Sokolskaja, D. M. Sayah, and J. Luban, "Target cell cyclophilin A modulates human immunodeficiency virus type 1 infectivity," (in eng), *J Virol*, vol. 78, no. 23, pp. 12800-8, Dec 2004.
- [156] L. Berthoux, S. Sebastian, E. Sokolskaja, and J. Luban, "Cyclophilin A is required for TRIM5{alpha}-mediated resistance to HIV-1 in Old World monkey cells," (in eng), *Proc Natl Acad Sci U S A*, vol. 102, no. 41, pp. 14849-53, Oct 11 2005.
- [157] M. Stremlau, B. Song, H. Javanbakht, M. Perron, and J. Sodroski, "Cyclophilin A: an auxiliary but not necessary cofactor for TRIM5alpha restriction of HIV-1," (in eng), *Virology*, vol. 351, no. 1, pp. 112-20, Jul 20 2006.
- [158] T. Hatziioannou, D. Perez-Caballero, S. Cowan, and P. D. Bieniasz, "Cyclophilin interactions with incoming human immunodeficiency virus type 1 capsids with opposing effects on infectivity in human cells," (in eng), *J Virol*, vol. 79, no. 1, pp. 176-83, Jan 2005.
- [159] Y. Li, A. K. Kar, and J. Sodroski, "Target cell type-dependent modulation of human immunodeficiency virus type 1 capsid disassembly by cyclophilin A," (in eng), *J Virol*, vol. 83, no. 21, pp. 10951-62, Nov 2009.
- [160] T. Ni *et al.*, "Intrinsic curvature of the HIV-1 CA hexamer underlies capsid topology and interaction with cyclophilin A," (in eng), *Nat Struct Mol Biol*, vol. 27, no. 9, pp. 855-862, Sep 2020.
- [161] V. B. Shah *et al.*, "The host proteins transportin SR2/TNPO3 and cyclophilin A exert opposing effects on HIV-1 uncoating," (in eng), *J Virol*, vol. 87, no. 1, pp. 422-32, Jan 2013.

- [162] M. Burse, J. Shi, and C. Aiken, "Cyclophilin A potentiates TRIM5 α inhibition of HIV-1 nuclear import without promoting TRIM5 α binding to the viral capsid," (in eng), *PLoS One*, vol. 12, no. 8, p. e0182298, 2017.
- [163] G. J. Towers, T. Hatzioannou, S. Cowan, S. P. Goff, J. Luban, and P. D. Bieniasz, "Cyclophilin A modulates the sensitivity of HIV-1 to host restriction factors," (in eng), *Nat Med*, vol. 9, no. 9, pp. 1138-43, Sep 2003.
- [164] A. Selyutina *et al.*, "Cyclophilin A Prevents HIV-1 Restriction in Lymphocytes by Blocking Human TRIM5 α Binding to the Viral Core," (in eng), *Cell Rep*, vol. 30, no. 11, pp. 3766-3777.e6, Mar 17 2020.
- [165] K. A. Matreyek and A. Engelman, "The requirement for nucleoporin NUP153 during human immunodeficiency virus type 1 infection is determined by the viral capsid," (in eng), *J Virol*, vol. 85, no. 15, pp. 7818-27, Aug 2011.
- [166] R. J. Miles, C. Kerridge, L. Hilditch, C. Monit, D. A. Jacques, and G. J. Towers, "MxB sensitivity of HIV-1 is determined by a highly variable and dynamic capsid surface," (in eng), *Elife*, vol. 9, Jun 17 2020.
- [167] R. Bernad, H. van der Velde, M. Fornerod, and H. Pickersgill, "Nup358/RanBP2 attaches to the nuclear pore complex via association with Nup88 and Nup214/CAN and plays a supporting role in CRM1-mediated nuclear protein export," (in eng), *Mol Cell Biol*, vol. 24, no. 6, pp. 2373-84, Mar 2004.
- [168] A. M. Meehan *et al.*, "A cyclophilin homology domain-independent role for Nup358 in HIV-1 infection," (in eng), *PLoS Pathog*, vol. 10, no. 2, p. e1003969, Feb 2014.
- [169] D. H. Lin, S. Zimmermann, T. Stuwe, E. Stuwe, and A. Hoelz, "Structural and functional analysis of the C-terminal domain of Nup358/RanBP2," (in eng), *J Mol Biol*, vol. 425, no. 8, pp. 1318-29, Apr 26 2013.
- [170] K. Bichel, A. J. Price, T. Schaller, G. J. Towers, S. M. Freund, and L. C. James, "HIV-1 capsid undergoes coupled binding and isomerization by the nuclear pore protein NUP358," (in eng), *Retrovirology*, vol. 10, p. 81, Jul 31 2013.
- [171] L. Xie *et al.*, "MxB impedes the NUP358-mediated HIV-1 pre-integration complex nuclear import and viral replication cooperatively with CPSF6," (in eng), *Retrovirology*, vol. 17, no. 1, p. 16, Jun 29 2020.
- [172] S. Hutten, S. Wälde, C. Spillner, J. Hauber, and R. H. Kehlenbach, "The nuclear pore component Nup358 promotes transportin-dependent nuclear import," (in eng), *J Cell Sci*, vol. 122, no. Pt 8, pp. 1100-10, Apr 15 2009.
- [173] L. Twyffels, C. Gueydan, and V. Kruys, "Transportin-1 and Transportin-2: protein nuclear import and beyond," (in eng), *FEBS Lett*, vol. 588, no. 10, pp. 1857-68, May 21 2014.
- [174] M. Arnold, A. Nath, J. Hauber, and R. H. Kehlenbach, "Multiple importins function as nuclear transport receptors for the Rev protein of human immunodeficiency virus type 1," (in eng), *J Biol Chem*, vol. 281, no. 30, pp. 20883-20890, Jul 28 2006.
- [175] J. Fernandez *et al.*, "Transportin-1 binds to the HIV-1 capsid via a nuclear localization signal and triggers uncoating," (in eng), *Nat Microbiol*, vol. 4, no. 11, pp. 1840-1850, Nov 2019.
- [176] A. M. Shamsuddin, "Metabolism and cellular functions of IP6: a review," (in eng), *Anticancer Res*, vol. 19, no. 5a, pp. 3733-6, Sep-Oct 1999.
- [177] D. L. Mallery *et al.*, "Cellular IP(6) Levels Limit HIV Production while Viruses that Cannot Efficiently Package IP(6) Are Attenuated for Infection and Replication," (in eng), *Cell Rep*, vol. 29, no. 12, pp. 3983-3996.e4, Dec 17 2019.

- [178] S. Kuroda, N. Nakagawa, C. Tokunaga, K. Tatematsu, and K. Tanizawa, "Mammalian homologue of the *Caenorhabditis elegans* UNC-76 protein involved in axonal outgrowth is a protein kinase C zeta-interacting protein," (in eng), *J Cell Biol*, vol. 144, no. 3, pp. 403-11, Feb 8 1999.
- [179] A. D. Maturana, T. Fujita, and S. Kuroda, "Functions of fasciculation and elongation protein zeta-1 (FEZ1) in the brain," (in eng), *ScientificWorldJournal*, vol. 10, pp. 1646-54, Aug 17 2010.
- [180] T. Fujita *et al.*, "Axonal guidance protein FEZ1 associates with tubulin and kinesin motor protein to transport mitochondria in neurites of NGF-stimulated PC12 cells," (in eng), *Biochem Biophys Res Commun*, vol. 361, no. 3, pp. 605-10, Sep 28 2007.
- [181] T. L. Blasius, D. Cai, G. T. Jih, C. P. Toret, and K. J. Verhey, "Two binding partners cooperate to activate the molecular motor Kinesin-1," (in eng), *J Cell Biol*, vol. 176, no. 1, pp. 11-7, Jan 1 2007.
- [182] J. J. Chua *et al.*, "Phosphorylation-regulated axonal dependent transport of syntaxin 1 is mediated by a Kinesin-1 adapter," (in eng), *Proc Natl Acad Sci U S A*, vol. 109, no. 15, pp. 5862-7, Apr 10 2012.
- [183] M. H. Naghavi, T. Hatziioannou, G. Gao, and S. P. Goff, "Overexpression of fasciculation and elongation protein zeta-1 (FEZ1) induces a post-entry block to retroviruses in cultured cells," (in eng), *Genes Dev*, vol. 19, no. 9, pp. 1105-15, May 1 2005.
- [184] J. Haedicke, C. Brown, and M. H. Naghavi, "The brain-specific factor FEZ1 is a determinant of neuronal susceptibility to HIV-1 infection," (in eng), *Proc Natl Acad Sci U S A*, vol. 106, no. 33, pp. 14040-5, Aug 18 2009.
- [185] E. Butkevich *et al.*, "Phosphorylation of FEZ1 by Microtubule Affinity Regulating Kinases regulates its function in presynaptic protein trafficking," (in eng), *Sci Rep*, vol. 6, p. 26965, Jun 1 2016.
- [186] V. Malikov and M. H. Naghavi, "Localized Phosphorylation of a Kinesin-1 Adaptor by a Capsid-Associated Kinase Regulates HIV-1 Motility and Uncoating," (in eng), *Cell Rep*, vol. 20, no. 12, pp. 2792-2799, Sep 19 2017.
- [187] M. D. Ruepp *et al.*, "Mammalian pre-mRNA 3' end processing factor CF Im 68 functions in mRNA export," (in eng), *Mol Biol Cell*, vol. 20, no. 24, pp. 5211-23, Dec 2009.
- [188] S. Dettwiler, C. Aringhieri, S. Cardinale, W. Keller, and S. M. Barabino, "Distinct sequence motifs within the 68-kDa subunit of cleavage factor Im mediate RNA binding, protein-protein interactions, and subcellular localization," (in eng), *J Biol Chem*, vol. 279, no. 34, pp. 35788-97, Aug 20 2004.
- [189] A. J. Price *et al.*, "CPSF6 defines a conserved capsid interface that modulates HIV-1 replication," (in eng), *PLoS Pathog*, vol. 8, no. 8, p. e1002896, 2012.
- [190] A. De Iaco, F. Santoni, A. Vannier, M. Guipponi, S. Antonarakis, and J. Luban, "TNPO3 protects HIV-1 replication from CPSF6-mediated capsid stabilization in the host cell cytoplasm," (in eng), *Retrovirology*, vol. 10, p. 20, Feb 15 2013.
- [191] T. Fricke *et al.*, "The ability of TNPO3-depleted cells to inhibit HIV-1 infection requires CPSF6," (in eng), *Retrovirology*, vol. 10, p. 46, Apr 26 2013.
- [192] K. Lee *et al.*, "HIV-1 capsid-targeting domain of cleavage and polyadenylation specificity factor 6," (in eng), *J Virol*, vol. 86, no. 7, pp. 3851-60, Apr 2012.
- [193] L. Lad *et al.*, "Functional label-free assays for characterizing the in vitro mechanism of action of small molecule modulators of capsid assembly," (in eng), *Biochemistry*, vol. 54, no. 13, pp. 2240-8, Apr 7 2015.

- [194] A. Saito *et al.*, "Capsid-CPSF6 Interaction Is Dispensable for HIV-1 Replication in Primary Cells but Is Selected during Virus Passage In Vivo," (in eng), *J Virol*, vol. 90, no. 15, pp. 6918-6935, Aug 1 2016.
- [195] T. C. Walther, M. Fornerod, H. Pickersgill, M. Goldberg, T. D. Allen, and I. W. Mattaj, "The nucleoporin Nup153 is required for nuclear pore basket formation, nuclear pore complex anchoring and import of a subset of nuclear proteins," (in eng), *Embo j*, vol. 20, no. 20, pp. 5703-14, Oct 15 2001.
- [196] C. R. Chin *et al.*, "Direct Visualization of HIV-1 Replication Intermediates Shows that Capsid and CPSF6 Modulate HIV-1 Intra-nuclear Invasion and Integration," (in eng), *Cell Rep*, vol. 13, no. 8, pp. 1717-31, Nov 24 2015.
- [197] C. Buffone *et al.*, "Nup153 Unlocks the Nuclear Pore Complex for HIV-1 Nuclear Translocation in Nondividing Cells," (in eng), *J Virol*, vol. 92, no. 19, Oct 1 2018.
- [198] Y. Koh *et al.*, "Differential effects of human immunodeficiency virus type 1 capsid and cellular factors nucleoporin 153 and LEDGF/p75 on the efficiency and specificity of viral DNA integration," (in eng), *J Virol*, vol. 87, no. 1, pp. 648-58, Jan 2013.
- [199] B. Wang *et al.*, "The COPII cargo adapter SEC24C is essential for neuronal homeostasis," (in eng), *J Clin Invest*, vol. 128, no. 8, pp. 3319-3332, Aug 1 2018.
- [200] S. S. Smaga, C. Xu, B. J. Summers, K. M. Digianantonio, J. R. Perilla, and Y. Xiong, "MxB Restricts HIV-1 by Targeting the Tri-hexamer Interface of the Viral Capsid," (in eng), *Structure*, vol. 27, no. 8, pp. 1234-1245.e5, Aug 6 2019.
- [201] O. Haller, P. Staeheli, and G. Kochs, "Interferon-induced Mx proteins in antiviral host defense," (in eng), *Biochimie*, vol. 89, no. 6-7, pp. 812-8, Jun-Jul 2007.
- [202] Z. Liu *et al.*, "The interferon-inducible MxB protein inhibits HIV-1 infection," (in eng), *Cell Host Microbe*, vol. 14, no. 4, pp. 398-410, Oct 16 2013.
- [203] I. Busnadiego *et al.*, "Host and viral determinants of Mx2 antiretroviral activity," (in eng), *J Virol*, vol. 88, no. 14, pp. 7738-52, Jul 2014.
- [204] C. Goujon *et al.*, "Human MX2 is an interferon-induced post-entry inhibitor of HIV-1 infection," (in eng), *Nature*, vol. 502, no. 7472, pp. 559-62, Oct 24 2013.
- [205] B. Schulte *et al.*, "Restriction of HIV-1 Requires the N-Terminal Region of MxB as a Capsid-Binding Motif but Not as a Nuclear Localization Signal," (in eng), *J Virol*, vol. 89, no. 16, pp. 8599-610, Aug 2015.
- [206] J. L. Fribourgh *et al.*, "Structural insight into HIV-1 restriction by MxB," (in eng), *Cell Host Microbe*, vol. 16, no. 5, pp. 627-638, Nov 12 2014.
- [207] A. Yu, K. A. Skorupka, A. J. Pak, B. K. Ganser-Pornillos, O. Pornillos, and G. A. Voth, "TRIM5 α self-assembly and compartmentalization of the HIV-1 viral capsid," (in eng), *Nat Commun*, vol. 11, no. 1, p. 1307, Mar 11 2020.
- [208] K. A. Skorupka, M. D. Roganowicz, D. E. Christensen, Y. Wan, O. Pornillos, and B. K. Ganser-Pornillos, "Hierarchical assembly governs TRIM5 α recognition of HIV-1 and retroviral capsids," (in eng), *Sci Adv*, vol. 5, no. 11, p. eaaw3631, Nov 2019.
- [209] L. Krishnan *et al.*, "The requirement for cellular transportin 3 (TNPO3 or TRN-SR2) during infection maps to human immunodeficiency virus type 1 capsid and not integrase," (in eng), *J Virol*, vol. 84, no. 1, pp. 397-406, Jan 2010.
- [210] A. Słońska, R. Polowy, A. Golke, and J. Cymerys, "Role of cytoskeletal motor proteins in viral infection," (in eng), *Postepy Hig Med Dosw (Online)*, vol. 66, pp. 810-7, Oct 30 2012.

- [211] R. P. Stidwill and U. F. Greber, "Intracellular Virus Trafficking Reveals Physiological Characteristics of the Cytoskeleton," (in eng), *News Physiol Sci*, vol. 15, pp. 67-71, Apr 2000.
- [212] A. Gennerich and R. D. Vale, "Walking the walk: how kinesin and dynein coordinate their steps," (in eng), *Curr Opin Cell Biol*, vol. 21, no. 1, pp. 59-67, Feb 2009.
- [213] J. M. Kollman, A. Merdes, L. Mourey, and D. A. Agard, "Microtubule nucleation by γ -tubulin complexes," (in eng), *Nat Rev Mol Cell Biol*, vol. 12, no. 11, pp. 709-21, Oct 12 2011.
- [214] J. Howard and A. A. Hyman, "Growth, fluctuation and switching at microtubule plus ends," (in eng), *Nat Rev Mol Cell Biol*, vol. 10, no. 8, pp. 569-74, Aug 2009.
- [215] D. A. Fletcher and R. D. Mullins, "Cell mechanics and the cytoskeleton," (in eng), *Nature*, vol. 463, no. 7280, pp. 485-92, Jan 28 2010.
- [216] E. Nogales, "Structural insights into microtubule function," (in eng), *Annu Rev Biochem*, vol. 69, pp. 277-302, 2000.
- [217] J. C. M. Meiring, B. I. Shneyer, and A. Akhmanova, "Generation and regulation of microtubule network asymmetry to drive cell polarity," (in eng), *Curr Opin Cell Biol*, vol. 62, pp. 86-95, Feb 2020.
- [218] E. Nogales, S. G. Wolf, and K. H. Downing, "Structure of the alpha beta tubulin dimer by electron crystallography," (in eng), *Nature*, vol. 391, no. 6663, pp. 199-203, Jan 8 1998.
- [219] M. Menéndez, G. Rivas, J. F. Díaz, and J. M. Andreu, "Control of the structural stability of the tubulin dimer by one high affinity bound magnesium ion at nucleotide N-site," (in eng), *J Biol Chem*, vol. 273, no. 1, pp. 167-76, Jan 2 1998.
- [220] G. M. Alushin, G. C. Lander, E. H. Kellogg, R. Zhang, D. Baker, and E. Nogales, "High-resolution microtubule structures reveal the structural transitions in $\alpha\beta$ -tubulin upon GTP hydrolysis," (in eng), *Cell*, vol. 157, no. 5, pp. 1117-29, May 22 2014.
- [221] L. G. Tilney *et al.*, "Microtubules: evidence for 13 protofilaments," (in eng), *J Cell Biol*, vol. 59, no. 2 Pt 1, pp. 267-75, Nov 1973.
- [222] Z. J. Donhauser, W. B. Jobs, and E. C. Binka, "Mechanics of microtubules: effects of protofilament orientation," (in eng), *Biophys J*, vol. 99, no. 5, pp. 1668-75, Sep 8 2010.
- [223] H. V. Goodson and E. M. Jonasson, "Microtubules and Microtubule-Associated Proteins," (in eng), *Cold Spring Harb Perspect Biol*, vol. 10, no. 6, Jun 1 2018.
- [224] A. Roll-Mecak, "Intrinsically disordered tubulin tails: complex tuners of microtubule functions?," (in eng), *Semin Cell Dev Biol*, vol. 37, pp. 11-9, Jan 2015.
- [225] L. A. Amos and D. Schlieper, "Microtubules and maps," (in eng), *Adv Protein Chem*, vol. 71, pp. 257-98, 2005.
- [226] D. Wloga and J. Gaertig, "Post-translational modifications of microtubules," (in eng), *Journal of Cell Science*, vol. 124, no. 1, pp. 154-154, 2011.
- [227] S. Westermann and K. Weber, "Post-translational modifications regulate microtubule function," (in eng), *Nat Rev Mol Cell Biol*, vol. 4, no. 12, pp. 938-47, Dec 2003.
- [228] Y. Song and S. T. Brady, "Post-translational modifications of tubulin: pathways to functional diversity of microtubules," (in eng), *Trends Cell Biol*, vol. 25, no. 3, pp. 125-36, Mar 2015.
- [229] A. Akhmanova and M. O. Steinmetz, "Control of microtubule organization and dynamics: two ends in the limelight," (in eng), *Nat Rev Mol Cell Biol*, vol. 16, no. 12, pp. 711-26, Dec 2015.

- [230] G. Drewes, A. Ebner, and E. M. Mandelkow, "MAPs, MARKs and microtubule dynamics," (in eng), *Trends Biochem Sci*, vol. 23, no. 8, pp. 307-11, Aug 1998.
- [231] S. Bodakuntla, A. S. Jijumon, C. Villablanca, C. Gonzalez-Billault, and C. Janke, "Microtubule-Associated Proteins: Structuring the Cytoskeleton," (in eng), *Trends Cell Biol*, vol. 29, no. 10, pp. 804-819, Oct 2019.
- [232] I. G. Karafyllidis and D. C. Lagoudas, "Microtubules as mechanical force sensors," (in eng), *Biosystems*, vol. 88, no. 1-2, pp. 137-46, Mar 2007.
- [233] G. J. Brouhard and L. M. Rice, "Microtubule dynamics: an interplay of biochemistry and mechanics," (in eng), *Nat Rev Mol Cell Biol*, vol. 19, no. 7, pp. 451-463, Jul 2018.
- [234] N. B. Gudimchuk *et al.*, "Mechanisms of microtubule dynamics and force generation examined with computational modeling and electron cryotomography," (in eng), *Nat Commun*, vol. 11, no. 1, p. 3765, Jul 28 2020.
- [235] G. J. Brouhard, "Dynamic instability 30 years later: complexities in microtubule growth and catastrophe," (in eng), *Mol Biol Cell*, vol. 26, no. 7, pp. 1207-10, Apr 1 2015.
- [236] E. Nogales, M. Whittaker, R. A. Milligan, and K. H. Downing, "High-resolution model of the microtubule," (in eng), *Cell*, vol. 96, no. 1, pp. 79-88, Jan 8 1999.
- [237] B. Vulevic and J. J. Correia, "Thermodynamic and structural analysis of microtubule assembly: the role of GTP hydrolysis," (in eng), *Biophys J*, vol. 72, no. 3, pp. 1357-75, Mar 1997.
- [238] M. K. Gardner, M. Zanic, and J. Howard, "Microtubule catastrophe and rescue," (in eng), *Curr Opin Cell Biol*, vol. 25, no. 1, pp. 14-22, Feb 2013.
- [239] D. N. Drechsel and M. W. Kirschner, "The minimum GTP cap required to stabilize microtubules," (in eng), *Curr Biol*, vol. 4, no. 12, pp. 1053-61, Dec 1 1994.
- [240] J. Roostalu, C. Thomas, N. I. Cade, S. Kunzelmann, I. A. Taylor, and T. Surrey, "The speed of GTP hydrolysis determines GTP cap size and controls microtubule stability," (in eng), *Elife*, vol. 9, Feb 13 2020.
- [241] C. Gell *et al.*, "Microtubule dynamics reconstituted in vitro and imaged by single-molecule fluorescence microscopy," (in eng), *Methods Cell Biol*, vol. 95, pp. 221-45, 2010.
- [242] A. A. Hyman, S. Salser, D. N. Drechsel, N. Unwin, and T. J. Mitchison, "Role of GTP hydrolysis in microtubule dynamics: information from a slowly hydrolyzable analogue, GMPCPP," (in eng), *Mol Biol Cell*, vol. 3, no. 10, pp. 1155-67, Oct 1992.
- [243] I. V. Sandoval and K. Weber, "Guanasone 5'-(alpha,beta-methylene)triphosphate enhances specifically microtubule nucleation and stops the treadmill of tubulin protomers," (in eng), *J Biol Chem*, vol. 255, no. 14, pp. 6966-74, Jul 25 1980.
- [244] S. N. Timasheff and L. M. Grisham, "In vitro assembly of cytoplasmic microtubules," (in eng), *Annu Rev Biochem*, vol. 49, pp. 565-91, 1980.
- [245] I. Arnal and R. H. Wade, "How does taxol stabilize microtubules?," (in eng), *Curr Biol*, vol. 5, no. 8, pp. 900-8, Aug 1 1995.
- [246] J. M. Andreu *et al.*, "Solution structure of Taxotere-induced microtubules to 3-nm resolution. The change in protofilament number is linked to the binding of the taxol side chain," (in eng), *J Biol Chem*, vol. 269, no. 50, pp. 31785-92, Dec 16 1994.
- [247] P. B. Schiff, J. Fant, and S. B. Horwitz, "Promotion of microtubule assembly in vitro by taxol," (in eng), *Nature*, vol. 277, no. 5698, pp. 665-7, Feb 22 1979.
- [248] H. Xiao *et al.*, "Insights into the mechanism of microtubule stabilization by Taxol," (in eng), *Proc Natl Acad Sci U S A*, vol. 103, no. 27, pp. 10166-10173, Jul 5 2006.

- [249] J. J. Field, J. F. Díaz, and J. H. Miller, "The binding sites of microtubule-stabilizing agents," (in eng), *Chem Biol*, vol. 20, no. 3, pp. 301-15, Mar 21 2013.
- [250] B. T. Castle, S. McCubbin, L. S. Prahl, J. N. Bernens, D. Sept, and D. J. Odde, "Mechanisms of kinetic stabilization by the drugs paclitaxel and vinblastine," (in eng), *Mol Biol Cell*, vol. 28, no. 9, pp. 1238-1257, May 1 2017.
- [251] P. B. Schiff and S. B. Horwitz, "Taxol stabilizes microtubules in mouse fibroblast cells," (in eng), *Proc Natl Acad Sci U S A*, vol. 77, no. 3, pp. 1561-5, Mar 1980.
- [252] S. G. Arbuck *et al.*, "Clinical development of Taxol," (in eng), *J Natl Cancer Inst Monogr*, no. 15, pp. 11-24, 1993.
- [253] A. Bukrinskaya, B. Brichacek, A. Mann, and M. Stevenson, "Establishment of a functional human immunodeficiency virus type 1 (HIV-1) reverse transcription complex involves the cytoskeleton," (in eng), *J Exp Med*, vol. 188, no. 11, pp. 2113-25, Dec 7 1998.
- [254] V. R. de Soultrait *et al.*, "HIV-1 integrase interacts with yeast microtubule-associated proteins," (in eng), *Biochim Biophys Acta*, vol. 1575, no. 1-3, pp. 40-8, May 3 2002.
- [255] N. R. Watts *et al.*, "HIV-1 rev depolymerizes microtubules to form stable bilayered rings," (in eng), *J Cell Biol*, vol. 150, no. 2, pp. 349-60, Jul 24 2000.
- [256] L. Caly, V. T. Kassouf, G. W. Moseley, R. J. Diefenbach, A. L. Cunningham, and D. A. Jans, "Fast track, dynein-dependent nuclear targeting of human immunodeficiency virus Vpr protein; impaired trafficking in a clinical isolate," (in eng), *Biochem Biophys Res Commun*, vol. 470, no. 3, pp. 735-740, Feb 12 2016.
- [257] S. Desfarges, B. Salin, C. Calmels, M. L. Andreola, V. Parissi, and M. Fournier, "HIV-1 integrase trafficking in *S. cerevisiae*: a useful model to dissect the microtubule network involvement of viral protein nuclear import," (in eng), *Yeast*, vol. 26, no. 1, pp. 39-54, Jan 2009.
- [258] T. Matanis *et al.*, "Bicaudal-D regulates COPI-independent Golgi-ER transport by recruiting the dynein-dynactin motor complex," (in eng), *Nat Cell Biol*, vol. 4, no. 12, pp. 986-92, Dec 2002.
- [259] D. Splinter *et al.*, "Bicaudal D2, dynein, and kinesin-1 associate with nuclear pore complexes and regulate centrosome and nuclear positioning during mitotic entry," (in eng), *PLoS Biol*, vol. 8, no. 4, p. e1000350, Apr 6 2010.
- [260] Y. Liu *et al.*, "Bicaudal-D uses a parallel, homodimeric coiled coil with heterotypic registry to coordinate recruitment of cargos to dynein," (in eng), *Genes Dev*, vol. 27, no. 11, pp. 1233-46, Jun 1 2013.
- [261] L. A. Martinez-Carrera and B. Wirth, "Dominant spinal muscular atrophy is caused by mutations in BICD2, an important golgin protein," (in eng), *Front Neurosci*, vol. 9, p. 401, 2015.
- [262] R. J. McKenney, W. Huynh, M. E. Tanenbaum, G. Bhabha, and R. D. Vale, "Activation of cytoplasmic dynein motility by dynactin-cargo adapter complexes," (in eng), *Science*, vol. 345, no. 6194, pp. 337-41, Jul 18 2014.
- [263] S. Strunze *et al.*, "Kinesin-1-mediated capsid disassembly and disruption of the nuclear pore complex promote virus infection," (in eng), *Cell Host Microbe*, vol. 10, no. 3, pp. 210-23, Sep 15 2011.
- [264] W. O. Hancock, "Bidirectional cargo transport: moving beyond tug of war," (in eng), *Nat Rev Mol Cell Biol*, vol. 15, no. 9, pp. 615-28, Sep 2014.

- [265] M. J. Müller, S. Klumpp, and R. Lipowsky, "Tug-of-war as a cooperative mechanism for bidirectional cargo transport by molecular motors," (in eng), *Proc Natl Acad Sci U S A*, vol. 105, no. 12, pp. 4609-14, Mar 25 2008.
- [266] A. Dharan and E. M. Campbell, "Role of Microtubules and Microtubule-Associated Proteins in HIV-1 Infection," (in eng), *J Virol*, vol. 92, no. 16, Aug 15 2018.
- [267] M. H. Naghavi, "HIV-1 capsid exploitation of the host microtubule cytoskeleton during early infection," (in eng), *Retrovirology*, vol. 18, no. 1, p. 19, Jul 6 2021.
- [268] L. G. Lippert *et al.*, "Angular measurements of the dynein ring reveal a stepping mechanism dependent on a flexible stalk," (in eng), *Proc Natl Acad Sci U S A*, vol. 114, no. 23, pp. E4564-e4573, Jun 6 2017.
- [269] L. S. Ferro, S. Can, M. A. Turner, M. M. ElShenawy, and A. Yildiz, "Kinesin and dynein use distinct mechanisms to bypass obstacles," (in eng), *Elife*, vol. 8, Sep 9 2019.
- [270] Y. Gao, S. M. Anthony, Y. Yu, Y. Yi, and Y. Yu, "Cargos Rotate at Microtubule Intersections during Intracellular Trafficking," (in eng), *Biophys J*, vol. 114, no. 12, pp. 2900-2909, Jun 19 2018.
- [271] A. B. Kolomeisky, "Motor proteins and molecular motors: how to operate machines at the nanoscale," (in eng), *J Phys Condens Matter*, vol. 25, no. 46, p. 463101, Nov 20 2013.
- [272] Y. Kato, T. Miyakawa, and M. Tanokura, "Overview of the mechanism of cytoskeletal motors based on structure," (in eng), *Biophys Rev*, vol. 10, no. 2, pp. 571-581, Apr 2018.
- [273] P. Höök and R. B. Vallee, "The dynein family at a glance," (in eng), *J Cell Sci*, vol. 119, no. Pt 21, pp. 4369-71, Nov 1 2006.
- [274] N. Hirokawa, Y. Noda, Y. Tanaka, and S. Niwa, "Kinesin superfamily motor proteins and intracellular transport," (in eng), *Nat Rev Mol Cell Biol*, vol. 10, no. 10, pp. 682-96, Oct 2009.
- [275] N. Arhel *et al.*, "Quantitative four-dimensional tracking of cytoplasmic and nuclear HIV-1 complexes," (in eng), *Nat Methods*, vol. 3, no. 10, pp. 817-24, Oct 2006.
- [276] G. Schiavo, L. Greensmith, M. Hafezparast, and E. M. Fisher, "Cytoplasmic dynein heavy chain: the servant of many masters," (in eng), *Trends Neurosci*, vol. 36, no. 11, pp. 641-51, Nov 2013.
- [277] B. J. Schnapp and T. S. Reese, "Dynein is the motor for retrograde axonal transport of organelles," (in eng), *Proc Natl Acad Sci U S A*, vol. 86, no. 5, pp. 1548-52, Mar 1989.
- [278] V. Belyy, M. A. Schlager, H. Foster, A. E. Reimer, A. P. Carter, and A. Yildiz, "The mammalian dynein-dynactin complex is a strong opponent to kinesin in a tug-of-war competition," (in eng), *Nat Cell Biol*, vol. 18, no. 9, pp. 1018-24, Sep 2016.
- [279] T. Torisawa *et al.*, "Autoinhibition and cooperative activation mechanisms of cytoplasmic dynein," (in eng), *Nat Cell Biol*, vol. 16, no. 11, pp. 1118-24, Nov 2014.
- [280] S. L. Reck-Peterson, "Dynactin revealed," (in eng), *Nat Struct Mol Biol*, vol. 22, no. 5, pp. 359-60, May 2015.
- [281] T. A. Schroer, "Dynactin," (in eng), *Annu Rev Cell Dev Biol*, vol. 20, pp. 759-79, 2004.
- [282] M. P. Dodding, "Backseat drivers: Regulation of dynein motility," (in eng), *Cell Res*, vol. 24, no. 12, pp. 1385-6, Dec 2014.
- [283] J. A. Cross and M. P. Dodding, "Motor-cargo adaptors at the organelle-cytoskeleton interface," (in eng), *Curr Opin Cell Biol*, vol. 59, pp. 16-23, Aug 2019.
- [284] A. Akhmanova and J. A. Hammer, 3rd, "Linking molecular motors to membrane cargo," (in eng), *Curr Opin Cell Biol*, vol. 22, no. 4, pp. 479-87, Aug 2010.

- [285] M. A. Olenick and E. L. F. Holzbaur, "Dynein activators and adaptors at a glance," (in eng), *J Cell Sci*, vol. 132, no. 6, Mar 15 2019.
- [286] S. L. Reck-Peterson, W. B. Redwine, R. D. Vale, and A. P. Carter, "The cytoplasmic dynein transport machinery and its many cargoes," (in eng), *Nat Rev Mol Cell Biol*, vol. 19, no. 6, pp. 382-398, Jun 2018.
- [287] M. A. Schlager, H. T. Hoang, L. Urnavicius, S. L. Bullock, and A. P. Carter, "In vitro reconstitution of a highly processive recombinant human dynein complex," (in eng), *Embo j*, vol. 33, no. 17, pp. 1855-68, Sep 1 2014.
- [288] C. M. Schroeder and R. D. Vale, "Assembly and activation of dynein-dynactin by the cargo adaptor protein Hook3," (in eng), *J Cell Biol*, vol. 214, no. 3, pp. 309-18, Aug 1 2016.
- [289] L. Urnavicius *et al.*, "The structure of the dynactin complex and its interaction with dynein," (in eng), *Science*, vol. 347, no. 6229, pp. 1441-1446, Mar 27 2015.
- [290] K. Zhang *et al.*, "Cryo-EM Reveals How Human Cytoplasmic Dynein Is Auto-inhibited and Activated," (in eng), *Cell*, vol. 169, no. 7, pp. 1303-1314.e18, Jun 15 2017.
- [291] A. J. Roberts *et al.*, "ATP-driven remodeling of the linker domain in the dynein motor," (in eng), *Structure*, vol. 20, no. 10, pp. 1670-80, Oct 10 2012.
- [292] A. J. Roberts *et al.*, "AAA+ Ring and linker swing mechanism in the dynein motor," (in eng), *Cell*, vol. 136, no. 3, pp. 485-95, Feb 6 2009.
- [293] J. Lin, K. Okada, M. Raytchev, M. C. Smith, and D. Nicastro, "Structural mechanism of the dynein power stroke," (in eng), *Nat Cell Biol*, vol. 16, no. 5, pp. 479-85, May 2014.
- [294] C. Cho and R. D. Vale, "The mechanism of dynein motility: insight from crystal structures of the motor domain," (in eng), *Biochim Biophys Acta*, vol. 1823, no. 1, pp. 182-91, Jan 2012.
- [295] T. A. Schroer and M. P. Sheetz, "Two activators of microtubule-based vesicle transport," (in eng), *J Cell Biol*, vol. 115, no. 5, pp. 1309-18, Dec 1991.
- [296] S. R. Gill, T. A. Schroer, I. Szilak, E. R. Steuer, M. P. Sheetz, and D. W. Cleveland, "Dynactin, a conserved, ubiquitously expressed component of an activator of vesicle motility mediated by cytoplasmic dynein," (in eng), *J Cell Biol*, vol. 115, no. 6, pp. 1639-50, Dec 1991.
- [297] S. Chowdhury, S. A. Ketcham, T. A. Schroer, and G. C. Lander, "Structural organization of the dynein-dynactin complex bound to microtubules," (in eng), *Nat Struct Mol Biol*, vol. 22, no. 4, pp. 345-7, Apr 2015.
- [298] T. Y. Yeh, N. J. Quintyne, B. R. Scipioni, D. M. Eckley, and T. A. Schroer, "Dynactin's pointed-end complex is a cargo-targeting module," (in eng), *Mol Biol Cell*, vol. 23, no. 19, pp. 3827-37, Oct 2012.
- [299] R. Qiu, J. Zhang, and X. Xiang, "p25 of the dynactin complex plays a dual role in cargo binding and dynactin regulation," (in eng), *J Biol Chem*, vol. 293, no. 40, pp. 15606-15619, Oct 5 2018.
- [300] S. Yan *et al.*, "Atomic-resolution structure of the CAP-Gly domain of dynactin on polymeric microtubules determined by magic angle spinning NMR spectroscopy," (in eng), *Proc Natl Acad Sci U S A*, vol. 112, no. 47, pp. 14611-6, Nov 24 2015.
- [301] R. J. McKenney, W. Huynh, R. D. Vale, and M. Sirajuddin, "Tyrosination of α -tubulin controls the initiation of processive dynein-dynactin motility," (in eng), *Embo j*, vol. 35, no. 11, pp. 1175-85, Jun 1 2016.
- [302] I. M. Palacios and D. St Johnston, "Kinesin light chain-independent function of the Kinesin heavy chain in cytoplasmic streaming and posterior localisation in the *Drosophila* oocyte," (in eng), *Development*, vol. 129, no. 23, pp. 5473-85, Dec 2002.

- [303] Q. Cai, C. Gerwin, and Z. H. Sheng, "Syntabulin-mediated anterograde transport of mitochondria along neuronal processes," (in eng), *J Cell Biol*, vol. 170, no. 6, pp. 959-69, Sep 12 2005.
- [304] E. E. Glater, L. J. Megeath, R. S. Stowers, and T. L. Schwarz, "Axonal transport of mitochondria requires mltin to recruit kinesin heavy chain and is light chain independent," (in eng), *J Cell Biol*, vol. 173, no. 4, pp. 545-57, May 22 2006.
- [305] Y. Y. Yip *et al.*, "The light chains of kinesin-1 are autoinhibited," (in eng), *Proc Natl Acad Sci U S A*, vol. 113, no. 9, pp. 2418-23, Mar 1 2016.
- [306] J. G. Gindhart, Jr., C. J. Desai, S. Beushausen, K. Zinn, and L. S. Goldstein, "Kinesin light chains are essential for axonal transport in *Drosophila*," (in eng), *J Cell Biol*, vol. 141, no. 2, pp. 443-54, Apr 20 1998.
- [307] H. Inomata *et al.*, "A scaffold protein JIP-1b enhances amyloid precursor protein phosphorylation by JNK and its association with kinesin light chain 1," (in eng), *J Biol Chem*, vol. 278, no. 25, pp. 22946-55, Jun 20 2003.
- [308] D. S. Friedman and R. D. Vale, "Single-molecule analysis of kinesin motility reveals regulation by the cargo-binding tail domain," (in eng), *Nat Cell Biol*, vol. 1, no. 5, pp. 293-7, Sep 1999.
- [309] K. A. Dietrich, C. V. Sindelar, P. D. Brewer, K. H. Downing, C. R. Cremo, and S. E. Rice, "The kinesin-1 motor protein is regulated by a direct interaction of its head and tail," (in eng), *Proc Natl Acad Sci U S A*, vol. 105, no. 26, pp. 8938-43, Jul 1 2008.
- [310] H. Y. Kaan, D. D. Hackney, and F. Kozielski, "The structure of the kinesin-1 motor-tail complex reveals the mechanism of autoinhibition," (in eng), *Science*, vol. 333, no. 6044, pp. 883-5, Aug 12 2011.
- [311] K. J. Verhey, D. L. Lizotte, T. Abramson, L. Barenboim, B. J. Schnapp, and T. A. Rapoport, "Light chain-dependent regulation of Kinesin's interaction with microtubules," (in eng), *J Cell Biol*, vol. 143, no. 4, pp. 1053-66, Nov 16 1998.
- [312] J. J. B. Cockburn, S. J. Hesketh, P. Mulhair, M. Thomsen, M. J. O'Connell, and M. Way, "Insights into Kinesin-1 Activation from the Crystal Structure of KLC2 Bound to JIP3," (in eng), *Structure*, vol. 26, no. 11, pp. 1486-1498.e6, Nov 6 2018.
- [313] G. Woehlke and M. Schliwa, "Walking on two heads: the many talents of kinesin," (in eng), *Nat Rev Mol Cell Biol*, vol. 1, no. 1, pp. 50-8, Oct 2000.
- [314] Y. Inoue, Y. Y. Toyoshima, A. H. Iwane, S. Morimoto, H. Higuchi, and T. Yanagida, "Movements of truncated kinesin fragments with a short or an artificial flexible neck," (in eng), *Proc Natl Acad Sci U S A*, vol. 94, no. 14, pp. 7275-80, Jul 8 1997.
- [315] K. S. Thorn, J. A. Ubersax, and R. D. Vale, "Engineering the processive run length of the kinesin motor," (in eng), *J Cell Biol*, vol. 151, no. 5, pp. 1093-100, Nov 27 2000.
- [316] B. G. Budaitis *et al.*, "Neck linker docking is critical for Kinesin-1 force generation in cells but at a cost to motor speed and processivity," (in eng), *Elife*, vol. 8, May 14 2019.
- [317] G. Woehlke, A. K. Ruby, C. L. Hart, B. Ly, N. Hom-Booher, and R. D. Vale, "Microtubule interaction site of the kinesin motor," (in eng), *Cell*, vol. 90, no. 2, pp. 207-16, Jul 25 1997.
- [318] A. Marx, A. Hoenger, and E. Mandelkow, "Structures of kinesin motor proteins," (in eng), *Cell Motil Cytoskeleton*, vol. 66, no. 11, pp. 958-66, Nov 2009.
- [319] B. Gigant *et al.*, "Structure of a kinesin-tubulin complex and implications for kinesin motility," (in eng), *Nat Struct Mol Biol*, vol. 20, no. 8, pp. 1001-7, Aug 2013.

- [320] Y. H. Song *et al.*, "Structure of a fast kinesin: implications for ATPase mechanism and interactions with microtubules," (in eng), *Embo j*, vol. 20, no. 22, pp. 6213-25, Nov 15 2001.
- [321] C. T. Friel and J. P. Welburn, "Parts list for a microtubule depolymerising kinesin," (in eng), *Biochem Soc Trans*, vol. 46, no. 6, pp. 1665-1672, Dec 17 2018.
- [322] J. Atherton *et al.*, "Conserved mechanisms of microtubule-stimulated ADP release, ATP binding, and force generation in transport kinesins," (in eng), *Elife*, vol. 3, p. e03680, Sep 10 2014.
- [323] Z. Abraham, E. Hawley, D. Hayosh, V. A. Webster-Wood, and O. Akkus, "Kinesin and Dynein Mechanics: Measurement Methods and Research Applications," (in eng), *J Biomech Eng*, vol. 140, no. 2, pp. 0208051-02080511, Feb 1 2018.
- [324] M. J. Schnitzer and S. M. Block, "Kinesin hydrolyses one ATP per 8-nm step," (in eng), *Nature*, vol. 388, no. 6640, pp. 386-90, Jul 24 1997.
- [325] P. R. Nicovich, J. Walsh, T. Böcking, and K. Gaus, "NicoLase-An open-source diode laser combiner, fiber launch, and sequencing controller for fluorescence microscopy," (in eng), *PLoS One*, vol. 12, no. 3, p. e0173879, 2017.
- [326] J. Y. Tinevez *et al.*, "TrackMate: An open and extensible platform for single-particle tracking," (in eng), *Methods*, vol. 115, pp. 80-90, Feb 15 2017.
- [327] P. O. Widlund *et al.*, "One-step purification of assembly-competent tubulin from diverse eukaryotic sources," (in eng), *Mol Biol Cell*, vol. 23, no. 22, pp. 4393-401, Nov 2012.
- [328] M. Castoldi and A. V. Popov, "Purification of brain tubulin through two cycles of polymerization-depolymerization in a high-molarity buffer," (in eng), *Protein Expr Purif*, vol. 32, no. 1, pp. 83-8, Nov 2003.
- [329] A. Hyman *et al.*, "Preparation of modified tubulins," (in eng), *Methods Enzymol*, vol. 196, pp. 478-85, 1991.
- [330] I. Gross, H. Hohenberg, and H. G. Kräusslich, "In vitro assembly properties of purified bacterially expressed capsid proteins of human immunodeficiency virus," (in eng), *Eur J Biochem*, vol. 249, no. 2, pp. 592-600, Oct 15 1997.
- [331] E. Barklis *et al.*, "Characterization of the in vitro HIV-1 capsid assembly pathway," (in eng), *Journal of molecular biology*, vol. 387, no. 2, pp. 376-389, 2009.
- [332] W. Zhang, S. Cao, J. L. Martin, J. D. Mueller, and L. M. Mansky, "Morphology and ultrastructure of retrovirus particles," (in eng), *AIMS Biophys*, vol. 2, no. 3, pp. 343-369, 2015.
- [333] K. D. Jayappa *et al.*, "Human immunodeficiency virus type 1 employs the cellular dynein light chain 1 protein for reverse transcription through interaction with its integrase protein," (in eng), *J Virol*, vol. 89, no. 7, pp. 3497-511, Apr 2015.
- [334] J. B. Bingham, S. J. King, and T. A. Schroer, "Purification of dynactin and dynein from brain tissue," (in eng), *Methods Enzymol*, vol. 298, pp. 171-84, 1998.
- [335] M. A. Welte, "Bidirectional transport along microtubules," (in eng), *Curr Biol*, vol. 14, no. 13, pp. R525-37, Jul 13 2004.
- [336] A. L. Jolly and V. I. Gelfand, "Bidirectional intracellular transport: utility and mechanism," (in eng), *Biochem Soc Trans*, vol. 39, no. 5, pp. 1126-30, Oct 2011.
- [337] M. P. Dodding and M. Way, "Coupling viruses to dynein and kinesin-1," (in eng), *Embo j*, vol. 30, no. 17, pp. 3527-39, Aug 31 2011.
- [338] M. H. Naghavi and D. Walsh, "Microtubule Regulation and Function during Virus Infection," (in eng), *J Virol*, vol. 91, no. 16, Aug 15 2017.

- [339] U. F. Greber and M. Way, "A superhighway to virus infection," (in eng), *Cell*, vol. 124, no. 4, pp. 741-54, Feb 24 2006.
- [340] J. Ren, S. Wang, H. Chen, W. Wang, L. Huo, and W. Feng, "Coiled-coil 1-mediated fastening of the neck and motor domains for kinesin-3 autoinhibition," (in eng), *Proc Natl Acad Sci U S A*, vol. 115, no. 51, pp. E11933-e11942, Dec 18 2018.
- [341] V. Henrichs *et al.*, "Mitochondria-adaptor TRAK1 promotes kinesin-1 driven transport in crowded environments," *Nature Communications*, vol. 11, no. 1, p. 3123, 2020/06/19 2020.
- [342] A. E. Twelvetrees, F. Lesept, E. L. F. Holzbaur, and J. T. Kittler, "The adaptor proteins HAP1a and GRIP1 collaborate to activate the kinesin-1 isoform KIF5C," (in eng), *J Cell Sci*, vol. 132, no. 24, Dec 13 2019.
- [343] S. R. Norris, M. F. Núñez, and K. J. Verhey, "Influence of fluorescent tag on the motility properties of kinesin-1 in single-molecule assays," (in eng), *Biophys J*, vol. 108, no. 5, pp. 1133-43, Mar 10 2015.
- [344] D. Cai, K. J. Verhey, and E. Meyhöfer, "Tracking single Kinesin molecules in the cytoplasm of mammalian cells," (in eng), *Biophys J*, vol. 92, no. 12, pp. 4137-44, Jun 15 2007.
- [345] P. J. Hooikaas *et al.*, "MAP7 family proteins regulate kinesin-1 recruitment and activation," (in eng), *J Cell Biol*, vol. 218, no. 4, pp. 1298-1318, Apr 1 2019.
- [346] S. M. Block, L. S. Goldstein, and B. J. Schnapp, "Bead movement by single kinesin molecules studied with optical tweezers," (in eng), *Nature*, vol. 348, no. 6299, pp. 348-52, Nov 22 1990.
- [347] A. Yildiz, M. Tomishige, R. D. Vale, and P. R. Selvin, "Kinesin walks hand-over-hand," (in eng), *Science*, vol. 303, no. 5658, pp. 676-8, Jan 30 2004.
- [348] S. R. Tymanskyj, B. H. Yang, K. J. Verhey, and L. Ma, "MAP7 regulates axon morphogenesis by recruiting kinesin-1 to microtubules and modulating organelle transport," (in eng), *Elife*, vol. 7, Aug 22 2018.
- [349] B. Y. Monroy, D. L. Sawyer, B. E. Ackermann, M. M. Borden, T. C. Tan, and K. M. Ori-McKenney, "Competition between microtubule-associated proteins directs motor transport," (in eng), *Nat Commun*, vol. 9, no. 1, p. 1487, Apr 16 2018.
- [350] D. Lau *et al.*, "Self-Assembly of Fluorescent HIV Capsid Spheres for Detection of Capsid Binders," (in eng), *Langmuir*, vol. 36, no. 13, pp. 3624-3632, Apr 7 2020.
- [351] T. E. Sladewski *et al.*, "Recruitment of two dyneins to an mRNA-dependent Bicaudal D transport complex," (in eng), *Elife*, vol. 7, Jun 26 2018.
- [352] M. A. McClintock *et al.*, "RNA-directed activation of cytoplasmic dynein-1 in reconstituted transport RNPs," (in eng), *Elife*, vol. 7, Jun 26 2018.

Chapter 8

Supplementary information

8.1. Immobilization of pre-assembled microtubules and HIV-1 capsids on modified surfaces

The surface chemistries for immobilizing assembled microtubules and HIV-1 capsid are schematically shown (**Fig. 8.1.A-B**). Immobilized microtubules and capsid were used for the TIRFm motility assay and the TIRFm capsid binding assay, respectively. Microtubules were immobilized by adding biotinylated anti- α -tubulin antibody to our standard PLL-PEG-biotin-streptavidin system. HIV-1 capsids were immobilized using a tandem-antibody system (a primary mouse anti-CA antibody and a secondary biotinylated anti-mouse IgG F(AB')₂ fragment) with our standard PLL-PEG-biotin-streptavidin system. Representative TIRFm images show immobilized microtubules (**Fig. 8.1.C**) and HIV-1 capsids (**Fig. 8.1.D**).

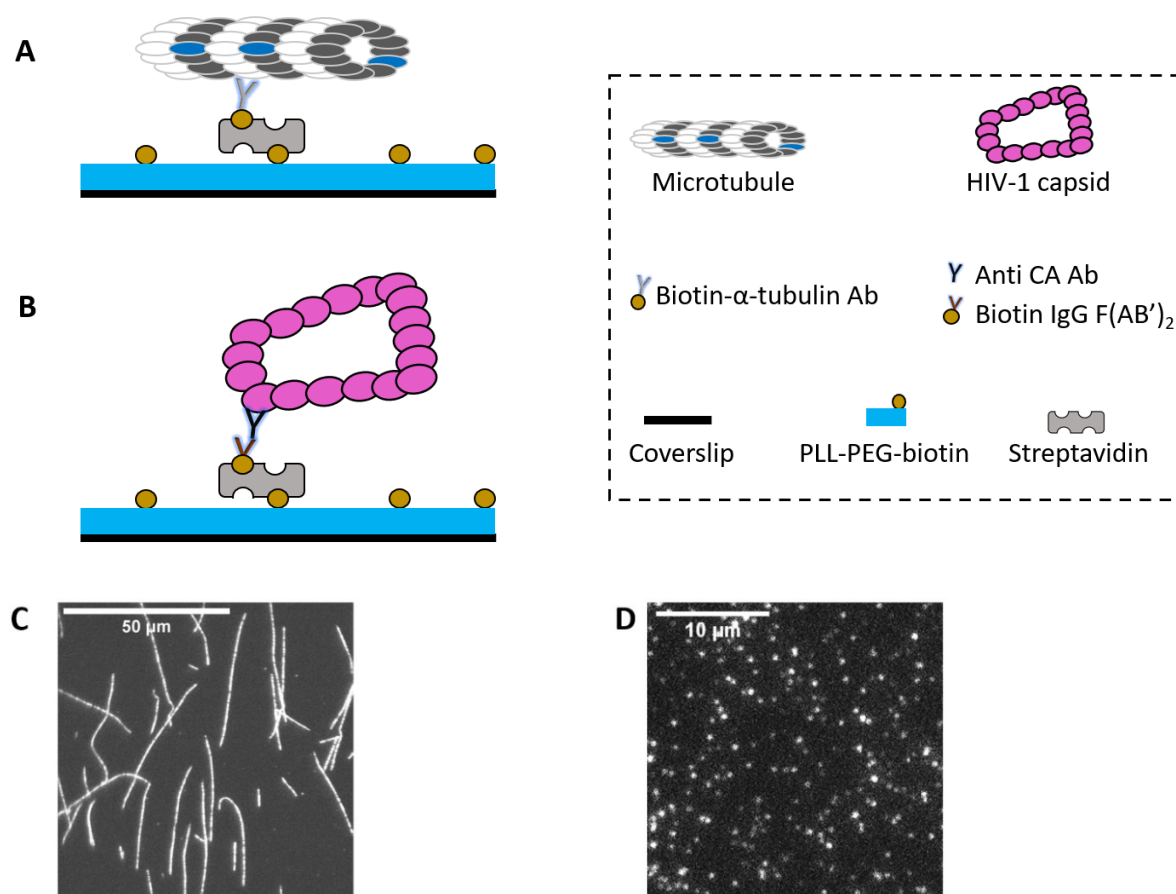


Fig. 8.1. Immobilization of assembled microtubules or HIV-1 capsids on modified surfaces. A-B. Schematic display of the surface chemistry for immobilizing assembled microtubules for motility assays (**A**) and HIV-1 capsids for capsid binding assays (**B**). **C-D.** Representative TIRFm images of immobilized microtubules (**C**) and HIV-1 capsids (**D**)

8.2. SDS PAGE showing the purified proteins

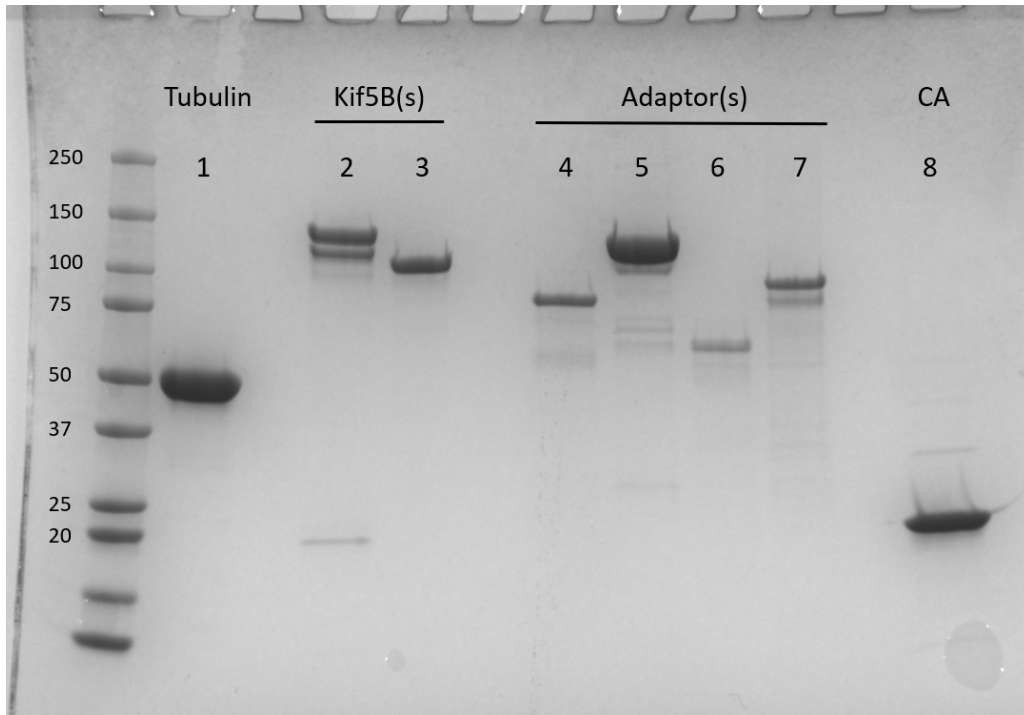


Fig. 8.2. Reducing SDS PAGE with Coomassie staining showing most of the purified proteins used in this thesis. 1. Tubulin. 2-3. hKif5B-mScarlet and dark hKif5B. 4-5. sfGFP-mBICD2_{N25-400} and sfGFP-mBICD2_{FL}. 6-7. Dark hFEZ1 and sfGFP-hFEZ1. 8. Represent HIV-1 CA protein of all the mutants.

8.3. Summary of the interaction measurements between BICD2 or FEZ1 and HIV-1 capsids assembled from CA A92E/A204C or CA A204C

In all the motility assays, we used capsids assembled with CA A92E/A204C (or CA R18G/A92E/A204C when applicable); the amino acid substitution A92E located in the Cyp binding loop on the exterior surface of the capsid improves the solubility of self-assembled capsid particles (see 3.3). To characterize the interactions between HIV-1 capsid and BICD2 or FEZ1, we used capsids assembled with either (1) CA A204C or (2) CA A92E/A204C (**Fig. 8.3**). Both BICD2 and FEZ1 showed significant differences in affinity for binding to capsids assembled from CA A92E/A204C or CA A204C, possibly resulting from measurement errors due to poor signal-to-noise and/or the proteins might make additional weak contacts with the CypA binding loop (e.g. leading to the ~5-fold increase in K_D of the complex formed with BICD2 upon introduction of the A92E substitution).

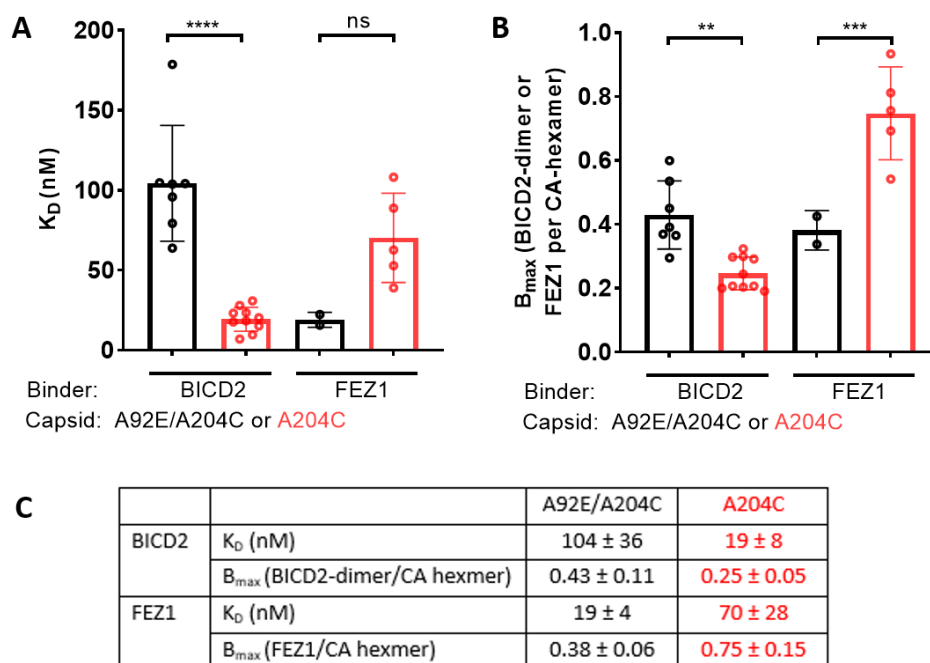


Fig. 8.3. Summary of BICD2 or FEZ1 binding to HIV-1 capsids assembled from CA A92E/A204C or A204C. Dissociation constant (**A**, K_D) and maximum molar binding ratio (**B**, B_{max}) for the BICD2 or FEZ1 binding assays performed using HIV-1 capsid A92E/A204C (black) and A204C (red). Values of K_D and B_{max} are shown in **C** (mean ± SD, $n \geq 6$). Statistical analysis performed using one-way ANOVA, Tukey's multiple comparisons test (****, $p < 0.0001$; ***, $0.0001 \leq p < 0.001$; **, $0.001 \leq p < 0.01$; ns, not significant).

8.4. Analysis to identify “pause” time and calculate average speed

We used the FIJI plugin TrackMate for detection and tracking of single particles in the field of view. The trajectories (X/Y-coordinates) from TrackMate were then further analyzed using a MATLAB script to identify pauses (displacement of less than 30 nm/s) and phases of motility and extract average speed (excluding pauses) and run length of KFC and KF particles. A kymograph of a typical trajectory with multiple pauses and the corresponding displacement trace used to identify pauses is shown in **Fig. 8.4**. Analysis of this trajectory provided the following parameters: walking time (44 s), pause time (30 s), and average speed (178 nm/s); the parameters highly matched with those based on manual analysis of the kymograph.

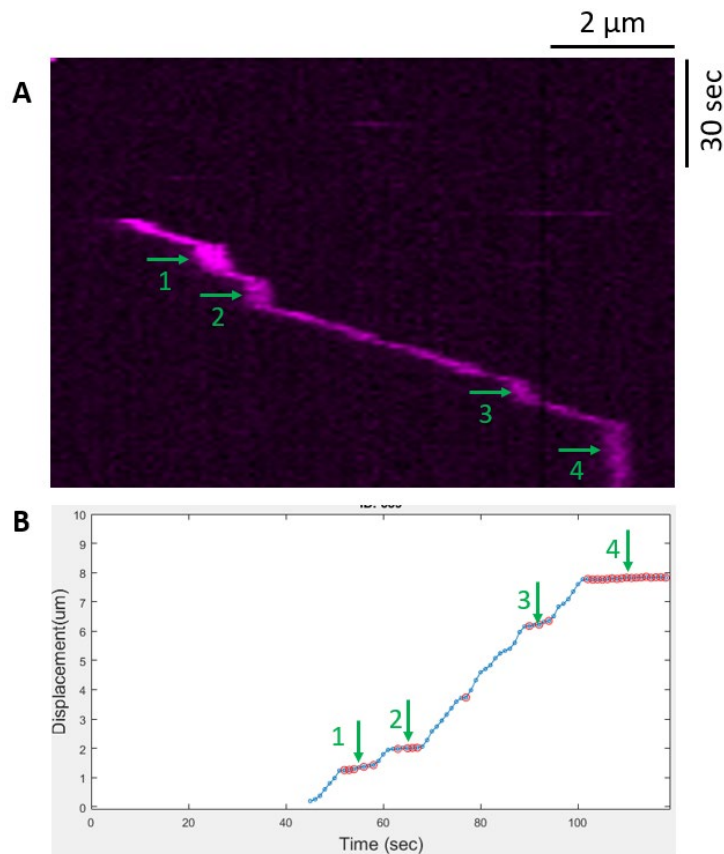


Fig. 8.4. Identification of pauses in an example trajectory. **A.** Kymograph of the capsid channel for a processive KFC particle. The particle walked for 7.9 μm over 74 s (44-119 s) with multiple pauses in the middle and at the end of the run (green arrows). **B.** Corresponding displacement trace. Pauses identified by the analysis script are highlighted with red circles.

8.5. Statistical analysis of the landing rates of KFC complexes with different composition

Table 8.1 contains the P values obtained by statistical analysis of the landing rate data shown in **Fig. 5.8.A**.

Tukey's multiple comparisons test	Summary	Adjusted P Value
K-dark_F-dark_C-488 vs. K-dark_F-dark_C-647	*	0.0237
K-dark_F-dark_C-488 vs. K-dark_F-gfp_C-647	ns	0.9945
K-dark_F-dark_C-488 vs. K-647_F-dark_C-488	ns	0.1061
K-dark_F-dark_C-488 vs. K-dark_F-dark_C-r18g-488	ns	0.097
K-dark_F-dark_C-488 vs. K-dark_F-dark_C-r18g-647	ns	0.0535
K-dark_F-dark_C-488 vs. K-dark_F-gfp_C-r18g-647	ns	0.2857
K-dark_F-dark_C-647 vs. K-dark_F-gfp_C-647	ns	0.2346
K-dark_F-dark_C-647 vs. K-647_F-dark_C-488	****	<0.0001
K-dark_F-dark_C-647 vs. K-dark_F-dark_C-r18g-488	****	<0.0001
K-dark_F-dark_C-647 vs. K-dark_F-dark_C-r18g-647	****	<0.0001
K-dark_F-dark_C-647 vs. K-dark_F-gfp_C-r18g-647	***	0.0009
K-dark_F-gfp_C-647 vs. K-647_F-dark_C-488	ns	0.0545
K-dark_F-gfp_C-647 vs. K-dark_F-dark_C-r18g-488	*	0.0499
K-dark_F-gfp_C-647 vs. K-dark_F-dark_C-r18g-647	*	0.0285
K-dark_F-gfp_C-647 vs. K-dark_F-gfp_C-r18g-647	ns	>0.9999
K-647_F-dark_C-488 vs. K-dark_F-dark_C-r18g-488	ns	>0.9999
K-647_F-dark_C-488 vs. K-dark_F-dark_C-r18g-647	ns	>0.9999
K-647_F-dark_C-488 vs. K-dark_F-gfp_C-r18g-647	ns	>0.9999
K-dark_F-dark_C-r18g-488 vs. K-dark_F-dark_C-r18g-647	ns	<0.0001
K-dark_F-dark_C-r18g-488 vs. K-dark_F-gfp_C-r18g-647	ns	>0.9999
K-dark_F-dark_C-r18g-647 vs. K-dark_F-gfp_C-r18g-647	ns	>0.9999

Table 8.1. One-way ANOVA-Tukey's with multiple comparisons test of the landing rates of KFC complexes with different compositions.

8.6. Preliminary analysis comparing the motility of KF and KFC complexes

Parameters extracted from the trajectories of KF and KFC complexes were compared to determine whether the duration of walking and pausing phases differed between these complexes (**Fig. 8.6**). While no significant change was observed for walking time, KFC complexes showed an increase in total time and pause time compared to KF complexes. Further investigation is needed to validate these differences and determine their molecular basis (e.g. whether there is a correlation of these parameters with the number of motors per complex).

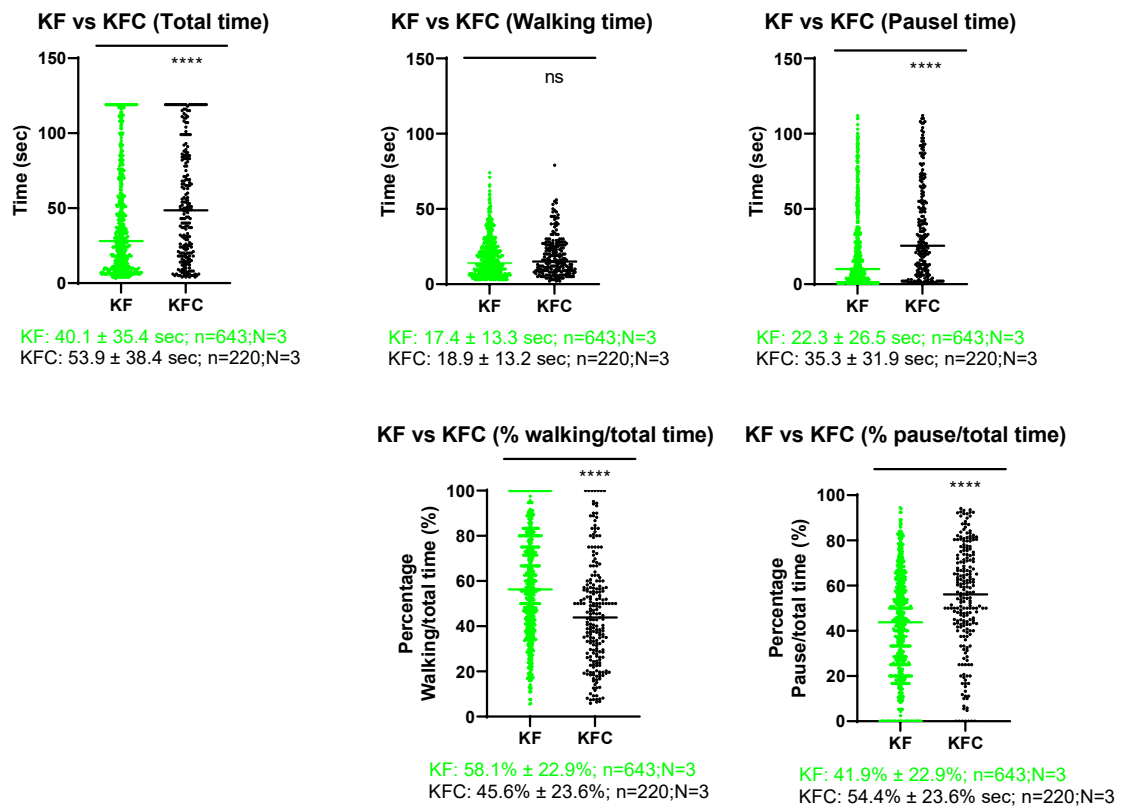


Fig. 8.5. Comparison of parameters describing the trajectories of KF and KFC particles. Total time of a processive particle remaining associated with the microtubule, walking time, and pause time were extracted from trajectories following the approach as described in section 8.4. Different groups in the bar charts were compared using an unpaired T test (****, $p < 0.0001$; ns, not significant, $p > 0.05$).